ABSTRACT

Title of Dissertation: NUMERICAL MODELING AND EXPERIMENTAL STUDY OF A NOVEL METAL-POLYMER COMPOSITE HEAT EXCHANGER FOR SENSIBLE AND LATENT THERMAL ENERGY STORAGE APPLICATIONS

Gargi Kailkhura, Doctor of Philosophy, 2022

Dissertation directed by: Professor Michael Ohadi, Mechanical Engineering Department

Compact, lightweight, and low-cost heat exchangers (HXs) have the potential to improve efficiencies and save power and carbon foot print in a wide array of applications. The present study investigates an entirely additively-manufactured novel metal-polymer composite heat exchanger, enabled by an innovative and patented cross-media thermal exchange approach, which yields an effective thermal conductivity of 130 W/m-K for the heat exchanger. This record-high thermal conductivity is more than an order of magnitude higher that the previously reported thermal conductivity for polymer and polymer composite HXs. Drawing on the concept of external flow over the tube banks, the proposed HX features a staggered arrangement of fins. This class of HXs are often used for gas-to-liquid sensible cooling applications. However, they can also be designed for latent thermal energy storage applications by employing low-

cost and high energy-storage-density phase change materials (PCMs) such as salt-hydrates and alike in either the hot or cold side of the HX, depending on the application. An extensive literature survey on tube banks shows that, though numerous correlations exist in the literature for flow over tube banks, these correlations usually fall outside the range for the current HX design for low-Reynolds number applications ($\boldsymbol{Re < 100}$). Furthermore, the PCM models present in the literature are either very challenging to solve analytically or are computationally expensive. Thus, the dissertation emphasizes developing computationally efficient and robust numerical models for sensible and latent cooling applications.

The numerical models compute the overall thermal and pressure-drop performance metrics based on segment-level modeling. They integrate the performance parameters such as Euler, Nusselt numbers, or latent thermal energy with the entire HX analytically, thus significantly reducing the computational cost. For steady-state sensible thermal energy storage applications, a high-fidelity 3D CFD-based modeling approach is used, based on the actual dimensions of the printed HXs rather than a traditional 2D CFD-based model. It also resolves the issues due to the 3D velocity field, which aren’t captured in the 2D CFD models, and are particularly important for HXs utilizing narrow/micro channels. This modeling approach is used to obtain optimized HXs for case examples of 5-40 kW air-conditioning applications and 250-W electronic cooling applications for nominal operating and flow conditions. The 250-W unit is further validated experimentally and is observed to be within 17% for waterside pressure drop, 11% for airside pressure drop, and within 8% for thermal resistance when compared against experimental measurements.

For transient latent thermal storage applications, an analytical-based 1D reduced order model (ROM) for segment-level modeling is developed based on 1D radial conduction inside the PCM. It is numerically validated with commercial CFD tools to within 10% except for cases where axial conduction in PCM is possible due to the high resistance of wire embedded in the PCM. The 1D ROM is used in optimizing a 1.44-MJ TES unit for peak-load building cooling applications and a 19.2-kJ HX for pulsed-power cooling applications. The 1.44-MJ unit is experimentally tested and observed to be within 17% for the melting time of complete PCM and about 8% for the freezing time of the complete PCM.

Lastly, another novel and hybrid thermal energy storage design is formulated, which utilizes two different PCMs: shape memory alloys (SMAs) instead of metal wires and salt-hydrates contained inside polymer channels similar to the reference designs. Besides the novel thermal energy storage design, a novel methodology on Wilson plot for finned surfaces on both fluid-sides is introduced, which is first of its kind in the literature. Ongoing and future work in both these areas is also recommended in the final chapter of the thesis.

NUMERICAL MODELING AND EXPERIMENTAL STUDY OF A NOVEL METAL-POLYMER COMPOSITE HEAT EXCHANGER FOR SENSIBLE AND LATENT THERMAL ENERGY STORAGE APPLICATIONS

by

Gargi Kailkhura

Dissertation submitted to the Faculty of the Graduate School of the
University of Maryland, College Park, in partial fulfillment
of the requirements for the degree of
Doctor of Philosophy
2022

Advisory Committee:
Professor Michael M. Ohadi, Chair
Professor Jelena Srebric
Professor Amir Riaz
Professor Bao Yang
Professor Liangbing Hu
Associate Professor Amir Shooshtari

Acknowledgments

I sincerely acknowledge the contribution of my advisor, Prof. Michael Ohadi, for his invaluable advice and guidance towards my research, for believing in me, and for allowing me to learn and perform to my best abilities time and again. I am also grateful to Dr. Raphael K. Mandel for always providing his technical expertise and advice. I have been fortunate enough to learn many technical skills from him. I also appreciate the technical advice, experience, and guidance of Dr. Amir H. Shooshtari in shaping my research profile. Working at the Advanced Heat Exchanger and Process Intensification Laboratory (AHXPI) has been an eventful journey full of learnings and experiences. I have gained experimental and numerical knowledge of heat exchangers related to thermal management. I am also thankful to my other committee members, Dr. Amir Riaz, Dr. Bao Yang, Dr. Jelena Sreberic, and Dr. Liangbing Hu, for agreeing to be a part of my defense. I appreciate their time and efforts.

I also want to express my special thanks to my lab-mates – Sevket Yuruker, Fabio Battaglia, Veeresh Ayyagari, Sasha Dessiatoun, Harsimranjit Singh, Zhengda Yao, Devashish Shreshtha, Sai Manish, and Soma Roy. They helped create a fun-loving and collaborative research environment where I got to learn something new from each of them every day. I am specifically thankful to my best friend of ten years, Kunal Ahuja, for his deep understanding and humor and always standing by me in my thick and thin. I am also grateful to have my beloved cat, Stella, for constant means of love and support.

Lastly, I want to express my sincere gratitude to my family for their love, patience, and understanding. I want to thank my parents, Ramesh Chandra Kailkhura and Hrita Kailkhura, for everything I have and I could because of their love, hard work, and sacrifices. I also want to thank my younger sister, Shraddha Kailkhura, for keeping the child inside me alive. And I am also grateful that my elder brother, Bhavya Kailkhura, guided me with his own Ph.D. experiences and proud research achievements.

In the end, I want to thank the U.S. Department of Energy/ARPA-E, Carrier, and Army Research Lab (ARL) for providing financial support and guidance helpful for my research.

Table of Contents

Acknowledgments ii

Table of Contents iv

List of Tables vii

List of Figures viii

List of Abbreviations xiii

Chapter 1: Introduction 1

1.1 Background and Motivation 1

1.2. Challenges associated with conventional polymer HXs 2

1.2.1. Sensible storage type 2

1.2.2. Latent thermal storage type 4

1.3. Major Novel Contributions of the Present Work 5

1.4. Dissertation Layout 6

Chapter 2: A Novel Metal Polymer Composite HX 9

2.1. The Cross-Media Heat Exchangers 9

2.1.1. Sensible storage based iCMHX unit 9

2.1.2. Latent thermal storage-based TES 11

2.2. Additive manufacturing Technique 12

2.3. Applications of Novel Metal Polymer Composite HXs 17

2.4. Summary 21

Chapter 3: Literature Review 22

3.1. Theoretical Background 22

3.1.1. Tube Banks 22

3.1.2. Phase Change Materials 28

3.2. Tube-Bank Correlations 30

3.3. PCM based models 38

3.4. Summary 1
Chapter 4: Numerical Modeling 2
4.1. Need for the Numerical Study 2
4.2. Sensible Storage Model 3
4.2.1. iCMHX Geometry 4
4.2.2. Traditional 2D CFD Segment Level Model 5
4.2.3. Analytical Model Based Entire HX Model 14
4.2.4. Realistic 3D CFD Segment Level Model 21
4.3. Latent Thermal Storage Model 30
4.3.1. ROM 30
4.3.2. Observed Trends 46
4.3.3. Non-dimensionalization 48
4.3.4. 2D CFD Axisymmetric Reference Model 49
4.3.5. ROM Test-case Setup 50
4.3.6. Validation with CFD 53
4.4. Summary 57
Chapter 5: Design Optimization 60
5.1. Optimization Algorithm 60
5.2. Sensible Cooling Applications 62
5.2.1. Problem Statement 62
5.2.2. Optimization Formulation 63
5.2.3. Assumptions 66
5.2.4. Case Studies 67
5.3. Latent Energy Storage Applications 77
5.3.1. Peak-Load Building Cooling Applications 77
5.3.2. Pulsed-Power Applications 82
5.4. Summary 87

Chapter 6: Experimental Study 88
  6.1. Sensible Cooling for electronic cooling of Desktop Computers 89
    6.1.1. Testing 1: Investigating the effect of coating via traditional experimental and numerical approach 89
    6.1.2. Testing 2: Improving experimental and numerical approach 107
  6.2. Latent Energy Storage 120
    6.2.1. Experimental Set-up 120
    6.2.2. Instrumentation and Calibration 122
    6.2.3. Data Reduction 122
    6.2.4. Experimental Results and Comparison with Numerical Study 122
  6.3. Summary 126
Chapter 7: Conclusion and Proposed Future Work 129
  7.1. Conclusion 129
  7.2. Proposed Future Work 132
    7.2.1. Numerical Work 132
    7.2.2. Experimental Work 141
  7.3. List of Publications 146
Appendices 147
  Appendix A 147
  Appendix B.1. 148
  Appendix B.2. 151
  Appendix C 152
Bibliography 156

List of Tables

Table 1: Evolution of a family of CMHXs developed at the AHXPI laboratory.........11
Table 2: Staggered tube-bank correlations for (a) Eu and (b) Nu.............................. 36
Table 3: Inline tube-bank correlations for (a) Eu and (b) Nu 37
Table 4: Design specifications of iCMHX.. 5
Table 5: Operating Conditions for Electronic Cooling Applications............................ 7
Table 6: Specifications of Mesh Levels 11
Table 7: Mesh-Independence Summary.. 13
Table 8: Measured dimensions of iCMHX due to printing variabilities..................... 23
Table 9: Design details, as measured, of the current iCMHX unit 23
Table 10: Assumptions and solver details for 3D model setup.................................. 28
Table 11: List of non-dimensional groups 49
Table 12: Geometrical and operating parameters for baseline test-case of single tube model.. 52
Table 13: Time-step independence study.. 53
Table 14: Overall range for dimensionless parameters.. 54
Table 15: Design optimization parameters 65
Table 16: Air and Brine properties as taken from EES.. 66
Table 17: Operating conditions and target for building cooling application 78
Table 18: Material Properties for PCM-to-gas CMHX.. 79
Table 19: Design Optimization Parameters for PCM-to-Gas CMHX 80
Table 20: Optimization Results.. 81
Table 21: Optimized Q/m values for different pressure-drops 81
Table 22: HX performance for 0.8mm aluminum wire with n-hexadecane PCM...... 82
Table 23: Glauber's salt-PCM Properties 84
Table 24: Problem Statement for Pulsed-Power Cooling Applications...................... 84
Table 25: Optimized design variables and performance parameters 86
Table 26: Detailed comparison of 5 units 89
Table 27: List of Specifications and uncertainties of equipment............................... 92
Table 28: Technical specifications of measuring instruments...................................110
Table 29: Operating conditions for the experiment 111
Table 30: Calculated Uncertainties for key pressure-drop and heat transfer parameters 112
Table 31: List of instruments and their uncertainties.. 122
Table 32: Operating conditions... 122
Table 33: Comparison of key parameters between experimental and numerical study 126

List of Figures

Figure 1:Polymer HX Concepts in Literature: (a) polymer-tube HX [14] (b) crossflow micro-passage HX [9] (c) hybrid metal-polymer HX [10] and (d) continuous wire-structure HX [11,12] 4
Figure 2: (a) A double-pass iCMHX design showing cross-media approach; (b) planar views showing staggered configuration; (c) planar views showing simplified heat transfer domain and (d) conventional HX with finned surfaces only on airside 10
Figure 3: HX Geometry (a) isometric view (b) cross-sectional view of XZ plane with cross-media shown in red highlights (c) cross-sectional view of XY plane and (d) cross-media approach as marked in (b) 12
Figure 4: Fabrication process of HXs for (a) crossflow liquid to gas sensible storage applications (b) gas-to-PCM for latent thermal energy storage applications at AHXPI laboratory 15
Figure 5: Additively manufactured and coated units (a) iCMHX and (b) air-to-PCM TES at the AHXPI Laboratory 16
Figure 6:Liquid cooling applications in CPU 18
Figure 7: peak-load shifting in building cooling applications (a) charging mode at night (b) discharging mode at peak-times during the day, and (c) without CMTES units at off-peak times during the day 21
Figure 8: Tube bank configurations for (a) external flow over tube banks for both fluids; and (b) planar views in the direction of fluid-flow across inline tube-bank configuration and (c) staggered tube-bank configuration 24
Figure 9: Physic of fluid flow across single cylinder/tube 26
Figure 10: Velocity definitions for (a) inline and (b) staggered tube-bank configurations 26
Figure 11: Variation of enthalpy with temperature during the PCM transition process 28
Figure 12: (a) Latent heat energy storage density and (b) material cost for different PCMs [33] 30
Figure 13: Availability of literature correlations for staggered tube-banks for different $\boldsymbol{ST/D}$ and $\boldsymbol{SL/D}$ values at different $\boldsymbol{Re}$ 3
Figure 14: Schematic of the iCMHX with detailed geometry and fluid paths 4
Figure 15: Overview of a modeling approach for iCMHX from segment level to entire HX level 5
Figure 16: Numerical set-up including domain and boundary conditions for segment level model of iCMHX 7
Figure 17: Meshed domain between tube-bundles consisting of 922,594 cells (top) and meshing as seen around the circular tube (bottom) 8
Figure 18: Methodology to compute mesh-independent Euler and Nusselt Numbers 11

Figure 19: Trend of liquid-side (a) Euler Number and (b) Nusselt numbers with Equivalent Mesh at particular Re value 13
Figure 20: Methodology for prediction of HX performance 17
Figure 21: Trend of airside Nusselt number with Reynolds 17
Figure 22: Methodology for computing pressure-drop 19
Figure 23: Trend of Euler number with Reynolds number 20
Figure 24: Trend of Nusselt number with Reynolds number for air and water 20
Figure 25: (a) SEM image for wire spacings and wire shape; and (b) microscope image of varying water channel width 22
Figure 26: Domain simplifications: (a) entire iCMHX domain; (b) simplification to segment-level water-side 3D domain (c) simplification to segment level air-side domain 26
Figure 27: Meshed domains for the ellipsoidal fin on the waterside domain for illustration purpose 27
Figure 28: Contour plots of (a) velocity and (b) temperature for some particular flow rate at symmetry plane of the air-side domain located $\boldsymbol{Wa/2}$ distance from the wall28
Figure 29: Convective heat transfer coefficients obtained from 3D CFD based on Equation (12) for (a) air side, and (b) water side 29
Figure 30: Design of gas-to-PCM TES system (a) isometric view (b) cross-sectional view of XY plane showing metal wires in tube-bank geometry (c) cross-sectional view of XZ plane with cross-media approach highlighted in red and (d) cross-media approach leading to melting of PCM 32
Figure 31: Domain simplification (a) Entire TES domain to single row domain and (b) single row domain to single wire radial domain 35
Figure 32: Example of PCM overlap for PCM-wire cylinders when visualized in tube-bank geometry 36
Figure 33:Comparing thermal masses for (a) cartesian and (b) radial PCM domains for neighboring wires with overlap regions $A1$ and $A2$ marked in red dashed circles..... 37
Figure 34: Different overlap cases governed by specific ST/SL values and controlled directions 38
Figure 35: Compute melt-front location at next time-step 46
Figure 36: Typical trends obtained from 1D ROM for (i) heat transfer rate vs time and (b) contour plot at a particular time on XY plane 47
Figure 37: 2D axisymmetric reference model 50
Figure 38: Effect of the overlapped area (Aratio) on the percentage difference ($\%\Delta 1$) between the 1D ROM model (continuous lines; dash lines for $rmax *= \infty$) and 2D cartesian model (discrete points) due to different ranges of $ST/SL$and $rmax *$........ 52
Figure 39: Effect of Dimensional parameters: (i) τ (ii) $Bi \times LR$ and (iii) $Rwire *$ on the performance parameter, $t * (\chi = 0.9)$; where solid lines represent ROM model while points represent 2D reference model 56

Figure 40: Flowchart for 1D ROM algorithm... 59
Figure 41: Methodology for design optimization using Exterior Penalty Method..... 62
Figure 42: Heat exchanger and fan configuration as stated in the problem statement 63
Figure 43: Operating conditions for the air-conditioning applications....................... 64
Figure 44: Types of iCMHX Orientation 64
Figure 45: Pareto set for Vertical Orientation 68
Figure 46: Effect of design parameters on optimal points for vertical orientation..... 69
Figure 47: Pareto set for Horizontal Orientation 70
Figure 48: Effect of design parameters on optimal points for horizontal orientation. 72
Figure 49: Pareto set for double-pass system 73
Figure 50: Effect of design parameters on optimal points for double-pass 73
Figure 51: Pareto set for CCC operating condition 74
Figure 52: Effects of design parameters on optimal points for CCC.......................... 75
Figure 53: Effect of orientation on CMHX performance 76
Figure 54: Effect of number of liquid passes on CMHX performance....................... 77
Figure 55: TES used as an energy storage HX in primary cooling of pulsed-power applications 83
Figure 56: TES System design for PCM-to-liquid applications 83
Figure 57: Modification of NL to incorporate continuous value of NL 85
Figure 58: Optimized TES design configuration 86
Figure 59: Comparison of the post-processed iCMHX units in terms of their airside clogging based on the light transmitted through them 90
Figure 60: Schematic of test-loop for iCMHX 91
Figure 61: Rotameter calibration: (a) schematic (b) calibrated data and (c) calibration curve.. 94
Figure 62: Coriolis flowmeter calibration: (a) schematic (b) calibration data (c) calibration curve.. 95
Figure 63: Pressure transducer calibration (a) schematic (b) calibration data and (c) calibration curve.. 96
Figure 64: Representation of Core Pressure Drop from Measured Pressure Drop including pressure losses.. 99
Figure 65: Measurement of waterside pressure-drop across the core of the reference iCMHX unit 100
Figure 66: Comparison of thermal performance for the same fabricated units 102
Figure 67: (a) Comparison of air-side pressure drop performance for the same fabricated units, (b) clogging observed on the fins of Unit 3, exposed to the airside and (c) Comparison of air-side pressure drop with 2D based CFD study for Unit 1 103
Figure 68: Comparison of waterside pressure-drop for the same fabricated units as well as with the 2D based CFD study.. 104
Figure 69: Comparison of waterside impedance with thinned sealant unit............. 106

Figure 70: Comparison of air impedance on the waterside before and after sealing of Unit 4 107
Figure 71: Experimental test loop (a) schematic (a) apparatus picture 109
Figure 72: Sealed thermocouples in water tubes 110
Figure 73: Comparison of experimental and numerical results of $\Delta T/Q$ for different mw 114
Figure 74: Comparison of experimental and numerical results of $\Delta pwcore$ for different mw 115
Figure 75: Choking effect around the nearest wires to the wall due to small spacing (S) (on left) and no-choking effect around those wires if S is increased (S') (on right) at some particular flow-rate 117
Figure 76: Comparison of experimental and numerical results of $\Delta T/Q$ for different ma 118
Figure 77: Comparison of experimental and numerical results of Δpa for different ma 118
Figure 78: Comparison of experimental $\Delta T/Q$ for different pumping powers $Ppumping$ for both iCMHX and conventional CPU radiator 119
Figure 79: Experimental setup for testing PCM-to-air TES unit at AHXPI laboratory (a) image (b) schematic 122
Figure 80: (a) Experimentally obtained temperature and heat transfer rate trends covering I-VII regimes; and Comparison of experimental temperature trend with 1D ROM for (a) Regime I-IV and (c) Regime V-VII 125
Figure 81: Different fin shapes depending on surface area/volume ratio 133
Figure 82: Internal fluid path inside the water channel in counterflow configuration for ribbon-shaped fins 134
Figure 83: Shifted ribbon design facilitating uniform flow distribution 135
Figure 84: Typical curve-fit forms for metamodel-development generated from MATLAB code for staggered circular fins 137
Figure 85: Effect of fin elongation (b) on fluid-side pressure-drop for different Re range 138
Figure 86: (a) Thermophysical properties for different PCMS: Cu SMAs, NiTi SMAs, Salt hydrates (Ongoing work by Dr. Ichiro Takeuchi) and (b) Estimation of properties of the SMAs as obtained from literature 139
Figure 87: (a) Segment level model for hybrid SMA-SH design for TES and (b) Typical contour plot for melting of SMA-wire (NiTi) and SH (Glauber's salt) PCMs in the hybrid TES design, obtained in Ansys Fluent 140
Figure 88: Comparison of different hybrid models (SH+SMA wire) and the reference TES model (SH + Cu wire) (a) Cumulative energy and (b) Cost analysis 141
Figure 89: Schematic of test loop for iCMHX used as CPU radiator in real-life CPU cooling environment 142

Figure 90: Wilson Plot for Waterside 144
Figure 91:Organization of dissertation 147
Figure 92: Range of S_T/S_L for different cases based on directions of overlap in ST ,SL and SD 150
Figure 93: Simplification of the computational domain of single wire domain 154

List of Abbreviations

Nomenclature

A	area, m2
Bi	Biot number
C	heat capacity, $\boldsymbol{W/K}$
C_p	heat capacity, W/kg-K
dT	positive temperature difference between inlet temperature of fluids, K
D	wire diameter, m
e	energy in single PCM-wire, J
Δe_{total}	energy in single row, J
ΔE	energy in TES, J
E_{total}	time-integrated energy in TES, J
Eu	Euler number
f	friction factor
Fo	Fourier number
G	mass flux density, kg/m^{2}s
h	heat transfer coefficient, W/m^2-K
H	latent heat of fusion, J/kg
k	thermal conductivity, W/m-K
L	flow length, m
LR	length-ratio
m	mass, kg
$\dot{m}$	mass flow rate, kg/s
Δm	transitioned mass, kg
Δm_{max}	Maximum untransitioned mass, kg
mp	fin-efficiency parameter
n or nc	number of channels
N	number/quantity of cells or fins
Nu	Nusselt number
P	Pumping power, W
ΔP	pressure, Pa
Pr	Prandtl number
Q	heat transfer rate, W
R	radius, m
R	thermal resistance, K/W
Re	Reynolds number
S_D	diagonal fin spacing, m
S_L	longitudinal fin spacing, m
S_T	transverse fin spacing, m
Ste	Stefan number
t	time, s
t_{wall}	wall thickness, m
Δt	time-step size, s
T	temperature, K

UA	thermal conductance, W/K
v	velocity of fluid, m/s
Vol	volume, m^3
W	width of channel, m

Greek Symbols

χ	liquid fraction
ε	effectiveness
μ	dynamic viscosity, kg/m-s
η	fin efficiency
ρ	density, kg/m3
τ	time constant

Subscripts

a	air
b	along water-flow length
avg	average
cs	cross-section
cond	conductive
cu	Copper
eff	effective
eqv	equivalent
h	hydraulic
max	maximum
min	minimum
nf	no flow direction
o	nominal
poly	polymer
r	ratio of minimum to maximum
th	thermal
Tot	total
W	water
X	direction along +x axis
y	direction along +y axis

Superscripts

*	non-dimensinalized number
c	effective length
cs	cross-section
cells	cells

chan	channel
eff	effective
fins	related to fins
in	inlet
m	melting
out	outlet

Abbreviations

AR	Aspect Ratio
ABS	Acrylonitrile Butadiene Styrene
AHXPI	Advanced Heat Exchanger and Process Intensification
CMHX	Cross Media Heat Exchanger
CMTES	Cross Media Thermal Energy Storage System
EFCAM	Embedded Fiber Composite Additive Manufacturing
EB	energy balance
FDM	Fused Deposition Modeling
FEA	Finite Element Method
FVM	Finite Volume Method
HX	Heat exchanger
iCMHX	Integrated Cross Media Heat Exchanger
LMTD	Log mean average temperature difference
NTU	Number of transfer units
PCM	Phase Change Material
PETG	Polyethylene Terapthalate
ROM	Reduced-order-model
SH	Salt Hydrates
SMA	Shape Memory Alloys
TES	Thermal Energy Storage
TIM	Thermal interface material

Chapter 1: Introduction

This chapter will first discuss the background and motivation behind the need for compact, low-cost, and lightweight heat exchangers (HXs), and the role metal polymer-based composite HXs can play in realizing such heat exchangers. Next, the second section of the chapter discusses the conventional polymer composite HX development reported in the literature and the challenges in their design approach. It also includes additional challenges arising from the phase change materials (PCMs)-based HXs for latent thermal storage applications. Finally, the last section presents the novel contributions of the entire research and dissertation layout which serves as an outline covering the different chapters of the thesis. These motivations and challenges lead to development of a novel metal-polymer composite HX based on a cross-media approach, which is the basis for the present research. The proposed system can be used for sensible and latent thermal storage applications.

1.1 Background and Motivation

For years, heat exchangers have remained as critically important solution to the fundamental problems involving heating and cooling applications in industries. As the industries are evolving towards more efficient and miniaturized devices for advanced high-power applications, there is a growing need to meet the thermal challenges associated with unwanted heat dissipation. Because compact heat exchangers are an integral part of energy exchange processes, their designs have continuously evolved to meet the growing demands of heat dissipation in diverse industries. Compact HXs for the sensible storage applications of gas-to-liquid typically consist of metal structures configured with different types of fins such as louver fins, wavy fins, and offset-strip fins [1] on the airside. The purpose is to enhance the airside heat transfer rate since the airside heat transfer coefficient is typically very low. However, such designs' liquid heat transfer area is typically only minimally enhanced, as the liquid heat transfer coefficient is already much higher than the air. Moreover, it can be challenging to fabricate complex geometries inside narrow liquid-side channels. Thus, compact, lightweight, low-cost, and low thermal resistance HX units are needed to meet the increasing power-dissipation requirements of diverse industrial applications.

Similarly, there is a need to reduce the mismatch between supply and demand of energy [2] due to the increasing demand for efficient energy systems. One such method of increasing the energy efficiency of the power systems is by developing latent thermal energy storage devices that can store energy from time-variable sources and match time-variable demands with a constant output source. Research interest in energy storage devices based on latent thermal energy storage using PCMs is rapidly growing due to their isothermal storage and high storage density [3], resulting in compact and reduced-weight systems [4,5].

1.2 Challenges associated with conventional polymer HXs

1.2.1. Sensible storage type

Due to the polymers' lightweight, low-cost, and anti-corrosive properties, several of the HX designs have focused on polymer HXs [6] (see Figure 1 (a)). But the lower thermal conductivity of polymer of about $0.2 \text{ to } 1 \text{ W/m} - \text{K}$ gives relatively higher conductive resistance across the HX structure. One way to resolve this issue is by increasing the thermal conductivity of the polymer HXs to up to 20 times by using metal fillers in the polymer media [7]. However, extensive research is still required to study the effect of metal fillers and polymers on the effective thermal conductivity and anisotropic properties of the HXs [8]. Another way to solve this problem is to reduce the polymer wall thickness by using thin-walled polymer HXs such as the crossflow micro-passage HXs [9] (see *Figure 1* (b)). But such thin structures are limited by manufacturing constraints. Alternatively, recent studies have innovatively developed metal-polymer composite HXs such as hybrid polymer HXs [10] (see *Figure 1* (d)) and continuous wire-HXs [11,12] (see *Figure 1* (c)). These hybrid polymer HXs consist of helically wound hybrid tubes of copper and polymer whose effective thermal conductivity increased from $0.1\,\mathrm{W/m-K}$ to $1\,\mathrm{W/m-K}$. But these HXs are constrained in their tube diameter size. The continuous wire-HXs consist of fine metal wires, with diameters as small as $0.105 - 0.25\,\mathrm{mm}$, woven/knitted through plastic walls. They draw comparisons with pin-fin arrays, which deliver the same performance as the conventional louvered fin HXs but at 22% less volume [13]. However, these HXs suffer from wire-curvature issues and lack a robust fabrication procedure.

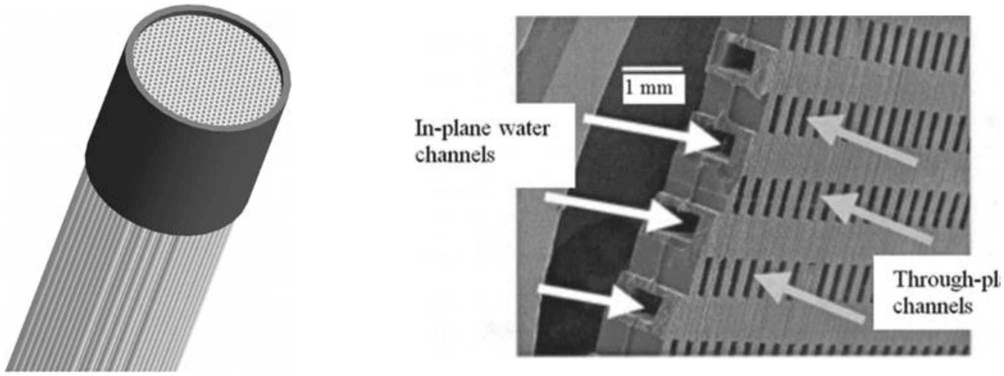

(a) (b)

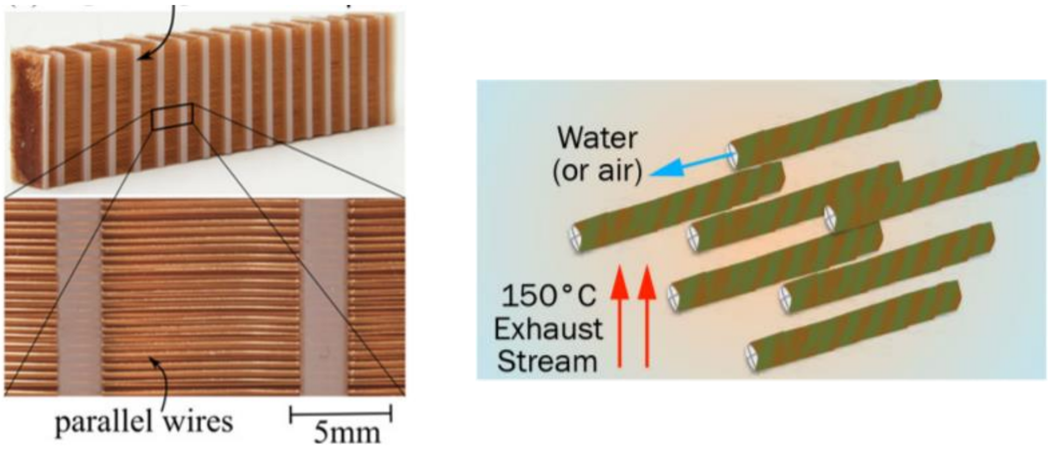

(c) (d)

Figure 1:Polymer HX Concepts in Literature: (a) polymer-tube HX [14] (b) crossflow micro-passage HX [9] (c) hybrid metal-polymer HX [10] and (d) continuous wire-structure HX [11,12]

1.2.2. Latent thermal storage type

Some conventional PCM-based HXs contain PCMs in rectangular, cylindrical, and spherical geometries. Several cylindrical PCM-based HXs consist of shell and tube HXs with an inner cylinder consisting of the flow passing inside the tube and the outer cylinder consisting of the PCM [15,16]. This cylindrical-based technique has been extended to PCM cylinders enclosing finned tubes [17] and other cylindrical-based latent heat storage systems [5,18,19]. But these HXs typically face challenges mainly associated with the PCM, such as its low thermal conductivity in the range of 0.22W/m-K [20], sub-cooling and phase-segregation issues [21], volume-expansion issues, and an expensive encapsulation process comprising up to 99% of the total PCM cost [22]. The present research, accordingly, meets the above challenges associated with sensible and latent thermal storage applications by utilizing a novel, entirely additively-manufactured, low-cost, and lightweight metal-polymer composite HX [23–26] with an effective thermal conductivity in the range of 130 W/m-K [26] and an effective PCM thermal conductivity of about 16 W/m-K. These highly effective thermal conductivities are attained due to high thermal conductivity metal wires. These HXs are based on a patented cross-media approach and are also called as CMHXs (Cross-Media Heat Exchangers). The present dissertation discusses the most advanced version of CMHXs, called iCMHXs (integrated CMHXs), where the word "integrated" refers to the integrated manifolds attached to the HX core during the additive manufacturing process. When integrated with the PCMs, these iCMHXs are referred to as thermal energy storage (TES) systems. The iCMHXs and TES systems use an optimized finned area on both airside and liquid-side surfaces to yield better thermal performance than the conventional units for sensible and latent thermal energy storage applications, respectively.

Thus, the numerical design, modeling and experimental study of these novel metal-polymer composite HXs form the basis for the entire thesis, whose major novel contributions are explained in the next section.

1.3 Major Novel Contributions of the Present Work

The present dissertation entails the following significant novel contributions:

- For the first time, a robust and computationally efficient partly numerical and partly-analytical model is developed to compute the entire CMHX performance for sensible thermal energy storage applications. This can be a useful design tool for CMHX applications.
- For the first time, a computationally efficient analytical model is developed, based on thermal resistance and energy conservation principles, for latent thermal energy storage applications. The model is a reduced-order model (ROM) based on 1D radial conduction inside PCMs and is also validated with commercial CFD tools.

- For the first time, the effects of dimensional variabilities on CMHX's performance due to the additive manufacturing process manufacturing deviations from the design are statistically studied. Furthermore, the robust numerical model is successfully used to compute the CMHX performance based on new dimensions, geometries and fabrication details.
- A multi-objective design optimization is performed using the in-house developed numerical model for diverse sensible and latent thermal storage applications.
- For the first time, developed a hybrid thermal energy storage model consisting of wires made from Shape Memory Alloys (SMAs) and containing salt-hydrate (SH) inside polymer channels.

1.4 Dissertation Layout

The novel contributions described above are presented in the in the remainder of this dissertation, as outlined in the following chapters.

Chapter 2: Novel Metal Polymer Composite HX

Chapter 2 describes in detail the novel design of the metal-polymer composite HX (iCMHXs and TES systems) based on the patented cross-media approach and a customized additive manufacturing technique using an in-house printer. It discusses the design flexibility of the HX's concept in adapting for both sensible and latent thermal storage applications.

Chapter 3: Literature Review

This chapter includes the theoretical and experimental validation knowledge required to understand the numerical model for the iCMHX and TES system. It further discusses the physics behind the external flow over the wires and material characteristics of the

PCMs. Then it reviews the open literature on empirical correlations for the flow in the HX and transient modeling of the PCM in the HXs and presents the shortcomings of the literature.

Chapter 4: Numerical Modeling

This chapter presents the robust numerical modeling of the entire HX, which is typically based on CFD modeling of a segment-level model in the case of iCMHXs in sensible heat transfer, and an analytical-based model in the case of TES systems in latent thermal energy storage applications. The CFD-based modeling is performed on metal wires arranged in an in-line or staggered orientation and for laminar flow conditions. It is non-dimensionalized using Euler (Eu) and Nusselt (Nu) numbers. The chapter also presents the adaptation of the robust modeling approach to new dimensions and geometries due to the additive manufacturing process. In addition to the manufacturing effects, the effects of coating thickness (i.e., sealant) is also studied. It is revealed that the shape of the HX's manufactured wire fins are ellipsoidal instead of the intended nominally circular shape due to precision error in the printer's extruding process. It is also revealed that dimensional effects, particularly for narrow-width liquid channels, significantly affect the liquid-side pressure drop. Additionally, for latent thermal storage applications, an analytical-based model is developed using 1D ROM consisting of 1D radial conduction inside PCMs. The model is non-dimensionalized using parameters based on time-constant, thermal resistance ratios, and geometric length ratios.

Chapter 5: Design Optimization

This chapter describes the optimization algorithm for the developed HX as related to different applications varying from air-conditioning to pulsed-power cooling. The optimization algorithm is based on the exterior penalty method to find optimum points for a multi-objective constrained optimization problem, yielding a Pareto curve of optimum points. The chapter also provides a sensitivity analysis concerning the design parameters.

Chapter 6: Experimental Study

This chapter presents an experimental study on a 120 mm × 120 mm × 16 mm iCMHX tested for air-to-water CPU cooling applications and a 260 mm × 290 mm × 120 mm air-to-PCM CMTES system for building cooling applications. The study also uses experimental data to compute airside heat transfer coefficients using a customized, in-house developed, Wilson plot algorithm.

Chapter 7: Conclusion and Proposed Future Work

The final chapter provides the main conclusions of the thesis along with the list of research publications and lays down a well-supported outline for future work. The research scope of the dissertation is also summarized in a workflow diagram.

Chapter 2: A Novel Metal Polymer Composite HX

2.1. The Cross-Media Heat Exchangers

The current novel metal-polymer composite HX is based on a patented cross-media heat exchanger approach, often referred to as CMHX (Cross-media heat exchanger), which can be designed for sensible and latent thermal storage applications.

2.1.1. Sensible storage based iCMHX unit

The additively-manufactured metal-polymer composite HX [23,24] comprises an HX core made of polymer and an array of metal wires, which act as fins for airside and liquid-side convective heat transfer, as shown in Figure 2 (a). The metal wires can be arranged in a staggered or inline tube-bank configuration. The heat exchanger can also include additively-manufactured integrated liquid manifolds of polymer, as shown in *Figure 2* (a). The customized 3D printing process utilizes a polymer and a metal-head based on a hybrid and innovative approach [27] designed and developed by the AHXPI students, as described in [26,28]. The polymer head prints layers of polymer media to build the airside and liquid-side channels using FDM. The metal head prints bare metal wires that continuously lay over the polymer media using EFCAM and forming a direct heat transfer route between the air and liquid sides. These wires transfer heat effectively, despite the low thermal conductivity of the polymer structure, as shown in *Figure 2* (a). This concept is referred to as the cross-media approach, and the HXs are referred to as integrated cross-media HXs (iCMHXs), a particular type of CMHXs. This approach facilitates higher and direct crossflow heat exchange than conventional HXs, which have fins only on the airside, as shown in *Figure 2* (d).

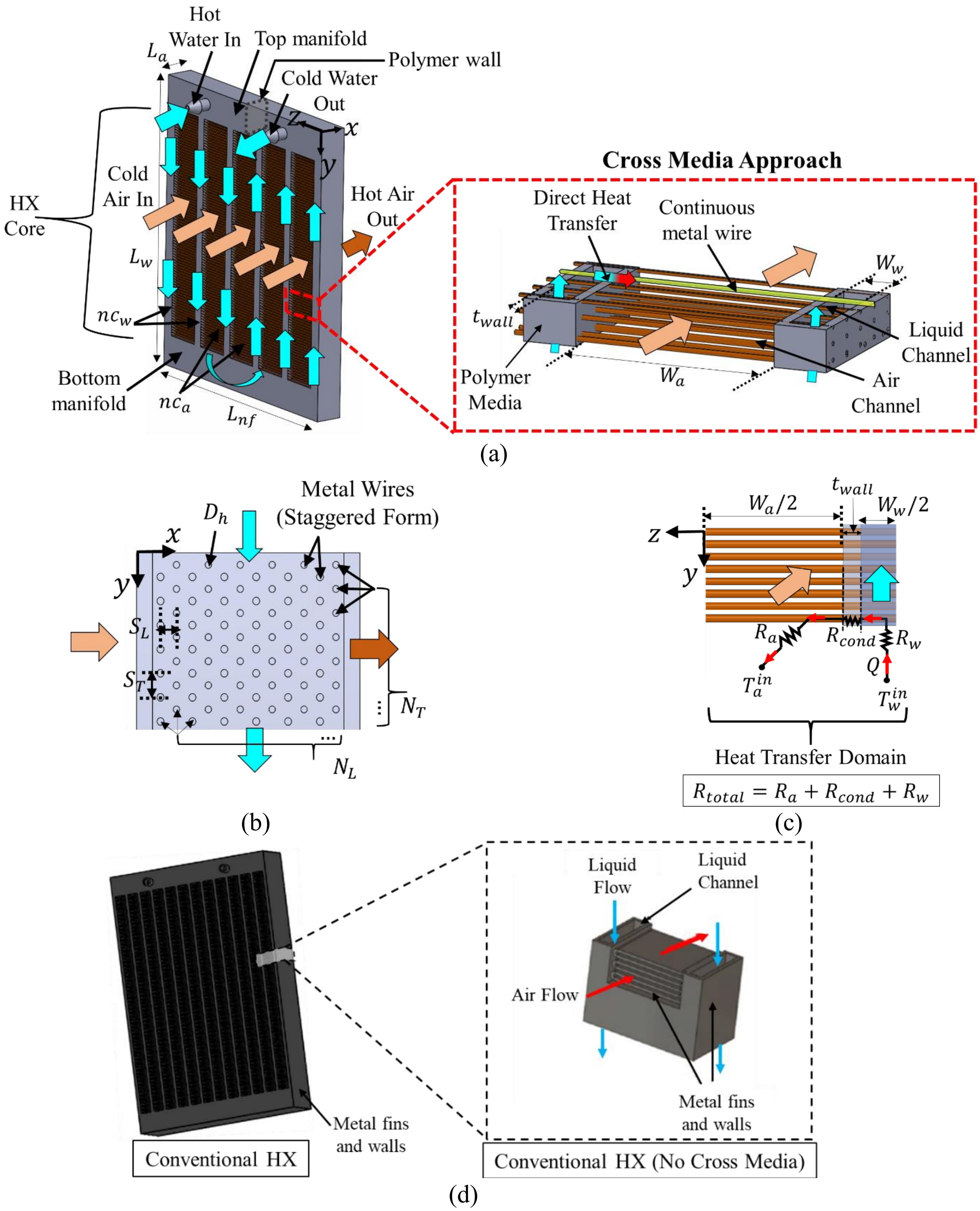

Figure 2: (a) A double-pass iCMHX design showing cross-media approach; (b) planar views showing staggered configuration; (c) planar views showing simplified heat transfer domain and (d) conventional HX with finned surfaces only on airside

A series of CMHX units have been manufactured in such a fashion at the University of Maryland's AHXPI laboratory (see *Table 1*). The current unit, the iCMHX shown in Figure 2 (a), is different from past CMHX units. It is the first of its kind additively-manufactured unit to feature a staggered-fin (tube-banks) configuration, copper wires, a double-liquid pass system, and most importantly - integrated liquid-side manifolds.

Table 1: Evolution of a family of CMHXs developed at the AHXPI laboratory

CMHX Models	Liquid Passes	Core Material	Wire	Tube-Bank Configuration	Liquid-side Manifolds
150W [29]	**1**	**PETG Polymer**	**Al**	**Inline**	**Absent**
1kW [30]					
350W [26]		**ABS Polymer**			
Current HX (Current Work)	**2**		**Cu**	**Staggered**	**Integrated**

2.1.2. Latent thermal storage-based TES

The cross-media based metal-polymer composite HX (see Figure 3 (a)) are similar to the ones for sensible storage applications as they consist of hot fluid flowing across alternate fluid channels (n_{fluid}) but instead of the other fluid flow, they include PCM contained polymer channels (n_{PCM}) as shown in Figure 3 (b). This results in low-cost macro-encapsulation of PCMs. Here, the cross-media approach provides a direct heat transfer route between the hot fluid and the PCM (see Figure 3 (c)), independent of the thermal conductivity of the polymer. At the interface of these fluid and polymer channels (see Figure 3 (d)), the metal wires are arranged in a geometric tube-bank pattern of staggered orientation parametrized by lateral (S_T) and longitudinal (S_L) spacings between the wires of diameter, D.

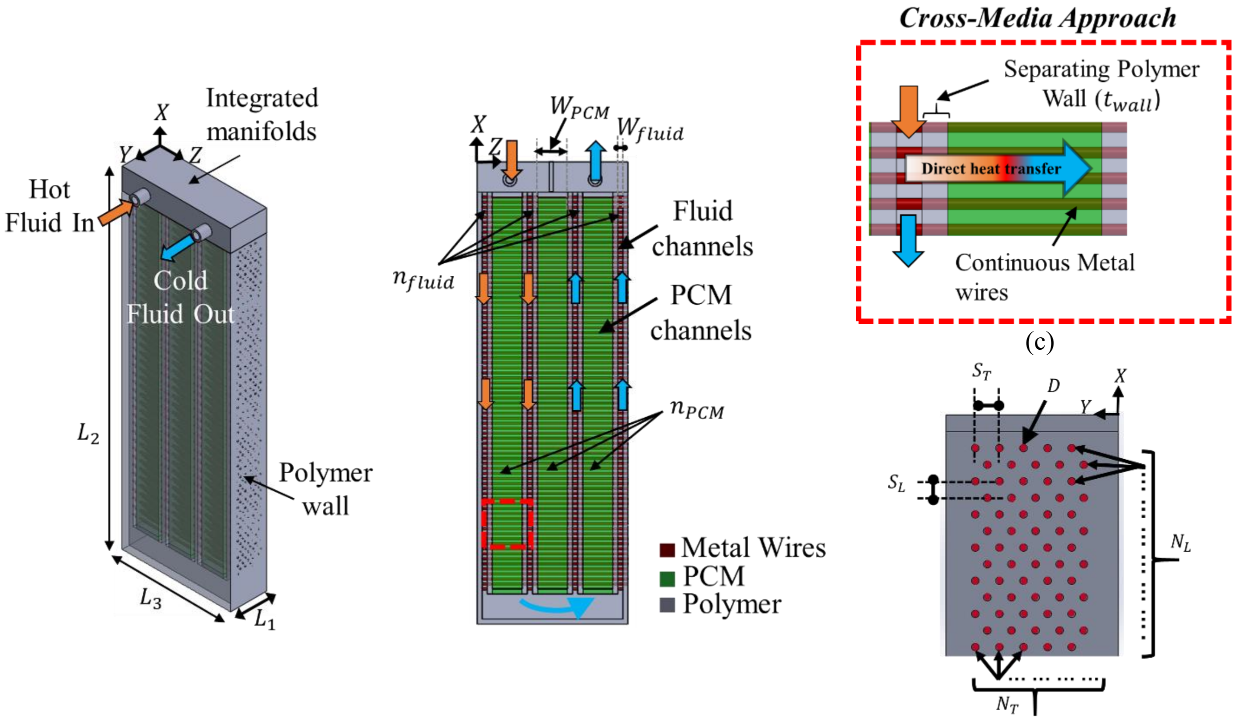

(a) (b) (d)

Figure 3: HX Geometry (a) isometric view (b) cross-sectional view of XZ plane with cross-media shown in red highlights (c) cross-sectional view of XY plane and (d) cross-media approach as marked in (b)

2.2. Additive manufacturing Technique

The iCMHXs are additively manufactured in-house using a customized proprietary 3D printer, automated via G-code programming based on a CAD drawing. The polymer composite HXs are fabricated using a hybrid additive manufacturing process of Fused Deposition Modeling (FDM) and Embedded Fiber Composite Additive Manufacturing (EFCAM) [31]. The process is explained in five steps, as shown in Figure 4 (a). In the first step, the polymer is extruded to create the bottom manifolds using polymer print-head via the FDM process. In the second step, a single, continuous metal wire layer is laid on the top of the printed polymer layer from Step 1, using a metal print-head via the EFCAM process. In Step 3, the metal print-head cuts the metal wires at the point of extrusion. And in the next step, another layer of polymer is printed over the laid metal wires from Step 2, using the polymer print-head. Lastly, in Step 5, the entire process of Steps 1-4 are repeated until the number of polymer layers with adequate wire-spacings is achieved. However, for latent thermal energy storage applications, as the PCM has to be contained inside the polymer channels, the polymer layers are printed differently from sensible storage applications (see Figure 4 (b)). In the end, when the HXs are entirely additively-manufactured as per the CAD design, they are then post-processed by dip-coating them in sealants such as polyurethane or epoxy to ensure leak-proof polymer-metal interfaces [23]. The HXs are also tested for their longevity and reliability by developing Arrhenius models at different temperatures and pressure conditions depending on the operating conditions of the HX applications. The post-processed HXs are then ready to be experimentally tested. Some such additively manufactured units by the printing team are shown in Figure 5. The 3D printer at the AHXPI laboratory has undergone several enhancements with the contribution of many team members over the years. However, successful printing of the cross-media heat exchangers and the thermal energy storage units would not have been possible without the creative efforts of Veeresh Ayyagari, a Ph.D. student in our AHXPI group.

Thus, based on the above different HX designs, these CMHXs can be termed novel due to the following salient features, which make them a preferable candidate over the conventional HX units:

- Innovative cross-media approach

- This approach enhances the overall effective heat transfer area on both the airside and the liquid side, which are finned surfaces compared to conventional HXs, resulting in a low thermal resistance unit.
- Robust additive manufacturing technique

  This automated manufacturing process can yield customizable HX units with just-in-time printing, which is otherwise difficult to implement in conventional manufacturing techniques.
- Lightweight polymer structure

The use of low-density polymers such as Acrylonitrile butadiene styrene (ABS) and Polyethylene terephthalate glycol (PETG) provides lighter weight to the HXs than the conventional HXs, which are entirely constituted of metal. For example, polymer weighs about 2 - 2.6 times less than aluminum for a given volume. Aluminum is one of the lightest and most common metals used in conventional HXs.

- High thermal conductivity metal fins (if using copper wires)

Copper has approximately 1.7-2 times higher thermal conductivity than the conventional units generally made of aluminum. But copper is also 3.3 times denser than aluminum, so that aluminum wires can be used instead of copper with applications requiring lightweight units. Since the overall CMHX weight includes the weight of the polymer, the overall HX weight should be compared with the conventional HX for a fair comparison.

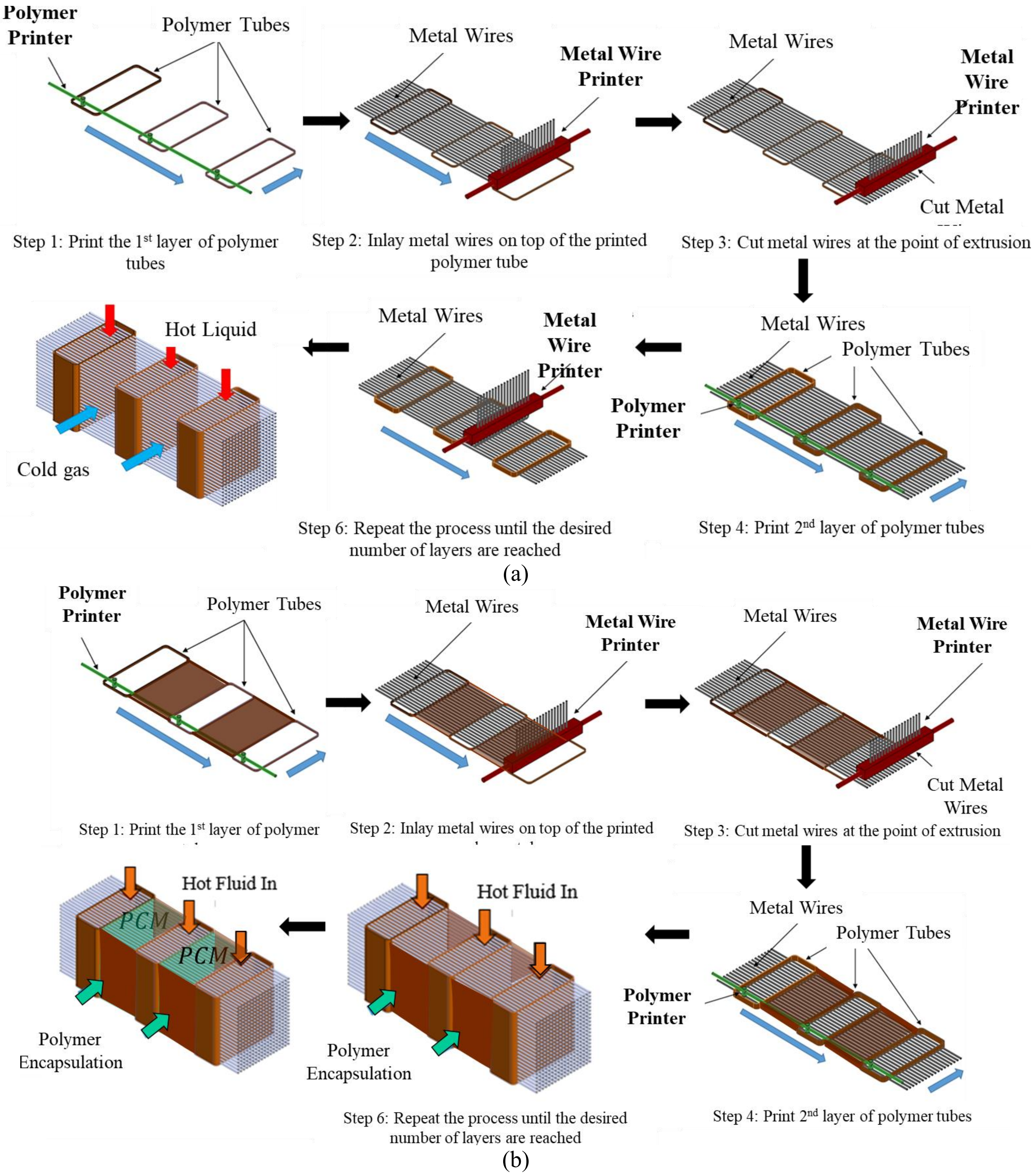

Figure 4: Fabrication process of HXs for (a) crossflow liquid to gas sensible storage applications (b) gas-to-PCM for latent thermal energy storage applications at AHXPI laboratory

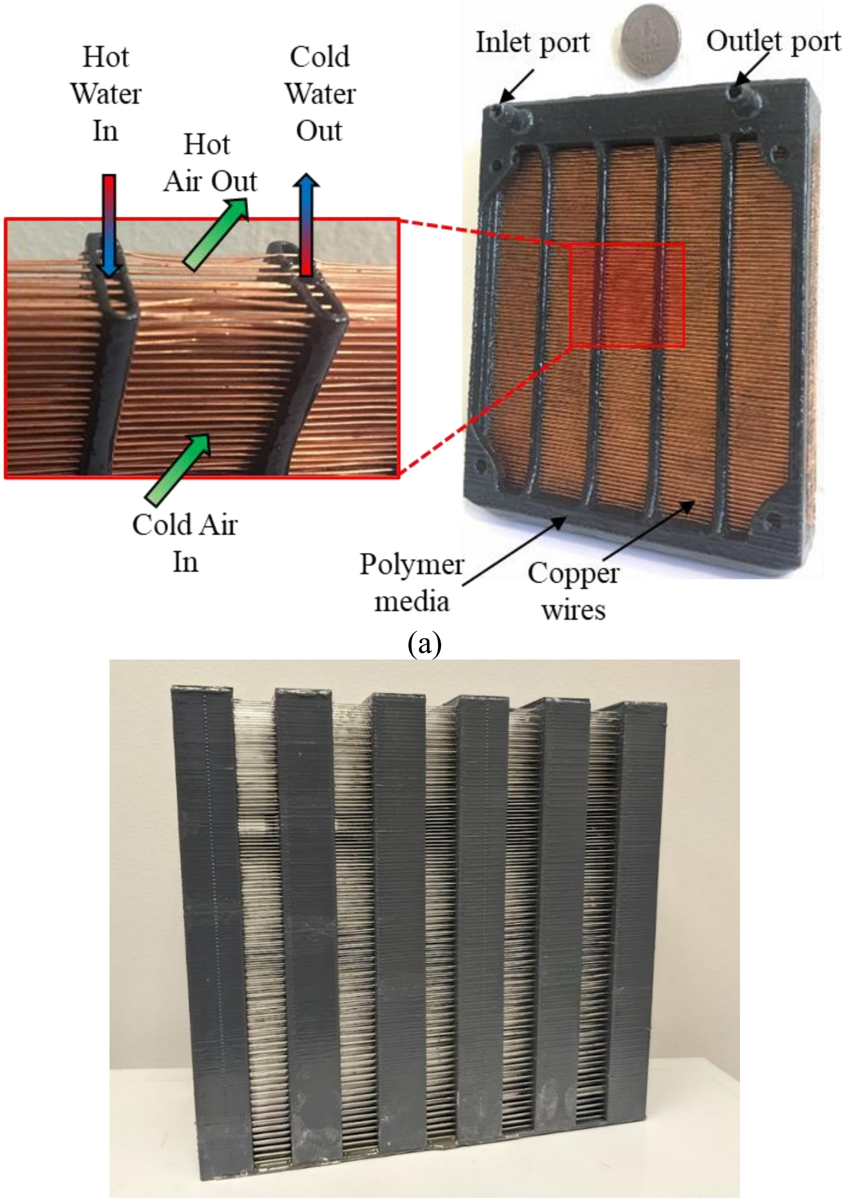

(a)

(b)

Figure 5: Additively manufactured and coated units (a) iCMHX and (b) air-to-PCM TES at the AHXPI Laboratory

- Scalability

The novel composite polymer HXs are scalable, which means that they can vary from as small as 120mm ×120mm face area to as large as about 24" × 24" depending upon their different applications.

- Design flexibility for different energy storage applications

Since some applications require liquid and gases for heat transfer, the HXs can be designed for sensible energy storage applications. And with slight modifications in the polymer printing layers, the same HX can be converted into a latent thermal energy storage unit consisting of PCMs.

- Low HX cost

As polymer and copper are cheaper than aluminum, the overall HX material cost is cheaper than conventional HXs. Additionally, using low-cost salt hydrates such as Glauber's salt as PCMs can lower the HX cost further.

- Integrated liquid-side manifolds

Since the fabrication of the composite polymer HXs involves an additive manufacturing technique that is customizable, the CMHXs can have liquid-side manifolds integrated with the core of the HX, similar to the conventional HXs.

Thus, the novelty of these current HX designs meets the challenges associated with conventional HXs, making them favorable to use in diverse applications, which will be discussed in the next section.

2.3. Applications of Novel Metal Polymer Composite HXs

These novel HXs have varied cooling applications that use a crossflow water-to-air HX. These applications include electronics cooling of computers, power plant applications, air-conditioning, automotive, aerospace and refrigeration, building cooling, and pulsed-power applications. The application discussed in the current dissertation focuses on the electronic cooling of desktop computers, air-conditioning, and peak-load shifting in building-cooling applications.

Electronics Cooling of Desktop Computers

Liquid cooling is one of the widely used techniques in cooling high-performance CPU units. It consists of a liquid-side loop and an air-side loop. The liquid-side loop consists of a cold plate, a pump, a reservoir, and liquid tubes, while the airside consists of a fan attached to the radiator (see Figure 6). The cold plate is attached via thermal interface material (TIM) to the motherboard. As the motherboard temperature increases, the liquid pumped out carries heat to the radiator through tubes. As the hot liquid enters the radiator, conjugate heat transfer occurs with the cold air blowing from the attached fan in crossflow, resulting in cold water flowing back to the pump via tubes and hot air exhausting out in the ambient air. This application is discussed in the numerical, experimental, and future work sections.

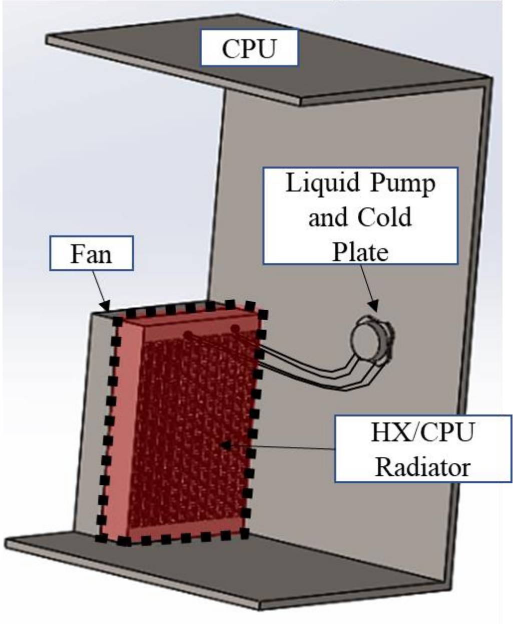

Figure 6:Liquid cooling applications in CPU

Air Conditioning Applications

The other application where novel polymer composite HXs can be used is an air-conditioning application where it can be used as an evaporator coil. They are used inside the duct for in-house applications above the air handling unit. The air first enters the room and is passed to the evaporator coil by the blower and the air handling unit. As the air passes through the Evaporator, it gets cooled down by the refrigeration effect facilitated by the condenser coil kept outside the house. The application is discussed here in the chapter on the design optimization section.

Peak-Load Shifting in Building-Cooling Applications

In applications requiring intermittent cooling, such as air-conditioning applications in buildings, CMHXs can be used as latent thermal energy storage devices, also called CMTES (Cross Media Thermal Energy Storage System), as explained graphically in Figure 7. Since the PCMs can store energy dissipated from the surroundings isothermally when in liquid-phase while releasing the stored energy back to the surroundings when in solid-phase, this property of PCMs is used to shift the peak-load during daytime in cooling building. For this, the PCMs based CMTES units, placed in an air-duct system, are first charged during the night by turning the air-conditioned (AC) on so that cold air freezes the PCM, releasing heat. However, the AC cooling loop is disconnected from the building as there is no cooling requirement present during the nighttime (see Figure 7 (a)). During the peak-cooling hours of the day, only the AC fan is turned on to facilitate airflow across the duct. The PCMs based CMTES units are then used to take away the heat from hot air and store the vast amount of it as latent thermal energy, leading to cold air exiting out through the HX (see Figure 7 (b)). But when the PCM has melted entirely, it can no longer be used to cool the buildings. Accordingly, the actual cooling loop using AC is used via by-passing the CMTES unit, in probably off-peak daytime hours.

Thus, all these applications require an optimized design to meet the desired operating conditions best. To obtain the required heat transfer rate and pressure-drop targets, the hydrodynamic performances can be evaluated if there are correlations present in the

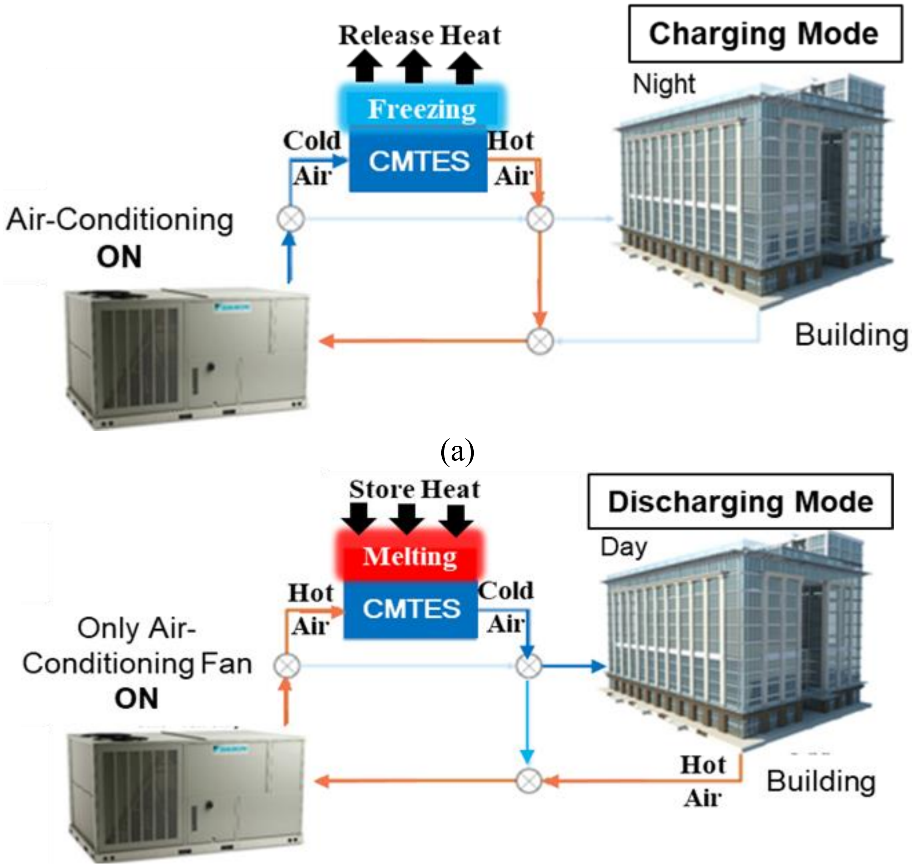

(a)

(b)

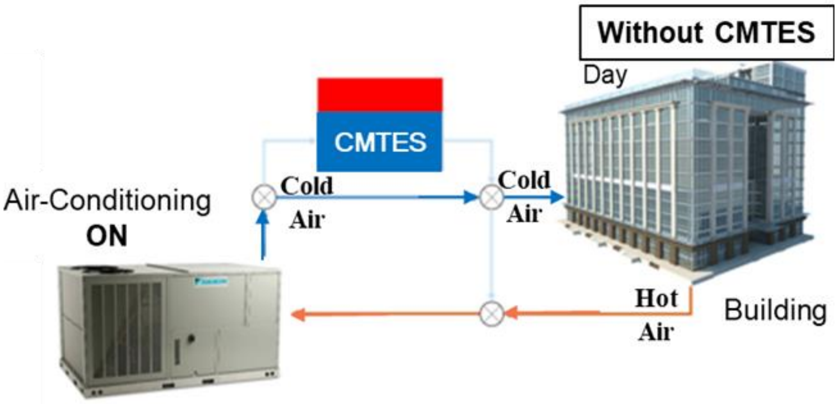

(c)

Figure 7: peak-load shifting in building cooling applications (a) charging mode at night (b) discharging mode at peak-times during the day, and (c) without CMTES units at off-peak times during the day

literature about the given geometrical and flow parameters. A literature study to explore the correlations is thus carried out, as shown in the next chapter.

2.4. Summary

A detailed design and fluid flow path for cross-media based novel metal-polymer composite HX was explained. The current dissertation focuses on an advanced version of the cross-media HXs, which is first of its kind to be additively manufactured. Their salient features such as low cost, low resistance and robust additive manufacturing technique, were discussed which make these HXs a strong potential candidate for diverse industrial applications. One of their novel features lead to design flexibility to work as iCMHXs for sensible thermal storage applications such as those of electronic cooling of desktop computers and as TES units for building cooling applications.

Chapter 3: Literature Review

3.1. Theoretical Background

This section covers the fundamental knowledge required to understand the physics behind heat transfer and pressure drop performance due to the CMHXs. It includes the basic understanding of external flow across tube banks, which represent the fluid flow across the arrangement of wires inside the CMHX channels. Moreover, it then talks about the details of the phase-change materials.

3.1.1. Tube Banks

The section explains the details about the (i) geometry of the tube banks arrangement formed by the metal fins embedded into the polymer media; (ii) fundamentals behind heat transfer and pressure drop performances during fluid flow across the tube-banks and; (iii) the literature correlations for thermal and hydrodynamic performances of the external flow across tube-banks.

(i) Geometry of tube-banks arrangement

The geometry of the tube bank consists of tube spacing parameters, the number of the wires, and the diameter of the wires. Here, the words tubes, wires, and fins are interchangeably used. The parameters are defined by their flow direction, which is either longitudinal (along the direction of fluid flow) or transverse (perpendicular to the direction of the fluid flow), as shown in Figure 8 (b) and (c). The tube spacing parameter in the longitudinal direction is represented by S_L, which is also the projected center-to-center distance in the longitudinal direction, between any two consecutive tubes in the longitudinal direction, as shown in Figure 8 (b) for inline configuration and in Figure 8 (c) for staggered configuration. Similarly, the tube spacing parameter in the transverse direction is represented by S_T, which is also the center-to-center distance between any two consecutive tubes in the transverse direction. The number of tubes in the longitudinal direction, separated by S_L distance away is defined by N_L rows while the number of tubes in the transverse direction, separated by S_T distance away is defined by N_T tubes. In the staggered configuration, the diagonal center-to-center distance between any two consecutive tubes in the longitudinal direction is defined by S_D. The flow regime across the tube banks is dependent on the arrangement of the tubes. The study considers the external flow of two fluids across the tube banks in a crossflow direction to each other, as shown in Figure 8 (a). Each fluid-side contains its respective flow parameters and the geometric parameters which affect the overall heat transfer and pressure-drop performance across the tube banks.

(ii) Fluid flow across tube-banks

The fluid flow across the tube banks is first explained via a simplified version of the tube bank study: a single fluid flow across the single tube. This case also acts as the limiting case for the fluid flow across tube banks when the tube-bank spacing is large such that the flow across the tubes resembles the flow across the single cylinder.

The external fluid flow across the single tube or single cylinder is characterized by the Reynold number of the incoming fluid and the size of the tube. The Reynolds number is defined based on the upstream velocity (v) of the fluid, nature of the fluid, and characteristic length, i.e., the tube diameter (D).

$$Re = \frac{\rho v D}{\mu}$$

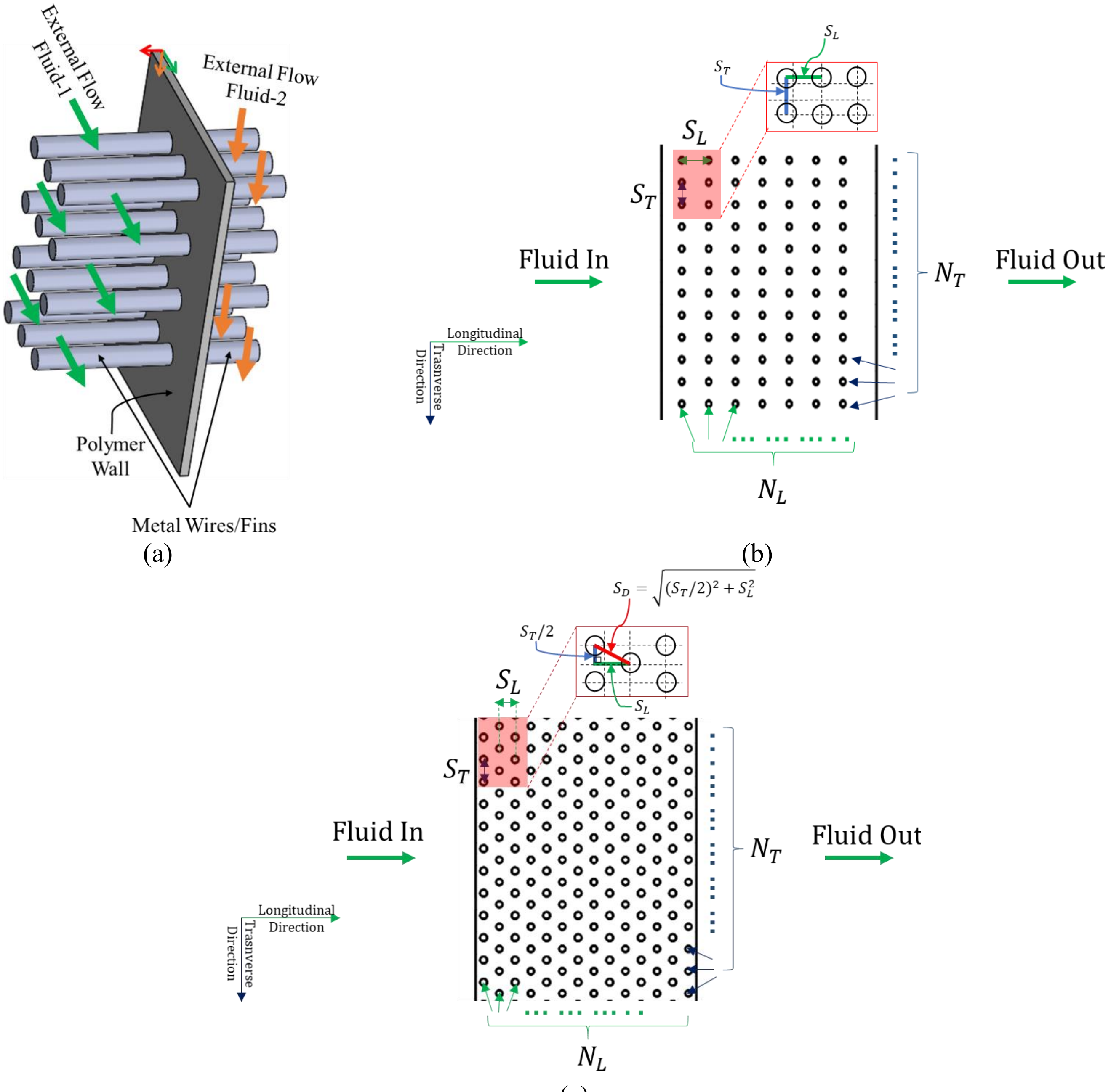

Figure 8: Tube bank configurations for (a) external flow over tube banks for both fluids; and (b) planar views in the direction of fluid-flow across inline tube-bank configuration and (c) staggered tube-bank configuration

As the fluid moves past the single-cylinder normally, it slows down as it approaches the upstream side of the cylinder and its velocity ultimately becomes zero at the point of contact (A_1) with the cylinder, as shown in Figure 9. $A_1$is called as the first stagnation point. The fluid velocity increases as it continues its path above and below the cylinder creating a boundary layer as shown in Figure 9. Near the cylinder-top and bottom, the fluid attains its maximum velocity (B_1 and B_2) after which its velocity starts deaccelerating as it goes downstream of the cylinder. Consequently, there comes the point at both the top and bottom side of the cylinder where the velocity gradient is zero (C_1 and C_2) and the continued downstream movement of the fluid is impossible. Thus, the boundary layer then separates and detaches from the cylinder surface resulting in the formation of stable or unstable wakes and vortices in the downstream region. The points of separation (C_1 and C_2) and the wakes/vortices formation are dependent on the Reynolds number and size of the cylinder (D). Eventually, the fluid increases its velocity before attaining its upstream velocity (v). Similarly, the pressure distribution varies according to the Bernoulli's equation, i.e., as the velocity increases, the pressure decreases. Thus, the pressure increases as the fluid approach the upstream side of the cylinder and is the maximum at A_1. It then decreases till it reaches the cylinder-top where it is the minimum (B_1 and B_2). It then goes downstream side of the cylinder and increases with decreasing velocity.

The flow is restricted for external flow across the tube bank because the spacing between the neighboring tubes is arranged in an inline or staggered configuration. The flow parameters are determined by computing the Reynolds number and fluid's Prandtl number. The Reynolds number is defined based on the maximum velocity of the fluid, the nature of the fluid, and the characteristic length, i.e., the diameter of the tube, as shown in the following Equation. The maximum velocity, v_{max} is based on the

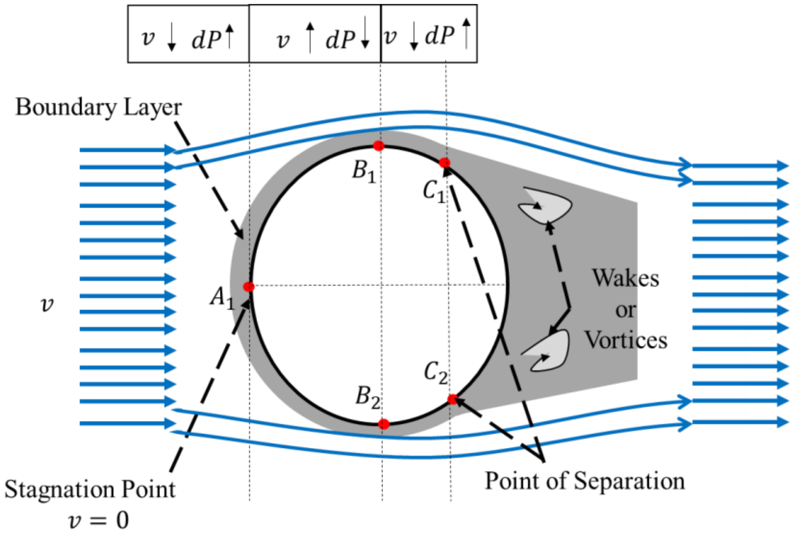

Figure 9: Physic of fluid flow across single cylinder/tube

minimum cross-sectional flow area for both inline and staggered configuration cases, as shown in Figure 10.

$$Re_D = \frac{\rho v_{max} D}{\mu}$$

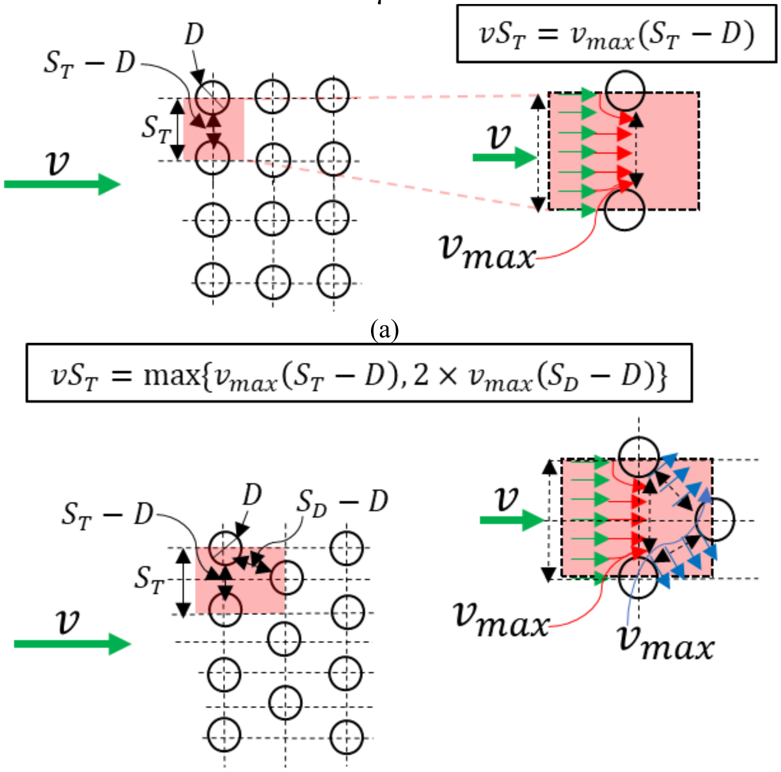

(a)

(b)

Figure 10: Velocity definitions for (a) inline and (b) staggered tube-bank configurations

These parameters affect the thermal and hydrodynamic performance resulting from the crossflow of hot fluid and cold fluids across the tube bank. The thermal performance for each fluid is generally quantified from its heat transfer rate (Q) in the form of Nusselt number, which is a dimensionless quantity and is also a function of Reynolds and Prandtl number for a given geometry (S_T/D and S_L/D), as shown in the following Equation.

$$Nu = \frac{hD}{k} = f(Re, Pr)\, |_{S_T/D, S_L/D\, =\, given}$$

The purpose of using Nusselt number is because it uses fewer input parameters such as Re and Pr when compared to physical variables such as Q, heat transfer coefficient (h), heat transfer area (A) and ΔT_{LMTD} as shown in Equations (4)-(5) for a given tube-bank geometry.

$$Q = hA\Delta T_{LMTD}$$

where

$$\Delta T_{LMTD} = \frac{(T_{in}^{hot} - T_{out}^{cold}) - (T_{out}^{hot} - T_{in}^{cold})}{\log \frac{T_{in}^{hot} - T_{out}^{cold}}{T_{out}^{hot} - T_{in}^{cold}}}$$

Similarly, the hydrodynamic performance is generally quantified from pressure drop in the form of Euler number, which is a dimensionless quantity and is also a function of Reynolds number for a given tube-bank geometry (S_T/D and S_L/D), as shown in the following Equation.

$$Eu = \frac{\Delta P}{\frac{1}{2}\rho V_{max}^2 N_L} = f(Re)\, |_{S_T/D, S_L/D\, =\, given}$$

3.1.2. Phase Change Materials

The phase change materials work when hot fluid flows in the TES such that the PCM melts. At first, the PCM starts sensible-heating due to enthalpy from the temperature difference between PCM and the fluid, if at different values (see Figure 11). Subsequently, as the PCM temperature reaches its phase-transition temperature, T_m, the PCM melts isothermally using a relatively large amount of enthalpy, $\Delta H.$ Similarly, when the cold fluid flows, the same PCM material freezes, releasing the stored latent heat. To determine the amount of latent thermal energy that would be transferred relative to sensible enthalpy, a dimensionless parameter, Ste, is used as shown below:

$$Ste = \frac{C_p(T_{in} - T_m)}{\Delta H}$$

where T_{in} refers to the surrounding fluid temperature

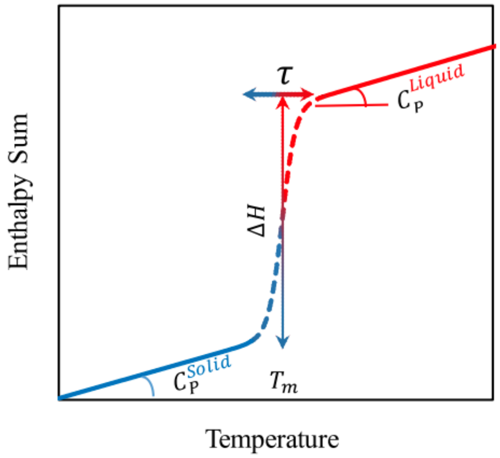

Figure 11: Variation of enthalpy with temperature during the PCM transition process

The PCMs can be categorized based on their transition phases - solid-liquid, solid-gas, and solid-solid such as Nitinol. Since solid-liquid and solid-solid types would have minimum volume change between their phases, these PCM types would yield more compact designs. Focusing on the solid-liquid type PCMs, the PCM materials can be selected based on the following criteria:

- Low cost, such as inorganic PCMs
- High heat of fusion per unit volume and mass and high thermal conductivity such as inorganic PCMs as compared to organic PCMs
- Non-inflammable, unlike organic PCMs.
- PCMs transition temperature close to temperature conditions of surroundings.
- Chemical stability per thermal cycle. It is generally recommended that PCMs withstanding up to 1000 thermal cycles [32] are reliable for use.
- Subcooling and phase-segregation issues [21] for inorganic PCMs. Issues can be resolved using agents such as Borax and Bentonite in Glauber's salt as PCM.
- Compatibility with containment materials, particularly for inorganic PCMs, which can be highly corrosive

Summarized PCM properties and costs can be found in Figure 12.

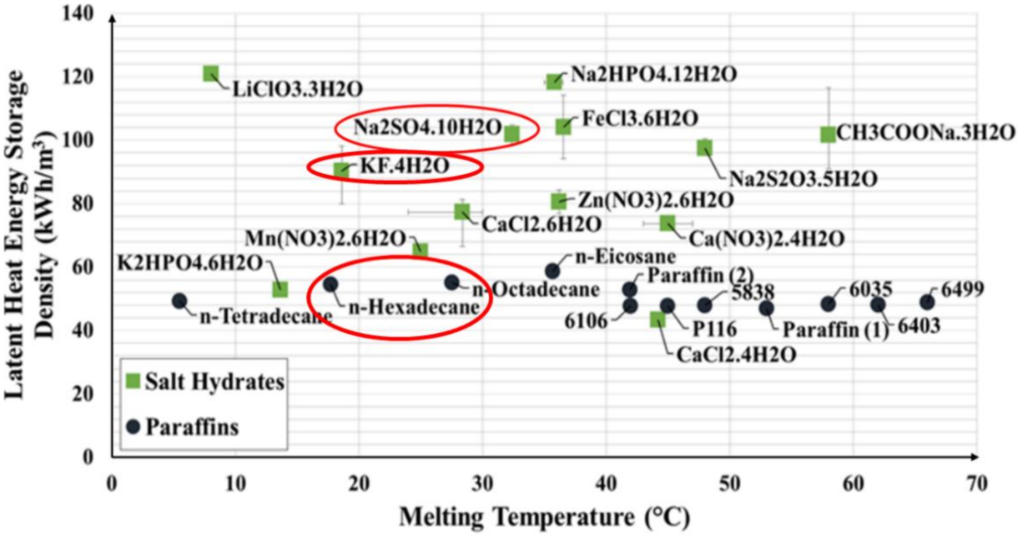

(a)

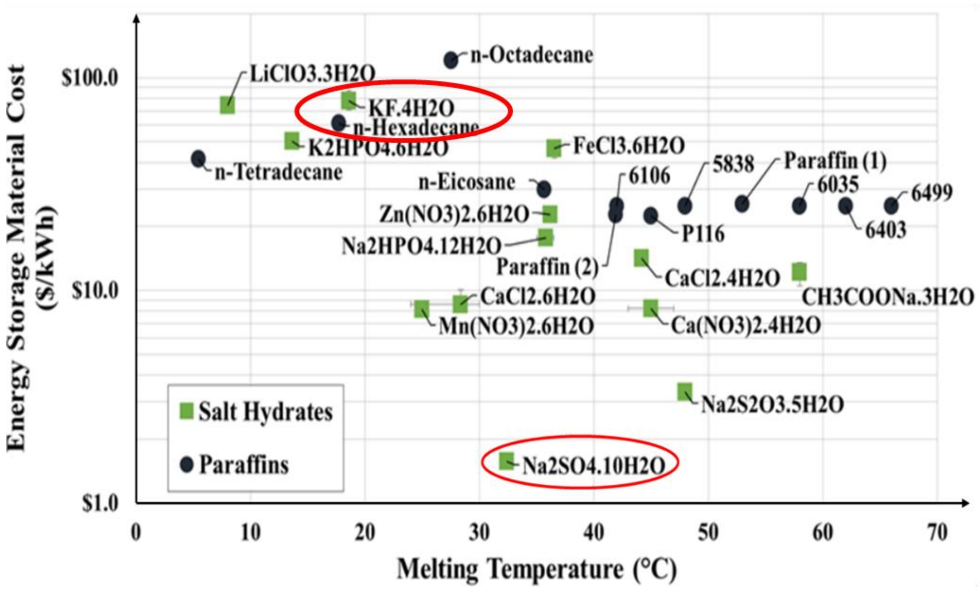

(b)

Figure 12: (a) Latent heat energy storage density and (b) material cost for different PCMs [33]

The present dissertation focuses on PCMs such as Glauber's salt, n-hexadecane, and potassium tetrahydrate based on the outlined criteria.

3.2. Tube-Bank Correlations

The physics behind the flow across the tube banks needs mathematical interpretation obtained by computing its thermal and hydrodynamic performances. This interpretation has been made in the literature in the past by (i) conducting experiments, (ii) performing numerical modeling, and (iii) by carrying analytical computations on tube bank designs based on different geometric and flow parameters. The literature studies use robust parameters such as Nusselt number and Euler number to evaluate the tube banks' thermal and hydrodynamic performances.

According to the tube-bank configurations, the entire literature survey on thermal and pressure-drop performances for tube banks has been divided based on configuration, i.e., staggered and inline, and then on Nu and Eu correlations.

The topic of tube banks has been studied for a long time as the earliest literature studies based on experiments date back to the 1930s. The studies intend to develop correlations for Euler and Nusselt numbers to study the effect of tube-spacing and flow parameters on the thermal and hydrodynamic performance of fluid across the tube banks. Over the period, several researchers started developing their correlations based on experiments and tried validating their work with the work done by other researchers. Several other researchers also used analytical methods to develop correlations by analyzing the naviers stokes equations governing the fluid flow across the tube banks. Around the 1970s, with the increase in computational power, researchers started using numerical methods such as CFD solver tools to obtain the Eu and Nu correlations for given geometric and flow ranges for external flow over the tube-banks. More recently, Machine Learning and Neural Networks have been used to develop correlations from extensive experimental or numerical data for wide geometry and flow ranges.

Euler Number| Staggered Configuration | Experimental Correlations

One of the earliest studies by Chilton and others, [34] explored the relationship between the friction factor or the Euler number in terms of Reynolds number for both staggered and inline configuration by analyzing experimental data on flow across the tube-banks. Consequently, within the next decade, several experimental works on tube banks were studied by Sieder [35], Pierson [36], Huge [37], Wallis [38], and Norris [39].

One of the most commonly used experimental data in the literature discusses Pierson's correlations [36] based on air-testing on 22 staggered tube bank arrangements with S_T/D ranging from 1.25 to 3 while S_L/D ranging from 0.6 to 3 for a flow range of Re_D

varying from $2000 - 40{,}000$. The Re_D was defined, based on mass-flow rate per unit minimum area in the bank, G.

$$Re_D = \frac{GD}{\mu}$$

The study presented a graphical relationship between Eu number synonymous with friction factor (f) with different Re_D corresponding to different S_T/D and S_L/D ratios and inferred that (i) Eu either remains constant or decreases with increasing Reynolds number and (ii) Eu number is greatly affected by the changes in the tube arrangement (S_T/D, S_L/D and tube configurations) as compared to the Nu number. The authors of the study also provided correction factors for N_L tubes, ranging from $1 - 10$ rows but didn't explain the trend satisfactorily. However, there were several unfavorable reviews about the use of correlations such as (i) 10-15% deviations when validated with correlations of other people's works [40] and (ii) unaccounted experimental uncertainties, which might affect the frictional factor results [41].

Extending the work of Pierson [36], another research was performed by Grimison [42] to provide correlations using the previously discussed data [36] [37] for Re_D varying from 2000 to 40,000. This work stated that the Euler number of friction factor, f, is a function of Re_D. The study also mentioned that the correction factors for $N_L > 10$ tubes were negligible. However, there were several unfavorable reviews regarding the usage of the correlations. One of them [43] was the significant deviations produced in mass velocity due to small details in experimental conditions under which the data was obtained.

To further improve the understanding behind friction factor curves based on Pierson's correlations [36], another research was conducted by Jakob [44] where a curve-fitting expression in terms of Re_D, S_T/D and S_L/D and friction factor was obtained. For staggered configuration, the correlation was proposed for Re_D ranging from 4000 to 32,000, S_T/D ranging from 1.25 to 3 and S_L/D ranging from 1 to 3.

$$f = Re_D^{-0.16}\left(0.25 + \frac{0.1175}{\left(\frac{S_T}{D} - 1\right)^{1.08}}\right)$$

However, some unfavorable reviews [42] intended to use more accurate and simpler correlations; substantiated by data from many sources. Thus, a study [40] developed an integrated, simple correlation by Gunther and others, valid for both staggered and inline configuration as well as for bare and extended-surface tubes. These correlations were valid for Re_D ranging from 3 to 70,000 and S_T/D and S_L/D ranging from 1.25 to 5. But, this work too had some unfavorable reviews [45], such as (i) huge deviations observed between the Gunther correlations [40] and some additional experimental data, (ii) equally same effect of tube spacing and arrangement for both turbulent and laminar flow cases, (iii) limited data available on tube spacing (two staggered equilateral and no inline arrangement cases) for laminar range, and (iv) some miscalculated Reynolds number values. Accordingly, another study [45] provided some corrections to the friction factor graphs based on the work of Gunther [40], valid for Re_D ranging from $90 - 70{,}000$ and for two different configurations – inline and staggered.

Eventually, one of the most widely used correlations based on Zukauskas's work [46] developed a more reliable, comprehensive, and widely covering wider ranges of tube spacing, tube arrangements, Reynolds, and Prandtl numbers. For staggered configuration, the correlations were valid for Re_D varying from 3 to 2,000,000, S_T/D

varying from 1.25-2.5 and S_L/D varying from 0.35-5.55. Though it is a widely used correlation, some unfavorable reviews regarding its applicability for discrete values and discontinuities in its correlations. For example, the correlations aren't valid for extreme tube-spacings in the laminar range, such as when $S_T/D = 2.5$ and $Re_D < 100$. Similarly, recent works by Gaddis [47] also developed comprehensive correlations for $N_L \geq 10$ rows, S_T/D ranging from 1.25 to 3, S_L/D ranging from 0.6 to 3 and Re_D ranging from 1 to 300,000. The N_L is computed based on v_{max} (see Figure 10 (b)). Here, Eu number is synonymous to the definition of the drag coefficient ξ used by the authors. The authors compute ξ for both laminar and turbulent cases for both inline and staggered configuration where ξ is a function of $Re_D, S_T/D$ and S_L/D.

Euler Number | Staggered Configuration | Numerical and Analytical Correlations

The alternate approach to developing correlations based on experiments is numerically developing the correlations by solving the Navier-stokes equations for flow over tube banks. The challenges were mainly the complex geometry and the computational power and cost. Meeting these challenges, the earliest attempts on numerical studies on tube-banks involved developing conformal meshes [48] and running a simplistic flow case over a single cylinder [49]. Later, [50] a study provided solutions for the stream function and vorticity equations and presented graphical pressure-drop results for square staggered tube banks ($S_T/D = 2(S_L/D)$) for Re_D within 1000 and S_T/D at 1.77 and 3. Their finite difference method used a hybrid grid approach − polar grid near cylinders and cartesian grid in the rest of the 2D domain, which included 2 rows of staggered quarter circles with symmetry boundaries at the tube-centerlines $S_T/2D$ distance away from each other and periodic boundaries at the inlet and the outlet. But there were some unfavorable reviews particularly due to its limited range of tube spacing.

Subsequently, another study [51] reported their work based on finite volume approach for Re_D ranging from 105 to 186,000, S_T/D and S_L/D ranging from 1.25 to 5 and N_L varying from 1 to 2. They, however, used Re based on mean velocity as defined below:

$$Re = \frac{\rho v D}{\mu \psi}$$

where $\psi = 1 - \frac{\pi}{\frac{4S_T}{D}}$ and all the above correlations for Eu number are discussed in *Table 2* (a).

Nusselt Number | Staggered Configuration

The works provided by some of the authors in the above section also included the Nu correlations, which will be discussed in brief here.

Following one of the earliest reported experimental data based on Pierson's work [36], the Nu correlations so obtained were valid for the same geometric and flow ranges as mentioned for Eu number. Their graphical results showed Nu increasing with $Re_D^{2/3}$. Besides that, Nu was also observed to have a dependence on tube arrangements such as S_T/D, S_L/D and tube configuration. However, the results reported were applicable for gases such as air only, and the effect of Pr number by using different fluids wasn't considered. Similarly, the study by Grimison [42] used the theory of similarity on Pierson's experimental data and proposed Nu correlations for the same geometric and flow conditions like Eu. F_a is the arrangement obtained graphically.

$$Nu = 0.284 \times F_a Re_D^{0.61} Pr^{0.31}$$

All the above correlations for the Nu number are discussed in *Table 2* (b).

Table 2: Staggered tube-bank correlations for (a) Eu and (b) Nu

Correlations Type	Authors	Geometric Range		Flow Range	No. of Rows	Contribution of Parameters towards Correlation					Unfavorable Review
		S_T/D	S_L/D	Re	N_L	S_T/ D	S_L/D	Re	N_L	Config	Authors
Experimental	**Pierson et al.**	$1.25-3$	$0.6-3$	$2\times10^3-4\times10^4$	$1-10$	X	X	X	X	X	• Gunther and Shaw • E. W. Still
	Grimison et al.	$1.25-3$	$1-3$	$2\times10^3-4\times10^4$	$10-\infty$	X	X	X		X	• E W Still • Zhang and Chen
	Jakob et al.	$1.25-3$	$0.6-3$	$4\times10^3-3.2\times10^4$	$31-10$	X		X	X	X	• Gunther and Shaw
	Gunther and Shaw et al.	$1.25-5$	$1.08-4.96$	$3-7\times10^4$	$3-\infty$	X	X	X	X		• Boucher and Lapple
	Boucher and Lapple	$1.25-5$	$1.08-4.96$	$90-7\times10^4$	$3-\infty$	X	X	X	X	X	
	Zukauskas et al.	{1.25,1.5,2} {2.5}	$0.35-5.55$	$3-2\times10^6$ $100-2\times10^6$	$1-\infty$	X	X	X		X	• Zhang and Chen
	Gaddis	$1.25-1.768$ $1.25-3$	$0.884-1.3$ $0.6-3$	$1-10^3$ $10^3-3\times10^5$	$5-\infty$	X	X	X		X	
Numerical and Analytical	**Launder and Massey**	$\{1.77,3\}$	$S_L/D=\frac{1}{2}(S_T/D)$	$1-10^3$	$7-\infty$	X		X			• Mandhani
	Wilson and Bassiouny	$1.3-5$	$1-1.5$ $1.5-5$	$105-1.86\times10^5$	$\{1,2\}$	X	X	X	X	X	• Mandhani
	Wang et al.			3-1000	10				X		
	Bacellar et al.	$1.2-4$		$20-1.6\times10^4$	$2-40$	X	X	X	X	X	
Experimental and Numerical	**Current Work**	{3.18,4.55}	{2.27,1.59}	$10-10^2$	$14-168$	X		X			

(a)

Correlations Type	Authors	Geometric Range		Flow Range		No. of Tubes	Fin Type	Contribution of Parameters towards Correlation						Unfavorable Review
		S_T/D	S_L/D	Re	Pr	N_L		S_T/ D	S_L/D	Re	Pr	N_L	Config	Authors
Experimental	**Pierson et al**	$1.25-3$	$0.6-3$	$2\times10^3-4\times10^4$	0.7	$1-10$	Bare Tubes	X	X	X		X	X	• Gunther and Shaw • E. W. Still
	Colburn			$10^3-4\times10^4$		$10-\infty$				X	X			
	Grimison et al.	$1.25-3$	$0.65-3$	$2\times10^3-4\times10^4$	$\{0.7,7,20,1.3\}$	$10-\infty$		X	X	X	X	X	X	• SP Soling • Zhang and Chen
	Gneilinski et al.	$1.02-4$	$1-5$	$8-2.7\times10^7$	$0.6-10^3$			X	X	X	X	X	X	
	Gaddis and Gnielinski	$1.25-3$	$1.2-3$	$1-3\times10^5$				X	X	X	X		X	
	Zukauskas et al.	-	-	$10-2\times10^6$	$0.7-500$	$1-\infty$		X	X	X	X	X	X	• Zhang and Chen
Numerical and Analytical	**Khan et al.**	$1.05-3$		$1-10^5$	$0.7-\infty$	$1-\infty$	Bare Tubes – Circular and Ellipsoidal	X	X	X	X		X	
	Dhaubedel et al	$\{2.12,2.6\}$	$0.75-1.06$	$10^2-4\times10^2$	0.7	5	Bare Tubes	X		X	X	X	X	
	Mandhani et al.	$2.41-11.6$	$1.15-5.5$	$1.11-2.22\times10^3$	$\{0.71,7.7\}$	$1-\infty$		X	X	X			X	• Shaboury
	Wilson and Bassiouny	$1.3-5$	$1-5$	10^2-10^5	0.7	$\{1,2\}$		X	X	X	X	X	X	• Mandhani
	Wung and Chen	$\{2\}$		$\{40,120,400,800\}$	$\{0.1,1,10\}$	-				X	X		X	• Mandhani
	Martin et al.	$1.02-3$	$0.6-3$	$1-2\times10^6$	$0.7-700$	$4-80$		X	X	X	X			
	Lindqvist et al.	$1.007-1.83$	$0.873-1.59$	$0-1.8\times10^4$		$1-\infty$		X	X	X	X	X		
	Bacellar et al.	$1.2-4$		$20-1.6\times10^4$	0.7	$2-40$		X	X	X	X	X	X	
Experimental and Numerical	**Current Work**	{3.18,4.55}	{2.27,1.59}	$10-10^2$	$\{0.7,5.19\}$	$14-168$		X	X	X	X		X	

(b)

Similarly, the literature studies for inline configuration are summarized in *Table 3*.

Table 3: Inline tube-bank correlations for (a) Eu and (b) Nu

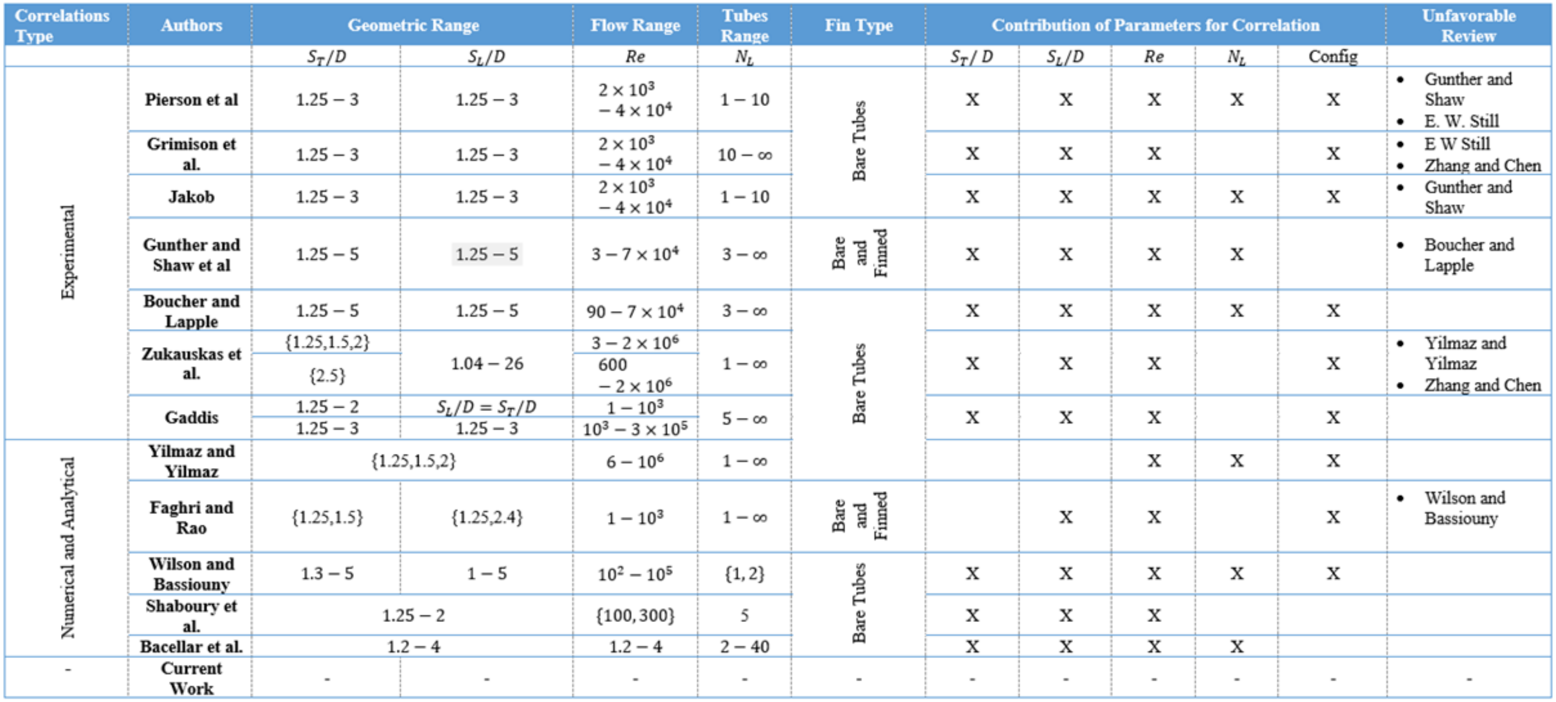

Correlations Type	Authors	Geometric Range		Flow Range	Tubes Range	Fin Type	Contribution of Parameters for Correlation					Unfavorable Review
		S_T/D	S_L/D	Re	N_L		S_T/D	S_L/D	Re	N_L	Config	
Experimental	**Pierson et al**	$1.25-3$	$1.25-3$	$2\times10^3-4\times10^4$	$1-10$	Bare Tubes	X	X	X	X	X	• Gunther and Shaw • E. W. Still
	Grimison et al.	$1.25-3$	$1.25-3$	$2\times10^3-4\times10^4$	$10-\infty$		X	X	X		X	• E W Still • Zhang and Chen
	Jakob	$1.25-3$	$1.25-3$	$2\times10^3-4\times10^4$	$1-10$		X	X	X	X	X	• Gunther and Shaw
	Gunther and Shaw et al	$1.25-5$	$1.25-5$	$3-7\times10^4$	$3-\infty$	Bare and Finned	X	X	X	X		• Boucher and Lapple
	Boucher and Lapple	$1.25-5$	$1.25-5$	$90-7\times10^4$	$3-\infty$	Bare Tubes	X	X	X	X	X	
	Zukauskas et al.	$\{1.25,1.5,2\}$ $\{2.5\}$	$1.04-26$	$3-2\times10^6$ $600-2\times10^6$	$1-\infty$		X	X	X		X	• Yilmaz and Yilmaz • Zhang and Chen
	Gaddis	$1.25-2$ $1.25-3$	$S_L/D=S_T/D$ $1.25-3$	$1-10^3$ $10^3-3\times10^5$	$5-\infty$		X	X	X		X	
Numerical and Analytical	**Yilmaz and Yilmaz**	$\{1.25,1.5,2\}$		$6-10^6$	$1-\infty$				X	X	X	
	Faghri and Rao	$\{1.25,1.5\}$	$\{1.25,2.4\}$	$1-10^3$	$1-\infty$	Bare and Finned		X	X		X	• Wilson and Bassiouny
	Wilson and Bassiouny	$1.3-5$	$1-5$	10^2-10^5	$\{1,2\}$	Bare Tubes	X	X	X	X	X	
	Shaboury et al.	$1.25-2$		$\{100,300\}$	5		X	X	X			
	Bacellar et al.	$1.2-4$		$1.2-4$	$2-40$		X	X	X	X		
-	**Current Work**	-	-	-	-	-	-	-	-	-	-	-

(a)

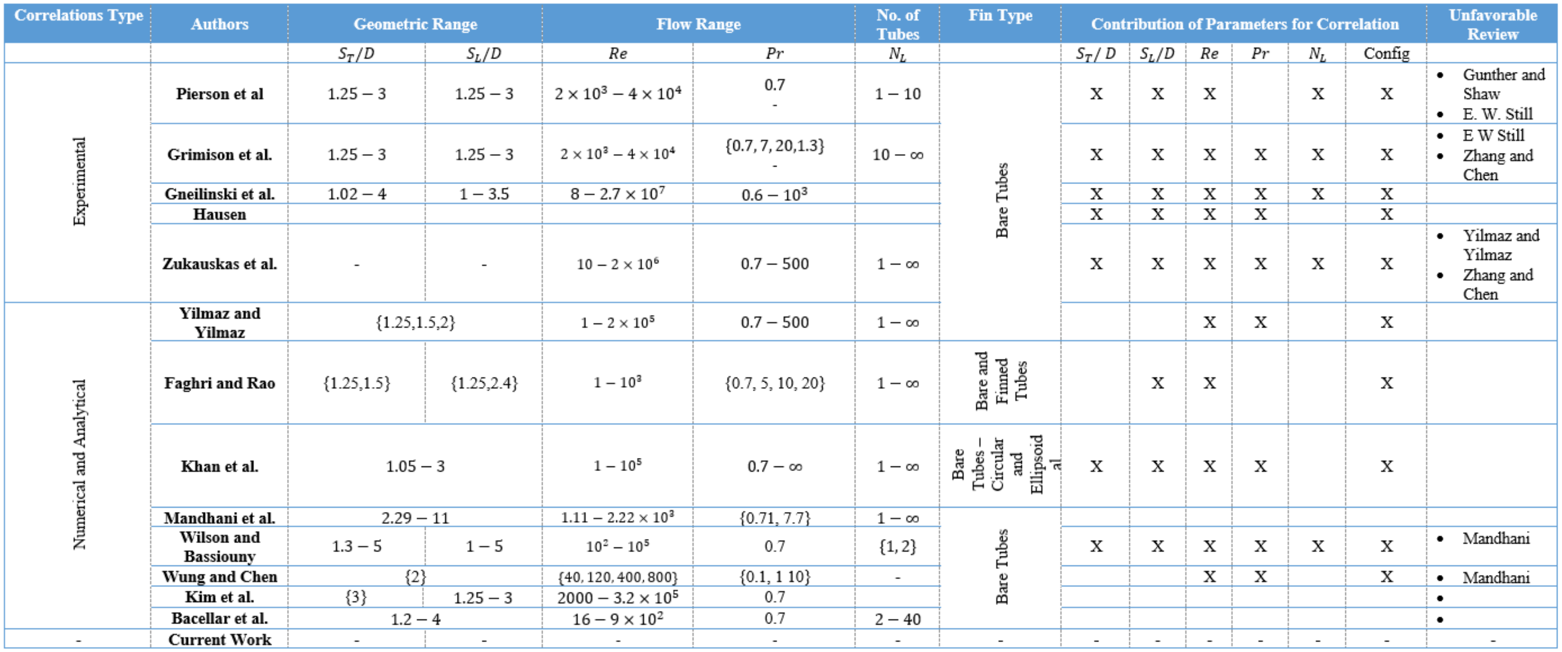

Correlations Type	Authors	Geometric Range		Flow Range		No. of Tubes	Fin Type	Contribution of Parameters for Correlation						Unfavorable Review
		S_T/D	S_L/D	Re	Pr	N_L		S_T/D	S_L/D	Re	Pr	N_L	Config	
Experimental	**Pierson et al**	$1.25-3$	$1.25-3$	$2\times10^3-4\times10^4$	0.7 -	$1-10$	Bare Tubes	X	X	X		X	X	• Gunther and Shaw • E. W. Still
	Grimison et al.	$1.25-3$	$1.25-3$	$2\times10^3-4\times10^4$	$\{0.7,7,20,1.3\}$ -	$10-\infty$		X	X	X	X	X	X	• E W Still • Zhang and Chen
	Gneilinski et al.	$1.02-4$	$1-3.5$	$8-2.7\times10^7$	$0.6-10^3$			X	X	X	X	X	X	
	Hausen							X	X	X	X		X	
	Zukauskas et al.	-	-	$10-2\times10^6$	$0.7-500$	$1-\infty$		X	X	X	X	X	X	• Yilmaz and Yilmaz • Zhang and Chen
Numerical and Analytical	**Yilmaz and Yilmaz**	$\{1.25,1.5,2\}$		$1-2\times10^5$	$0.7-500$	$1-\infty$				X	X		X	
	Faghri and Rao	$\{1.25,1.5\}$	$\{1.25,2.4\}$	$1-10^3$	$\{0.7, 5, 10, 20\}$	$1-\infty$	Bare and Finned Tubes		X	X			X	
	Khan et al.	$1.05-3$		$1-10^5$	$0.7-\infty$	$1-\infty$	Bare Tubes – Circular and Ellipsoidal	X	X	X	X		X	
	Mandhani et al.	$2.29-11$		$1.11-2.22\times10^3$	$\{0.71, 7.7\}$	$1-\infty$	Bare Tubes							
	Wilson and Bassiouny	$1.3-5$	$1-5$	10^2-10^5	0.7	$\{1,2\}$		X	X	X	X	X	X	• Mandhani
	Wung and Chen	$\{2\}$		$\{40,120,400,800\}$	$\{0.1, 1\ 10\}$	-				X	X		X	• Mandhani
	Kim et al.	$\{3\}$	$1.25-3$	$2000-3.2\times10^5$	0.7									•
	Bacellar et al.	$1.2-4$		$16-9\times10^2$	0.7	$2-40$								•
-	**Current Work**	-	-	-	-	-	-	-	-	-	-	-	-	-

(b)

3.3. PCM based models

Several kinds of research have been done in the literature on the numerical study of the phase-change process, in general. The first approach taken in the literature was by mathematically treating the phase-change problems as the moving boundary problems, also called Stefan problems [52] [53], and provided an exact solution [54] by solving heat equations and interface equations based on energy conservation at the phase-change boundary. However, the interface energy equations are challenging to solve due to interface issues such as non-linear nature and physical discontinuities due to change in properties from one phase to another. Thus, the exact solutions are valid only for simple geometries and boundary conditions. Similarly, other analytical approaches, such as calculation of variation, successive approximation, and perturbation methods [52], are also limited to simplified 1D domains and boundary conditions.

The alternative approach uses numerical techniques generally based on temperature-based and enthalpy-based finite-difference and finite-element methods. The temperature-based methods track the phase-change boundary by solving two separate temperature equations on the solid and liquid computational domains through energy balance at the phase-change boundary [52,55]. However, these methods are not robust and are challenging to program due to interface issues. The enthalpy-based methods don’t track the phase-change interface but rather treat the problem as a typical heat conduction problem without phase-change by solving a single governing equation on the combined liquid and solid computational domain. It thus, avoid interface issues, unlike temperature-based methods. These methods are also robust and easier to program. Similar to the enthalpy-based methods, other methods commonly used are source-term-based methods and heat-capacity methods [4], velocity transitioned modeling [56], and first and second thermodynamics-law models [57]. Thus, these numerical techniques can potentially resolve the multidimensionality and complexity of versatile analytical problems.

The most common application of these numerical approaches is modeling energy storage processes in shell and tube storage units. Some numerical approaches use enthalpy-based [15] methods, while some use heat-capacity-based [16]. They formulate the PCM problem surrounding the tubes as a 2D axisymmetric problem with an inner cylinder consisting of the flow passing inside the tube. In contrast, the outer cylinder consists of the PCM. These cylindrical-based studies have been extended to model PCM cylinders enclosing finned tubes using traditional enthalpy-based approaches [17]. Some studies also use the enthalpy-based approaches directly via commercial solvers such as Ansys Fluent [58]. Similar applications on cylindrical latent heat storage systems have also been made using analytical approaches based on second thermodynamics law [18] and moving boundary methods [5]. Besides the traditionally used approaches, some other simple numerical approaches that have been developed are the temperature and thermal resistance iteration method [19] based on energy conservation and implemented for concentric tube storage units. However, most of these transient studies are based on the 2D computational domain, which is still computationally expensive.

The present study, thus, focuses on developing a computationally efficient ROM for 1D radial conduction in PCM, which is later validated with conventional enthalpy-based approaches via commercial solvers.

3.4. Summary

This chapter discussed the theoretical background behind the design and working of the cross-media HXs. Since such HXs consist of wires in a tube-bank geometry, a fundamental understanding behind external flow across tube-banks was explained. Extending the concept of tube-banks led to a detailed review of literature correlations for Eu and Nu numbers for both staggered and inline configurations. It was observed that these literature correlations are applicable only for a given range of tube-bank geometry. It was shown that although the applications considered for were typically used in laminar flow conditions, very few correlations are available that can be used directly for computing the cross-media HX performance of interest in this thesis. Moreover, from optimization point of view, a robust approach is required to compute the optimum HX performance since the available literature correlations are valid for discrete geometric ranges.

Additionally, the properties and challenges associated with PCM, such as expensive encapsulation process and low PCM thermal conductivity were explained. It was suggested that such shortcomings can be met by the macro-encapsulation of PCM-metal structures present in the TES units. Furthermore, the transient modeling of conduction in the PCMs is challenging using analytical approaches and is computationally expensive depending on the domain and transition period. These shortcomings can be more pronounced if one is to conduct multi-scale design optimization, as it involves multiple runs of design points and associated complexities.

Chapter 4: Numerical Modeling

This chapter describes the numerical modeling of the HX for both the sensible and latent thermal energy storage applications. It consists of three main sections. The first section discusses numerical modeling for respective applications and how the present numerical models meet those needs and challenges. The second section deals with the development of a numerical model for sensible thermal storage applications. It requires performing 2D CFD simulations at the segment level of the HX and requires less computational cost than the CFD modeling of the entire HX. A mesh-independence study based on the curve-fitting approach is also carried out to obtain mesh-independent thermal and hydrodynamic parameters. However, the numerical model computes the entire HX performance by integrating the performance parameters from the CFD of segment level such as Eu and Nu numbers to that of the entire HX domain. Since the geometrical parameters might affect the flow field of the fluids across the HX, a high-fidelity 3D CFD model for the segment level of the HX is developed, which also tries to consider the effects of additive manufacturing on the HX geometric dimensions. The last section discusses a reduced-order model (ROM) for modeling 1D radial conduction inside PCM enveloping the wires. It uses an analytical approach, which saves a lot of computation power compared to the actual transient CFD simulations of the PCM-wire model.

4.1. Need for the Numerical Study

As discussed, the literature includes the correlations ($\boldsymbol{Nu}$ for thermal and $\boldsymbol{Eu}$ for pressure-drop) only for some fixed ranges and flow conditions. However, there are no direct correlations available in the literature for a wide range of tube-bank and flow parameters for laminar crossflow over staggered tube-banks (see Figure 13).

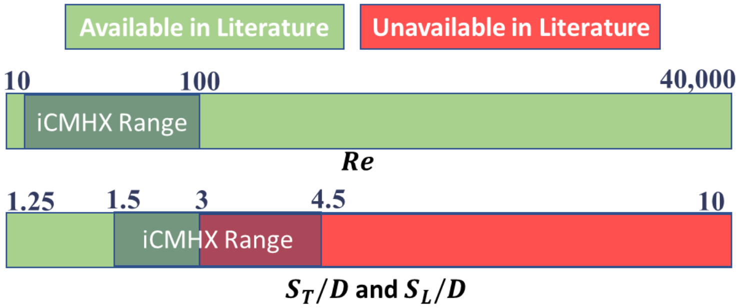

Figure 13: Availability of literature correlations for staggered tube-banks for different $\boldsymbol{S_T/D}$ *and* $\boldsymbol{S_L/D}$ *values at different* $\boldsymbol{Re}$

This shortcoming in the literature can be overcome by performing a CFD study of the tube-bank geometry to obtain the entire HX performance for sensible storage applications. The present dissertation uses two different approaches for CFD modeling. The first approach is based on 2D CFD-based modeling related to nominal CAD dimensions of the iCMHX. In contrast, the second approach is based on 3D CFD-based modeling related to realistic and actual dimensions and geometry of iCMHX when measured via microscope and SEM.

Similarly, for the latent thermal storage applications, there are no closed-form analytical solutions present in the literature to simulate transient heat transfer in PCM for the present TES concept. Moreover, using CFD tools to compute the entire TES performance directly is computationally expensive. Thus, this creates a need to develop a computationally-efficient CFD model for simulating transient heat transfer in PCM.

4.2. Sensible Storage Model

The applications of iCMHX as a CPU radiator for the electronic cooling of desktop computers have been discussed here.

4.2.1. iCMHX Geometry

The iCMHX cools the hot liquid, which carries away the heat from the CPU via cross-flowing cold ambient air. The cold air flows across the airflow length (L_a) of the iCMHX. Similarly, the hot liquid (water) enters the liquid manifolds and is distributed into the first half of the liquid channels ($\frac{N_w^{chan}}{2}$), which is separated from their other half via a thin ABS polymer wall. This fluid path is shown in *Figure 14*. At the same heat transfer area, the double-pass system yields double the flow rate compared to the single-pass system, resulting in a higher heat transfer coefficient than the single-pass system but at the cost of a higher pressure drop. The details of the iCMHX design are summarized in Table 4.

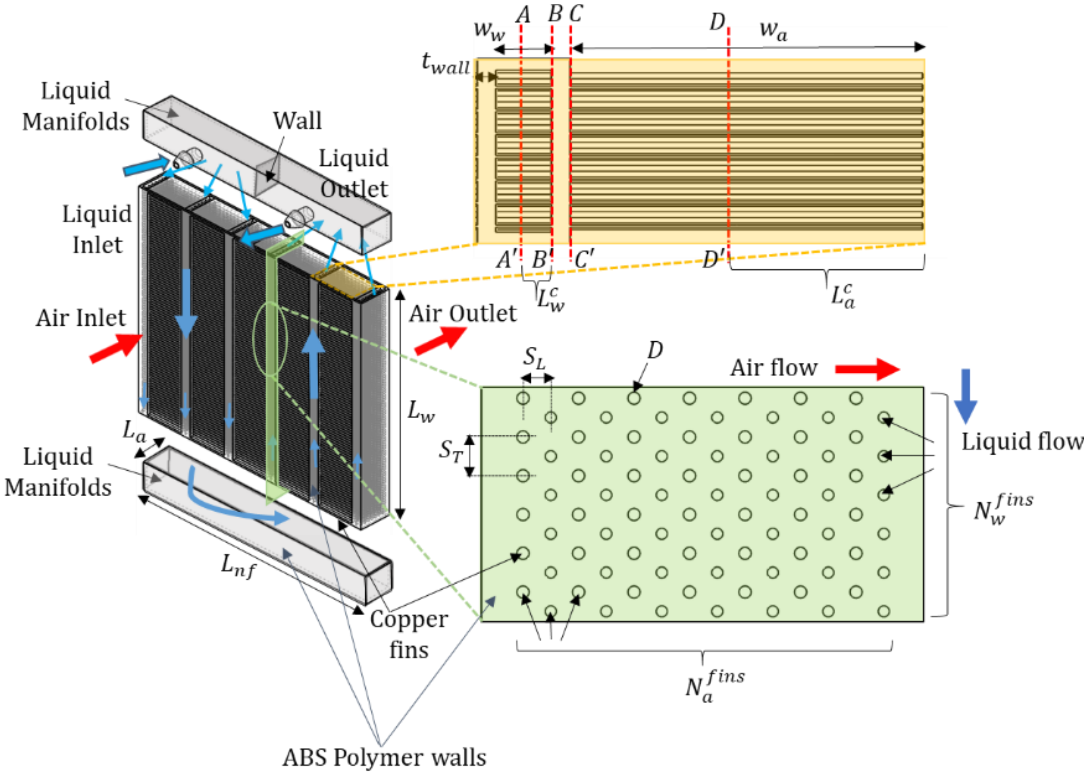

Figure 14: Schematic of the iCMHX with detailed geometry and fluid paths

Table 4: Design specifications of iCMHX

CMHX Dimensions	
L_a	16 mm
L_{nf}	119 mm
L_w	119.6 mm
w_a	19 mm
w_w	2 mm
t_{wall}	1 mm

Weight	
Total weight	253.2 g

Tube-banks Geometry	
N_a^{chan}	5
N_w^{chan}	6
D	0.44 mm
S_T	1.4 mm
S_L	1 mm
N_a^{fins}	14
N_w^{fins}	84

The modeling process from the segment level to the entire iCMHX will now be discussed, as illustrated in *Figure 15*.

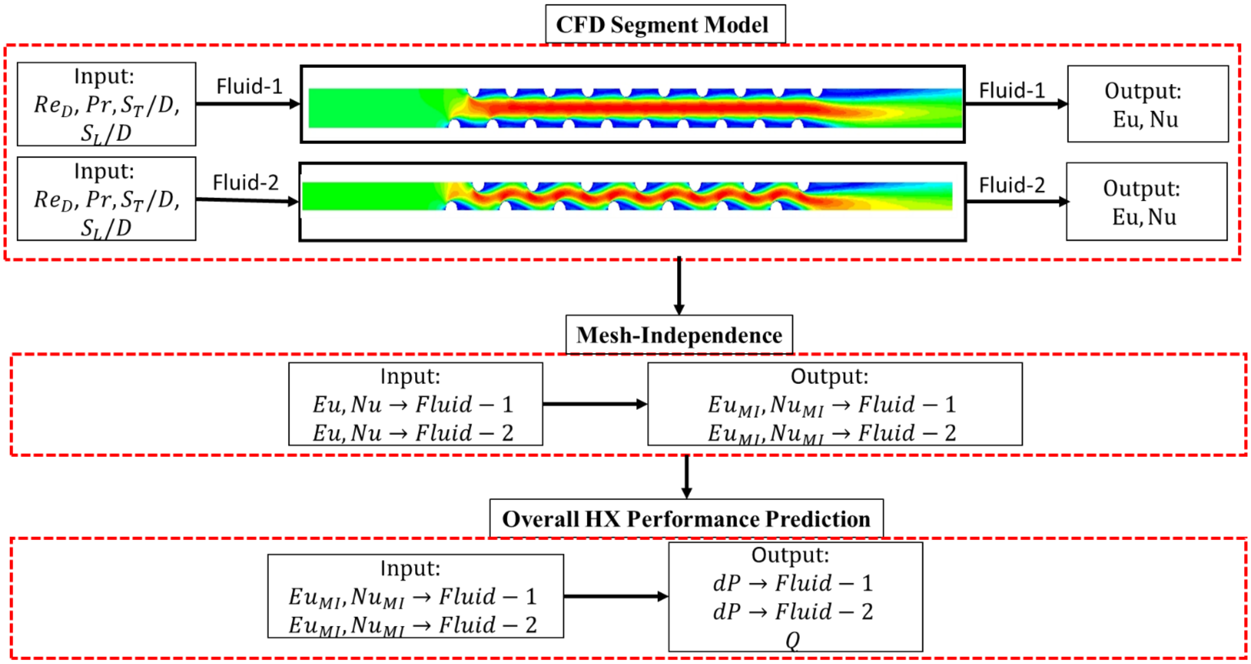

Figure 15: Overview of a modeling approach for iCMHX from segment level to entire HX level

4.2.2. Traditional 2D CFD Segment Level Model

Later, a mesh-independence technique is described and implemented on the CFD results of Eu and Nu numbers. The section is divided into four subsections: (i)

Numerical Setup, (ii) Nusselt Number, (iii) Euler Number, and (iv) Mesh-Independence Study. A detailed study can also be found in [59].

4.2.2.1. Numerical Setup

The Euler and Nusselt numbers for the iCMHX are obtained using a detailed CFD study performed independently on both air and liquid sides, as traditionally done in the literature. They are modeled independently since assuming constant properties, $\boldsymbol{Eu}$ and $\boldsymbol{Nu}$ depend only on the geometry and the flow conditions such as fluid velocity [60]. The staggered tube banks were modeled as a 2D-symmetric model of a tube bank since 3D is computationally expensive. The flow conditions of the iCMHX application of CPU cooling serve as the boundary conditions for CFD simulations. The low Reynolds flow of both liquid and air sides results in a symmetrical flow field ([61]) and no vortex shedding, suggesting a 2D symmetric steady-state model. The domain and boundary conditions are given in *Figure 16*. A velocity inlet is applied on the left, while a pressure outlet is given on the right. The top and bottom are treated as symmetrical. The inlet and outlet are placed at around 11D from the first and last tube to ensure that the upstream or downstream boundary conditions do not affect the results. The computational cost is further saved by restricting the maximum number of tubes for modeling to 20.

The operating conditions for this application used in CFD modeling are shown in Table 5.

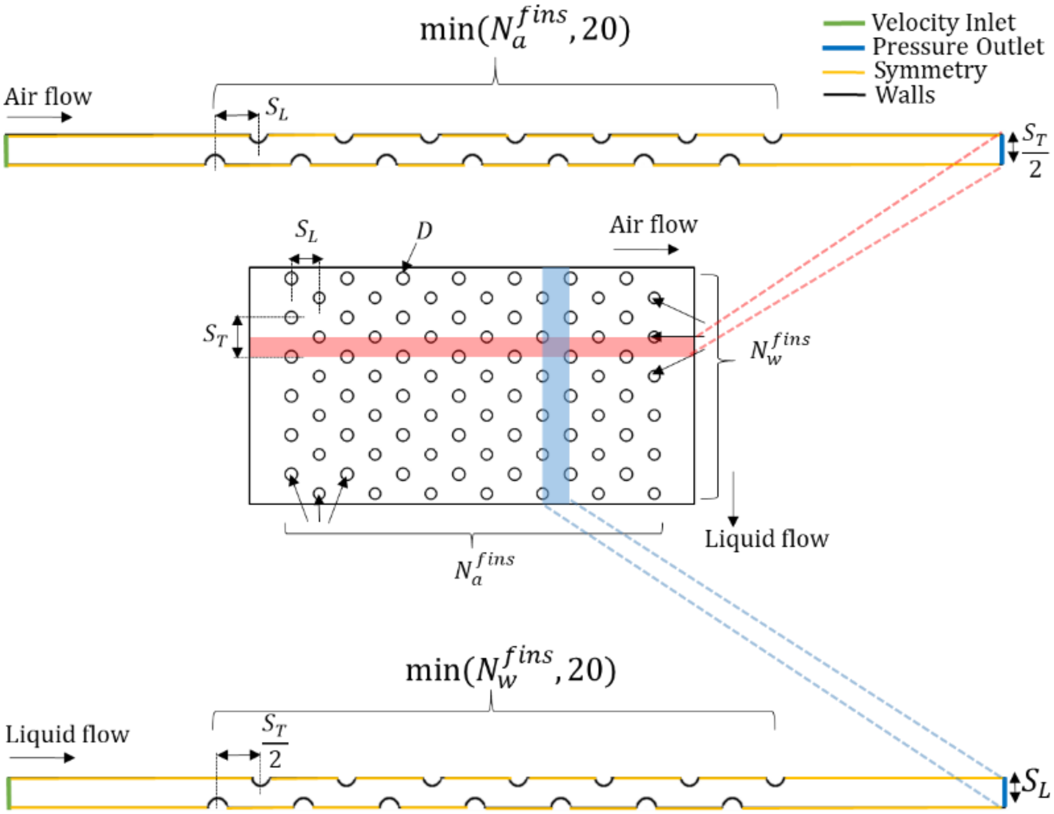

Figure 16: Numerical set-up including domain and boundary conditions for segment level model of iCMHX

Table 5: Operating Conditions for Electronic Cooling Applications

Thermal Conditions	
dT_{in}	20℃
Flow Conditions	
Re_a	$13 - 64$
Re_w	$16 - 78$
Simulation Statistics	
Total Cases	156

In the first step of the modeling, the geometry and boundary conditions were set up (see Figure 16) and mesh operations were performed, including edge-sizing and face-meshing consisting of unstructured triads elements in GAMBIT 2.4.6, as shown in Figure 17.

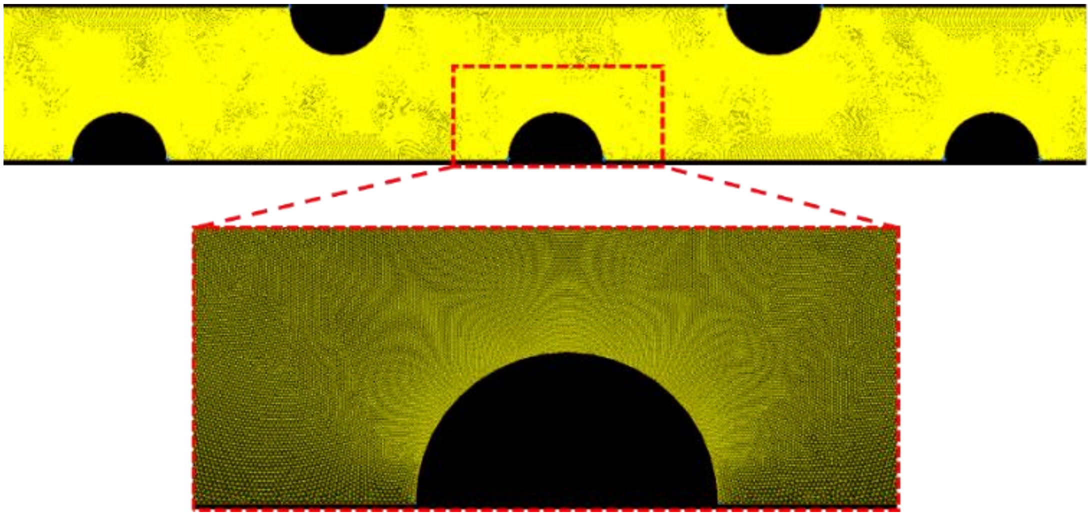

Figure 17: Meshed domain between tube-bundles consisting of 922,594 cells (top) and meshing as seen around the circular tube (bottom)

In the next step, the meshed model was exported to Ansys Fluent 18.2 for running CFD simulations holding the following assumptions:

- Laminar, steady-state, incompressible-flow, and iso-thermal flow with negligible work done by gravity, pressure, and viscous forces
- Constant fluid properties

The boundary conditions for the model include conditions imposed on the velocity inlet, symmetry, walls, and the pressure outlet. The velocity inlet takes the corresponding air-side and liquid-side v_b in the x-direction along with some constant temperature (T^{inlet}) as input as the temperature doesn't affect Eu and Nu values. The symmetry boundary in Fluent implicitly sets the gradients of flow and temperature variables in the y-direction to zero. The wall boundary condition is taken to be isothermal at some temperature (T_{wall}). The pressure-outlet boundary condition sets the outlet pressure (P^{outlet}) to zero.

The resulting governing Navier-Stokes equations for the 2D-CFD model are given in Equations (1)–(3):

Continuity: $$\nabla \cdot \vec{v} = 0 \tag{1}$$

Momentum: $$\nabla \cdot (\rho \vec{v}\vec{v}) = -\nabla \mathrm{P} + \nabla \cdot \bar{\bar{\tau}} \tag{2}$$

Energy: $$\nabla \cdot (\rho \vec{v} C_p T) = \nabla \cdot (\mathrm{k}\nabla \mathrm{T}) \tag{3}$$

where $\vec{v}, P$ and T are solved for both x and y directions and $\bar{\bar{\tau}}$ term represents the shear stress present in the fluid.

The simulations were run by setting up the solver details to attain faster convergence. The solver consists of PRESTO for pressure, first-order upwind for momentum and energy, and a residual limit of 1e-5 for continuity and momentum and 1e-12 for energy. The final step of the CFD study includes a post-processing procedure to compute Euler and Nusselt numbers for both air and liquid sides from output parameters such as the area-weighted average of P computed at the velocity-inlet boundary ($\mathbf{P^{inlet}}$) and the mass-weighted average of T computed at the pressure-outlet boundary ($\boldsymbol{T^{outlet}}$), respectively.

4.2.2.2. Nusselt Number

$\mathbf{Nu}$ is computed using the $\boldsymbol{\varepsilon} - \mathbf{NTU}$ method. Since the air side and liquid side are modeled separately, the $\boldsymbol{\varepsilon} - \mathbf{NTU}$ relationship for independent flow-configuration is employed to get $\mathbf{NTU}$ from $\boldsymbol{\varepsilon}$ for each side. $\boldsymbol{\varepsilon}$ is first evaluated for air and liquid sides, followed by NTU.

$$\varepsilon_i = \frac{T_i^{outlet} - T_i^{inlet}}{T_{wall} - T_i^{inlet}} \tag{4}$$

$$NTU = -\log(1 - \varepsilon_i) \tag{5}$$

where the index $\boldsymbol{i}$ takes the value of a and $\boldsymbol{w}$.

The heat transfer coefficients ($\boldsymbol{h_i}$) are then computed from $\boldsymbol{NTU}$ using the following equation.

$$h_i = NTU_i \frac{\dot{m}_\iota C_{p_i}}{A_i} \tag{6}$$

where $\boldsymbol{\dot{m}_\iota}$and $\boldsymbol{A_i}$ refer to the mass-flow rate and flow-area corresponding to the CFD domain, respectively. $\boldsymbol{Nu}$ is obtained from $\boldsymbol{h}$ for both air and liquid-side using Equation (7).

$$Nu_i = \frac{h_i D}{k_i} \tag{7}$$

where the index $\boldsymbol{i}$ takes the value of a and $\boldsymbol{w}$.

4.2.2.3. Euler Number

Similarly, Euler numbers for both air and liquid-sides are obtained using Equation (8) where $\boldsymbol{dP}$ is defined from the simulations as the ($\mathbf{P^{inlet}}$ - $\mathbf{P^{outlet}}$) and $\boldsymbol{N_L}$ as $\mathbf{min}(\boldsymbol{N_{L_i}^{fins}}, \mathbf{20})$.

$$Eu_i = \frac{dP_i}{\frac{1}{2}\rho_i v_{max_i}^2 N_{L_i}^{fins}} \tag{8}$$

where the index $\boldsymbol{i}$ takes the value of a and $\boldsymbol{w}$.

4.2.2.4. Mesh-Independence Study

The accuracy of the CFD results is improved via a mesh independence study on Eu and Nu using three different mesh levels for air-side and liquid-side refinements. The methodology is shown in Figure 18 and described in detail below.

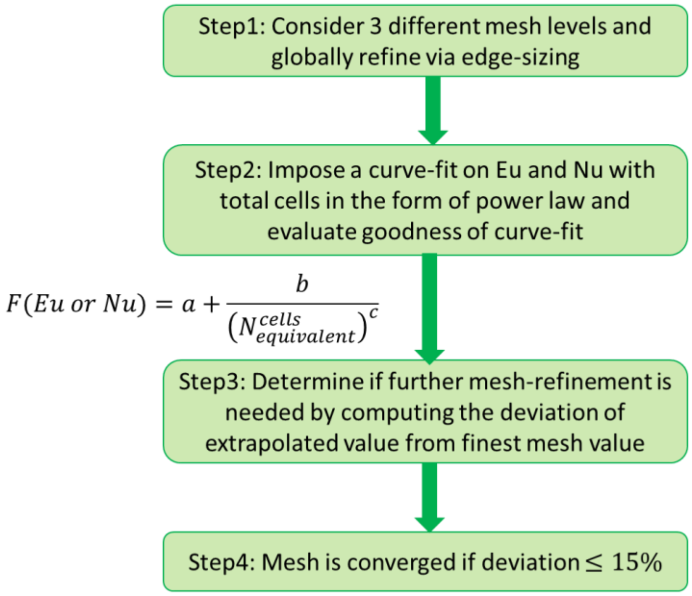

Figure 18: Methodology to compute mesh-independent Euler and Nusselt Numbers

- *Step1:* The mesh is globally refined by varying the edge-intervals during edge-sizing operation in Gambit, as shown in Table 6. Here, the number of equivalent cells, $\mathbf{N_{eqv}^{cells}}$ is defined from total number of cells for both air and liquid side as shown by Equation (9):

$$N_{eqv}^{cells} = \sqrt{\text{Total Cells}} \tag{9}$$

Table 6: Specifications of Mesh Levels

Mesh-Levels	Total Cells	
	Airside	Liquid-side
1	588268	540864
2	922594	1226264

3	2329468	2222450

- *Step 2:* A curve-fit for an equivalent number of total cells (N_{eqv}^{cells}) is adopted in lieu of Richardson extrapolation [62]. A power law curve is fitted mathematically as shown in Equation (10):

$$F = a + \frac{b}{\left(N_{eqv}^{cells}\right)^{c}} \tag{10}$$

where F stands for a generalized curve-fitted term representing Eu and Nu corresponding to the respective N_{eqv}^{cells} for both air and liquid sides, and a, b, and c represent some fitting coefficients. The finest three mesh values (f_1, f_2 and f_3) representing Eu or Nu corresponding to the three mesh-levels 1, 2, and 3, respectively, are considered for the curve-fitting process.

From Equation (10), the asymptotic values/extrapolated solutions, when $N_{eqv}^{cells} = \infty$, are given by the a coefficients of the curve-fits. To check the goodness of the curve-fit, $\%\Delta_{\text{diff}}$ is defined as the maximum % difference between the mesh and corresponding curve-fit values.

- *Step 3:* To determine whether the mesh is sufficiently refined to provide the mesh value closest to the extrapolated solution, a parameter denoted by $\%\delta_{\text{dev}}$ is introduced. It is used for comparing the deviation of the extrapolated solution, a, obtained from Step2 from the finest mesh-value, 'f_3 ,' as shown in Equation (11):

$$\%\delta_{\text{dev}} = \frac{f_3 - a}{a} \times 100 \tag{11}$$

- Step 4: If the $\%\delta_{\text{dev}}$ obtained from Step 3 is less than its tolerance limit, then the mesh is said to converge. The extrapolated solution a is taken as the mesh-independent value for Eu and Nu for both air and liquid sides at different Reynold numbers. A tolerance limit of 15% was set for $\%\delta_{\text{dev}}$.

The mesh was found to converge for all the cases for both the air side and liquid side. For clarity, the liquid-side trend for only one Reynolds number is shown to highlight the curve-fitting approach (see Figure 19). In cases with no mesh convergence, the desired $\%\delta_{\text{dev}}$ can be achieved by running finer mesh, which comes at a high computational cost.

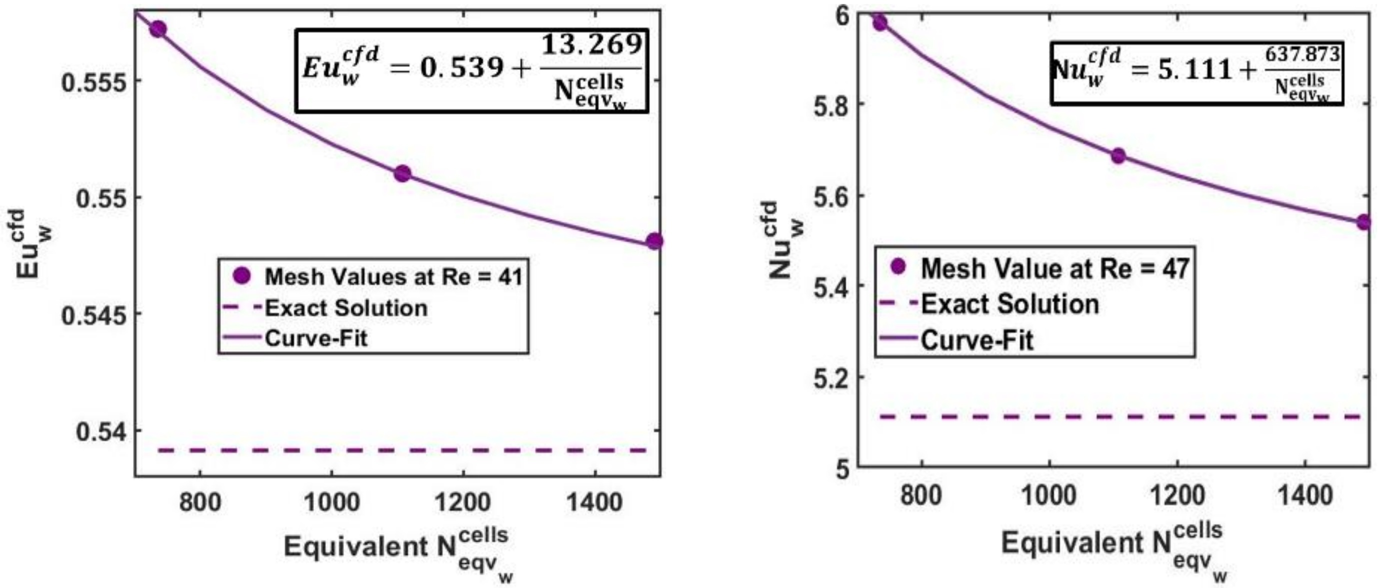

(a) (b)

Figure 19: Trend of liquid-side (a) Euler Number and (b) Nusselt numbers with Equivalent Mesh at particular Re value

Table 7: Mesh-Independence Summary

	Airside		Liquid-side	
	Eu	**Nu**	**Eu**	**Nu**
Maximum $\%\Delta_{\text{diff}}$	0.0389%	0.0335%	0.112%	0.0216%
Maximum $\%\delta_{\text{dev}}$	0.547%	1.711%	1.906%	11.3%

It is to be noted that the curve-fitting approach utilizes the value of coefficient c as 1, as it is representative of the first order of discretization used by the Fluent solver. The curve-fit such obtained demonstrates a good curve-fit lying within the maximum 0.1% for both Euler and Nusselt numbers for both the fluids (see

Table 7). This demonstration suggests that our assumption of keeping c as 1 is justifiable. It is also worth noting that the maximum $\%\delta_{\mathrm{dev}}$ observed in Nu and Eu is for higher Reynolds numbers ($\mathrm{Re} = 66, \mathrm{Re} = 78$) obtained on the liquid side. Thus, fine mesh refinement on the liquid side should be taken care of.

4.2.3. Analytical Model Based Entire HX Model

The mesh-independent Euler and Nusselt numbers for both the fluids are then used to compute the overall HX performance.

4.2.3.1. Heat transfer

The authors based the heat transfer study across the iCMHX to the concept of heat transfer across staggered tube banks. The heat transfer coefficient is calculated from Nu for both air and liquid, as shown in Equation (12). Since Nu correlations are absent in the literature for the current geometry, it is obtained from mesh-independent CFD simulations, which is explained through Equations (4) $-$ (7).

$$h_i = \frac{Nu_i k_i}{D} \tag{12}$$

where the index i takes the value of a and w.

Once the heat transfer coefficients are determined for both air and liquid/water, the overall thermal resistance (see Equations **(18)**) is calculated using the thermal circuit model, formed due to the (i) air-side convective resistance on the fins, (ii) the water-side convective resistance on the fins and (iii) the conductive resistance across $\boldsymbol{t_{wall}}$.

The fins for air-side convection are considered in-between planes $\boldsymbol{CC' - DD'}$ (see Figure 14) while the fins for the liquid-side convection are considered in-between planes $\boldsymbol{AA' - BB'}$ such that they all have adiabatic tips due to geometrical symmetry. The region between the two planes in each case is defined as an interface. For wall resistance, the interface is said to be the region between the planes $\boldsymbol{BB' - CC'}$ separated by $\boldsymbol{t_{wall}}$ distance. Drawing this analogy on the entire iCMHX, there is a total of $\mathbf{n} = \mathbf{2}(\boldsymbol{N_w^{chan}} - \mathbf{1})$ interfaces formed by the planes, or $\mathbf{n} = \mathbf{10}$ for the current design.

Therefore, to calculate the overall thermal resistance, the fin-efficiency ($\boldsymbol{\eta}$) has to be first determined using fin-parameter ($\boldsymbol{mp}$) and effective fin length ($\boldsymbol{L_C}$) for both air and liquid sides.

$$mp_i = \sqrt{\frac{4h_i}{k_{cu}D}} \tag{13}$$

$$L_i^c = \frac{w_i}{2} + \frac{D}{4} \tag{14}$$

$$\eta_i = \frac{\tanh(mp_i L_i^c)}{mp_i L_i^c} \tag{15}$$

where the index $\boldsymbol{i}$ takes the value of a and $\boldsymbol{w}$.

Following the thermal circuit model, the overall thermal resistance is then calculated using Equation (18) from (i) the air side, (ii) the liquid side, and (iii) the walls, using the mentioned heat transfer fin areas derived in Equations (16) and (17):

$$A_{Cu}^{cs} = \pi \frac{D^2}{4} N_a^{fins} N_w^{fins} n \tag{16}$$

$$A_i^{fin} = \pi D w_i N_a^{fins} N_w^{fins} N_i^{chan} \tag{17}$$

where the index $\boldsymbol{i}$ takes the value of a and $\boldsymbol{w}$.

$$R_{total} = \left(\frac{1}{h_a A_a^{fins} \eta_a}\right)_{airside} + \left(\frac{1}{h_w A_w^{fins} \eta_w}\right)_{liquidside} + \left(\frac{t_{wall}}{k_{cu} A_{Cu}^{cs}}\right)_{walls} \tag{18}$$

After $\boldsymbol{R_{total}}$ is calculated, the overall thermal performance parameter such as heat transfer rate ($\boldsymbol{Q}$) is calculated using the $\boldsymbol{\varepsilon - \mathrm{NTU}}$ method (see Equations (21) –(23)), considering that the CMHX operates in a cross-flow configuration with both fluids unmixed. For the $\boldsymbol{\varepsilon - \mathrm{NTU}}$ method, the overall NTU has to be calculated using conductance ($\boldsymbol{UA_{overall}}$). Since $\boldsymbol{R_{total}}$ is known, $\boldsymbol{UA_{overall}}$ is calculated as shown below:

$$UA_{overall} = \frac{1}{R_{total}} \tag{19}$$

$$C_{min} = \min\{\dot{m}_a C_{p_a}, \dot{m}_w C_{p_w}\} \tag{20}$$

$$NTU_{overall} = \frac{UA_{overall}}{C_{min}} \tag{21}$$

$$\varepsilon_{\mathrm{HX}} = 1 - e^{\frac{1}{C_r} * NTU_{overall}^{0.22} \left(e^{-C_r * NTU_{overall}^{0.78}} - 1\right)} \tag{22}$$

$$Q = \varepsilon_{\mathrm{HX}} C_{min} dT \tag{23}$$

The methodology is also explained via a flowchart, as in Figure 20.

Besides this, some typical trends are observed. $\boldsymbol{Nu}$ is shown to increase with increasing $\boldsymbol{Re\ and\ Pr}$ [63] following a power-law trend, as shown below.

$$Nu = f(Re, Pr, S_T, S_L, D) \tag{24}$$

$$Nu = A + CRe^m \tag{25}$$

where $\boldsymbol{A}$, $\boldsymbol{C}$ and $\boldsymbol{m}$ are some fitting coefficients.

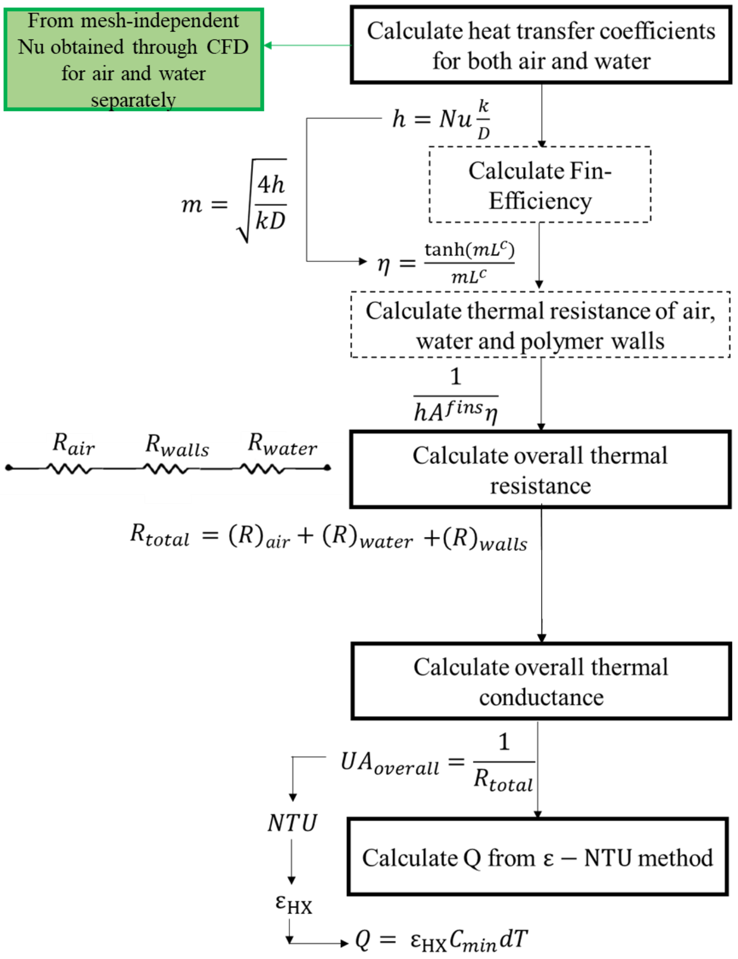

Figure 20: Methodology for prediction of HX performance

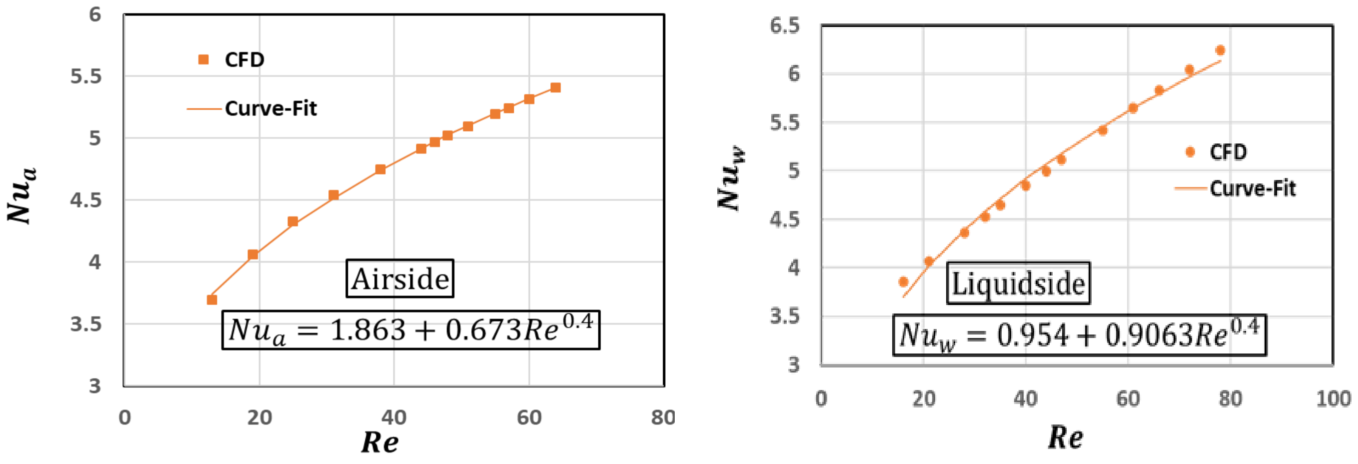

(a)

(b)

Figure 21: Trend of airside Nusselt number with Reynolds

From Equation **(25)**, it can be seen that the curve-fit deviates from the conventional form mentioned in the literature [64,65] with an offset. This deviation can be explained because the literature correlations are generally applicable for higher Reynolds flow where Nusselt value continuously varies with the increase in the size of recirculation zones due to turbulent flow. However, when the Reynolds number is very small, $\mathbf{Nu}$ appears to be fairly constant, equivalent to the offset, $\mathbf{A}$. The constant $\mathbf{Nu}$ value is, thus, interpreted to be the fully-developed $\mathbf{Nu}$ value ([66] and [67]), which along with the developing flow-term enables this curve-fit to work even for low $\boldsymbol{Re}$ conditions. The effect of $\mathbf{Pr}$ is incorporated with the coefficient $\mathbf{C}$. An assumption of $\mathbf{m = 0.4}$ is made to be in agreement with the correlations-form given in the literature ([68] and [69]). Since the curve-fit is good)—that is, maximum of $\%\boldsymbol{\Delta}_{\mathbf{diff}}$ is within 1.2% except one point with $\%\boldsymbol{\Delta}_{\mathbf{diff}}$ of around 4%—our assumption seems to be justifiable.

Also, there is an effect of geometrical parameters on $\mathbf{Nu}$ for the air side ($\boldsymbol{S_T}$ = 1.4 mm, $\boldsymbol{S_L = 1\,mm}$) and liquid side ($\boldsymbol{S_T}$ = 2 mm, $\boldsymbol{S_L} =$0.7 mm). Since they share different geometries, $\boldsymbol{Nu}$ is curve-fitted separately for each side. As the geometrical parameters vary, the recirculation region space changes. The recirculation zones expand as the flow becomes more tortuous, leading to better mixing between the fluid and the fins ([70]). Thus, the effect of $\boldsymbol{Nu}$ due to $\boldsymbol{S_T}$ and $\boldsymbol{S_L}$ depends on their contribution towards formation of recirculation zones behind the tubes at different Reynolds numbers.

4.2.3.2. Pressure-Drop

The flow impedance, or the air and liquid pressure drops, is governed by the independent variables, including geometric spacing and air and liquid flow rates. The pressure drop is calculated from $\boldsymbol{Eu}$ using Equation (13), as mentioned below. Like $\boldsymbol{Nu}$, $\boldsymbol{Eu}$ correlations are also absent in the literature. They are also obtained from mesh-independent CFD results as discussed in Equation (8).

$$dP_i = \frac{1}{2}\rho_i v_{b_i}^2 Eu_i N_i^{fins} \tag{26}$$

where the index $\boldsymbol{i}$ takes the value of a and $\boldsymbol{w}$.

This can also be explained through flow-chart, as shown in ***Figure 22***.

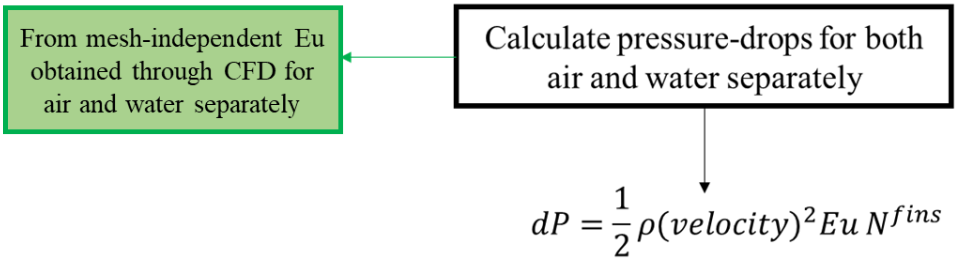

Figure 22: Methodology for computing pressure-drop

Like $\boldsymbol{Nu}$ vs. $\boldsymbol{Re}$, the relationship between the $\boldsymbol{Eu}$ with Reynolds number for air side and liquid sides was found to follow the inverse power-series, according to the trend observed in the literature [68,69]. The goodness of the curve-fit lies (see Figure 23 and Figure 24) within the maximum of 2.7%, thus the trend of $\boldsymbol{Eu}$ decreasing with increasing $\boldsymbol{Re}$ can be quantified mathematically as shown below:

$$Eu = f(Re, S_T, S_L, D) \tag{27}$$

$$Eu = \frac{A}{Re} + B \tag{28}$$

where A and B are some fitting coefficients.

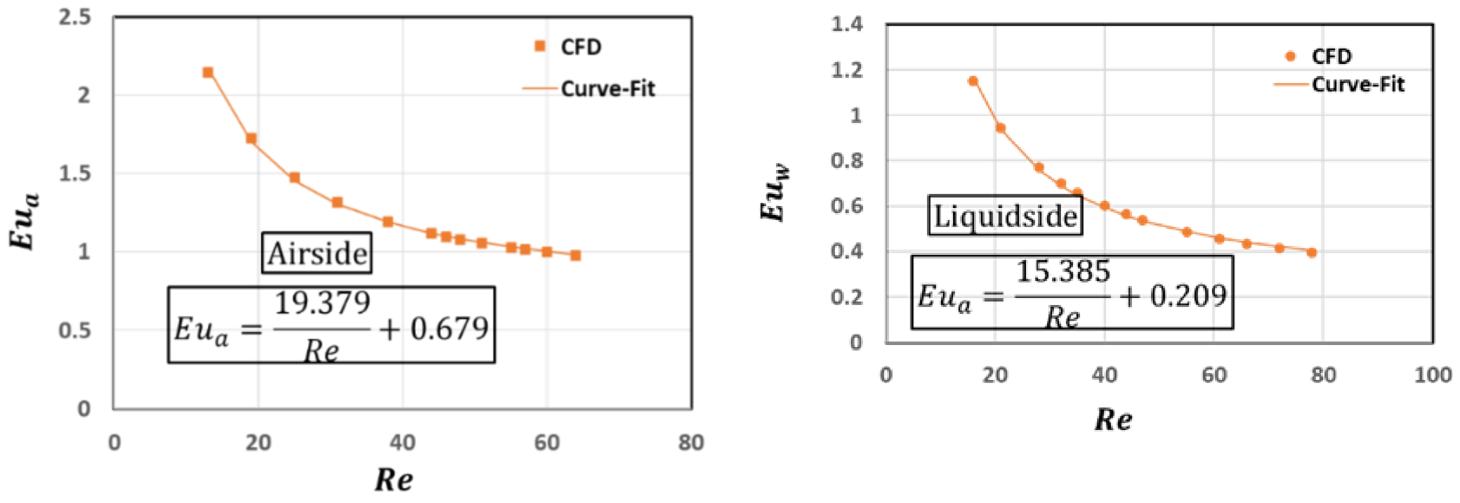

(a) (b)

Figure 23: Trend of Euler number with Reynolds number

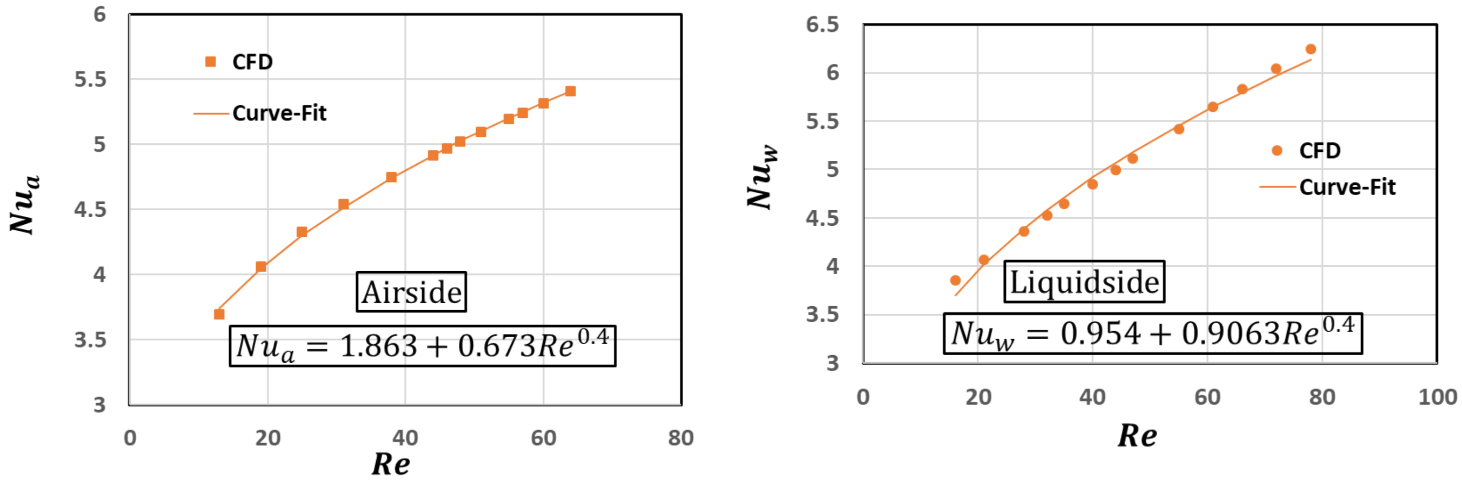

(a) (b)

Figure 24: Trend of Nusselt number with Reynolds number for air and water

Since $\boldsymbol{Eu}$ also depends on the geometrical parameters of the tube banks, the air-side and liquid-side $\boldsymbol{Eu}$ are reported to have different Euler numbers even at the same Reynolds number, since they have different $\boldsymbol{S_T}$ and $\boldsymbol{S_L}$. From Figure 23 and Figure 24, it can be noted that $\boldsymbol{Eu_a}$ has higher value compared to $\boldsymbol{Eu_w}$, as $\boldsymbol{S_T}$ for the air side (1.4 mm) is less than that for the liquid side (2 mm). This justifies the reasoning that the flow impedance increases if the tubes are placed close to each other in the transverse direction of flow [71]. The effect of $\boldsymbol{S_L}$ is observed to have considerably less influence on Euler numbers, since the flow is passing through the tubes such that the longitudinal spacing doesn't affect the fluid path significantly.

4.2.4. High-Fidelity 3D CFD Segment Level Model

A detailed study regarding this can be found in [72].

4.2.4.1. Effect of Printing Variabilities

Since the iCMHX is additively manufactured, the effect of printing variabilities on the iCMHX dimensions needs to be studied and then implemented in the numerical model to predict the iCMHX performance better. For this study, the iCMHX was first hardened using an Allied epoxy-set of resin and hardener to retain its original dimensions and then machined into different segments (see Figure 25), which were analyzed using Keyence VR3200 microscope and Hitachi SU-70 FEG SEM.

Some major printing variabilities are discussed below:

- The wires were excessively squashed in the water flow direction (y-axis), such that they acquired spatially-varying ellipsoidal shapes instead of nominal circular shapes (see Figure 25 (a)). This squashing could be due to the improper functioning of the wire-extruder mechanism of the printer's metal head.

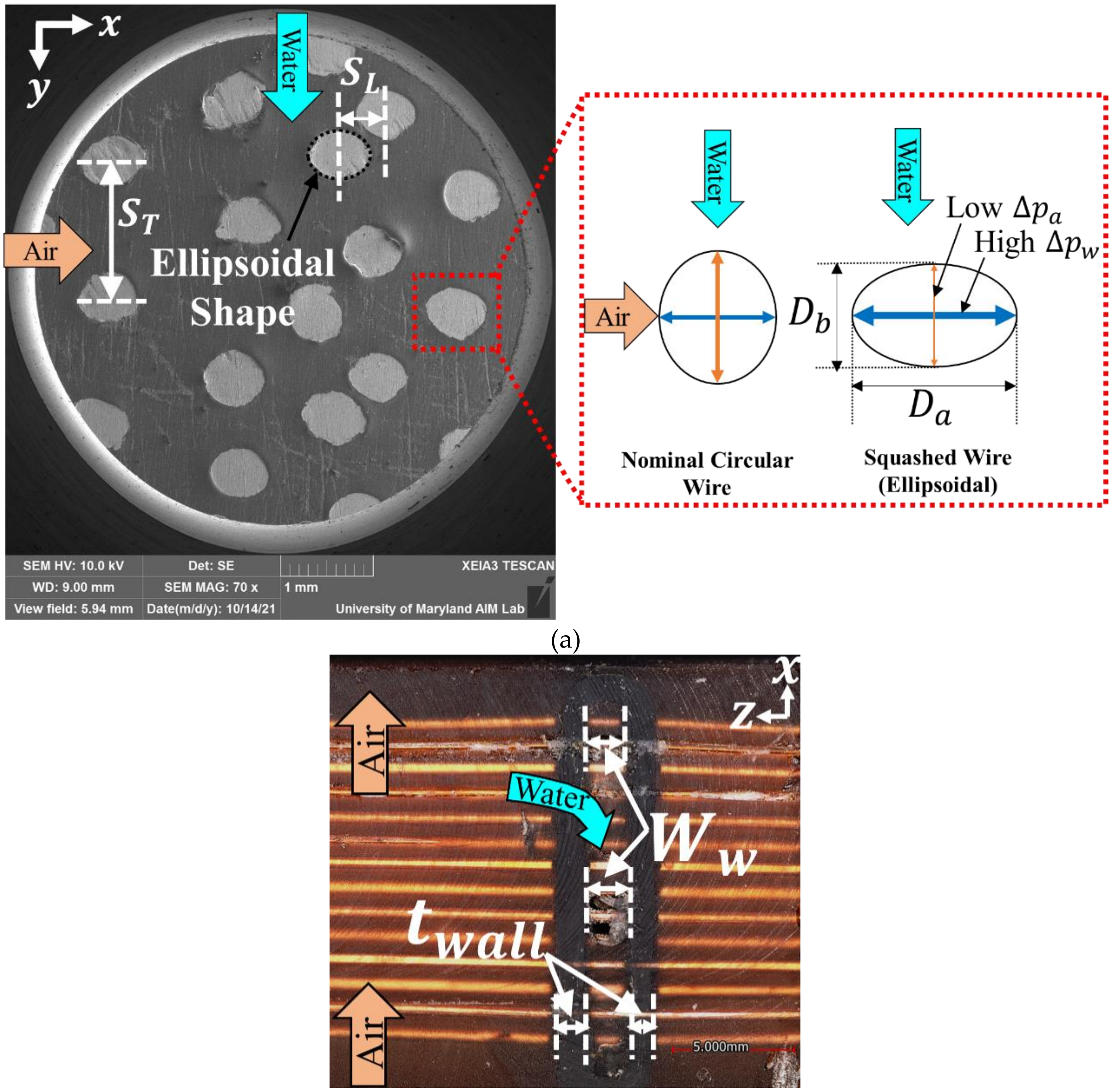

(a)

(b)

Figure 25: (a) SEM image for wire spacings and wire shape; and (b) microscope image of varying water channel width

- The wire spacings, particularly SL, varied with a high standard deviation, as shown in Figure 25 (a). This misalignment among a few rows of wires deviated from the nominal staggered configuration. It might have occurred due to the precision error in the movement of the printer’s metal head.

- The water channel width, Ww, also varied spatially due to variable polymer wall thickness (see Figure 25(b)), possibly caused by the precision error in the movement of the printer's polymer head. The deviation in the average reading of width of the water channel from its nominal reading was the highest of all the geometrical parameters.

- The coating thickness of polyurethane sealant (t_{coat}) from the dip-coating process around the wire was around 20 μm.

A statistical analysis on the measured dimensions was carried out, the summarized dimensions shown in Table 8.

Table 8: Measured dimensions of iCMHX due to printing variabilities

	Nominal	**Measured**			
	[mm]	Average [mm]	Standard Deviation [mm]	Range [mm]	Number of Measurement Points
$\mathbf{D_a}$	0.44	0.48	0.042	0.343-0.686	982
$\mathbf{D_b}$	0.44	0.42	0.045	0.275-0.566	1025
$\mathbf{S_T}$	1.4	1.4	0.15	0.472-2.78	941
$\mathbf{S_L}$	1	0.94	0.253	0.224-1.74	850
$\mathbf{W_w}$	2	1.79	0.18	1.23-2.13	106
$\mathbf{t_{wall}}$	1	1.08	0.127	0.85-1.48	49

Based on the average measured dimensions, the overall iCMHX design parameters (see Figure 14) are formulated as shown in Table 9.

Table 9: Design details, as measured, of the current iCMHX unit

	iCMHX
$\mathbf{L_a}$ **[mm]**	16
$\mathbf{L_w}$ **[mm]**	119.6
$\mathbf{L_{nf}}$ **[mm]**	119
$\mathbf{m_{HX}}$ $[mm]$	253.2

$\mathbf{Vol_{HX}}$ $[mm^3]$	2.27×105
$\mathbf{W_a}$ $\mathbf{[mm]}$	19
$\mathbf{W_w}$ $\mathbf{[mm]}$	1.79
$\mathbf{t_{wall}}$ $\mathbf{[mm]}$	1.08
$\mathbf{nc_a}$	5
$\mathbf{nc_w}$	6
$\mathbf{S_T}$ $\mathbf{[mm]}$	1.4
$\mathbf{t_{fin}}$ $\mathbf{[mm]}$	-
$\mathbf{S_L}$ $\mathbf{[mm]}$	0.9
$\mathbf{D_a}$ $\mathbf{[mm]}$	0.48
$\mathbf{D_b}$ $\mathbf{[mm]}$	0.42
$\mathbf{N_T}$	14
$\mathbf{N_L}$	84

The numerical study is then carried out in the next section using the above dimensions.

4.2.4.2. 3D CFD Numerical Setup

The segment-level-based 3D CFD study is performed on ellipsoidal-shaped wires or tube banks. Though several studies have been performed on ellipsoidal shaped tube-banks [73–78], little work has been done directly related to the current study's elliptical eccentricity, tube-bank spacing parameters, and laminar flow conditions. The water-side domain for the current study is obtained by simplifying one of the water channels of the iCMHX, as shown in Figure 26 (a) and (b). This simplification is done by assuming a uniform fluid flow and temperature profile across all the water inlets. As shown, the water-side domain is first reduced from a single water channel to a single symmetrically half water channel consisting of $\boldsymbol{L_a \times W_w/2 \times L_w}$ dimensions. The 3D domain, however, can be further reduced along $\boldsymbol{L_a}$ and $\boldsymbol{L_w}$ dimensions. A symmetric flow field is expected along the y-direction for given flow ranges ($\boldsymbol{30 < Re_w < 80}$), as similarly observed in the literature [61]. Thus, $\boldsymbol{L_a}$ dimensions, including $\boldsymbol{N_L}$ wires, can be reduced to a symmetric domain consisting of two consecutive wires in the $\boldsymbol{x}$-direction, $\boldsymbol{S_L}$ distance apart. The effect of the wall boundary in the x-direction is modeled separately using similar domain and boundary conditions. For the $\boldsymbol{L_w}$ dimension, the computational domain in the y-direction can be reduced by using at least 20 wires, as the equivalent number of wires in the longitudinal direction to water flow ($2\boldsymbol{N_T}$) is too large. These equivalent wires are defined based on the longitudinal spacing between the wires (S_T/2) along the water flow direction. Since the water channels are too narrow, the ratio of the width of the water channel (W_w) to the transverse spacing

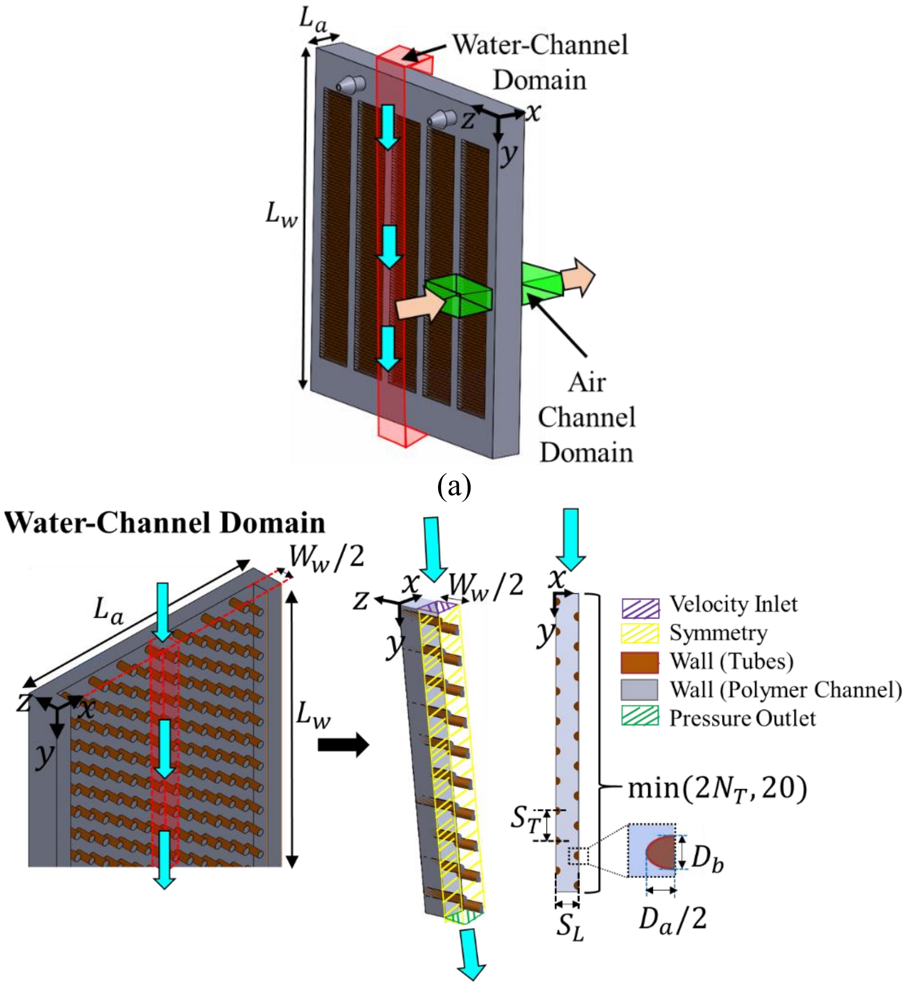

(a)

(b)

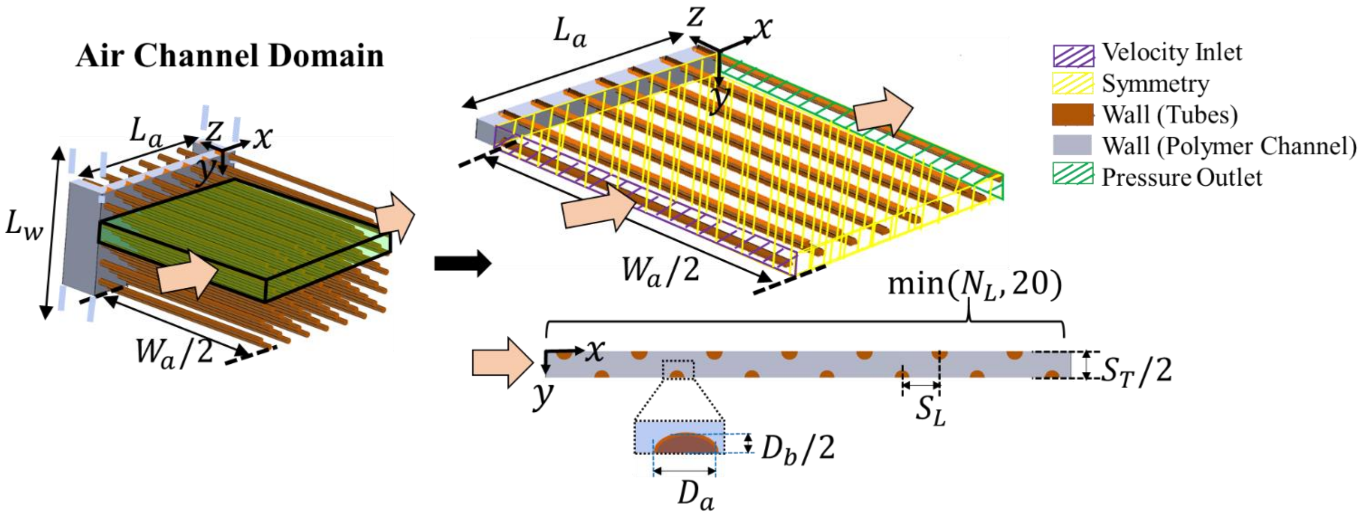

(c)

Figure 26: Domain simplifications: (a) entire iCMHX domain; (b) simplification to segment-level water-side 3D domain (c) simplification to segment level air-side domain

between the wires ($2S_L$) is much less than 5. Therefore, the velocity component and gradients of the velocity field of the water flow in the z-direction cannot be neglected, as explained in the literature [12]. Thus, the wall boundary condition on the polymer wall must be modeled.

Similarly, the air-side domain can be obtained from one of the air channels of the entire iCMHX, as shown in Figure 26 (a) and (c). As shown, the air-side domain is first reduced to a single symmetrically half air channel consisting of $\boldsymbol{L_a} \times \boldsymbol{W_a/2} \times \boldsymbol{L_w}$ dimensions. As the airflow is also expected to have a symmetric flow field in the x-direction for the given flow ranges ($\boldsymbol{25 < Re_a < 70}$), the 3D domain is then further reduced along $\boldsymbol{L_w}$ dimensions, including $\boldsymbol{N_T}$ wires, to a symmetric domain consisting of two consecutive wires in the y-direction, $\boldsymbol{S_T/2}$ distance apart. The rest of the other dimensions can be simplified. Since the air channels are too wide ($\boldsymbol{W_w/S_T >> 5}$), the wall boundary condition in the z direction might not be needed. However, it is modeled as a 3D domain like the water side for consistent boundary conditions.

The air-side and water-side computational domains are created in Gambit software using MATLAB scripting. Each computational domain is obtained by first using edge-meshing operation and mesh-refinement on the wire edges, followed by face meshing operation on the surface using triangular elements and pave scheme. Later, hexahedral and wedge-type elements and a cooper scheme suitable for cylindrical surfaces mesh the entire domain volume.

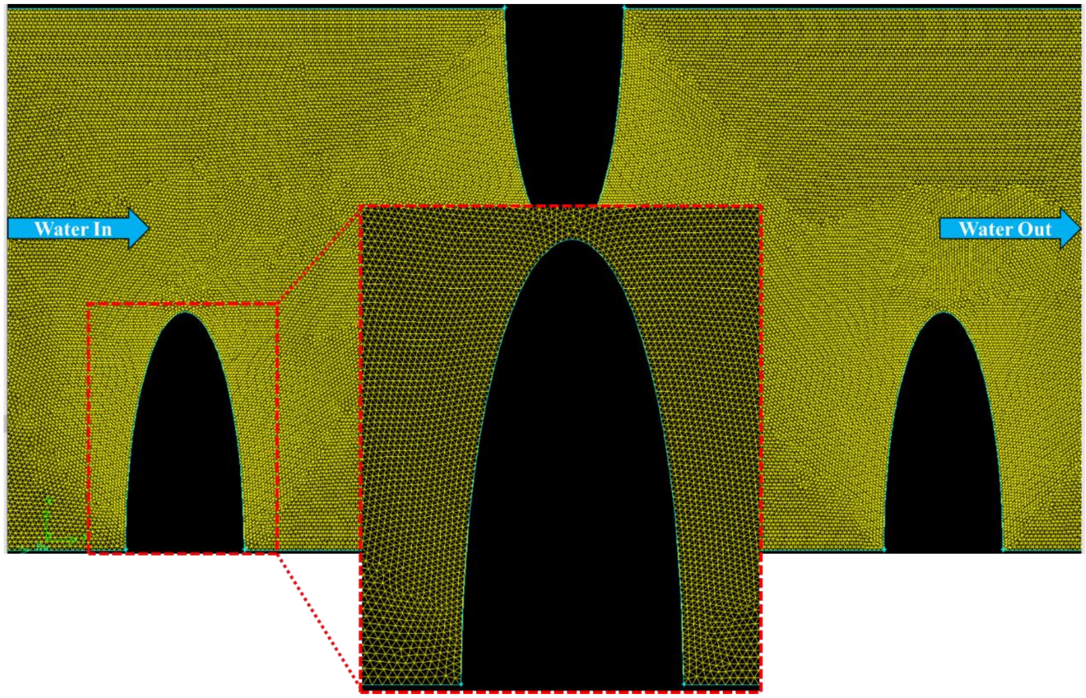

Figure 27: Meshed domains for the ellipsoidal fin on the waterside domain for illustration purpose

A velocity inlet condition is imposed on the surfaces where the fluids enter their respective domains, while a pressure-outlet condition of zero Pa is imposed on the surfaces where the fluids exit the domains. To ensure that the upstream and downstream boundary conditions don't affect the results, the inlet and outlet are kept at around $11D_h$ from the first and last wires, as done in the authors' past study [24]. A temperature Dirichlet wall-boundary condition is imposed on the ellipsoidal wires. Some constant temperatures can be considered at the inlet and the wires as the temperature don't affect the Nusselt number, assuming that the thermophysical properties are constant. The meshed domains are separately simulated in Ansys Fluent for different flow velocities, $\boldsymbol{v_b}$, with the assumptions and solver details mentioned in ***Table 10***.

Table 10: Assumptions and solver details for 3D model setup

Assumptions
Laminar flow, steady-state, incompressible flow
Constant fluid and material properties
Uniform fluid flow and temperature profiles at the inlets
Solver Details and Methods
PRESTO for pressure
1st order upwind for momentum and energy
Coupled scheme for pressure and velocity
Convergence tolerance: 10^{-6} for continuity and momentum; 10^{-14} for energy

For thermal performance, the Nusselt numbers for both fluids are obtained using the Eff-NTU method as detailed in [24]. Typical velocity and temperature contour plots at some given flow rate for the air-side domain are shown in Figure 28.

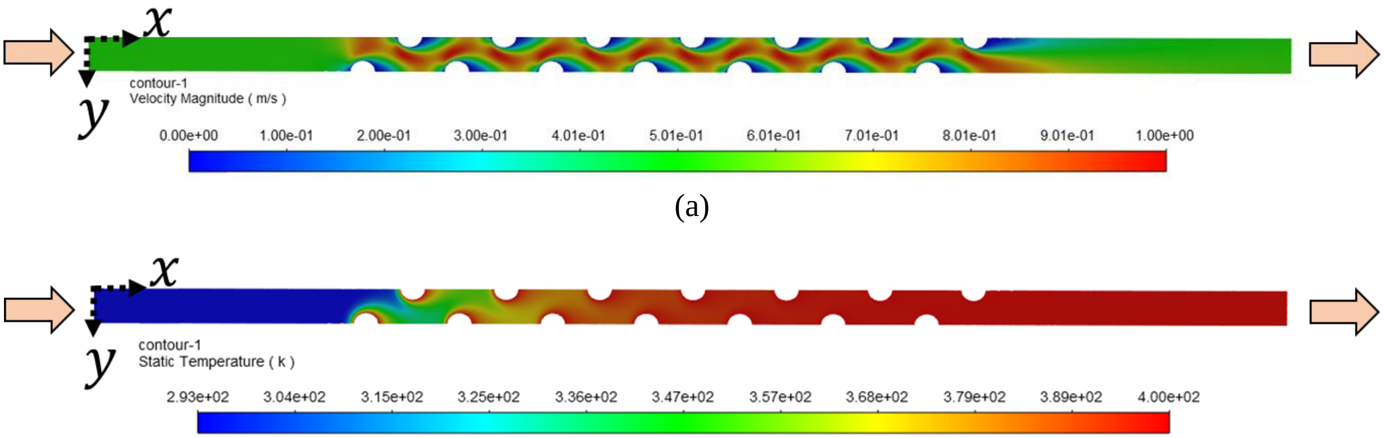

(a)

(b)

Figure 28: Contour plots of (a) velocity and (b) temperature for some particular flow rate at symmetry plane of the air-side domain located $\boldsymbol{W_a/2}$ distance from the wall

The Nu and Eu numbers are obtained using similar methodology as discussed in Sections 4.2.2.2 and 4.2.2.3. Similarly, they are then integrated to compute the heat transfer coefficients for the airside ($\boldsymbol{h_a}$) and waterside ($\boldsymbol{h_w}$) using Equation (12).

Furthermore, to check the independence of the CFD results from convergence tolerances and mesh sizes, a residual independence study is carried out, followed by a mesh independence study. For the residual independence study for a given mesh, the continuity residuals are varied from $\mathbf{10^{-5}}$ to $\mathbf{10^{-6}}$ and the Euler and Nusselt numbers are observed to vary within $\mathbf{0.02}\%$. For the mesh-independence study, the residual independent values of Euler and Nusselt numbers are used for a given mesh. The mesh cells are varied uniformly in all x-, y- and z-directions. For the air side, as the mesh cells vary from 880,000 cells to about 2,100,000 cells, $\boldsymbol{Eu_a}$ and $\boldsymbol{Nu_a}$ are found to vary within 0.7%. Similarly, for the water side, as the mesh cells vary from 340,000 cells to about 3,600,000 cells, the $\boldsymbol{Eu_w}$ and $\boldsymbol{Nu_w}$ are found to vary within 2%.

A graphical representation of the CFD-obtained convective heat transfer coefficients ($\boldsymbol{h_a}$ and $\boldsymbol{h_w}$) is shown in Figure 29.

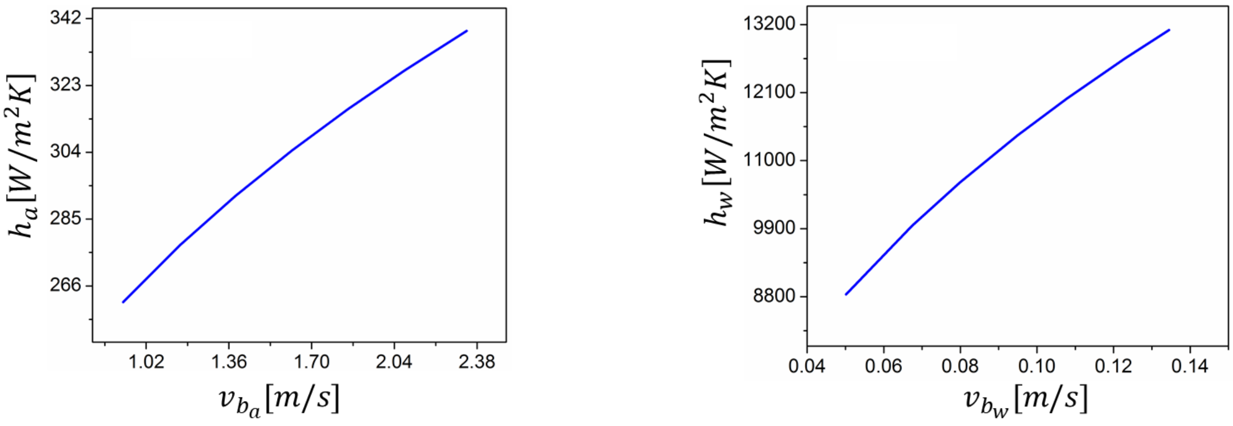

(a) (b)

Figure 29: Convective heat transfer coefficients obtained from 3D CFD based on Equation (12) for (a) air side, and (b) water side

However, there is also an additional convective resistance due to the polyurethane coating on the wire. The resulting heat transfer coefficient due to the coating can be defined based on the cylinder thermal resistance, as defined in the literature [60] and shown in Equation (29). It is computed to be around 11,483 $\boldsymbol{W/m^2K}$.

$$\boldsymbol{h_{coat}} = \frac{\boldsymbol{2k_{coat}}}{\boldsymbol{D_h} \log\left(\frac{\boldsymbol{D_h/2 + t_{coat}}}{\boldsymbol{D_h/2}}\right)} \tag{29}$$

The effective heat transfer coefficients can, thus, be calculated as shown below:

$$\frac{\boldsymbol{1}}{\boldsymbol{h_{eff_i}}} = \frac{\boldsymbol{1}}{\boldsymbol{h_i}} + \frac{\boldsymbol{1}}{\boldsymbol{h_{coat}}} \tag{30}$$

Thus, the heat transfer rate for the entire iCMHX is ultimately obtained using the effective heat transfer coefficients in Equations (13)-(23) instead of just the heat transfer coefficients.

4.3. Latent Thermal Storage Model

This section focuses on developing a computationally-efficient ROM for 1D radial conduction in PCM enveloping metal wires in a tube-bank geometry, which is later validated with conventional enthalpy-based approaches via commercial solvers.

4.3.1. ROM

4.3.1.1. TES Geometry

The novel TES system includes the cross-media based metal-polymer composite HX (see Figure 30 (a)) consisting of hot fluid (or cold fluid in the reverse heat release process) flowing across alternate fluid channels (n_{fluid}) of width, W_{fluid} and PCM-contained polymer channels (n_{PCM}) of width, W_{PCM}, as shown in Figure 30 (c). Here, the TES system is relatable to the iCMHX as the terminology W_{fluid}, W_{PCM}, n_{fluid} and n_{PCM} used here is representative of the iCMHX design parameters: W_a, W_f, N_a^{chan} and N_w^{chan} respectively. As the hot fluid flows across the fluid channels, convective heat transfer occurs between the hot fluid and the metal wires, of diameter, D, exposed on the fluid side which are arranged in a tube-bank geometry governed by lateral (S_T) and longitudinal (S_L) spacing parameters (see *Figure 30* (b)). The heat then continuously conducts through the wires axially, up to t_{wall} length, until it reaches the PCM side. This concept of laying small-diameter continuous metal wires of high thermal conductivity such as copper across all the fluid and PCM channels, providing a direct heat transfer route between the hot fluid and the PCM, is called the cross-media approach (see *Figure 30* (c) and (d)). Since the heat transfer route is independent of the thermal conductivity of the polymer, the resulting TES system is a low-resistance unit. When the wire reaches the PCM side, the heat starts conducting to the PCM, and when the PCM temperature reaches its phase-transition temperature (T_{PCM}), the PCM starts melting and stores the heat isothermally in the form of latent thermal energy. These TES systems are entirely additively-manufactured in-house using a customized proprietary 3D printer consisting of two print heads: polymer and metal; designed and developed by a few of the co-authors. A detailed description of their fabrication technique can be found here [28,30].

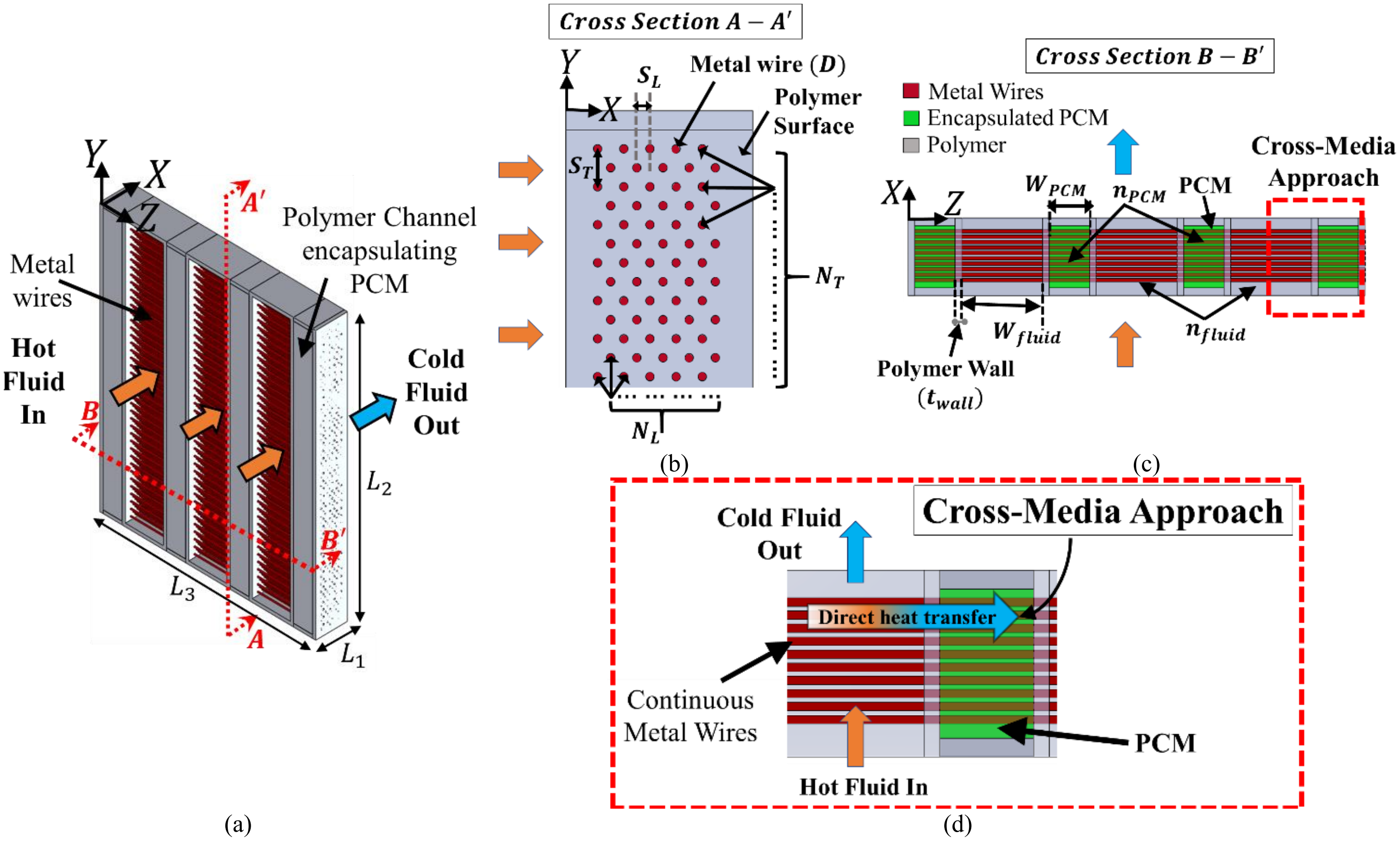

(b) (c)

(a) (d)

Figure 30: Design of gas-to-PCM TES system (a) isometric view (b) cross-sectional view of XY plane showing metal wires in tube-bank geometry (c) cross-sectional view of XZ plane with cross-media approach highlighted in red and (d) cross-media approach leading to melting of PCM

The present study focuses on simulating the melting process of PCM enveloping the metal wires in a PCM-to-fluid HX. It can be easily extended to perform a simulation for the freezing process, which is similar to the simulation of the melting process, but with minor adjustments.

4.3.1.2. Domain Assumptions and Simplifications

Since the modeling of the entire HX domain is computationally expensive, it can be easily simplified to an independent segment-level based model, using the following assumptions:

1. Constant and isotropic material properties of fluid, polymer, metal, and PCM (both liquid and solid phases)
2. Flow is fully developed.
3. No hysteresis in the melting temperature of the PCM (T_{PCM})
4. Entire PCM at its melting temperature (T_{PCM}) initially
5. Negligible effects of gravity
6. Heat only transfers through wire fins, and conduction through polymer wall is negligible
7. Uniform fluid flow (v_{in}) and temperature (T_{in}) profiles at the inlet
8. 1D radial conduction in PCM
9. Quasi-steady-state approximation ($Ste < 0.1$) or negligible thermal capacitance of PCM. Here, $Ste = C_p(T_{in} - T_{PCM})/H$.

Since the fluid is assumed to have uniform fluid flow and temperature distribution across n_{fluid} inlet channels in the x=0 plane of the entire TES domain (see Figure 31 (a)), the fluid flow across every single channel would have the same inlet velocity (v_{in}) and inlet temperature (T_{in}). Now, using symmetry conditions, a single-channel can be further reduced to a half-channel domain such that the wires of lengths $W_{fluid}/2$ and $W_{PCM}/2$ will acts as fins for the fluid and the PCM-side, respectively.

This simplification results in an equivalent inlet velocity of v_{in} and uniform temperature of T_{in} uniformly distributed over the entire half-channel in the y-direction. Now, for determining the inlet flow and temperature distribution across the wires in the tube-bank geometry, an index system of i ($1 \leq i \leq N_L$) in the x-direction and j ($1 \leq j \leq N_T$) in the y-direction is used to identify each wire. As the temperature profiles are uniformly distributed across the inlet plane-x=0, the flow and temperature profiles for each ith wire would also be the same in the y-direction, i.e. $T_{1,j} = T_1$ for all $1 \leq j \leq N_T$ (see Figure 31 (a)). Extending this for any ith wire, $T_{i,j} = T_i$. Similarly, for the flow profile, as the velocity is uniformly distributed over the entire area across for any ith and jth wire, $v_{i,j} = v$. This means that for a given ith wire, all the wires will have identical thermal performance along the y-direction. Thus, all wires for any given ith row will have identical thermal performance along the y-direction. Thus, $T_i \neq f(y)$ and only N_L wires need to be simulated instead of $N_T \times N_L$. This simplifies the half-channel domain to a single row domain, as shown in Figure 31 (a).

However, the single row domain includes N_L different fluid inlet temperatures (T_i for i=1:N_L) that need to be calculated at a known time. As the fluid flows from any i^{th} wire to the $(i+1)^{th}$ wire, the fluid outlet temperature from i^{th} wire (T_i^{out}) becomes the fluid inlet temperature (T_{i+1}) for the $(i+1)^{th}$ wire and so on. In this way, T_i for any i^{th} index of N_L can be computed from the values of the previous wires. Since the fluid flow model across different N_L wires, is otherwise identical and independent, for a given T_i, the model can be reduced from the single row domain to a single PCM-wire cartesian domain, as shown in Figure 31 (b).

But, the single PCM-wire cartesian domain in Figure 31 (b) includes three (cartesian: x, y, z) directions of conduction for the PCM. Using the assumption of 1D radial conduction, the directions of conduction can be reduced from three to one (Radial: r).

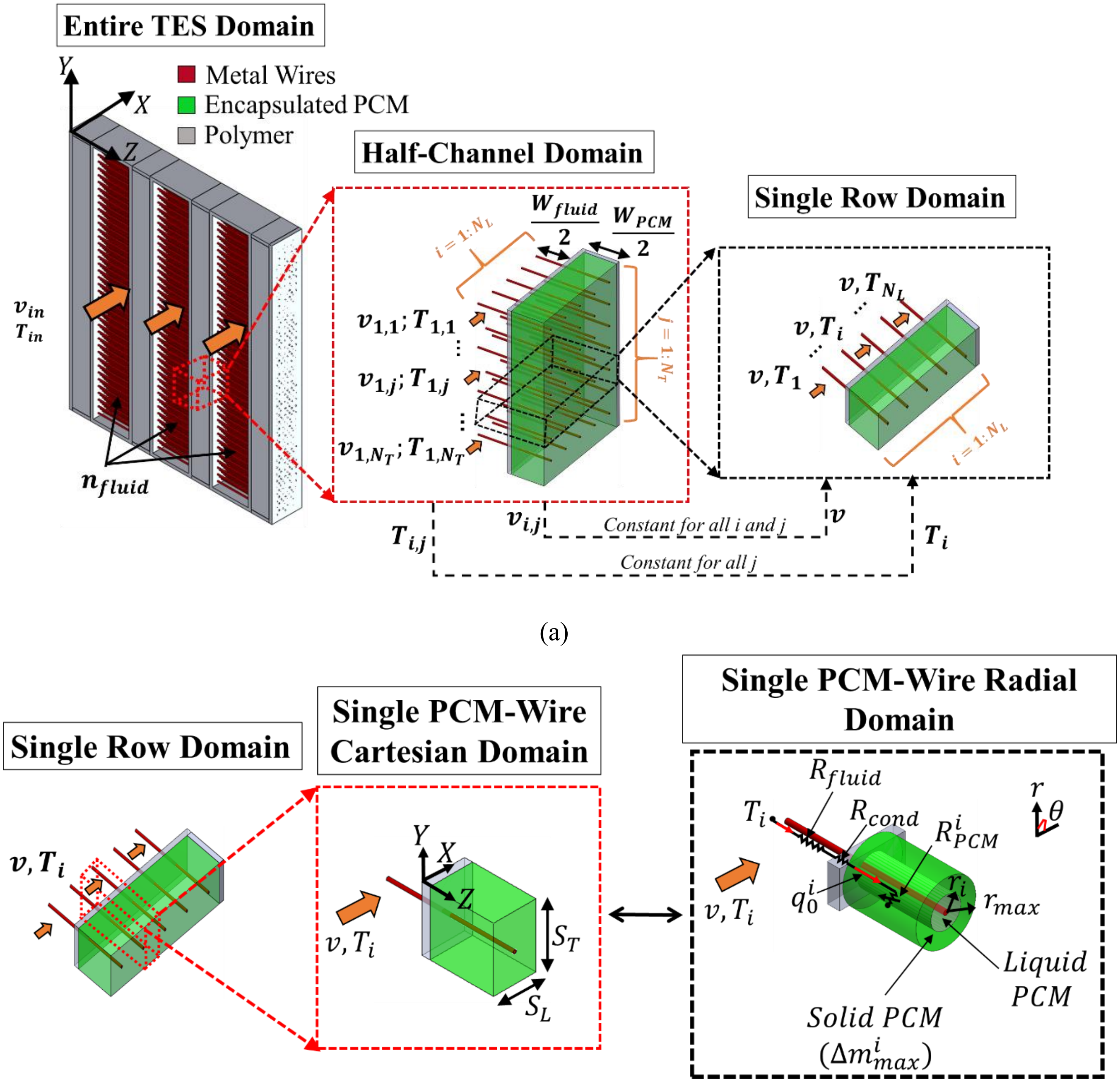

(b)

Figure 31: Domain simplification (a) Entire TES domain to single row domain and (b) single row domain to single wire radial domain

This simplification can be done by treating the single wire surrounded by the cartesian PCM domain as a single wire surrounded by a cylindrical PCM domain. It contains the same thermal mass of the PCM as the cartesian domain.

But geometrically speaking, when the single wire radial domains are arranged in the tube-bank geometry for all i and j values, some overlap regions might occur between the radial PCM domains of the neighboring wires (see Figure 32).

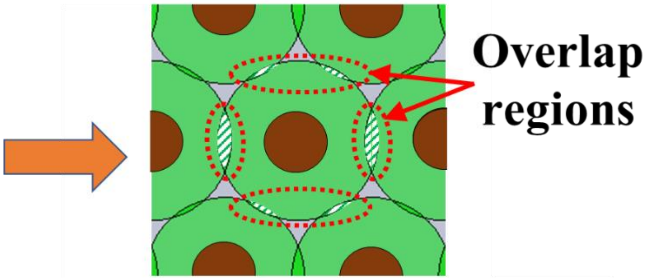

Figure 32: Example of PCM overlap for PCM-wire cylinders when visualized in tube-bank geometry

Thus, the following section entails a detailed analysis needed to compute r_{max} and understand the geometric behavior of the overlap regions.

4.3.1.3. Geometrical Study of PCM-Wire Cylinders

This section includes the realistic and simplified geometry consisting of the neighboring single wire radial domains with the same thermal mass as the equivalent single wire cartesian domains. The geometric behavior of the overlap regions can be captured as shown in Figure 33.

First, the maximum cylindrical radius is computed. Since the thermal mass is directly proportional to the PCM domain area for the same domain length - $W_{PCM}/2$, the 2D PCM domain areas are computed for both the cartesian ($A_{cartesian}$) and radial (A_{radial}) domains (see Figure 33) and are equated with each other to yield the condition for the maximum equivalent cylindrical radius (r_{max}):

$$\frac{S_T S_L}{2} - \frac{\pi r_0^2}{2} = \pi\left(\frac{r_{max}^2}{2} - \frac{r_0^2}{2}\right)$$

where $r_0 = D/2$ and $A_{cartesian}$ is the L.H.S. term while A_{radial} is the R.H.S. term.

Solving for r_{max} gives:

$$r_{max} = \sqrt{\frac{S_T S_L}{\pi}} \tag{31}$$

Thus, the maximum allowable PCM radius for the 1D ROM is obtained from Equation (31).

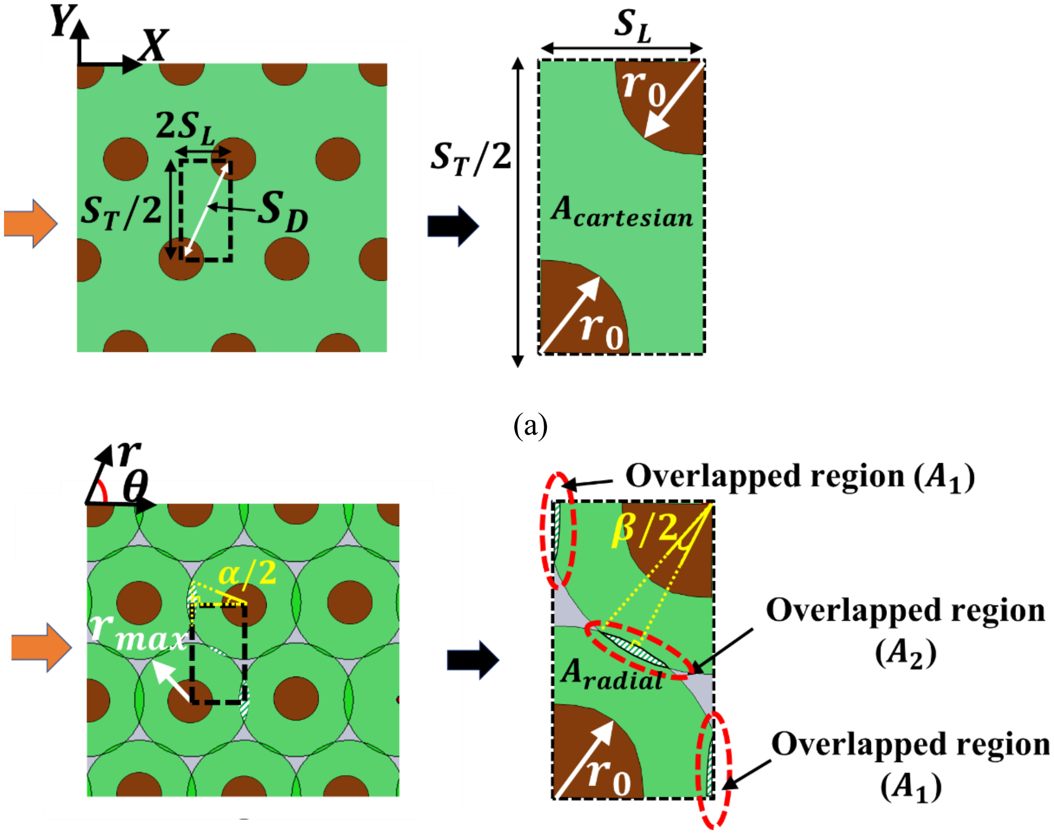

(a)

(b)

Figure 33:Comparing thermal masses for (a) cartesian and (b) radial PCM domains for neighboring wires with overlap regions A_1 and A_2 marked in red dashed circles.

Now, as discussed, the PCM overlap regions A_1 and A_2 (see Figure 33 (b)) formed due to the geometrical spacing of the adjacent cylinders are studied. The overlap regions of the ROM domain could be problematic as they can impact the conduction inside the region and the time taken to melt the PCM completely. As the neighboring radial PCM domains equally share the overlap region, the direction of conduction in this region gets affected by both the neighboring PCM domains. This effect leads to PCM conduction in both x- and y- directions instead of the 1D radial direction. Also, the time taken to melt the PCM in the radial domain completely would be relatively less than the time taken to melt the PCM in the cartesian domain completely. This is because when the PCM in the overlap region is compared to its corresponding region in the cartesian domain, the overlap region of the radial domain seems much closer to the wire than that of the cartesian domain. This provides a shorter conduction path for the radial domain as compared to the cartesian domain and thus less melting time.

Mathematically, the overlap regions exist in five different cases controlled by the geometrical spacings between the neighboring PCM cylinders: (i) in the direction of S_T (x- direction); (ii) in the direction of S_D (see Figure 33 (a) on xy plane); and (iii) in the direction of S_L (y- direction). These different cases of overlap regions are governed by specified ranges of S_T/S_L ratios which are derived mathematically (see Appendix B.1. for complete derivation and analysis) and summarized as shown in Figure 34. Here, the controlled directions for the different overlap-cases are also marked. It is to be noted that the neighboring PCM cylinders only cause these overlaps; without overlapping with the wires and thus are investigated only for that particular range of S_T/S_L.

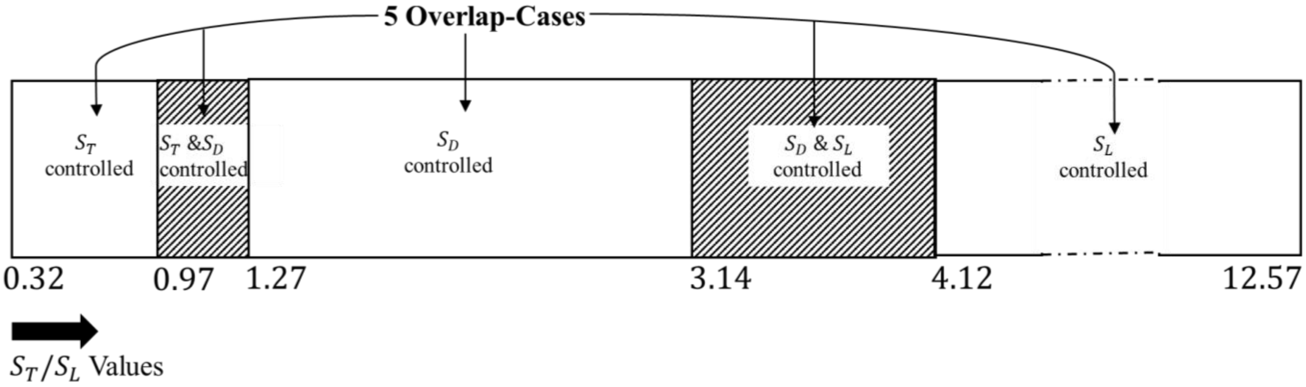

Figure 34: Different overlap cases governed by specific S_T/S_L values and controlled directions

The geometric behavior of the overlap regions is quantified by the ratio (A_{ratio}) of the PCM overlap region ($A_{overlap} = 2A_1 + A_2$) to the total PCM region (A_{radial}). A detailed mathematical analysis is carried out in *Appendix B.2.*

Thus, the geometric parameter, A_{ratio}, can be determined by just knowing the S_T/S_L and r_{max}/r_0 values, as obtained from Equation (76) in Appendix B.1. and as shown below.

$$A_{ratio} = \frac{\left(\frac{r_{max}}{r_0}\right)^2 \left(\alpha - \sin(\alpha) + 2(\beta - \sin(\beta))\right)}{\pi(\left(\frac{r_{max}}{r_0}\right)^2 - 1)} = f\left(\frac{r_{max}}{r_0}, \frac{S_T}{S_L}\right)$$

4.3.1.4. Governing Equations

As the TES design is set up, the governing equations of an analytical model of the TES are discussed. First, the modeling starts with the segment level based single PCM-wire radial model to compute the phase-front location (r_i) for a given time-step by utilizing the thermal resistance approach based on energy conservation. In this way, the latent thermal energy stored in i^th^ single-wire model (Δe_i) is determined. Second, the latent thermal energy stored in the single PCM-wire model is extended to the single row domain (see Figure 31). Since the inlet temperatures are different for N_L wire-rows (see Figure 31), each of the wire-rows would have a different magnitude of the latent thermal energy stored. Thus, all the wire-rows are individually iterated using the thermal-resistance analogy, and the total latent energy stored (Δe_{total}) in the single row domain (see Figure 31) is additively obtained. Third, the single-row model is extended to the entire TES model. As the single-row domain is identical for different PCM channels of the entire TES, the total latent thermal energy, ΔE, stored in the entire TES is again additively obtained. Lastly, the total latent thermal energy stored, E_{total}, in the entire TES domain is integrated for different time-steps by predicting the next phase-front location (r_i) for the next time-step ($i + 1$). The model is simulated until the entire PCM has been completely transitioned or when latent thermal energy is required for a specified period. Since each wire-row has a different magnitude of latent thermal energy stored, the phase-front advancement will be different for each wire-row at different times. The wires closer to the inlet plane of the TES would quickly melt completely than the ones placed farther away. The entire model has been programmed in MATLAB.

4.3.1.4.1. Latent Thermal Energy Storage in Single Wire-PCM Domain, e_i

The literature's traditional models for phase-change processes typically involve non-linear transient heat equations [54], which are often expressed in terms of Stefan's number [79]. In general, Ste is assumed to be very small (less than 0.1), which means that the sensible energy is negligible as compared to the latent energy and, thus, a quasi-steady-state approximation is considered valid [54]. As the entire PCM is initially at its melting temperature (T_{PCM}), there is zero conduction present through the solid PCM at all the times. Thus, the steady-state thermal modeling of i^{th} single wire radial domain (see Figure 31 (b)) includes only the conduction through the transitioned or liquid PCM which can be computed analytically.

The total resistance for the i$^{\text{th}}$ single wire radial domain, R_{total}^{i}, at a time, t, is computed using the thermal resistance analogy (see Figure 31 (b)), as shown below.

$$R_{total}^{i} = R_{fluid} + R_{wire} + R_{PCM}^{i} \tag{32}$$

where the index i takes the value of 1 to N_L wires

As R_{total}^{i} can be obtained from the three resistances, which are connected in series across a known inlet temperature, T_i, and T_{PCM}, these resistances are individually calculated for an i^{th} single wire, as discussed in the following sections.

1. Calculation of Fluid Convective Resistance, $\mathbf{R_{fluid}}$

The fluid thermal resistance, R_{fluid}, is calculated using Equation (33).

$$R_{fluid} = \frac{1}{\eta_{fluid} h_{fluid} A_{fluid}^{surf}} \tag{33}$$

where $A_{fluid}^{surf} = \pi D \frac{W_{fluid}}{2}$

Here, h_{fluid} is computed using CFD by considering flow parameters including Re number, flow properties including Pr number, and geometrical tube-bank parameters including $\frac{S_T}{D}$ and $\frac{S_L}{D}$. Similarly, η_{fluid} is calculated using h_{fluid}, wire properties such as k_{wire} and geometrical parameters, including W_{fluid} and D. The authors previously studied this methodology mentioned in detail in the reference [24]. Since the flow is assumed as fully-developed, h_{fluid} is constant for all i$^{\text{th}}$ wires. This subsequently leads to constant η_{fluid} and R_{fluid} for all the i$^{\text{th}}$ wires ($1 \leq i \leq N_L$) and thus a steady-state condition is assumed.

2. Calculation of Wire Conductive Resistance, $\boldsymbol{R_{cond}}$

The conductive wire resistance of the portion of wire embedded in polymer wall of thickness, t_{wall}, (see Figure 31 (b)) is calculated analytically ([60]) using Equation (34), by assuming 1D axial conduction.

$$R_{cond} = \frac{t_{wall}}{k_{wire}A_c} \tag{34}$$

where the cross-sectional wire area, $A_C = \pi D^2/4$

Since it is computed analytically and independent of any ith wire row, it is considered a constant and steady-state condition.

3. Calculation of the PCM Conductive Resistance, R_{PCM}

Since quasi-steady-state approximation is valid, h_{PCM}^{i} is computed analytically by assuming steady-state heat transfer through a cylindrical pipe [60]. It uses geometric parameters, including r_i and r_0 and PCM properties including k_{PCM}, as shown in Equations (35) and (36).

$$R_{cylinder}^{i} = \frac{\log\left(\frac{r_i}{r_0}\right)}{2\pi k_{PCM}} \tag{35}$$

$$h_{PCM}^{i} = \frac{1}{R_{cylinder}^{i}A_{cylinder}} = \frac{k_{PCM}}{\mathrm{r}_0(\log\left(\frac{r_i}{r_0}\right))} \tag{36}$$

where the index i takes the value of 1 to N_L tubes

Here, the fin-efficiency, η_{PCM}^{i} for the single-wire-domain is computed using a similar methodology used for the fluid-side. The η_{PCM}^{i} for the wire-length of ($L_{c_{PCM}} = \frac{W_{PCM}}{2}$) on the PCM-side is obtained using the following Equations (37)-(38):

$$mp_{PCM} = \sqrt{\frac{4h_{PCM}^{i}}{k_{wire}D}} \tag{37}$$

$$\eta_{PCM}^{i} = \frac{\tanh(mp_{PCM} L_C^{PCM})}{mp_{PCM}^{i} L_C^{PCM}} \tag{38}$$

where the index i takes the value of 1 to N_L tubes

Thus, the instantaneous PCM conductive resistance, R_{PCM}, for any i^th^ wire with a known melt-front location r_i at time t is computed analytically using Equation (39).

$$R_{PCM}^{i} = \frac{1}{\eta_{PCM}^{i} h_{PCM}^{i} A_{PCM}^{surf}} \tag{39}$$

where the index i takes the value of 1 to N_L wires and $A_{PCM}^{surf} = \pi D \frac{w_{PCM}}{2}$

This approach saves computational time as compared to the otherwise transient and multi-dimensional CFD modeling of the PCM domain as R_{PCM}^{i} is computed analytically. It is to be noted that the computed instantaneous thermal resistance is a transient term as r_i will vary for i_{th} wire, unlike the other resistances.

Using Equations (33)-(39), R_{total}^{i} is obtained (see Equation (32)), and is now used to compute the nominal heat transfer rate (q_0) which can give latent energy (Δe_i) for the i^{th} single wire at time, t. The nominal heat transfer rate is computed using Equation (40).

$$q_0 = \frac{T_i - T_{PCM}}{R_{total}^{i}} \tag{40}$$

where the index i takes the value of 1 to N_L tubes

However, in practice, we need to limit q_0 so that it isn't larger than the maximum available heat transfer rate required to melt the available non-transitioned PCM ($\Delta \mathrm{m}_{\mathrm{max}}$) completely (see Figure 31 (b)). Thus, the maximum available heat transfer rate (q_{max}) obtained from the maximum available latent heat-related to $\Delta \mathrm{m}_{\mathrm{max}}$ in Δt time is evaluated as shown below.

$$q_{max} = \frac{\Delta m_{max}^{i} H}{\Delta t} \tag{41}$$

where the index i takes the value of 1 to N_L wires

Here, Δm_{max}^{i} is computed based on the present melt-front location (r_i) and the maximum melt-front location (r_{max}), as shown below:

$$\Delta m_{max} = \pi(r_{max}^2 - r_i^2)\rho_{PCM}\left(\frac{W_{PCM}}{2}\right) \tag{42}$$

where the index i takes the value of 1 to N_L wires

Thus, the heat transfer rate of the i^{th} wire can be calculated as shown in Equation (43).

$$q_i = \min(q_0, q_{max}) \tag{43}$$

where the index i takes the value of 1 to N_L wires

Eventually, the latent energy stored by the i^{th} single wire during this time-step is given in Equation (44).

$$\Delta e_i = \mathrm{q_i} \Delta t \tag{44}$$

4.3.1.4.2. Latent Thermal Energy Storage in Single Row-PCM Domain, Δe_{total}

The latent energy stored in the i^{th} single wire is now integrated to compute the latent energy stored in an entire single row (see Figure 31 (b)), consisting of a total N_L different wires. The modeling of each i^{th} wire can be determined using Section 4.3.1.4.1. However, the inlet temperatures for all the N_L wires needs to be known (see Equation (40)). This can be obtained by using energy balance between the nominal heat transfer rate for the PCM (q_i) and the sensible heat lost by the fluid across the i^{th} wire, as shown below:

$$T_{i+1} = \frac{q_i}{\dot{m}C_{p_{fluid}}} + T_i \tag{45}$$

where the index i takes the value of 1 to N_L wires

As T_i for all N_L tubes are now known, the latent energy stored (Δe_{total}) for all the N_L wires are obtained using Section 4.3.1.4.1. Thus, the total latent energy stored for the entire single row is obtained by adding the latent energy stored (Δe_i) for all the N_L wires.

$$\Delta e_{total} = \sum_{i=1}^{N_L} \Delta e_i \tag{46}$$

4.3.1.4.3. Latent Thermal Energy Storage in Entire TES Domain, $\boldsymbol{\Delta E(t)}$

Similarly, the latent thermal energy stored for the entire TES (ΔE) for the given time, t, is computed by simply integrating the latent thermal energy stored in the single rows for the remaining N_T rows of wires across n_{PCM} channels of the HX.

$$\Delta E(t) = \Delta e_{total}(2 \times n_{PCM})N_T \tag{47}$$

4.3.1.4.4. Time Integrated Latent Thermal Energy Storage in Entire TES, $\boldsymbol{E_{total}}$

As the latent thermal energy stored in the TES is computed for a known r_i for a given ith wire at a time (t), the next step is to compute the latent thermal energy stored in the TES for the subsequent time steps. However, as the melt-front progresses with time, an updated melt-front location, $r_i(t + \Delta t)$, for a given ith wire needs to be determined. Thus, the ROM uses the “forward Euler” method in time to compute $r_i(t + \Delta t)$ for a given ith wire for the next discretized time-step, Δt. As the latent thermal energy storage for the single wire (Δe_i) leads to the melting of Δm_i PCM (see Figure 35), the energy-conservation at the melting interface, is used to compute the updated melt-front location ($r_i(t + \Delta t)$ for the next time-step, as shown in Equation (48).

$$r_i(t + \Delta t) \ = \sqrt{r_i^2(t) + \frac{\Delta e_i}{\rho_{PCM} \pi H \left(\frac{W_{PCM}}{2}\right)}} \tag{48}$$

where the index i takes the value of 1 to N_L wires

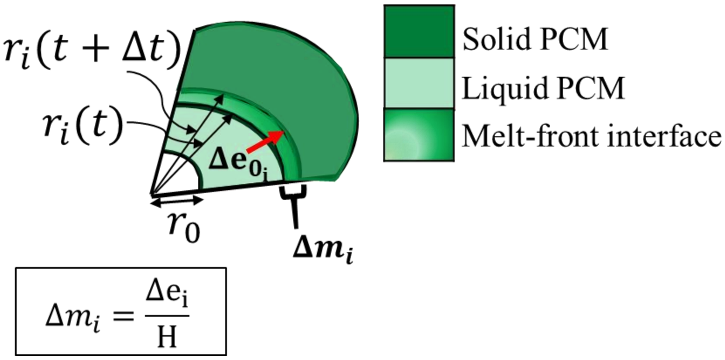

Figure 35: Compute melt-front location at next time-step

As $r_i(t + \Delta t)$ is known for each time-step; the time-integrated latent-thermal energy for the entire TES under a specified nominal time of t_0, can be obtained, as shown in Equation (49).

$$\mathrm{E_{total}} = \sum_{t=0}^{t_0} \Delta E(t) \tag{49}$$

4.3.2. Observed Trends

Graphically, some typical trends obtained from the ROM for some given operating and boundary conditions are shown in Figure 36. From Figure 36 (a), it can be seen that the heat transfer rate follows two trends. For $t < 4.2s$, the heat transfer rate decreases continuously with time as the PCM resistance increases with time (see Equation (40)).

Physically, the PCM resistance increases with time as more PCM is melted with time, causing the heat to travel a larger distance from the wire to reach the melt-front location. Thus, a longer conduction path is formed, leading to higher PCM resistance and thus decreasing heat transfer rate with time.

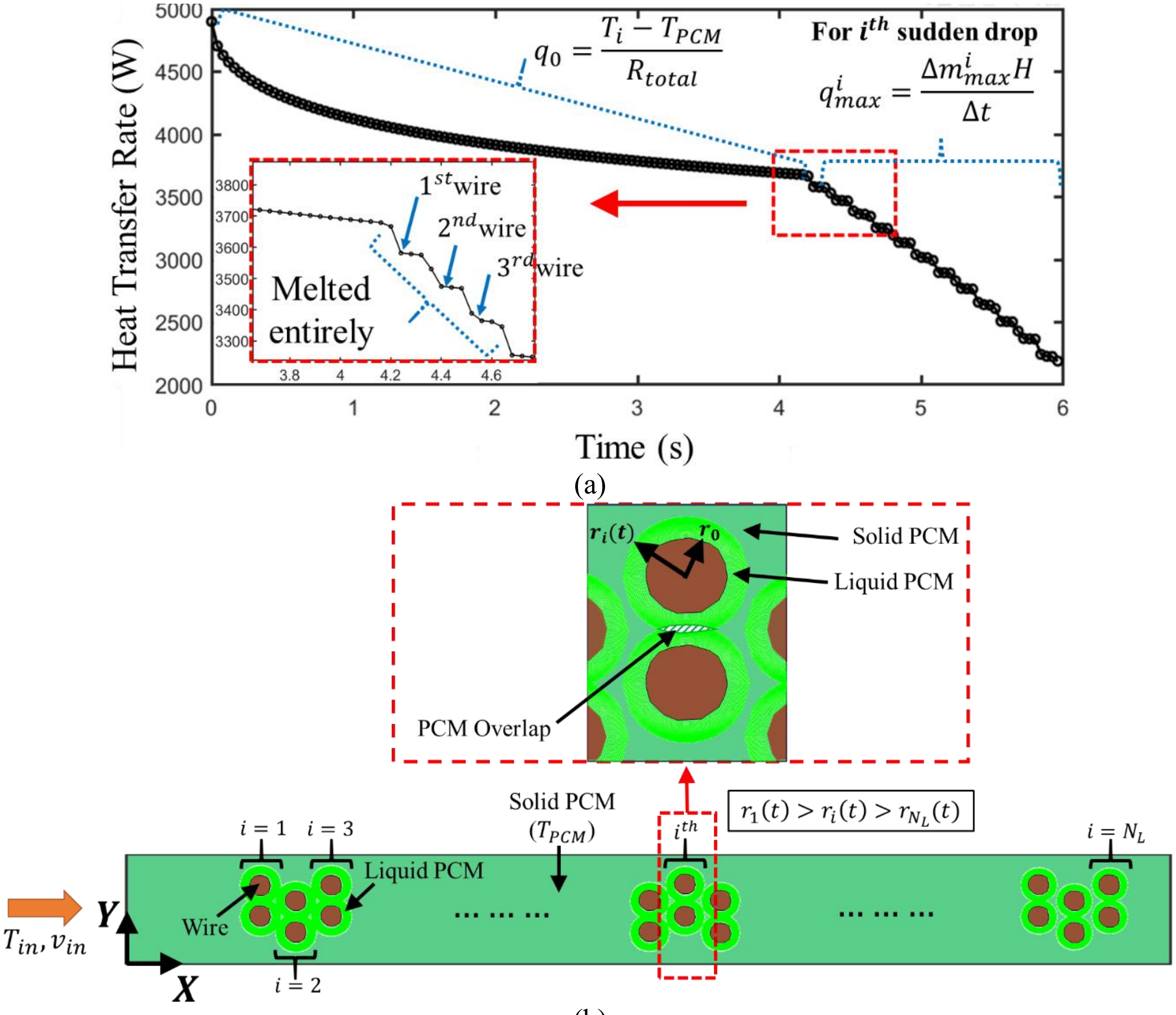

Figure 36: Typical trends obtained from 1D ROM for (i) heat transfer rate vs time and (b) contour plot at a particular time on XY plane

However, for $t > 4.2s$, the heat transfer rate decreases discretely with time (see Equation (41)) where every sudden drop corresponds to the complete melting of PCM of the i^{th} wire in the ascending order. The order of melting of the wires is better explained in Figure 36 (b), where it can be seen that there is more melted PCM in the first few rows ($i = 1,2,3$) as compared to the last wire ($i = N_L$), which is due to the decreasing approach temperature ($T_i - T_{PCM}$) from $i = 1$ to N_L.In addition to the thermal performance of the TES, hydrodynamic performance of the TES is computed in terms of fluid-side pressure drop (ΔP_{fluid}) which is determined via CFD by using flow parameters such as v_{in} and geometric parameters such as $\frac{S_T}{D}, n_{fluid}, N_L\ and \frac{S_L}{D}$. The details of which can be found in the reference [24].

4.3.3. Non-dimensionalization

The governing equations of the ROM are non-dimensionalized to obtain critical parameters dictating the TES performance. Since the main governing equations are based on thermal-resistance analogy (see Equation (40)) for latent thermal energy stored for an i^{th} single PCM-wire, its non-dimensionalization is shown for the single PCM-wire model only. The non-dimensionalization is performed by non-dimensionalizing the independent variables of the main governing equations: r_i and t into r_i^* and t^* respectively, as shown in Equations (50) and (51):

$$r_i^* = \frac{r_i}{r_0} \tag{50}$$

$$t^* = \frac{t}{t_0} \tag{51}$$

Thus, Equation (77) can be non-dimensionalized as r_i* and t* (see for details about the derivation) as shown in Equation.

$$\tau dt^{*} = r_i^{*}\left(\left(\frac{1}{Bi \times LR}\right)R_{wire}^{*} + \frac{\log(r_i^{*})}{f(r_i^{*}, R_{wire}^{*})}\right)dr_i^{*} \tag{52}$$

Here, , $Bi \times LR$ and R_{wire}^{*} are defined in *Table 11*.

Table 11: List of non-dimensional groups

Non-Dimensional Groups	**Mathematical definition**	**Physical Meaning**
τ	$Ste * Fo = \left(\frac{T_i - T_{PCM}}{\mathrm{H}}\right)\left(\frac{k_{PCM} t_0}{\rho_{PCM} r_0^2}\right)$	Time-constant
$Bi * LR$	$\frac{h'_{fluid}(2r_0)}{k_{wire}} \frac{W_{PCM}}{r_0}$	Proportional to the ratio of wire resistance embedded in PCM to fluid-side resistance
R^{*}	$\frac{2k_{PCM}}{k_{wire}} \frac{W_{PCM}^2}{r_0^2}$	Proportional to the ratio of wire resistance embedded in PCM to maximum PCM resistance

4.3.4. 2D CFD Axisymmetric Reference Model

A 2D axisymmetric model, typically used in the literature [15] [16] for cylindrical geometries, is developed as a reference model to validate the present 1D ROM. It is simulated in Fluent, which utilizes an enthalpy-based model [80]. The domain and boundary conditions of the 2D axisymmetric model are shown in Figure 37. Here, the convective boundary of h'_{fluid} on the wire-cross-section is taken such that the equivalent resistance is the same as $R_{fluid} + R_{cond}$. The 2D CFD axisymmetric reference model is set-up using the same initial, boundary and operating conditions as the ROM but it also includes axial conduction inside the PCM. The ROM only includes radial conduction inside the PCM (see Section 4.3.1.2).

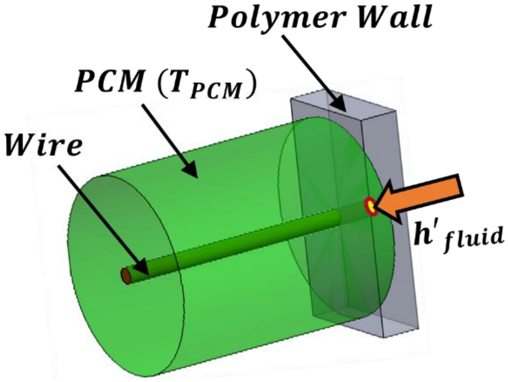

Figure 37: 2D axisymmetric reference model

4.3.5. ROM Test-case Setup

A test-case condition needs to be set up as a baseline case. Since the overlap regions in the 1D ROM can be problematic, a detailed analysis is first carried out to find the range of applicability for given geometrical parameters: $\frac{S_T}{S_L}$ and r^*_{max} (see Equation (76)). The effect of the overlapping on the ROM model is investigated by comparing the performance parameters of the single PCM-wire radial models with an actual 2D cartesian model (see Figure 33 (a)) for varying S_T/S_L and r^*_{max} values. The 2D cartesian domain includes the overlapping effect and is simulated for the same initial, boundary, and operating conditions, via CFD-based commercial solver, Ansys Fluent, using standard enthalpy-based methodology as detailed in the literature [80]. The performance parameter considered is dimensionless time (t^*) at a liquid-fraction, χ, of 0.9 for the different geometric ranges. For simplicity, the above analysis is carried out for a limiting case of $\eta_{PCM} = 1$ or $R^* = 0$. Since this condition also makes the governing equation of the 1D ROM yield a closed-form solution (see for details), the analytical solution of the 1D ROM (see Equation (53)) is directly used to compare with the simulated results of the 2D cartesian model.

$$\frac{t^*}{1/\tau} = \frac{{r^*}^2}{2}\left(\log(r^*) - \frac{1}{2} + \frac{R^*_{fluid}}{2}\right) - \frac{R^*_{fluid}}{4} + \frac{1}{4} \tag{53}$$

where R^*_{fluid} is defined similar to R^*_{wire} but using R_{fluid} instead of R_{wire} in their definitions.

The percentage difference ($\%\Delta_1$) for t^* ($\chi = 0.9$) between the 1D ROM and the 2D cartesian model is then used to validate the effect of overlaps, as shown in Figure 38. From the graph, it can be seen that for a given r^*_{max}, A_{ratio} or the relative overlap region varies across five different regimes bifurcated by S_T/S_L values (see Figure 34). In the first regime ($0.32 < S_T/S_L < 0.97$), the overlap region starts decreasing with increasing S_T/S_L values as the neighboring PCM cylinders start moving far from each other, which decreases the common overlap region between them in the direction of S_T. In the second regime ($0.97 < S_T/S_L < 1.27$), the overlap region continues decreasing in the direction of S_T, but the overlap region in the direction of S_D starts increasing as the PCM cylinders in the direction of S_D start getting closer to each other. Thus, there exists a minimum overlap region around S_T/S_L of 1.27. As S_T/S_L increases further, it transitions into the third regime ($1.27 < S_T/S_L < 3.14$) where the PCM cylinders in the direction of S_T are much far from each other yielding no overlap in the direction of S_T. But this brings the PCM cylinders closer to each other in the direction of S_D; increasing the overlap region or A_{ratio}. However, as S_T/S_L continues increasing in the fourth regime ($3.142 < S_T/S_L < 4.12$), the PCM cylinders now start distancing away from each other in the direction of S_D leading to decrease in A_{ratio}. But the cylinders in the direction of S_L start getting closer to each other leading to increase in A_{ratio}. Thus, there again exists an optimum overlap region around S_T/S_L close to 3.5.

Finally, in the last regime, as the S_T/S_L increases beyond 4.12, there is no more overlap present due to cylinders in the direction of S_D, but the cylinders in the direction of S_L start getting closer to each other resulting in increasing A_{ratio}. Similarly, at a given S_T/S_L value, the A_{ratio} is observed to decrease with increasing r^*_{max} because for a given overlap region ($A_{overlap}$), the available PCM domain area (A_{radial}) starts increasing. These trends also seem to correlate well with the percentage deviation ($\%\Delta_1$) observed in the performance parameters between the 1D radial and 2D cartesian models.

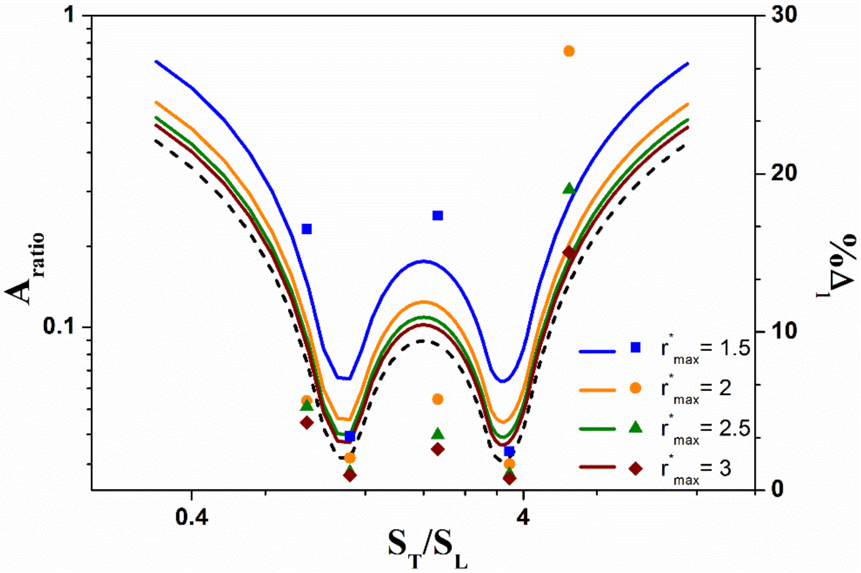

Figure 38: Effect of the overlapped area (A_{ratio}) on the percentage difference ($\%\Delta_1$) between the 1D ROM model (continuous lines; dash lines for $r^*_{max} = \infty$) and 2D cartesian model (discrete points) due to different ranges of S_T/S_L and r^*_{max}

Thus, a test-case scenario is constructed with $S_T/S_L = 1.2$ and $r^*_{max} = 3$, such that the A_{ratio} is the minimum or the $\%\Delta_1$ between the radial model and the cartesian model is the minimum. The summarized geometrical and physical parameters for the test-case condition are specified in Table 12.

Table 12: Geometrical and operating parameters for baseline test-case of single tube model

r_{wire} [mm]	t_0 [s]	k_{wire} [W/m-K]	S_T/S_L	r^*_{max}	τ	$Bi \times LR$	R^*_{wire}

0.2	6	400	1.2	3	3.68	1.29	1.943

Since the 1D radial model utilizes a time-discretized approach, a time-step independence study is carried out to obtain time-step independent results. A typical time-step independence result for the test-case scenario involves quantifying the difference (Δ_2) between the performance parameters, $t^*(\chi = 0.9)$, between consecutive time-step sizes. The consecutive time-step sizes are obtained by refining the reference step-size by halving, as shown in Table 13. The performance parameter is reported to be time-step independent to within 1% when the step-size is halved as the lowest time-step is sufficient enough to capture the simplest physics phenomenon of linear trend of r with respect to time. The equivalent number of steps ($t_0/\Delta t$) corresponding to this reference are 300 and thus, this can be used as a reference for all the studies with a given t_0.

Table 13: Time-step independence study

Time-Step Size (Δt)	$t_0/\Delta t$	$t^*(\chi = 0.9)$	%Diff (Δ_2)
0.02	300	0.878	-
0.01	600	0.887	1%
0.005	1200	0.89	0.38%

4.3.6. Validation with CFD

Since the HX model relies on the ROM model based on segment-level single wire domain, the single-wire model is validated with a reference 2D axisymmetric model (see Figure 37), based on test-case conditions. The 2D axisymmetric model uses commercial CFD solvers such as Ansys Fluent, with equivalent initial and boundary conditions, using a detailed parametric study.

4.3.6.1. Parametric Study

The 1D radial model is validated with the reference 2D model for a wide range of dimensionless parameters: $\tau, Bi \times LR^2, R^*_{wire}$ as shown below:

Table 14: Overall range for dimensionless parameters

τ	$Bi \times LR$	R^*_{wire}
$0.3 - 50$	$0.001 - 10$	$0.01 - 100$

1. **Effect of τ**

The parameter τ, representing dimensionless time-constant, is varied within the range specified in Table 14, while the other parameters are kept constant at the test-case conditions (see Table 13). As τ increases, which is also equivalent to the approach temperature increasing, there is more nominal heat provided to the PCM at a specific time resulting in faster melting of the PCM or decreasing t^*, as shown in Figure 39 (a). It can also be mathematically observed that τ is inversely related to t^* (see Equation (52)). The ROM model also seems to be well-validated with the 2D reference model to within 10%.

2. **Effect of $Bi \times LR$**

Similarly, the dimensionless parameter, $Bi \times LR$, representing resistance ratios of R_{wire} to R_{fluid}, is varied within the range specified in Table 14, while the other parameters are kept constant at the test-case conditions (see Table 13). As $Bi \times LR$ increases for a given τ, which is equivalent of decreasing R_{fluid} or decreasing total resistance (see Equation (40)) which increases the nominal heat provided to PCM resulting in faster melting of the PCM or decreasing t^* (see Figure 39 (b)). There is, however, a steep change in t^* when $Bi \times LR$ increases from 0.001 to 0.1, which is mainly due to very high fluid-side resistance as compared to PCM resistance

(R_{fluid}/R_{PCM} =61) and high R_{total}. This results in very less nominal heat transfer to the PCM, which remains almost constant with time (see Equation (32) and (40)); converting the transient PCM model to almost a steady-state PCM model and taking a very long time to melt the PCM at $\chi = 0.9$. For cases with $Bi \times LR \leq 0.1$, R_{fluid}/R_{PCM} <1, which retains the transient nature of the PCM model and thus have significantly lesser R_{total} leading to faster melting times (t^*). But the trend of nominal heat transfer rate increases gradually with increasing $Bi \times LR$ from 0.1 to 1 as R_{total} decreases considerably. But in the transition of $Bi \times LR$ from 1 to 10, there is very small decrease in R_{total} at a given τ, though R_{fluid}/R_{PCM} decreases by the same factor. Thus, the melting times are almost the same for larger $Bi \times LR$ values. The ROM model also seems to be well-validated with the Reference 2D CFD model to within 10%, with more significant deviations observed for larger values of $Bi \times LR$.

3. Effect of R^*_{wire}

Now, the dimensional parameter, R^*_{wire}, representing the resistance ratios of R_{wire} to R^{max}_{PCM}, is varied within the range specified in Table 14, while the other parameters are kept constant at the test-case conditions (see Table 13) for different τ values, as shown in Figure 39 (c). As R^*_{wire} increases, R_{wire} relatively increases for a given τ, which decreases the fin-efficiency of the PCM (η_{PCM}), leading to increased R_{PCM} and R_{total} (see Equations (32),(39) and (40)). Thus, depending on the magnitude of total resistance, the nominal heat transfer rate provided to the PCM decreases, leading to longer melting times at a given τ. However, when R^*_{wire} transitions from 0.01 to 1, the PCM fin-efficiency, which is highly non-linear, varies slightly, thus leading to a very small increase in total resistance. The nominal heat transfer rate, thus, decreases slightly, resulting in almost comparable performances. Now, as the ROM model is compared with the 2D CFD reference model, it validates well for smaller ranges for R^* to within 10% but for higher values of $R^*_{wire} = 10$ and 100, considerable deviations of about 15-65% were observed. This is majorly because for larger R^*_{wire} values where R_{wire} is large, the more melting of the PCM axially near the wire rather than melting radially.

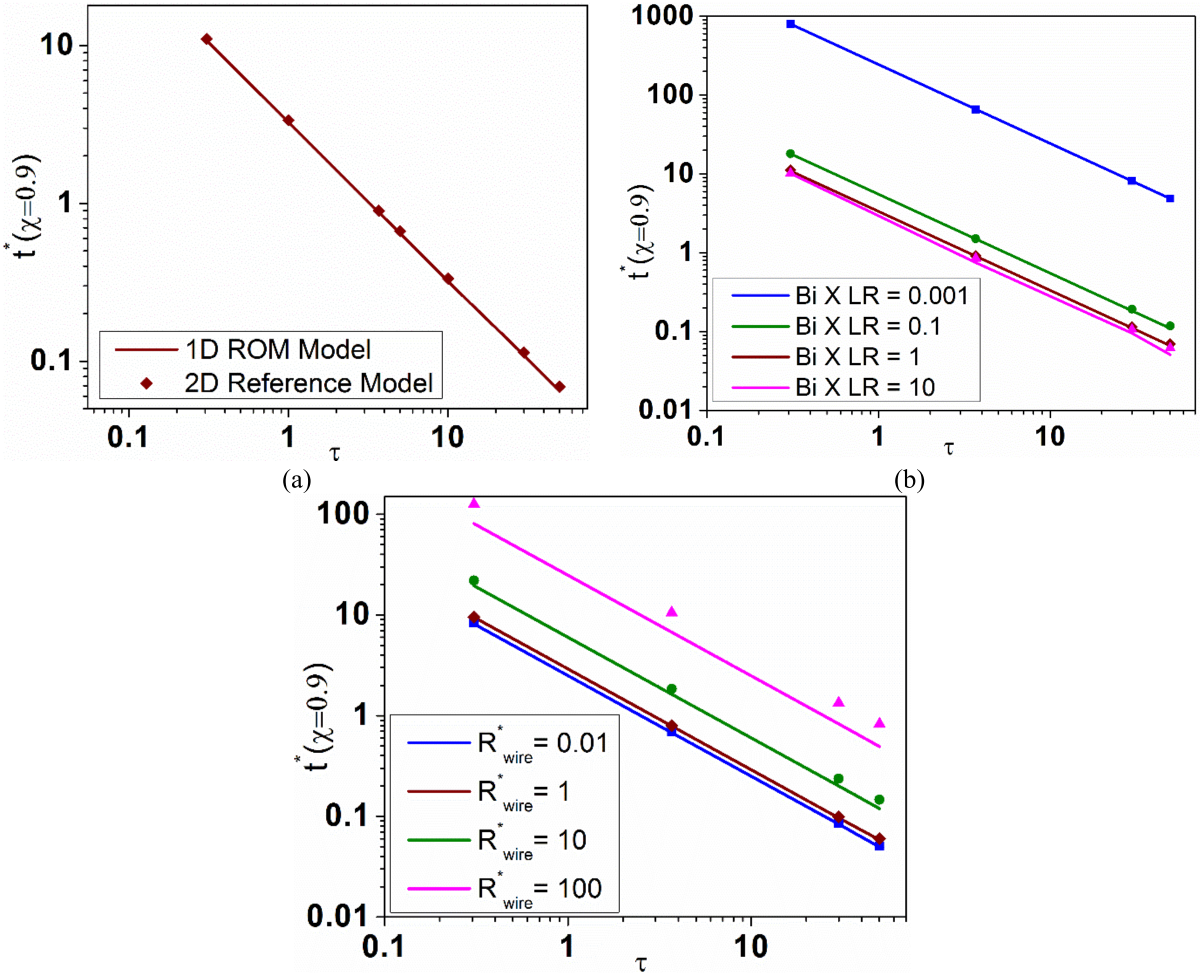

(a) (b)

(c)

Figure 39: Effect of Dimensional parameters: (i) τ (ii) $Bi \times LR$ and (iii) R^*_{wire} on the performance parameter, $t^*(\chi = 0.9)$; where solid lines represent ROM model while points represent 2D reference model

4.4. Summary

A novel iCMHX, consisting of a double-pass, staggered fins, and an integrated liquid-manifold, with applications particularly of interest to the electronics cooling sector, was numerically investigated and validated for its thermal and pressure-drop performance characteristics. The mesh-independence study used a curve-fitting approach for $\boldsymbol{Eu}$ and $\boldsymbol{Nu}$ to obtain extrapolated solutions from a well-defined curve-fit of the finest three values of Euler and Nusselt numbers with their equivalent mesh cells in the form of power-law equation. $\boldsymbol{Eu}$ and $\boldsymbol{Nu}$ for the airside underwent three mesh refinement levels, with the finest mesh having a maximum percentage deviation from the extrapolated solution of about 0.6% for $\boldsymbol{Eu}$ and about 1.7% for $\boldsymbol{Nu}$. Likewise, for the liquid side, the maximum percentage deviation of $\boldsymbol{Eu}$ and $\boldsymbol{Nu}$ for three levels of refinement was about 1.9% and 11.3%, respectively. Thermal performance metrics were evaluated using $\boldsymbol{Nu}$ and $\boldsymbol{Q}$. $\boldsymbol{Nu}$ was observed to increase with increasing $\boldsymbol{Re}$ in a power-law form with the power-law exponent matching that from the literature.

The chapter also provided details about a traditional 2D CFD-based segment level model, which also has been used in the literature. It also provides a more accurate 3D CFD-based segment level model that can capture the 3D velocity field that is otherwise absent in the traditional 2D CFD approach and is particularly helpful for narrow/mini channel-based flow through HXs. The 3D CFD approach is based on the actual dimensions of the fabricated novel metal-polymer composite HX and, thus, it is called as a high-fidelity 3D CFD-based model.

Lastly, a computationally efficient and analytical-based 1D ROM was developed for radial conduction inside the PCMs enveloping the metal wires. The algorithm has been summarized graphically as shown below, Figure 40. Some critical parameters based on time-constant and resistance ratios of the fluid-side, PCM-side, and wire, for the 1D ROM, have been identified, such as τ, $Bi \times LR$ and R^*_{wire}. The effect of these non-dimensional parameters was studied. The 1D ROM was validated with a reference 2D CFD axisymmetric model, commonly used in the literature, simulated in Ansys Fluent. It is observed that the 1D ROM is accurate as long as the resistance in the wire embedded in the PCM matrix is small, facilitating only radial conduction inside the PCM.

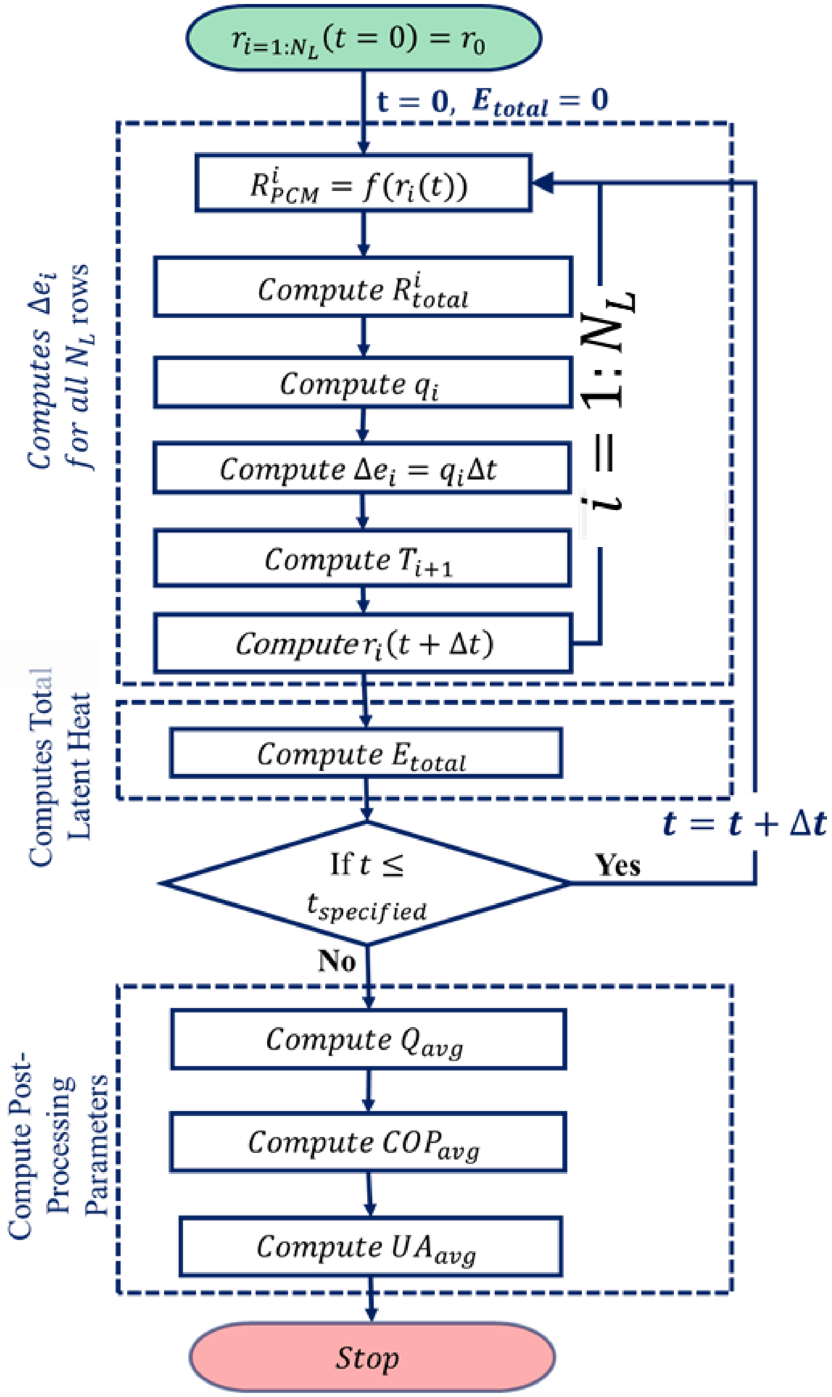

Figure 40: Flowchart for 1D ROM algorithm

Chapter 5: Design Optimization

This chapter focuses on multi-objective design optimization of the CMHXs by using the exterior penalty method as the optimization algorithm. The optimization technique is applied to different case examples problem statements, such as air-conditioning, peak-load building cooling, and pulsed power cooling applications.

5.1. Optimization Algorithm

The HX performance parameters are dependent on the design variables such as geometric spacings of the tube bank. For example, Nu increases with decreasing S_T/D but this also increases the pressure drop. Thus, to meet the objectives of CMHX design, which typically is to maximize heat transfer rate while minimizing the pressure-drop losses, the design parameters have to be optimized to satisfy the constraints in place while giving the individual optimum results.

The optimization algorithm that is discussed here is the exterior penalty method. The methodology is described below, as shown in Figure 41.

- The first step is to formulate the optimization problem by identifying the objective function, constraints, and design variables. The objective of the current problem statement is taken from the industrial problem statement, which is generally to maximize Q or minimum R_{th} or maximize Q/m. The design variables are the geometric variables critical to the CMHX design, such as $W_a, W_w, N_a^{fins}, S_T, S_L$ and D.
- The second step is to evaluate the CMHX performance via CFD using initial guess values for the design variables. Since the optimization process is iterative, it might

require performing numerous CFD simulations which are computationally heavy. A metamodel is developed to save computational time, which replaces the need to perform CFD time and again. The metamodel includes correlations for Euler and Nusselt numbers as a function of Reynolds number and Prandtl number and the tube-bank geometric parameters ($\frac{S_T}{D}$ and $\frac{S_L}{D}$). The present work includes an already developed metamodel for circular fins.

- The third step is to conduct constrained optimization using the exterior penalty method, a gradient-based robust optimization technique to determine local minima. The CMHX performance parameters computed from the second step are then used to check if the constraints are violated. The objective function is modified to incorporate the penalties in case of violation. Suppose there is a constraint violation corresponding to the initial design point. In that case, a penalty is imposed, and the local minimum of the modified objective function is obtained for that initial guess. The local minima are obtained using “fmincon”, a packaged MATLAB minimization tool. Thus, a Pareto set of local minima is obtained.
- The optimization algorithm is run for different ranges of mass constraints, and a Pareto curve of the objective function such as Q for different CMHX masses is obtained.

The optimization algorithm is implemented for sensible cooling in indoor air-conditioning applications where the CMHX is used as an evaporator.

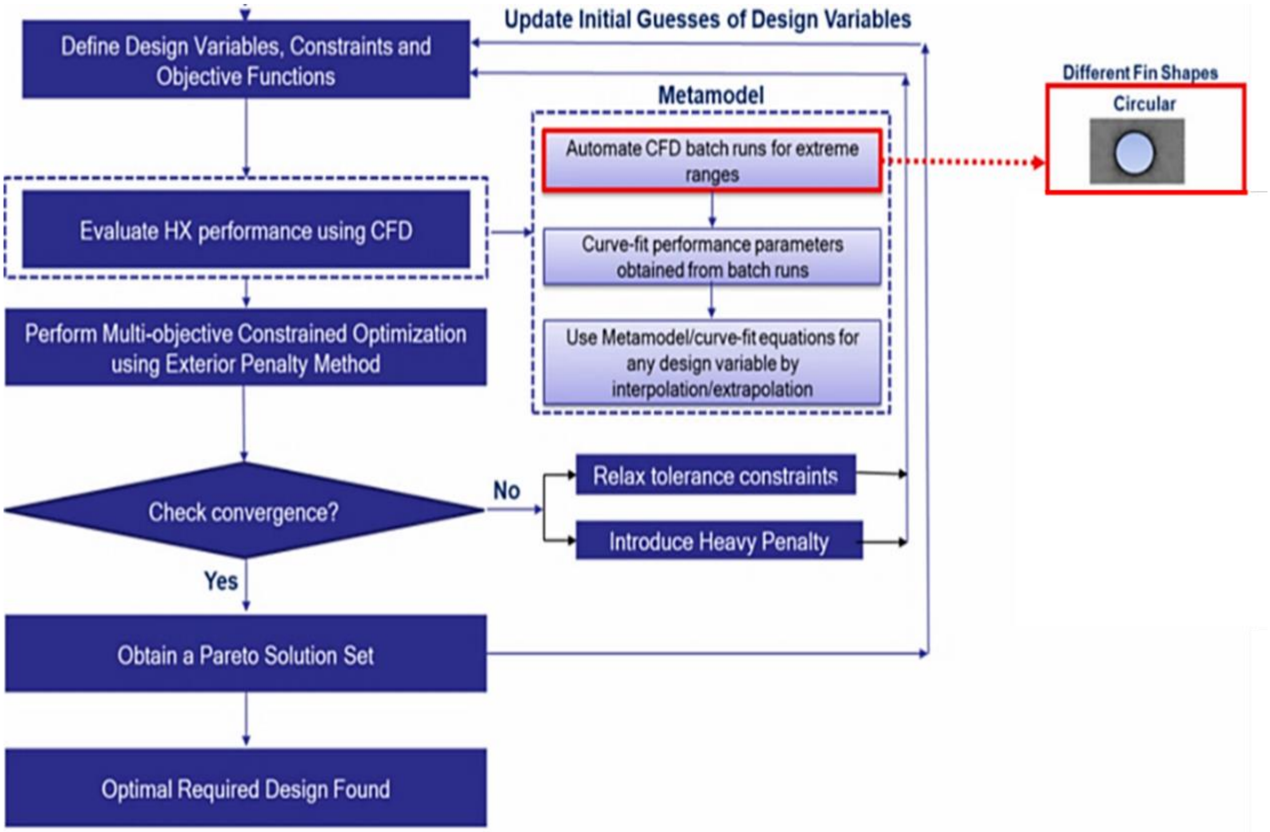

Figure 41: Methodology for design optimization using Exterior Penalty Method

5.2. Sensible Cooling Applications

5.2.1. Problem Statement

The problem statement aims to investigate an optimal air-to-brine (40% PG) heat exchanger design with the least overall material utilization of the system for given geometry constraints and operating conditions. The design system includes a general ‘V’ module consisting of two heat exchangers (HXs) and a fan attached at the top of the HXs enclosing the closed system, as shown in Figure 42.

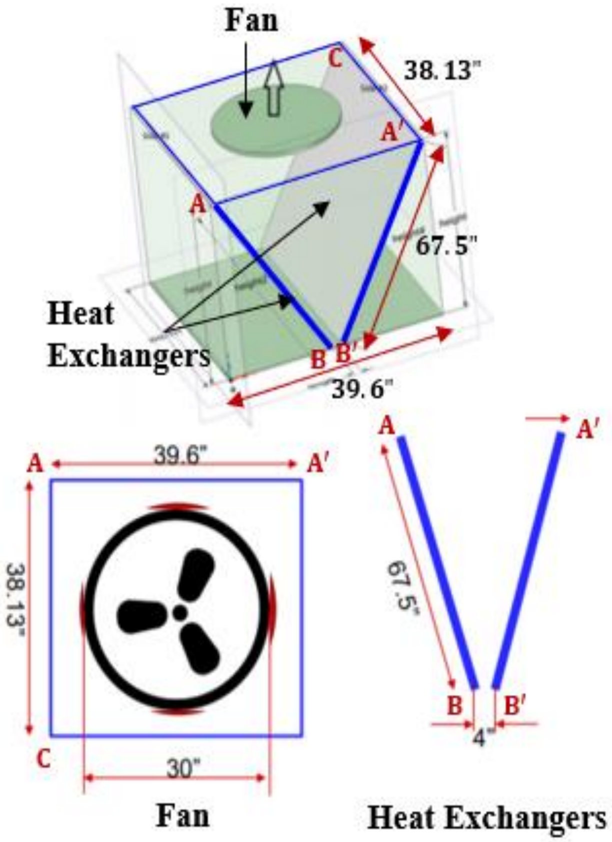

Figure 42: Heat exchanger and fan configuration as stated in the problem statement

The geometry constraints include the fixed coil face area and fixed relative position of the fan and the HXs. The operating conditions include two different cases – high load condition (DCC) and low load condition (CCC), as shown in *Figure 43* (a). The fan curve is provided for the airside pressure drop constraint corresponding to the total volumetric airflow rate for 2 HX1s, as shown in Figure 43 (b).

5.2.2. Optimization Formulation

The CMHX is built from ABS polymer and aluminum wires. The design optimization is performed based on different parameters such as orientations of the CMHX (Figure 44), the number of liquid passes, and different operating conditions. Based on the CMHX orientations, there are two types – the first type considers liquid flow in the

	DCC	CCC
T_{air}^{in}	12.8 ℃	4.4 ℃
T_{water}^{in}	23.9 ℃	12.2 ℃
$\dot{m}_{water}$	15.217 m^3/hr or 4.3749 kg/s	9.54 m^3/hr or 2.7427 kg/s
dP_{water}	$\leq 24.8\ kPa$	$\leq\ 12.6\ kPa$

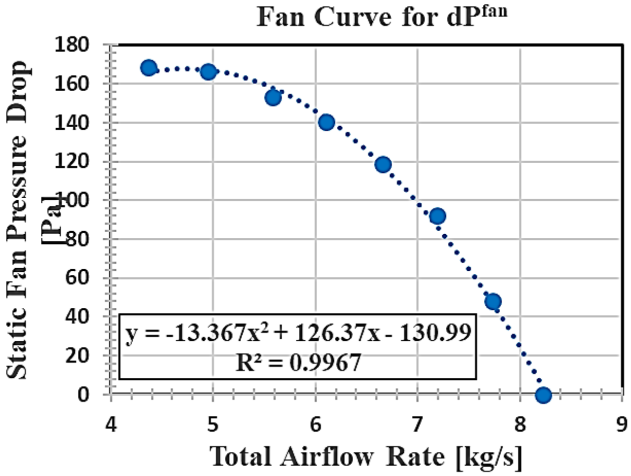

(a) (b)

Figure 43: Operating conditions for the air-conditioning applications

vertical orientation, which means L_w is along $A'B'$ direction. The second type considers liquid flow in the horizontal orientation, which means L_w is along $A'C$ direction.

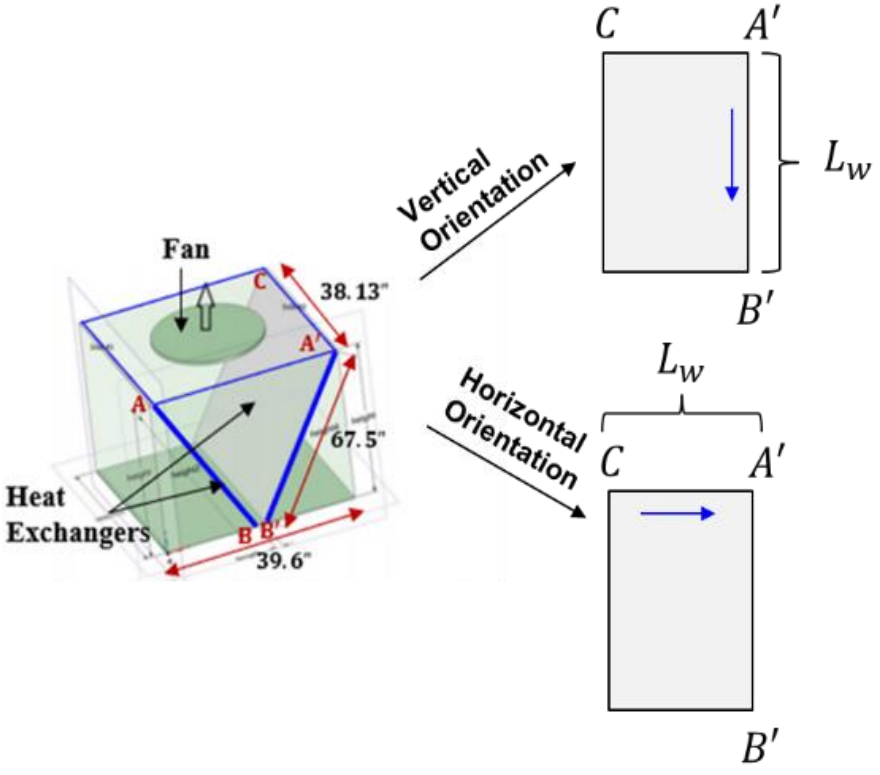

Figure 44: Types of iCMHX Orientation

Based on the number of liquid passes, the CMHX considers two types – single-pass and double-pass of the liquid flow. The CMHX considers DCC and CCC conditions depending on the different operating conditions. The airside flow length is noted to have its maximum size limited to $BB' = 4''$ where BB' is the center-to-center distance between the two CMHXs. The header is approximated to be a 1.95" ABS polymer pipe. The dynamic losses inside the header are as small as 10% of the total CMHX core pressure drop to facilitate even flow distribution across CMHX and ensure minor pressure losses inside the header. These cases can be summarized as shown in Table 15 and can be studied in detail with the help of 4 different case studies as described in the following sections.

Table 15: Design optimization parameters

	Vertical Orientation	**Horizontal Orientation**	
	Single Pass	Single Pass	Double Pass
Objective Function	Max. (Q)		
Constraints	$L_a \leq 0.102$m		
	$2 \times S_L \geq D + 1$mm (Printing constraint)		
	$dP_a \leq -13.367 \times (2 \times \dot{m_a})^2 + 126.37 \times (2 \times \dot{m_a}) - 130.99$		
	$mass \leq 5\ to\ 40\ kg$		
	$dP_w \leq 24.8\ kPa$ (DCC)		$dP_w \leq 24.8\ kPa$ (DCC) $dP_w \leq 12.6kPa$(CCC)
Parameters	$L_w = 1.615$m	$L_w = 0.865$m	
	$L_{nf} = 0.969$m	$L_{nf} = 1.715$m	
	$\dot{m_w} = 4.375kg/s$ (DCC)		$\dot{m_w} = 4.375kg/s$ (DCC) $\dot{m_w} = 2.743kg/s$ (CCC)
Design Variables	$1mm \leq W_a, W_w \leq 100cm, 1 \leq N_a^{fins} \leq \frac{0.091}{D}, 2.18kg/s \leq m_a \leq 4.114kg/s,$ $1.1D \leq S_T \leq 10D, 1.1D \leq S_L \leq 5D$		
	$D = 0.4$mm and 0.8mm		$D = 0.4$mm
Operating Conditions	$dT = 11.1$℃ (DCC)		$dT = 11.1$℃ (DCC) $dT = 7.8$℃ (CCC)

5.2.3. Assumptions

Several assumptions are made while carrying out the optimization study. They are listed below.

- The total airflow rate from the fan is assumed to be double the airflow rate across each CMHX unit, i.e. even distribution of flow between both heat exchangers.
- The air pressure head and its corresponding flow-rate follow the fan curve.
- The airflow is assumed to enter the CMHX normal to the face area and exclude the pressure drop due to the turning effect from the V-configuration of the CMHXs.
- Airflow is assumed to be uniformly distributed across the face area of a CMHX unit.
- The air and brine properties do not vary with temperature
- The brine properties are evaluated at 14.15 ℃, the mean temperature of the highest and lowest brine temperature possible from DCC and CCC operating conditions.

Table 16: Air and Brine properties as taken from EES

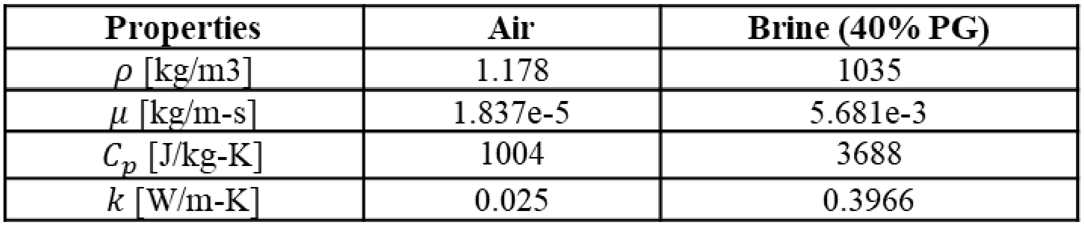

Properties	Air	Brine (40% PG)
ρ [kg/m3]	1.178	1035
μ [kg/m-s]	1.837e-5	5.681e-3
C_p [J/kg-K]	1004	3688
k [W/m-K]	0.025	0.3966

- The properties of Aluminum material are assumed to have a thermal conductivity of $237 W/mK$ and density of $2700\ kg/m^3$ while the properties of ABS polymer are assumed to have a thermal conductivity of $0.22 W/mK$ and density of $1070 kg/m^3$.

- The pressure losses inside the headers such as the bending losses and the losses due to expansion and contraction aren't considered. Only the core friction pressure drop is considered.
- The CMHX mass calculation includes the mass of the aluminum fins, the ABS polymer walls, and the ABS polymer headers.
- Since the pumping power due to hydrostatic head (including CMHX's vertical height) is zero in a closed-loop system, the pressure drop across the pump is thus independent of the orientation of the CMHX i.e., vertical or horizontal. So, the waterside pressure-drop measurements across the CMHX core (24.8 kPa for DCC and 12.6 kPa for CCC) synonymous with the pressure drop across the pump are taken at face value irrespective of the orientation of the CMHX. In other words, it is assumed that the given liquid-side pressure drops are all due to frictional losses.

5.2.4. Case Studies

Case 1: Vertical Orientation (Single Pass, DCC)

When the CMHX is oriented vertically, the optimization parameters are taken accordingly from Table 15. The optimization study is carried out, and the Pareto solution, including different optimal points corresponding to different CMHX masses, is obtained and plotted, as shown in Figure 45. The CMHX mass includes the total header mass of around 0.328 kg.

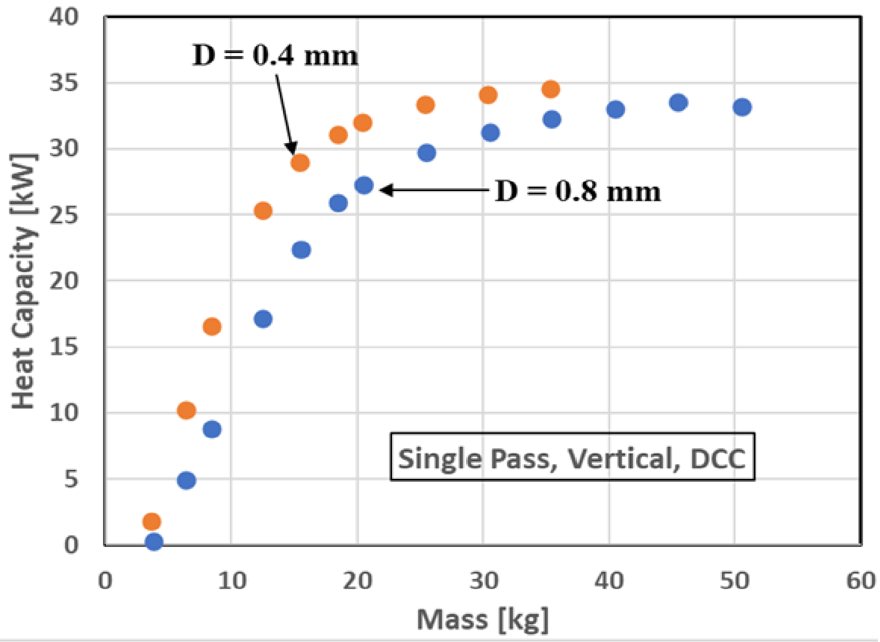

Figure 45: Pareto set for Vertical Orientation

The average Q/m is observed to be around 0.956 kW/kg for D = 0.8mm, while it is around 1.29 kW/kg for D = 0.4mm case. The case with D = 0.4mm performs better than D = 0.8mm case. For a given HX mass, D=0.4mm has a higher surface area to volume ratio than D=0.8 mm thus it can give a greater number of airside fins, waterside fins, and water inlets with increased HX thickness compared to D=0.8mm case. This results in more heat transfer area and higher NTU or higher effectiveness giving higher Q than larger wire diameter for a given mass.

The optimal points of the Pareto set lie at the fan operating points with maxed-out waterside pressure drop. With increasing heat capacity, the thickness of the CMHX (L_a) appears to increase until it reaches its maximum thickness value, producing the maximum capacity on the Pareto curve. Thus, the optimal design variables are found to vary until the L_a is maxed out. The range of the Pareto curve is decided when the

CMHX thickness reaches the maximum airflow length. The effect of the various parameters can be studied graphically, as shown in Figure 46.

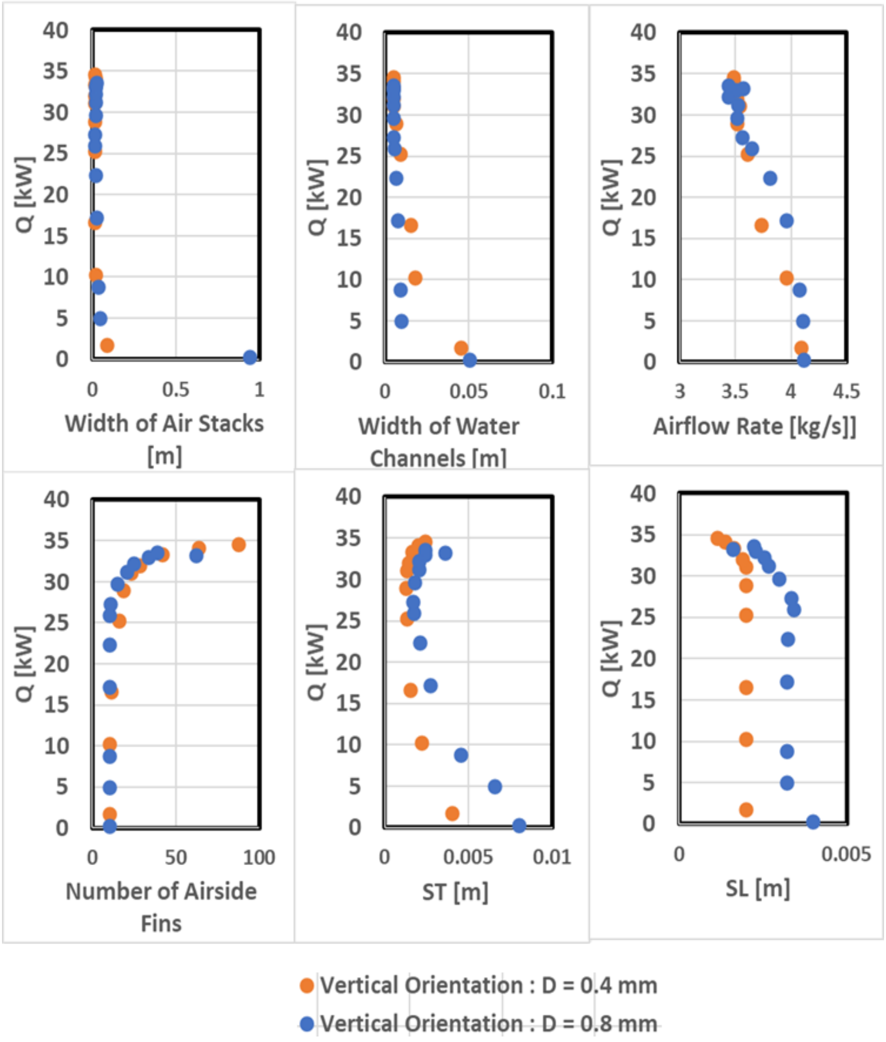

Figure 46: Effect of design parameters on optimal points for vertical orientation

As the objective function, i.e., Q, increases, the conductance also increases constrained with the increasing airside pressure drop. This also increases effectiveness and NTU, which physically represents the heat transfer area. As the area increases the HX mass also increases. The optimizer thus tends to go towards decreasing S_T or increasing the number of waterside fins and decreasing S_L or increasing the number of airside fins, facilitating denser HXs with increasing Q. The optimizer also favors decreasing the width of water channels, reducing the cross-section area or increasing the velocity on the waterside and the Reynolds number. This further increases the waterside heat transfer coefficient and the frictional losses i.e. waterside pressure drop. The cumulative effect of the increased heat transfer coefficient with the heat transfer area results into reduced waterside thermal resistances or increased thermal conductance. Though the increase in frictional losses is more than the increase in thermal performance, it is not varying as the waterside pressure drop is held constant.

Case 2: Horizontal Orientation (Single Pass, DCC)

When the CMHX is oriented horizontally, the optimization parameters are taken from Table 15. The Pareto curve is obtained for two different wire-diameters, as shown below.

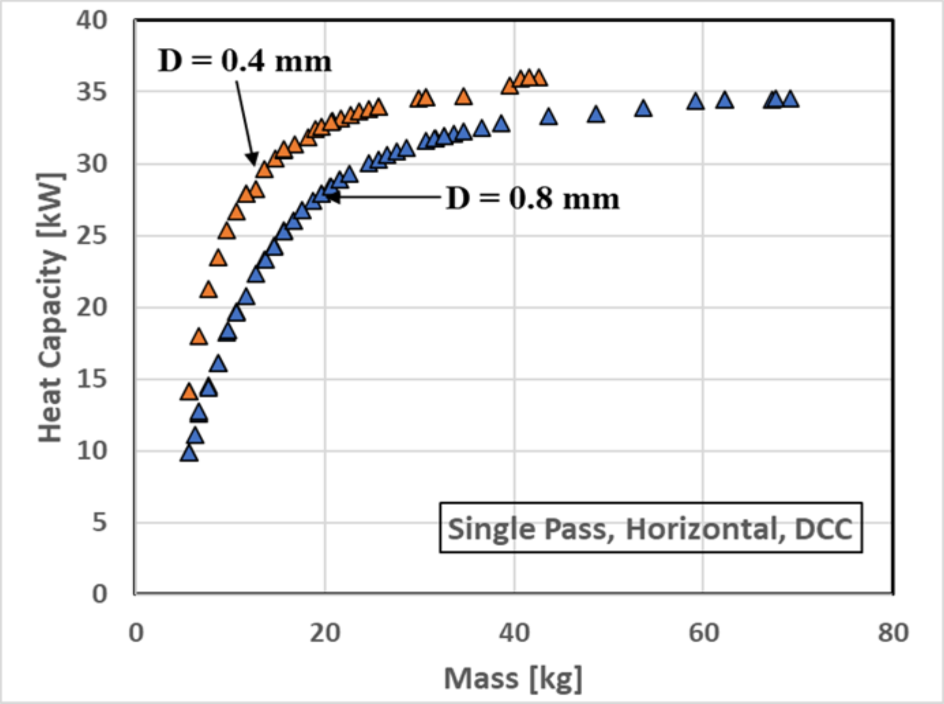

Figure 47: Pareto set for Horizontal Orientation

The CMHX mass includes the total header mass of around 0.582 kg. The average Q/m for $D = 0.4mm$ is around 1.762 kW/kg, while for $D = 0.8mm$ case, it is around

1.328kW/kg. It can be noted that the smaller the wire diameter, the better is the Q/m ratio. The optimizer follows a similar trend for most design variables as observed in the previous case study. It should be noted that the waterside flow length has decreased compared to the vertical orientation. Thus, to compensate for equivalent pressure drop as vertical orientation, SL from vertical orientation should be decreased, and the number of waterside fins from vertical orientation should be increased. Also, since the no flow length has increased, the number of inlets has considerably increased for the horizontal orientation.

The optimal points of the Pareto curve are found to be on the fan-operating point with maxed-out waterside pressure-drop. This explains the fact that the optimum thermal performance is attained at the maximum pressure drop constraints. The effect of the design variables on the optimal points can be studied graphically from below.

Case 3: Double-Pass (D=0.4mm, Horizontal Orientation, DCC)

The third case study focuses on a double-pass CMHX in the horizontal orientation. Since $D = 0.4mm$ performs better than $D = 0.8mm$, the present study includes $D = 0.4mm$ condition. The Pareto curve for such a case is obtained as shown below. The optimal points contain the same traits observed in the previous case studies. The average Q/m of the Pareto curve is observed to be around 1.562kW/kg.

The effect of the design parameters with increasing heat capacity can be seen below. The sensitivity of the design parameters is similar to that observed in the previous case study. The heat capacity is found to increase with decreasing width of air passages (W_a) and width of water channels (W_w) or with the increasing number of water channels. Similarly, the heat capacity is seen to increase with a slightly decreasing airflow rate.

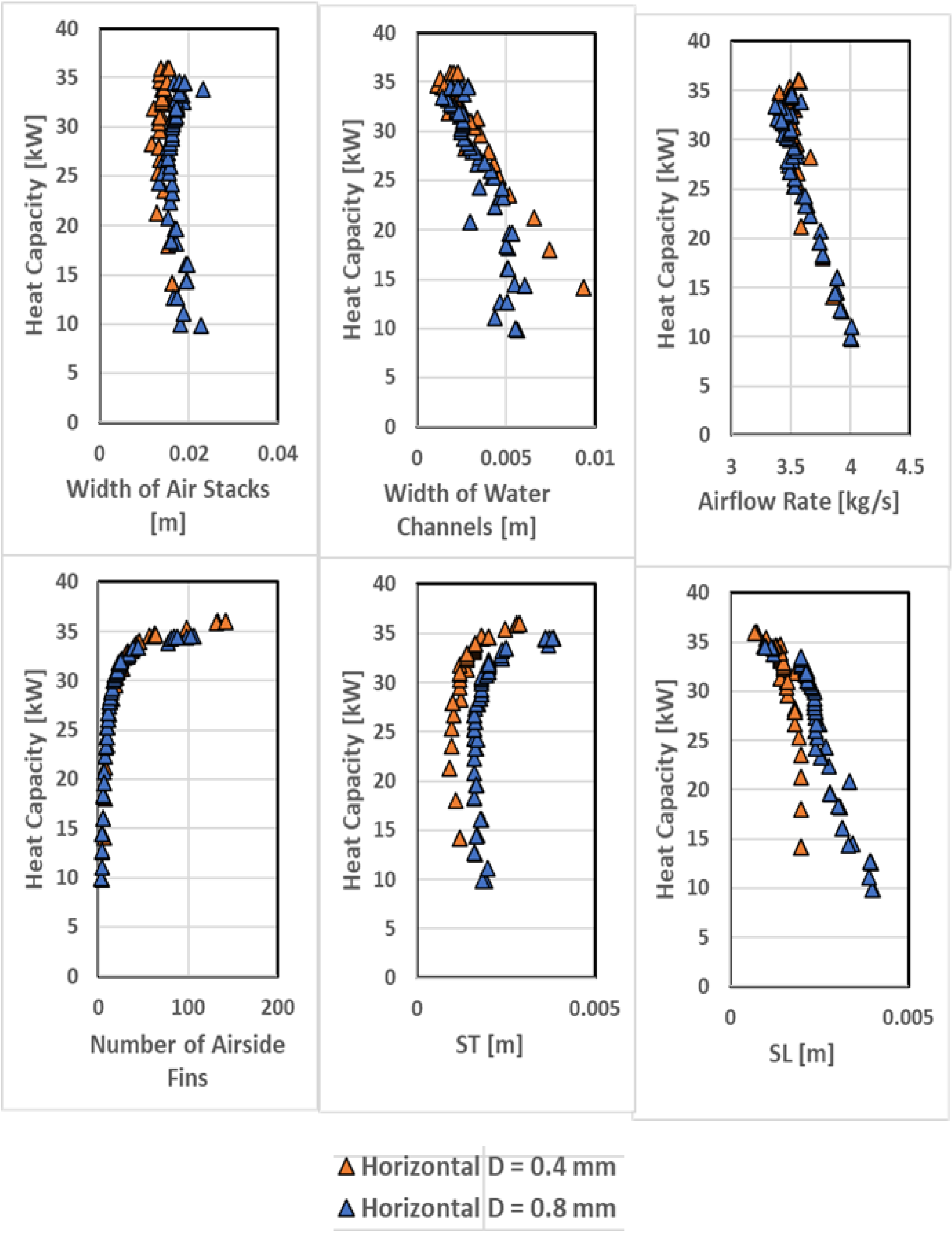

Figure 48: Effect of design parameters on optimal points for horizontal orientation

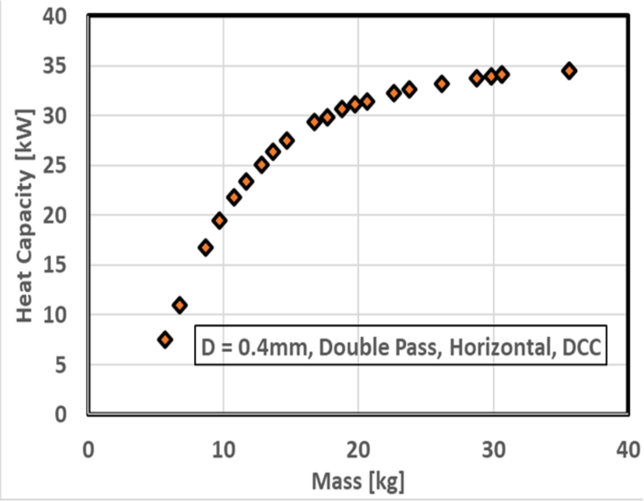

Figure 49: Pareto set for double-pass system

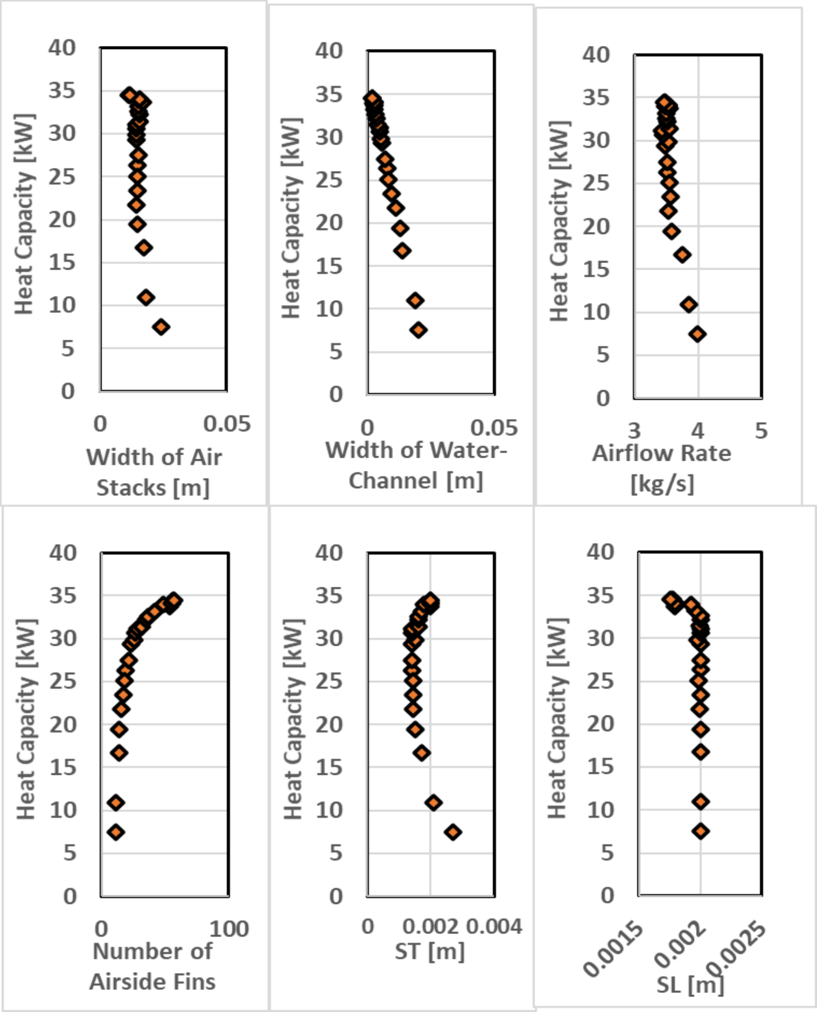

Figure 50: Effect of design parameters on optimal points for double-pass

Case 4: CCC Operating Condition (D=0.4mm, Double Pass, Horizontal Orientation)

The last case study talks about CMHX performance under CCC operating conditions. The case considers double-pass horizontal orientated CMHX with a wire diameter of 0.4mm. The Pareto curve can be found as shown in Figure 51. The average Q/m for this case is observed to be around 0.857 kW/kg. The effect of the design parameters on the heat capacity is seen in Figure 52.

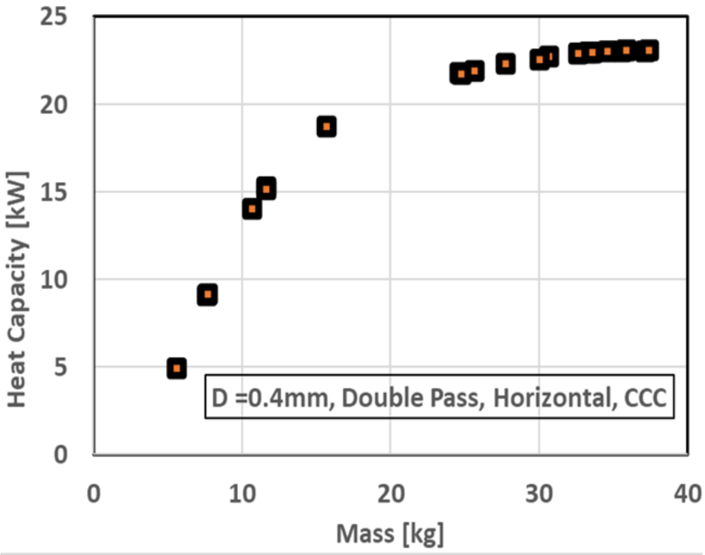

Figure 51: Pareto set for CCC operating condition

Discussion

All in all, Pareto sets are obtained for different case studies ranging from about 35 kW for about 35-60 kg under the DCC condition to ranging about 25kW for about 40kg under CCC condition. Analyzing the different case studies gives us a glimpse of CMHX performance for different parameters such as orientation, size of wire diameter, and the number of liquid passes.

(i) Wire diameter

As seen from Figure 45 and Figure 47, $D = 0.4mm$ performs better than $D = 0.8mm$ case. The maximum heat capacity is obtained for lesser CMHX mass in case of $D = 0.4mm$. It can, thus, be inferred that the reducing wire diameter by half produces higher Q/m as it helps in reducing the CMHX mass by a factor of $1/4$ per fin.

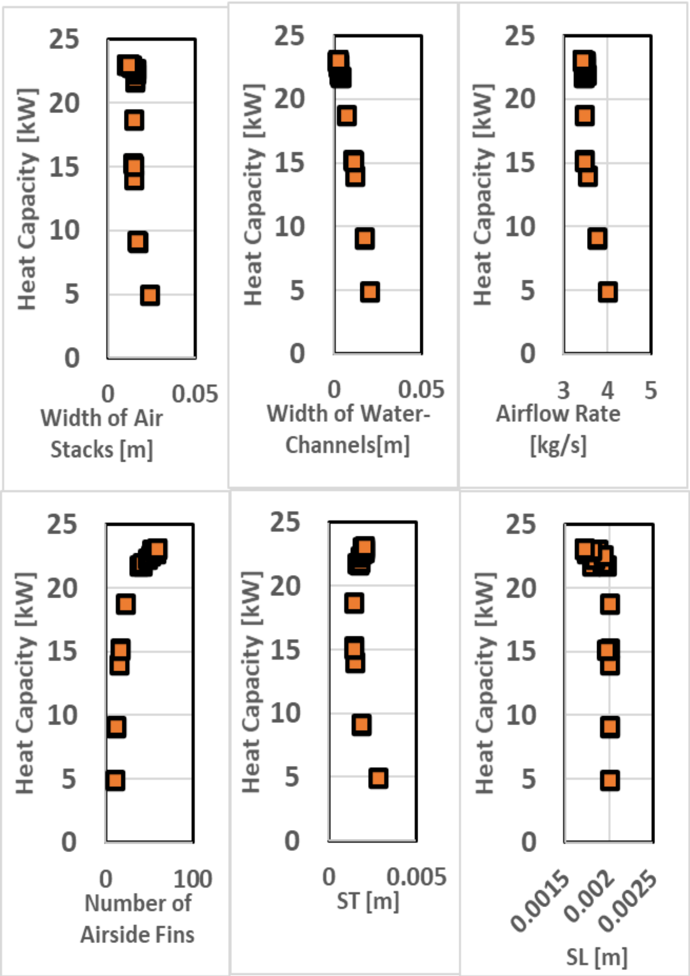

Figure 52: Effects of design parameters on optimal points for CCC

(ii) CMHX orientation

The first and second case studies show that orientation plays a vital role in deciding the CMHX performance. When the vertical orientation is compared to the horizontal orientation (see Figure 53), the water flow length is reduced by approximately two times but has the same available pressure drop. Thus, there is more room to improve the thermal performance for the same pressure-drop constraint in case of horizontal orientation.

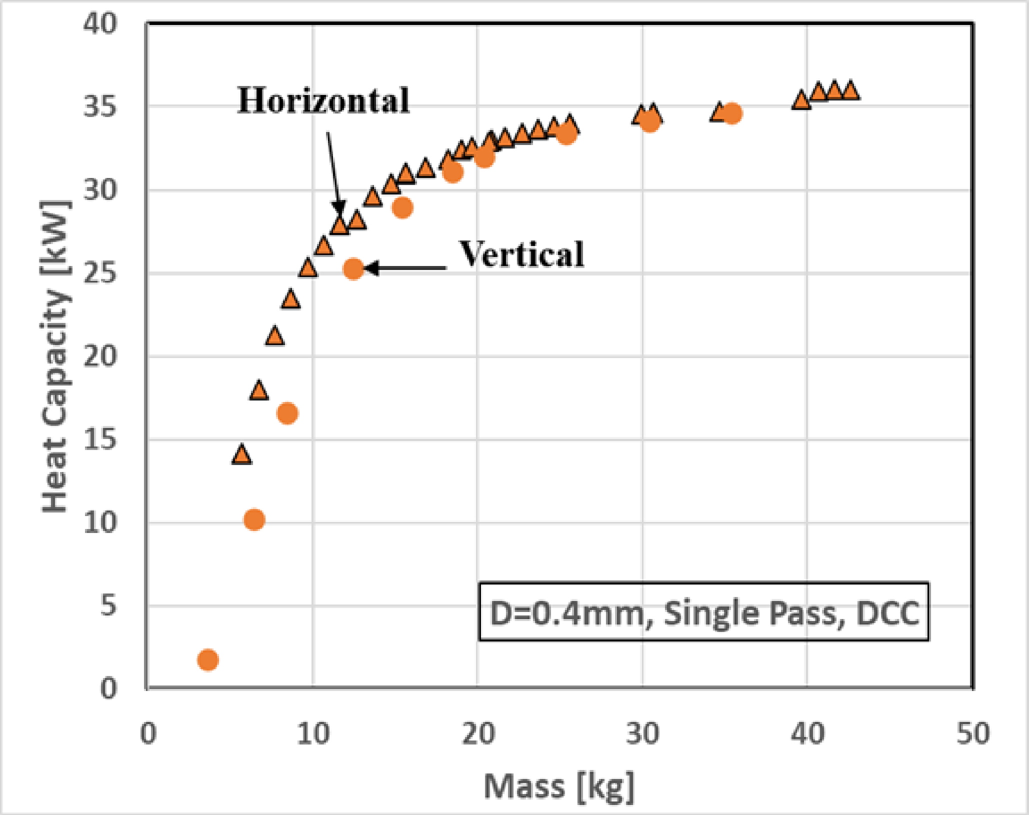

Figure 53: Effect of orientation on CMHX performance

(iii) Number of liquid passes

CMHXs can be designed either having a single pass or a double pass liquid system as per the industrial requirements. The single-pass system (average Q/m = 1.762kW/kg) performs better than the double pass (average Q/m = 1.562kW/kg) for the same waterside pressure drop limit, as shown in Figure 54.

There are, however, some issues to be resolved for future work. The metamodel currently being used for design optimization isn't mesh-independent and needs to be updated. This comprises one of the significant tasks for setting up the own metamodel for future work.

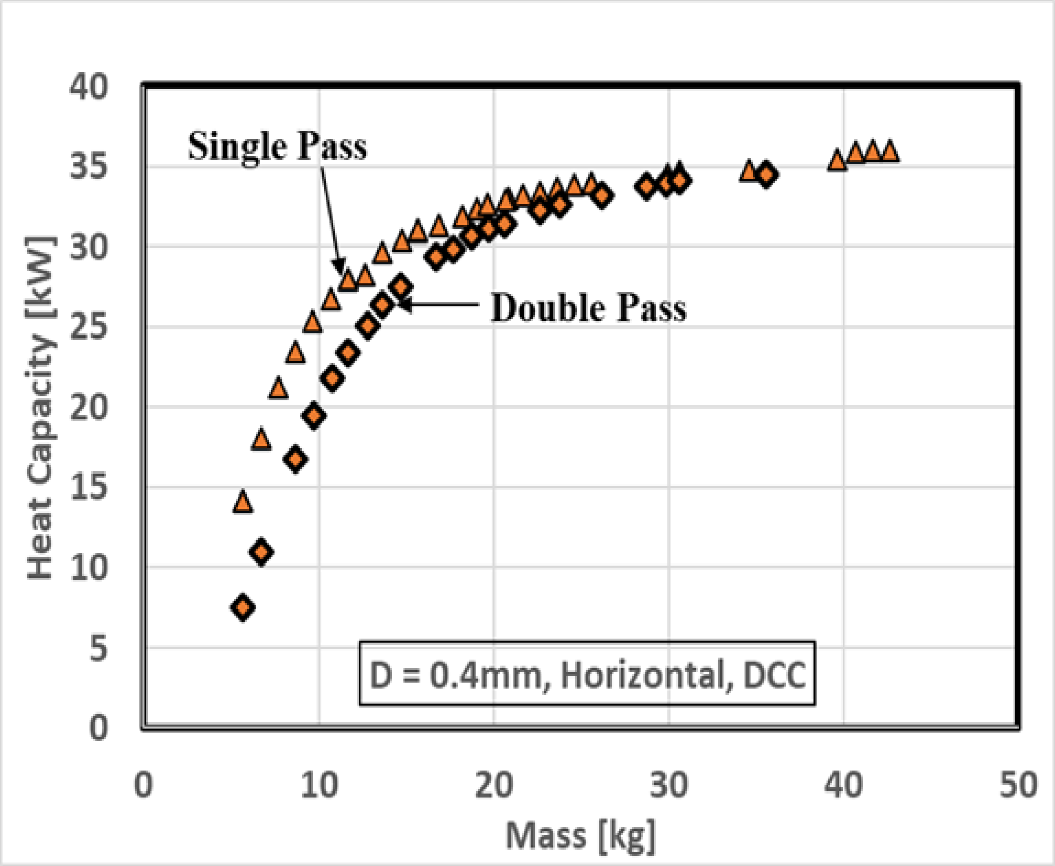

Figure 54: Effect of number of liquid passes on CMHX performance

5.3. *__Latent Energy Storage Applications__*

5.3.1. Peak-Load Building Cooling Applications

5.3.1.1. Problem Statement

The problem statement formulated for the cooling mode of the PCM-to-air TES system used in building cooling applications. The operating and target conditions for the HX design can be found in Table 17. The fluid temperatures for day and night are considered from the values used in the literature [81] [82]. The charging period is taken as 6 hours while the discharging period is taken as 3 hours which is within the recommended range of 2 to 6 hours [81] [82]. The flow rates are taken in the range of commonly used flow-rate values for ducts [82] such that the caloric resistance is small enough to give dominating fluid conductance values that can meet the target conditions. The pressure-drop target (dP_{target}) is expected to be in the range of 0.1 inch of water column which is taken in lieu of the values typically obtained across coils inside the ducts [83]. The target condition of 1.44 MJ is to be achieved, as shown in the following table.

Table 17: Operating conditions and target for building cooling application

Operating Conditions		
	Day	Night
T_{in}[°C]	25	14.5
t[hrs]	3	6
$\dot{m}_{fluid}[kg/s]$	0.04	
$dP_{target}[Pa]$	15 to 35	

Targets	
$E_{target}[MJ]$	1.44

5.3.1.2. Optimization Formulation

PCM Selection

Since salt hydrates such as Glauber's salt offer very high latent storage density and have lost cost (see Figure 12) compared to other PCM materials, Glauber's salt is a favorable candidate for the PCM. But, the melting point of Glauber's salt is ~32 °C [84], which can be further reduced to ~ 18 °C [85] by adding some amount of $NaCl$ to Glauber's salt.

However, the chemical study regarding the composition of Glauber's salt is still undergoing. Since organic PCMs have traditionally been used even though they have low thermal storage capacity, they have sharp transition temperature and no undercooling and phase-segregation issues. For the given range specified in the problem statement, n-hexadecane can also be used as a practical choice for PCM for preliminary analysis.

Formulation

To meet the given target and operating conditions, the TES system is designed from low-cost and lightweight ABS polymer and high thermal conductivity wires. The copper wires is chosen due to its higher thermal conductivity over aluminum. It utilizes low-cost inorganic PCM, $Na_2SO_4.10H_2O$, which is mixed with some amount of $NaCl$ to bring down its melting temperature from 32°C to 20°C. The material properties of all of these can be found in *Table 18*. Its properties [86] are currently taken at the melting/fusion temperature ($T_{PCM} = 32.4$°C). Since, in the literature, it is known that some % addition of $NaCl$ on Glauber's salt can lower the T_{PCM} to as low as 18°C [85], the present PCM properties are thus considered to have a T_{PCM} of about 20°C.

Table 18: Material Properties for PCM-to-gas CMHX

Material Properties					
	Air	Na_2SO_4		Polymer	Copper
		Solid	Liq.		
$\rho[\frac{kg}{m^3}]$	1.18	1395 (Mean)		1070	8960
$\mu[\frac{kg}{ms}]$	1.84e-5	-	-	-	-
$k[\frac{W}{mK}]$	0.0253	0.7	0.54	0.22	400
$C_P[\frac{W}{kgK}]$	1004	-	-	-	-
$L[\frac{J}{kg}]$	-	241000		-	-
T_{PCM}[°C]	-	20		-	-

Once the initial operating and boundary conditions are set up, the best lightest HX design meeting the given target conditions is obtained using the numerical model. An optimization technique using the exterior penalty method is employed. The details of its formulation can be found in Table 19.

Table 19: Design Optimization Parameters for PCM-to-Gas CMHX

Objective Function	**Min. ($\boldsymbol{m_{HX}}$)**
Constraints	$\lvert(L_2 - L_3)\rvert / L_3 \leq 5\%$ (Same Aspect Ratio)
	$2 \times S_L \geq D + 1$mm (Printing constraint)
	$\lvert(S_T$ - $S_L)\rvert / S_T \leq 2\%$ (small PCM overlap)
	$dP \leq dP_{target}$
	$E_{melting} \geq E_{target}$
Parameters	$\dot{m}_{fluid} = 0.04kg/s$
	$n_{step} = 150$
Design Variables	$2mm \leq W_{fluid}, W_{PCM} \leq 100cm, 1 \leq N_L \leq 1000, 1 \leq N_T \leq 1000$, $1.1D \leq S_T \leq 10D$, $1.1D \leq S_L \leq 10D$ $2 \leq n_{chan} \leq 50$
	$D = 0.4$mm

5.3.1.3. Optimized Design

The optimized HX design for $dP = 15Pa$ is obtained as shown in Table 20. It can be seen that the target conditions are easily met by using an optimal HX design which utilizes the maximum available dP and almost the entire 97.3% of the PCM during melting. Also, there is an excellent energy balance between the amount of heat gained/lost by the fluid and the PCM during melting and freezing, which is nearly 0. The optimized HX design satisfies all the constraints. The overall HX weighs about 7.86 kg with its face-size close to that of a square-cross-section duct of an aspect ratio of nearly 1.1. Overall, the cooling load performance is about 137.96 W.

Table 20: Optimization Results

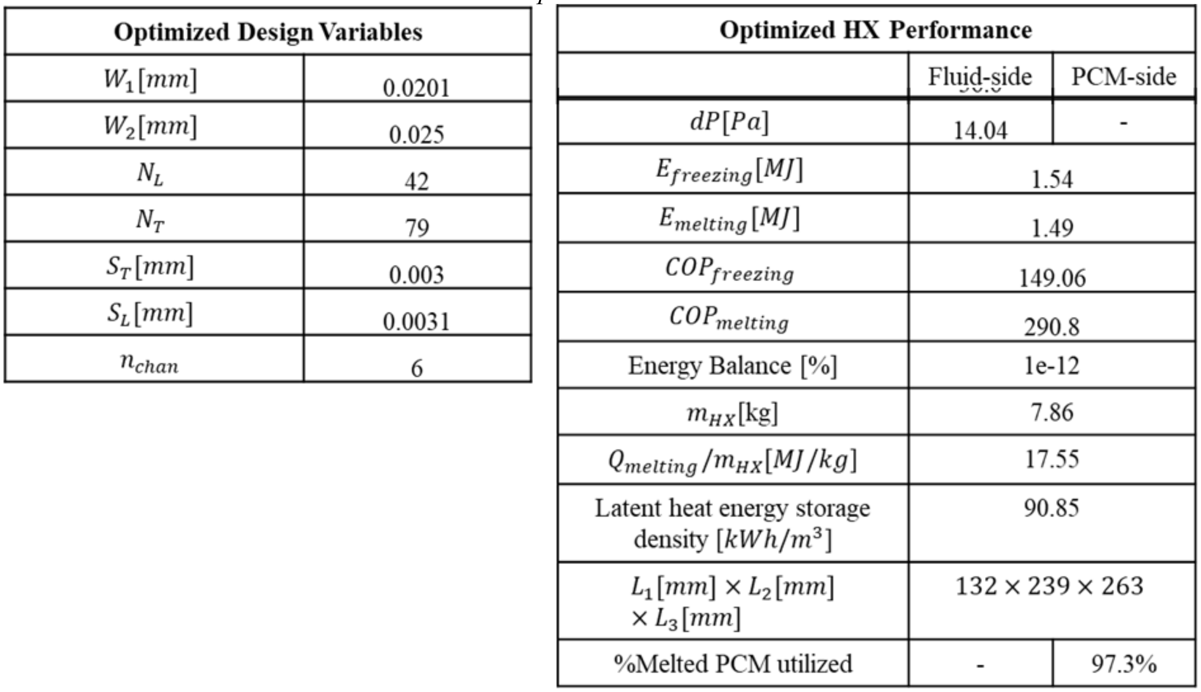

Optimized Design Variables	
$W_1[mm]$	0.0201
$W_2[mm]$	0.025
N_L	42
N_T	79
$S_T[mm]$	0.003
$S_L[mm]$	0.0031
n_{chan}	6

Optimized HX Performance		
	Fluid-side	PCM-side
$dP[Pa]$	14.04	-
$E_{freezing}[MJ]$	1.54	
$E_{melting}[MJ]$	1.49	
$COP_{freezing}$	149.06	
$COP_{melting}$	290.8	
Energy Balance [%]	1e-12	
m_{HX}[kg]	7.86	
$Q_{melting}/m_{HX}[MJ/kg]$	17.55	
Latent heat energy storage density $[kWh/m^3]$	90.85	
$L_1[mm] \times L_2[mm] \times L_3[mm]$	$132 \times 239 \times 263$	
%Melted PCM utilized	-	97.3%

Similarly, the design is run for different dP values, and the Q/m value is noted in Table 21. The primary reason behind the large Q/m values can be attributed to the low polymer and PCM weight.

Table 21: Optimized Q/m values for different pressure-drops

$dP[Pa]$	$E_{freezing}[MJ]$	m_{HX}[kg]	$Q_{melting}/m_{HX}[MJ/kg]$
25	1.44	7.41	17.99
35	1.438	7.38	18.04

Similarly, HX design has been designed for $D = 0.8\ mm$ aluminum wire for Glauber's salt. But for preliminary analysis during the experimentation, the same design has also been used for $n-$hexadecane. Since n-hexadecane has almost half Glauber's salt density, the maximum available latent energy reduces to almost half. The performance for this scenario is shown below:

Table 22: HX performance for 0.8mm aluminum wire with n-hexadecane PCM

D [mm] (Aluminum)	0.8
W_1 [mm]	22.3
W_2 [mm]	26.5
N_L	30
N_T	67
S_T [mm]	3.77
S_L [mm]	3.84
n_{stacks}	5

dP_a	36.8 Pa
$E_{freezing}$	0.815 MJ
$E_{melting}$	0.815 MJ
m_{HX}	4.7 kg

5.3.2. Pulsed-Power Applications

5.3.2.1. Problem Statement

The problem statement formulated for the cooling of laser diodes (device) in pulsed-power cooling applications. The TES system is coupled with high flux power electronics, a manifold microchannel heat sink, as shown in Figure 55. Besides the primary loop containing TES and high-power electronics, there is a secondary refrigeration loop that also contributes to the laser diode's cooling in pulsed-power cooling applications.

However, the objective is to design a compact and low-cost TES unit (see *Figure 56*) that can store 19.2 kJ of dissipated energy. The operating conditions on inlet temperature of about 18 °C and melting time of about 6s and freezing time of about 54s,

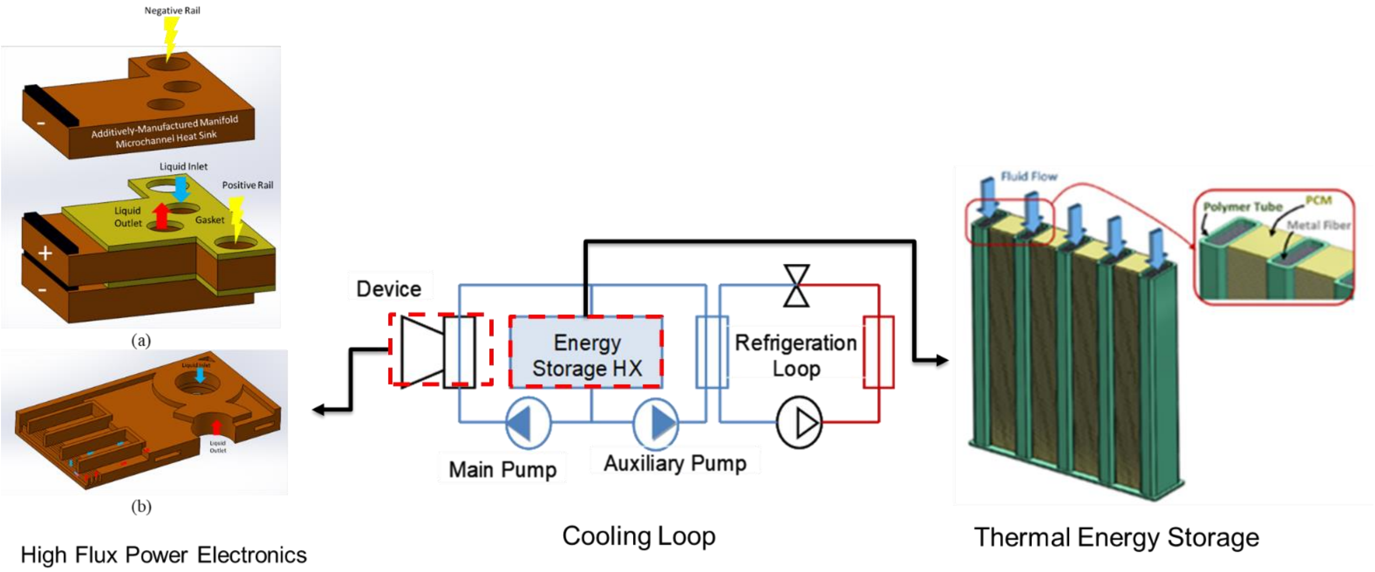

Figure 55: TES used as an energy storage HX in primary cooling of pulsed-power applications

are based on laser-diode cooling applications. The working fluid used is a standard electronic coolant, FC-72. The pressure-drop target (dP_{target}) is expected to be in the range of 20kPa, typical for FC-72 based HX devices.

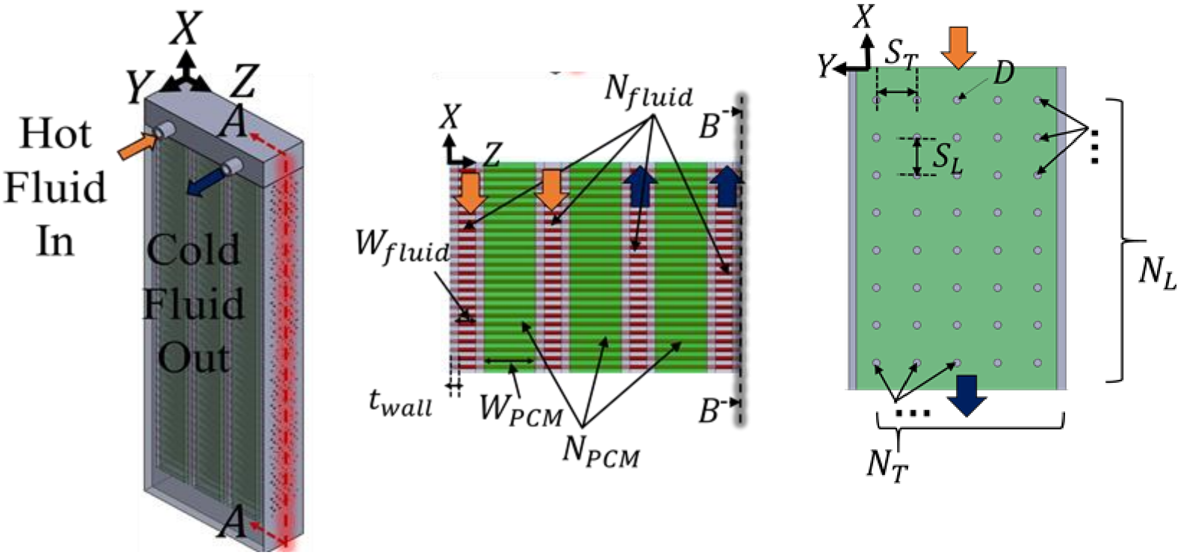

Figure 56: TES System design for PCM-to-liquid applications

5.3.2.2. Optimization Formulation

PCM

Glauber's salt is selected as the PCM due to its properties, as discussed above. Its transition temperature is also very close to the operating conditions of the pulsed-power cooling applications of 18°C. The PCM properties used are listed in Table 23.

Table 23: Glauber's salt-PCM Properties

PCM Properties [84]				
Glauber's Salt	$\rho\ [kg/m^3]$	$k\ [W/mK]$	$L\ [kJ/kg]$	T_{PCM} [°C]
Solid	1395 (mean)	0.7	241	20
Liquid		0.54		

Formulation

The TES system is designed from low-cost and lightweight ABS polymer and high thermal conductivity copper wires to meet the given target and operating conditions. An optimization technique using the exterior penalty method is employed and the details of the formulation details can be found in *Table 24*.

Table 24: Problem Statement for Pulsed-Power Cooling Applications

Constraints		
$E_{stored} \geq E_{target}(19.2kJ)$		
$\dot{m}_{fluid} = 0.5kg/s$		
Charging: $t = 54s; T_{in} = 18°C$		
Discharging: $t = 6s; T_{in} = 32°C$		
Printing	**Modeling**	**User-defined**
$2 \times S_L \geq D + 0.5mm$	$\lvert(S_T - S_L)\rvert / S_T \leq 5\%$	$dP \leq 17kPa$
$W_{fluid}, W_{PCM} \geq 2mm$	$1.1D \leq S_T, S_L \leq 10D$	
Optimization Variables		
$W_{fluid}, W_{PCM}, N_L, N_T, N_{PCM}, N_{fluid}, S_T, S_L$		
Objective		
Min. (Vol_{HX})		

However, for optimization, the design variables have to be continuous. For sensible cooling applications, the number of wires was assumed as continuous during optimization but were later rounded off to integer values. But for latent cooling applications, the 1D ROM iterates the PCM-wire for N_L rows. Thus, N_L has to be an integer to be iterated. Thus, the modeling has been modified to incorporate the nature of continuous N_L wires by rounding up N_L to the nearest integer. But the PCM mass for the last tube is adjusted to correspond to the non-integer area representing the continuous values of N_L wires, as shown in *Figure 57*.

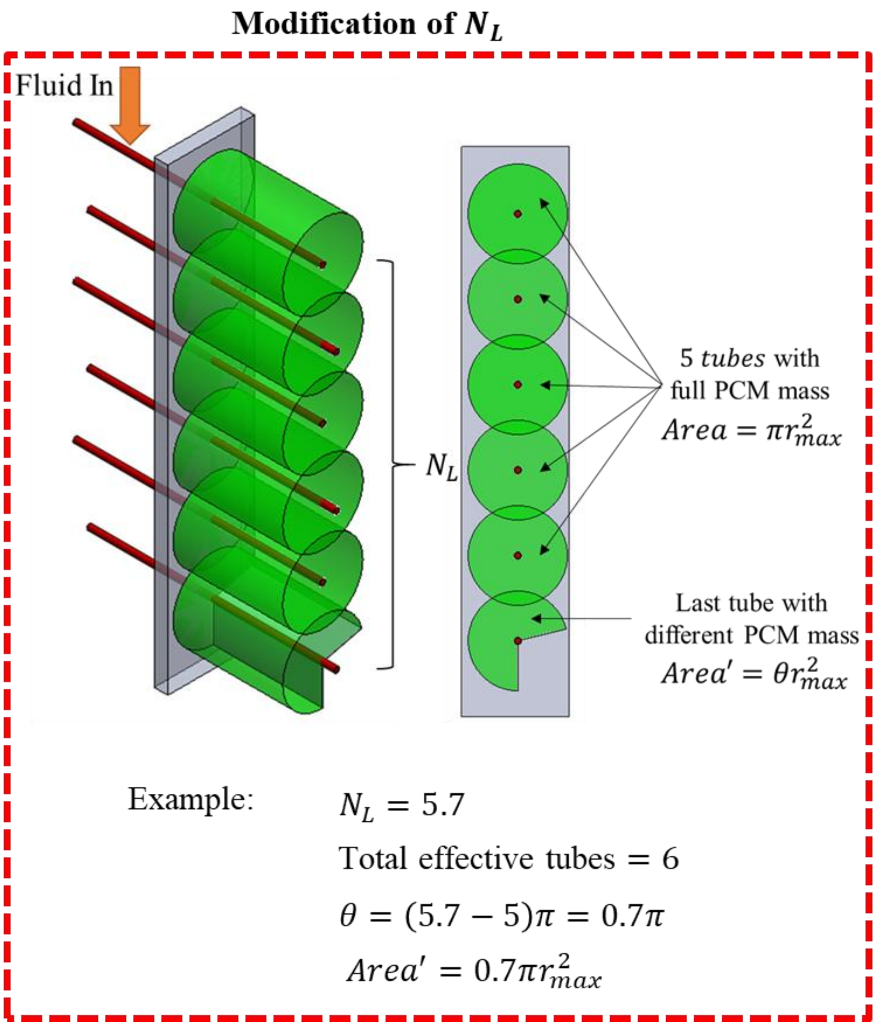

Figure 57: Modification of NL to incorporate continuous value of N_L

5.3.2.3. Optimized Design

The optimized design details have been shown in *Table 25*, and its schematic has been shown in *Figure 58*.

Table 25: Optimized design variables and performance parameters

Optimized Design Variables			
$W_{fluid}[mm]$	2.9	N_{PCM}	5
$W_{PCM}[mm]$	11.2	N_{fluid}	6
N_L	25	$S_L[mm]$	0.61
N_T	224	$S_T[mm]$	0.58

TES Performance ($D = 0.4mm$ | Staggered Config.)		
	Charging	Discharging
$t[s]$	54	6
$dP[Pa]$	2440	
$E[kJ]$	20.3	
COP	1020	
Energy Balance	✓	✓
$m_{HX}[kg]$	0.677	
%PCM Utilized	91.5	
Energy Storage Density $[MJ/m^3]$	104	
HX Size $[L_1 \times L_2 \times L_3]$: mm	$17.3\times 133 \times 85.4$	

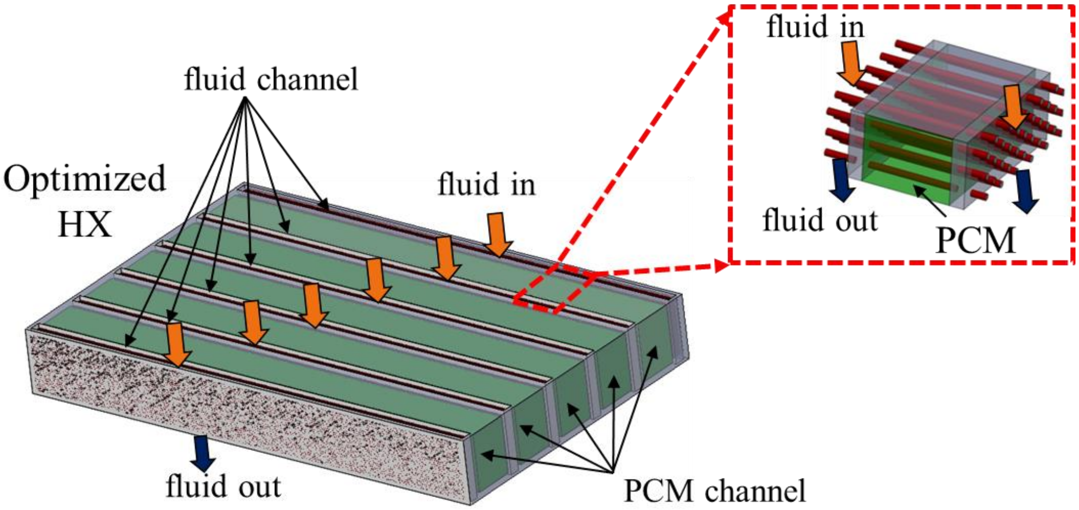

Figure 58: Optimized TES design configuration

5.4. Summary

An exterior penalty algorithm for multi-objective constrained optimization is discussed. Its application for different sensible cooling and latent cooling applications is explained. The first case example application focuses on iCMHX used as an evaporator in air-conditioning applications. A case study is carried out based on the iCMHX orientation, fin-wire size and number of liquid passes and it's determined that the best design based on the pareto curves and understanding is the iCMHX with small wire size ($D = 0.4mm$), horizontal orientation and single-pass system for a given pressure drop constraint. Similarly, for latent cooling applications, a TES unit, 239mm $\times$ 263mm $\times$ 132mm size and weighing about 7.8 kg, is designed for storing 1.44MJ for peak-load building cooling applications in which the charging time (melting) is of 3 hours and discharging time is of 6 hours. Another case example demonstrated was designing a TES unit, of size $133mm$×$85.4mm$×17.3mm and weighing 0.677 kg for storing 19.2kJ for pulsed power cooling applications with charging time of 6s and discharging time 54s.

Chapter 6: Experimental Study

The novel polymer composite HX is additively manufactured and post-processed before testing experimentally for sensible and latent cooling applications. The iCMHX testing is performed in two different testing cases for sensible cooling applications. The first test comprised of investigating the effect of coating using traditional experimental approach and then comparing its results with a traditional 2D based CFD study (see Section 4.2.2). It comprised the testing of five geometrically-identical polymer composite HXs but with different coating processes. The second test comprised of meeting the shortcomings from the first test case by improving the accuracy of both the experimental and numerical study by reducing experimental uncertainties of the experimental study and by using a high-fidelity 3D CFD-based study (see Section 4.2.4) for comparison with the experiments. However, it involves testing a reference iCMHX unit and analyzing in detail the performance of one of the CMHX units and its comparison with the numerical model and an experimentally tested conventional HX. For latent cooling applications, the TES unit is tested for building cooling applications, and then its performance is compared with the results predicted by 1D ROM.

6.1. Sensible Cooling for electronic cooling of Desktop Computers

6.1.1. Testing 1: Investigating the effect of coating via traditional experimental and numerical approach

6.1.1.1. A Set of Five iCMHX Units

A set of five geometrically identical iCMHX units (see Figure 59) is experimentally tested, with differences in the units based on their post-processing methods described in Table 26. Their geometric and fluid-flow path details have been discussed in length in Section 4.2.1. The post-processed iCMHX units are seen to differ on their airside clogging, as shown in Figure 59, where a light source is kept behind the iCMHX units, and their images are captured from the front under the same setup conditions. The units with lesser transmitted light, such as Unit 3 and Unit 5, represent higher airside clogging of fins as they scatter more light because of the rough and uneven coating surfaces present on the fins. Similarly, the units with higher transmitted light, such as Unit 1 and Unit 4 represent limited airside clogging of the fins.

Table 26: Detailed comparison of 5 units

iCMHX Units	Post-Processing Details	Observations
Unit 1	2 layers of polyurethane coating	Limited to Moderately clogged Airside fins
Unit 2		
Unit 3		Highly clogged Airside fins
Unit 4	1 layer of polyurethane coating	Limited clogged Airside fins
Unit 5	2 layers of thinned polyurethane coating	Highly clogged Airside fins

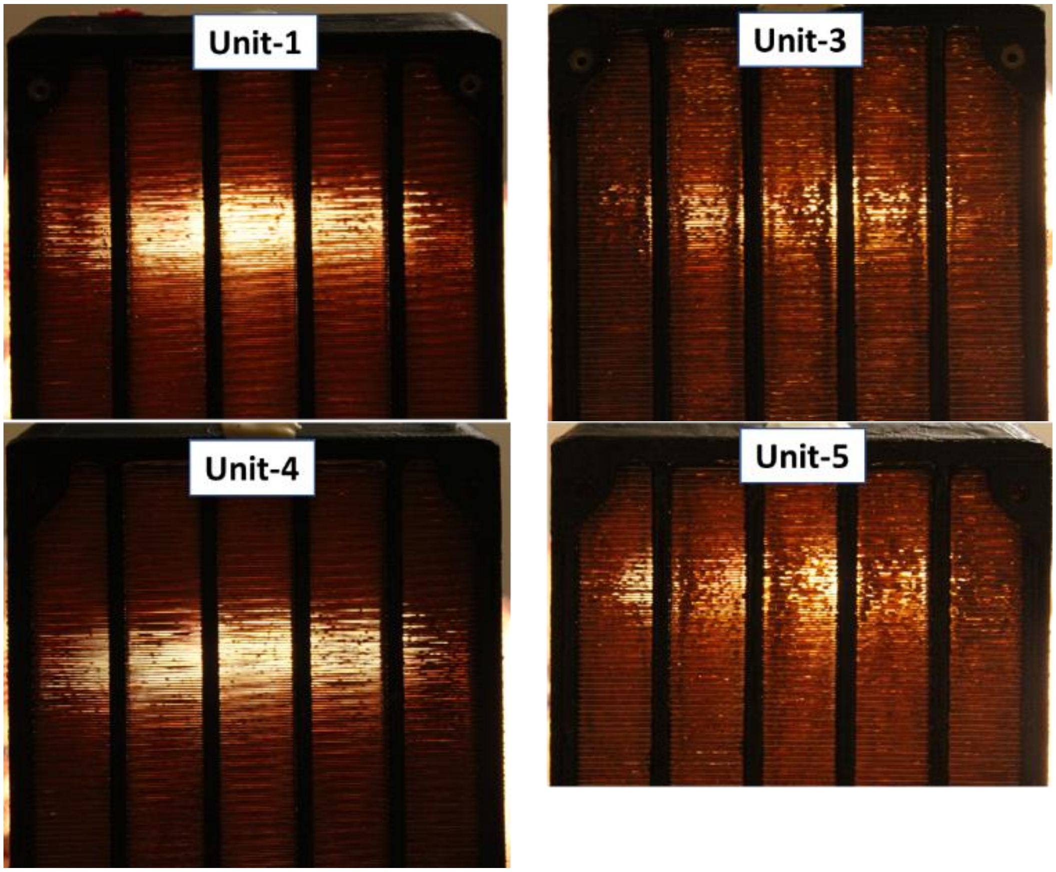

Figure 59: Comparison of the post-processed iCMHX units in terms of their airside clogging based on the light transmitted through them

6.1.1.2. Experimental Setup

The test setup consists of an air-side open-loop and a waterside closed-loop, as shown in Figure 60. The air-side loop consists of a blower, rotameter, and static mixer. The blower drives the room air (at ambient temperature) through a foam-insulated duct system and blows the air past the rotameter, which measures the flow rate. The airflow rate is manually varied in the range of 9 g/s to 30 g/s via the blower's variable frequency drive. The rotameter readings are then recorded. The inlet air continues to flow inside the duct and is mixed using a static mixer to provide a uniform temperature profile. The mixed air then reaches the diverging airside manifold section, flows past through the air passages of the iCMHX core, and then exhausts to the room via the converging airside manifold section. The internal flow path of the air can be seen in *Figure 14*. Temperature measurements using T-type thermocouples are taken at the diverging airside manifold section before the inlet of the core and the exit of the converging airside manifold section after the core outlet.

Similarly, pressure measurements are taken by taking an area-weighted average of pressure at four equidistant points just before the inlet of the test section and at the exit of the test section. A differential analog pressure gauge measures the averaged pressure drop. A DAQ reads the airside temperature measurements via a thermocouple card while the airside pressure drop readings are manually noted.

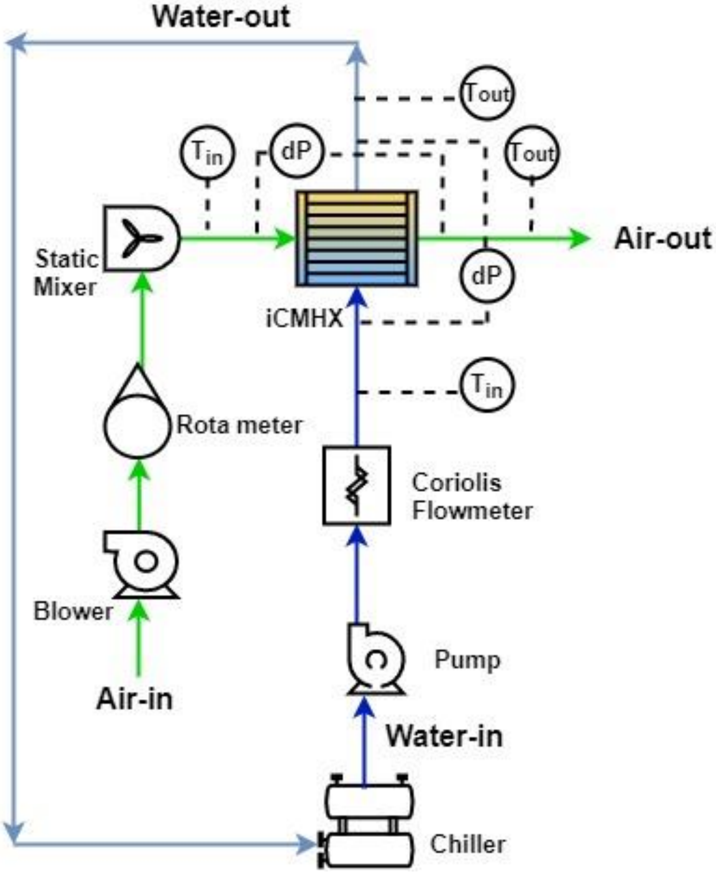

Figure 60: Schematic of test-loop for iCMHX

The waterside loop consists of a chiller, a pump, and a Coriolis flowmeter, as shown in Figure 60. The chiller supplies heat to the inlet water by regulating its temperature to around 35 ℃ to 37 ℃. The hot water flows through the pump, controlled by 0-5 V input from the DAQ through the output voltage card. The flow rate is varied in 3 g/s to 10 g/s as measured by a Coriolis flowmeter. The DAQ reads the readings from the Coriolis flowmeter through the input voltage card. The hot water then passes through the core via the inlet port and supplies heat. It then exits via the outlet port to the sink of the chiller, forming a closed loop. Since the core is a double-pass liquid system, the water flows through the inlet port to the three water channels, separated from the remaining channels by a 1-mm thick polymer wall. The water flows through the channels to the bottom of the liquid-side manifolds without polymer wall separation. It then returns to the outlet port at the top liquid-side manifold and exits, as shown in *Figure 14*. Temperature measurements are taken at the entrance and exit of the core using T-type thermocouples. Similarly, pressure-drop measurements across the core are taken by a differential pressure-transducer attached right before the entrance and after the exit of the core. The DAQ reads the temperature readings via a thermocouple and pressure-drop readings via an input voltage card.

6.1.1.3. Instrumentation and Calibration

Instrumentation

A summary of the equipment used in the experiment and their uncertainties are shown in Table 27.

Table 27: List of Specifications and uncertainties of equipment

	Equipment	Specifications	Uncertainty
Airside Loop	Blower	1.84 kW at 230V and 7A, 3450 rpm	NA

	(Baldor Industrial Motor; Model R5325A-2)		
	Rotameter (Fischer & Porter; Model 10A4557S)	0 - 31.4 g/s	0.3 g/s
	Analogue pressure gauge (Magnehelic Dwyer Instruments)	0 to 62 Pa	1.25 Pa
Waterside Loop	Chiller (ThermoNESLAB RTE7; 115V-60Hz Model)	20℃ to 80℃ (1.2 ℃/min, −0.92℃/min)	NA
	Pump (Micropump; Model I-Drive)	0 g/s to 20 g/s, 0 to 5V control	NA
	Coriolis flowmeter (Endress+Hauser Promass A; Model 1/12")	0 g/s to 28 g/s	±0.1%
	Differential pressure transducer (Valedyne; Model P855D)	0 to 1.4 kPa	±0.1% FS

Calibration

To know the accuracy and reliability of the measuring instruments, instrumentation calibration is performed on flow-measurement instruments such as (i) rotameter, (ii) Coriolis flowmeter, (iii) differential pressure transducer, and (iv) thermocouples using conventional methods.

(i) The rotameter is calibrated using a reference flowmeter. The present study uses a calibrated Coriolis flowmeter as the reference. The Coriolis flowmeter is kept in series with the rotameter, which has one end open to the ambient, creating an open loop. Air is passed through the system, and the rotameter readings corresponding to the Coriolis flowmeter readings are noted.

(ii) Likewise, the Coriolis flowmeter is calibrated using a bucket and scale. Water is pumped through the flowmeter and collected in a bucket over a measured amount of time. The output voltage from the flowmeter is read through the DAQ. The collected water is then weighed, and the flow rate is computed for that recorded time.

(iii) The differential pressure transducer for the waterside is calibrated by using a manometer. The manometer readings are noted manually, and the voltage output from the transducer is read through the DAQ.

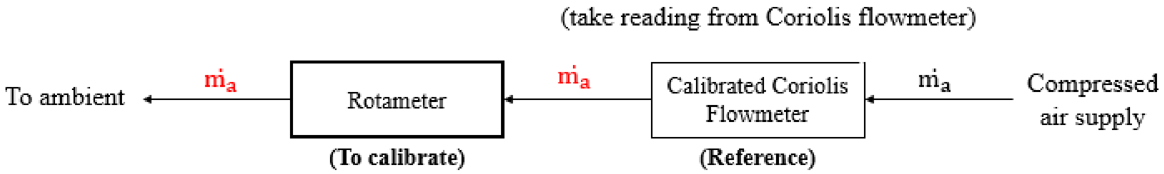

(a)

Rotameter [g/s]	Coriolis Flowmeter [g/s]
7±0.3	4.45±0.0445
13±0.3	8.15±0.0815
19±0.3	11.84±0.1184
23±0.3	14.3±0.143
26±0.3	16.2±0.162
30±0.3	18.56±0.1856
35±0.3	21.5±0.215
40±0.3	24.5±0.245

(b)

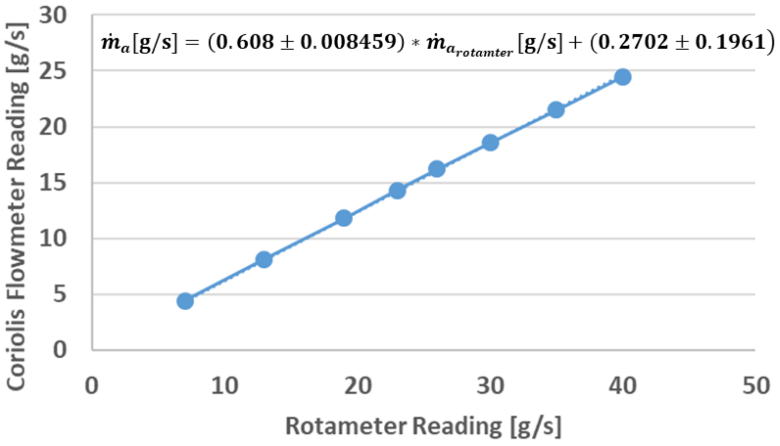

(c)

Figure 61: Rotameter calibration: (a) schematic (b) calibrated data and (c) calibration curve

(iv) The thermocouples are calibrated using an ice-water bath at 0°C kept in a room. The thermocouples are continuously stirred in the ice-water bath, and their temperatures are noted via DAQ and Labview software. Each thermocouple is calibrated to within 0.5°C, which is the uncertainty of a single thermocouple.

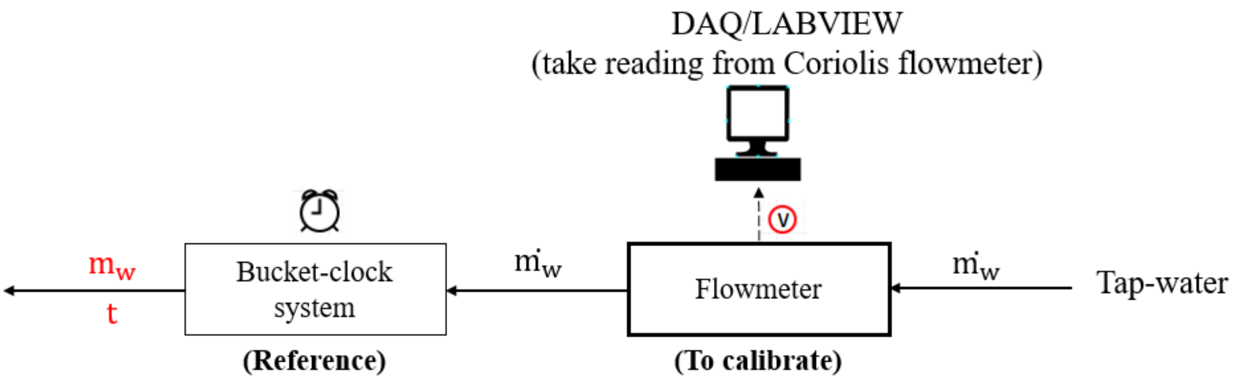

(a)

m_w (g)	Time (s)	$\dot{m}_w$ (g/s)	Voltage (V)
980.1±0.1	120±0.5	8.1678±0.03404	2.045±0.001
747.3±0.1	120±0.5	6.228±0.02596	1.548±0.001
484.8±0.1	120±0.5	4.04±0.01685	1.01±0.001
239.5±0.1	120±0.5	1.996±0.008358	0.4974±0.001

(b)

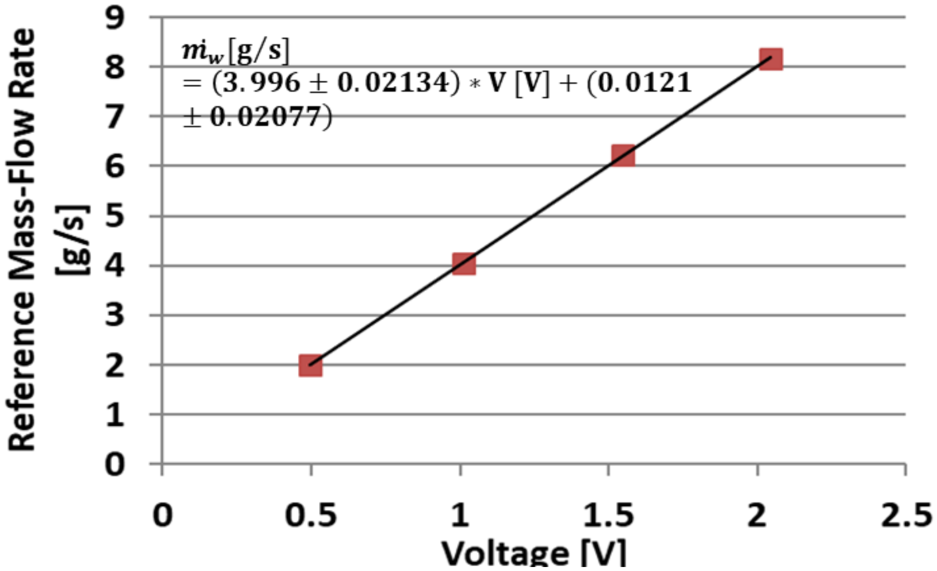

(c)

Figure 62: Coriolis flowmeter calibration: (a) schematic (b) calibration data (c) calibration curve

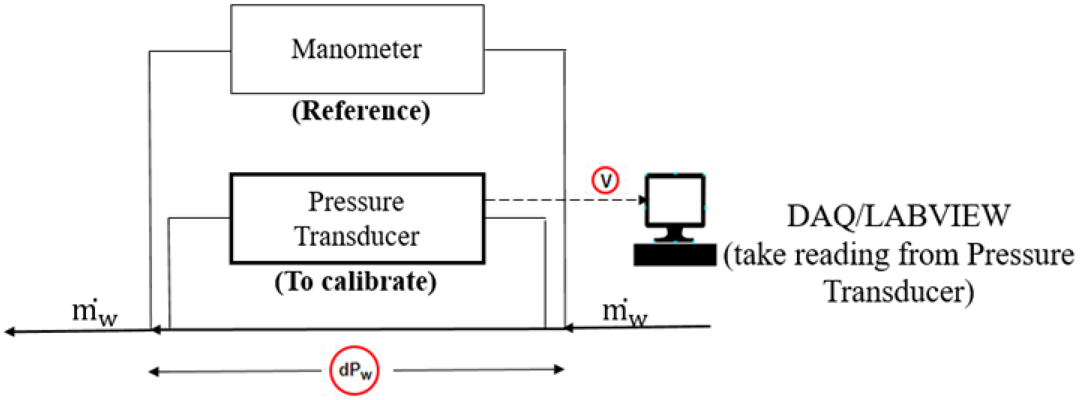

(a)

Higher Level [cm]	Lower Level [cm]	dP_w [Pa]	Voltage [V]
0±0.1	0±0.1	0±13.85	0.48±0.001
44.9±0.1	19.5±0.1	2487±13.85	1.736±0.001
46.3±0.1	18±0.1	2771±13.85	2.02±0.001
56±0.1	8.4±0.1	4660±13.85	3.71±0.001
59±0.1	5±0.1	5287±13.85	4.32±0.001
61.5±0.1	2.5±0.1	5776±13.85	4.753±0.001

(b)

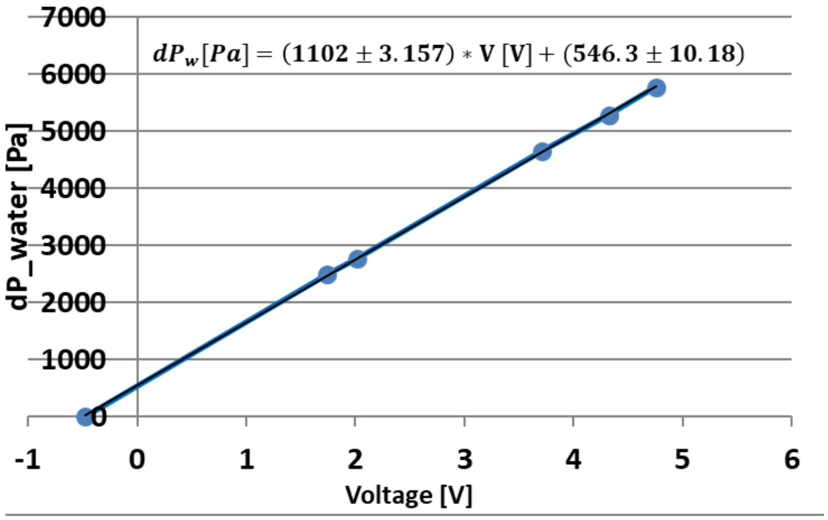

(c)

Figure 63: Pressure transducer calibration (a) schematic (b) calibration data and (c) calibration curve

6.1.1.4. Data Reduction

The thermal and hydrodynamic performance of the iCMHX is quantified by derived parameters, such as thermal resistance, and measured parameters, such as airside and waterside pressure drops.

6.1.1.4.1. Thermal Performance

The heat transfer rate from both the airside and liquid side is derived from measured flowrates, temperatures, and specific heat capacities C_p, as shown in Equations (54)-(57).

$$C_a = \dot{m}_a {C_p}_a \tag{54}$$

$$C_w = \dot{m}_w {C_p}_w \tag{55}$$

$$Q_a = C_a(T_a^{out} - T_a^{in}) \tag{56}$$

$$Q_w = {C_p}_w(T_w^{in} - T_w^{out}) \tag{57}$$

The energy balance is computed from the average heat transfer rate as shown in Equation (58) and (59). The present study's experimental data is taken within 16% energy balance criteria.

$$Q_{avg} = \frac{Q_a + Q_w}{2} \tag{58}$$

$$EB = \frac{Q_w - Q_a}{Q_{avg}} \times 100\ [\%] \tag{59}$$

The overall thermal resistance is then evaluated from measured inlet temperatures of air and water, as shown below in Equation (60).

$$R_{th} = \frac{dT}{Q_{avg}} \tag{60}$$

Moreover, the air and fluid's convective heat transfer coefficients can be computed from their respective convective heat transfer equations involving the fluids and the metal wire interface (see Equation (61)).

$$Q = hA(T_f - T_s) \tag{61}$$

where T_f is the fluid temperature while T_S is the solid metal wire temperature.

But it is difficult to obtain the measurement of the T_S of the complicated total heat transfer area (A) of the surfaces of the wires. Hence, the alternative method to obtain the heat transfer coefficients is by employing unique methods such as the Wilson plot method, as discussed in the following subsection.

6.1.1.4.2. Hydrodynamic Performance

The pressure-drop values are obtained from the direct measurements taken by the airside's analog pressure gauge and the differential pressure transducer on the waterside. The measured airside pressure drop gives the airside core pressure-drop directly; however, the measured waterside pressure-drop (dP_w^{losses}) gives the waterside core pressure drop ($dP_w^{measured}$) along with some other additional pressure drop or pressure losses (dP_w^{losses}), as shown in Equation (62).

$$dP_w^{measured} = dP_w^{core} + dP_w^{losses} \tag{62}$$

The additional pressure drop, dP_w^{losses}, includes the pressure drop from the tubes, dP^{tubes}, connecting the measurement point to the core and the pressure drop from the integrated waterside manifolds, $dP^{manifolds}$. To compute the pressure losses from the tubes, the iCMHX is bypassed, and the measured pressure-drop corresponding to the tube pressure losses is obtained. However, the pressure losses from the waterside manifolds are challenging to compute, as they cannot be measured directly. So, an empty iCMHX unit (only polymer; without any wires) is 3D printed, and the pressure drop is measured across it. The pressure drop of the empty iCMHX unit includes the tube-pressure losses, the pressure losses from the manifolds, and the pressure drop from the empty core (without wires). The pressure drop from the empty iCMHX core is calculated analytically using correlations for developing laminar flow through rectangular ducts, as shown in the literature [87](using references [88,89]). Since the tube-pressure losses and pressure-drop from empty iCMHX core are now known, the manifolds' pressure-drop is computed.

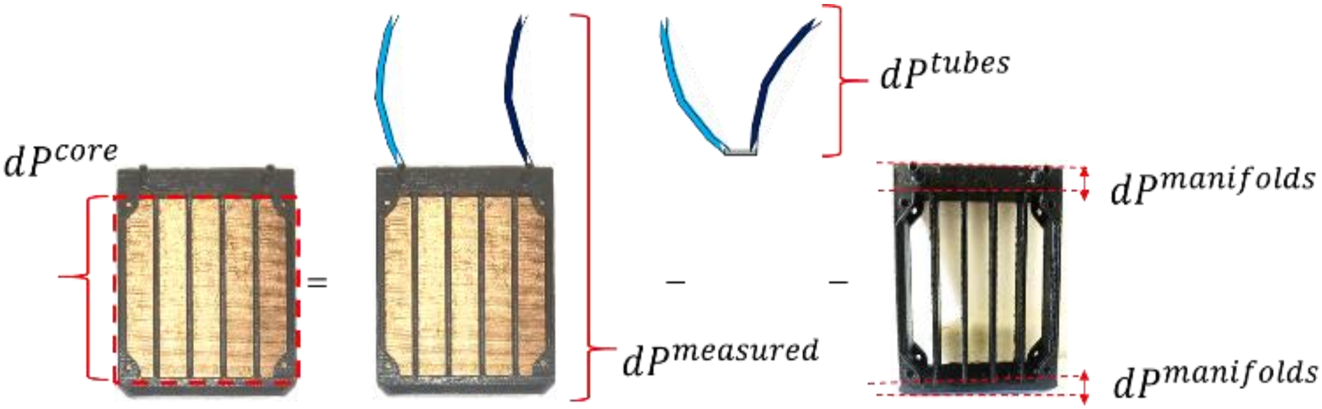

Figure 64: Representation of Core Pressure Drop from Measured Pressure Drop including pressure losses

The waterside core-pressure drop, calculated from the measured pressure drop by excluding tube-pressure losses and the losses from the manifolds, can be seen graphically in Figure 65.

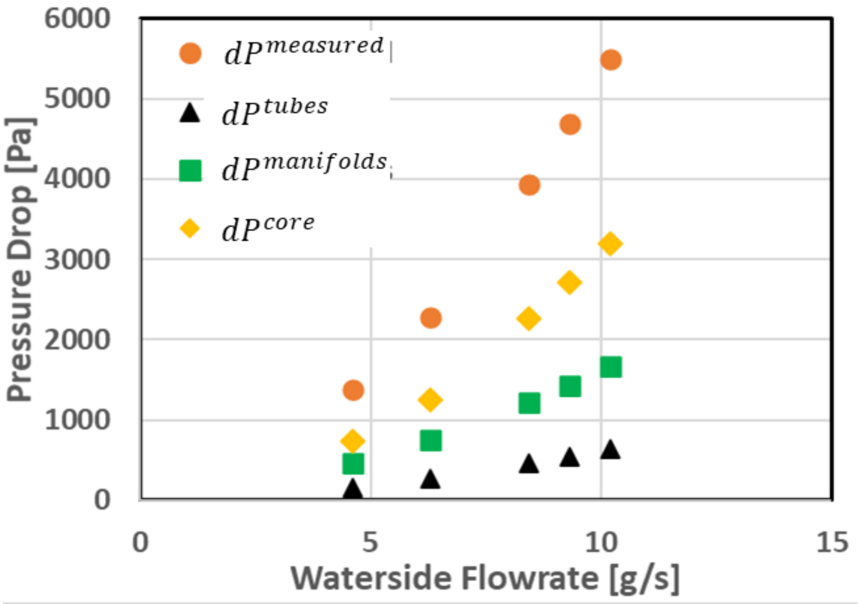

Figure 65: Measurement of waterside pressure-drop across the core of the reference iCMHX unit

6.1.1.5. Uncertainty Analysis

The derived quantities (f_i) computed from above are based on measured data (x_i) containing some instrumental uncertainties (α_{x_i}) [90]. For example, analog instruments, including the rotameter and pressure gauge, have inbuilt uncertainties as they cannot provide a reading smaller than the resolution of their scales. The list of such instrumental uncertainties can be found in Table 27. An uncertainty analysis [91] is carried out to compute uncertainties in any derived quantity (α_f) as shown in Equation (63):

$$\alpha_f = \sqrt{\sum_{i=1}^{n}\left\{\left(\frac{\partial f}{\partial x_i}\right)^2 \alpha_{x_i}^2\right\}} \tag{63}$$

where, x_i includes $\dot{m}_a$, $\dot{m}_w$,T_a^{in}, T_a^{out}, T_w^{in}, T_w^{out}, dP_a and dP_w; and f_i includes Q_w, Q_a and R_{th}

6.1.1.6. Experimental Results

This section discusses the thermal and hydrodynamic performance of the iCMHXs from two test cases differentiated by their post-processing approaches.

Case 1: Same post-processing method

As described in Table 26, Unit 1, Unit 2, and Unit 3 share the same geometry and post-processing procedure of two layers of polyurethane sealant. The thermal and pressure-drop performances of these units are compared experimentally. Unit 1 is arbitrarily chosen as a reference. The experimental results of the reference unit are then also compared to a 2D CFD-based numerical study, the details of which are provided in length in Section 4.2.2.

First, the thermal performances of all the units are compared experimentally in terms of the thermal resistance, as shown in Figure 66. The units show almost comparable thermal performances and follow the inverse power law curve for the airflow rate. The thermal resistances of Units 2 and 3 lie within 4% from that of the reference unit, which is well within the uncertainty range of the reference unit. Furthermore, the experimental thermal performance of the reference unit is reported to be compared with its 2D CFD-based study in terms of heat transfer rate. It is observed to be well within 3%.

Second, the hydrodynamic performances of all units are compared experimentally in terms of airside pressure drops. Figure 68 (a) shows that the pressure drop curves for the airside and waterside increase with the increasing flow rate, following a parabolic trend. The figure also shows error bars on the reference unit representing

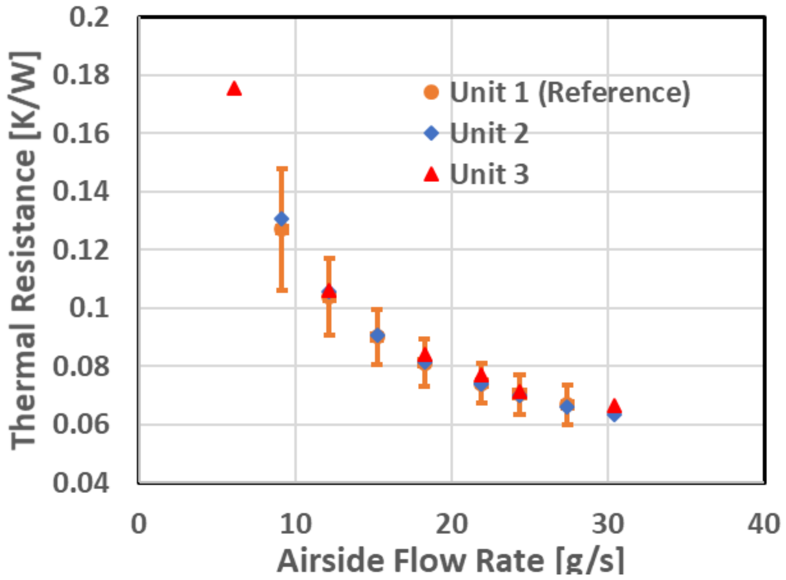

Figure 66: Comparison of thermal performance for the same fabricated units

corresponding uncertainty of 0.3 g/s in the airflow rate, 1.25 Pa in the air-side pressure drop, and 1.4 Pa in the waterside pressure drop. The minimum air-side and waterside impedance is observed for Unit 1, while the maximum is observed for Unit 3. From Figure 68 (a), the airside pressure drop of Unit 2 deviates from the reference unit by within 8.7-18%, while that of Unit 3 deviates from the reference unit by within 37-54%. Even though they share the same post-processing procedure, this high deviation of Unit 3 from the reference unit can be explained by undesirable coating residue left during improper removal of excess sealant during the air-drying process. For Unit 3, the residue is significantly higher than other units, resulting in air-side clogging (see Figure 68 (b)) and higher air-side impedance. Furthermore, the experimental airside hydrodynamic performance of the reference unit is reported to be compared with its CFD prediction in terms of pressure drop. It is observed to be well within 13%, as shown in Figure 68 (c).

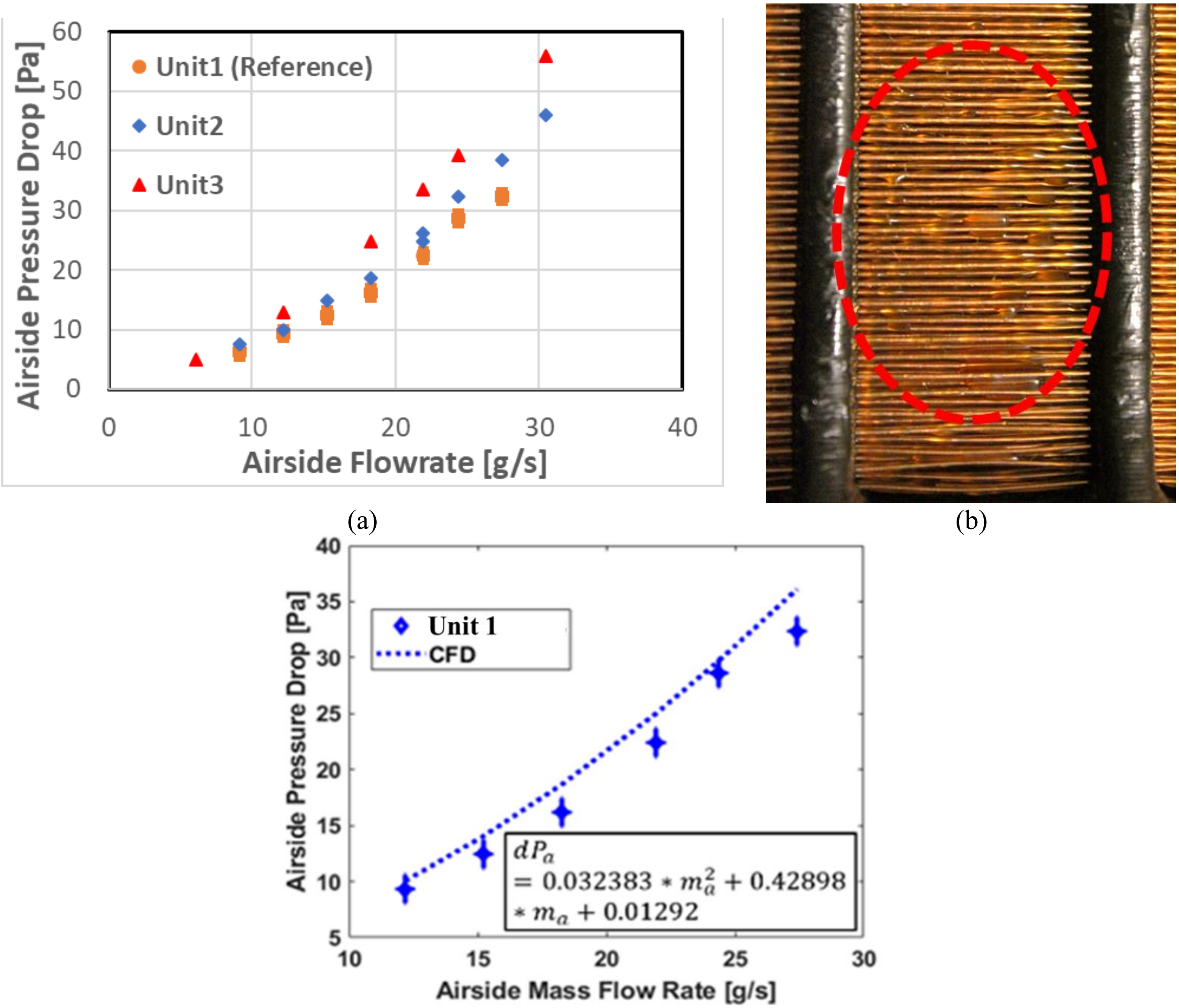

(a) (b)

(c)

Figure 67: (a) Comparison of air-side pressure drop performance for the same fabricated units, (b) clogging observed on the fins of Unit 3, exposed to the airside and (c) Comparison of air-side pressure drop with 2D based CFD study for Unit 1

However, the waterside pressure drop comparison amongst all units shows some differences. Unit 3 has the highest waterside flow impedance, deviating from the reference unit by 70-100%, while Unit 2 shows comparable impedance performance as the reference unit, well within 5.4%. The high deviation in the waterside impedance for Unit 3 can be due to significantly higher waterside clogging inside the water channels.

Clogging is more likely present on the waterside fins due to the dominant surface tension forces across the 2 mm-wide water channels. The narrow channels make removing the excess sealant during the air-drying process post-processing method difficult. Furthermore, the experimental waterside hydrodynamic performance of the reference unit is observed to outperform the CFD results by 53-67% (see Figure 68 (c)). These large deviations could be either due to inaccurate experimental results or could be due to inaccurate 2D CFD results.

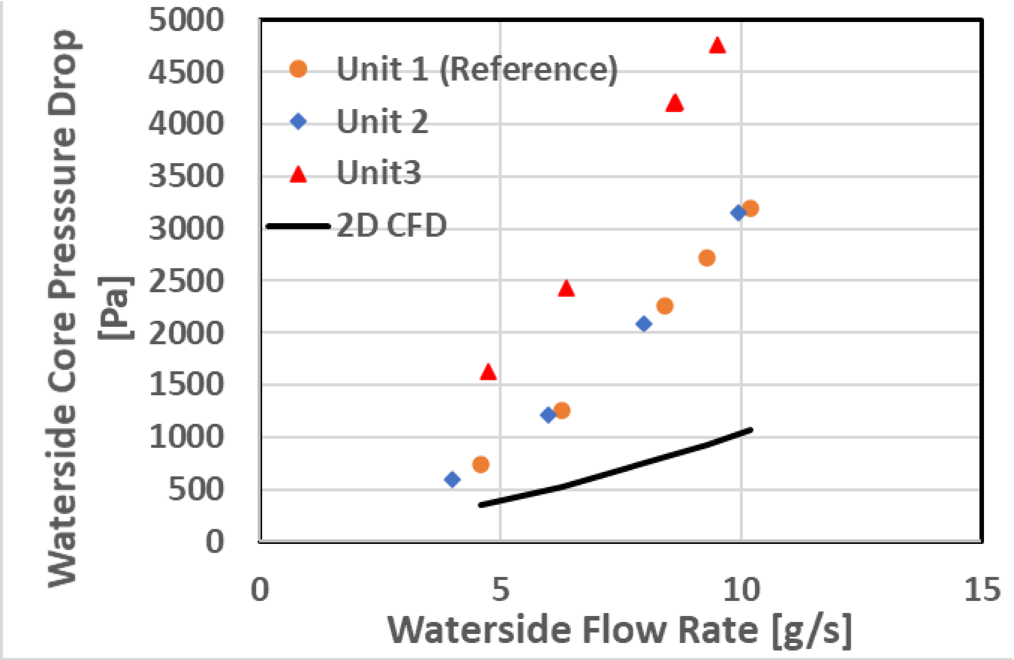

Figure 68: Comparison of waterside pressure-drop for the same fabricated units as well as with the 2D based CFD study

The experimental results could have included the effect of clogging, which can be investigated by studying the effect of different post-processing techniques. The first technique involves thinning the sealant. The second involves just applying a single layer of sealant on the iCMHX. The two iCMHX units, Unit 4 and Unit 5, are used in this case study.

All in all, however, an important point to note is the comparable thermal performance amongst all the units, which stands in stark contrast to the high pressure-drop deviation of Unit 3 from the rest of the units. This can be explained by the fact that pressure drop is more sensitive to the change in diameter than thermal resistance or due to the inaccurate 2D CFD-based study, which didn't capture the realistic effects of the iCMHX design.

Case 2: Different post-processing methods

Thinning Sealant Method:

In this method, clogging is predicted to be reduced by using a thinned sealant, which would lessen the thickness of the sealant layer and thus reduce clogging. The sealant is thinned by mixing polyurethane with acetone in a 2:1 ratio. This double-thinned sealed unit, Unit 4, is tested by passing water through its water channels. The effect on the waterside pressure drop to determine whether clogging is reduced is investigated by comparing it with the reference unit, as shown in Figure 69.

The waterside pressure-drop performance of Unit 4 is comparable with that of the reference unit to within 13%. This implies that the thinned coating also doesn't affect the pressure-drop performance of the waterside and thus doesn't reduce clogging as suspected from the deviations observed between the CFD and experimental results.

Effect of Single Layer of Coating

The effect on waterside pressure drop before and after internally sealing the unit is studied in this section. This is done by carrying out a different post-processing method

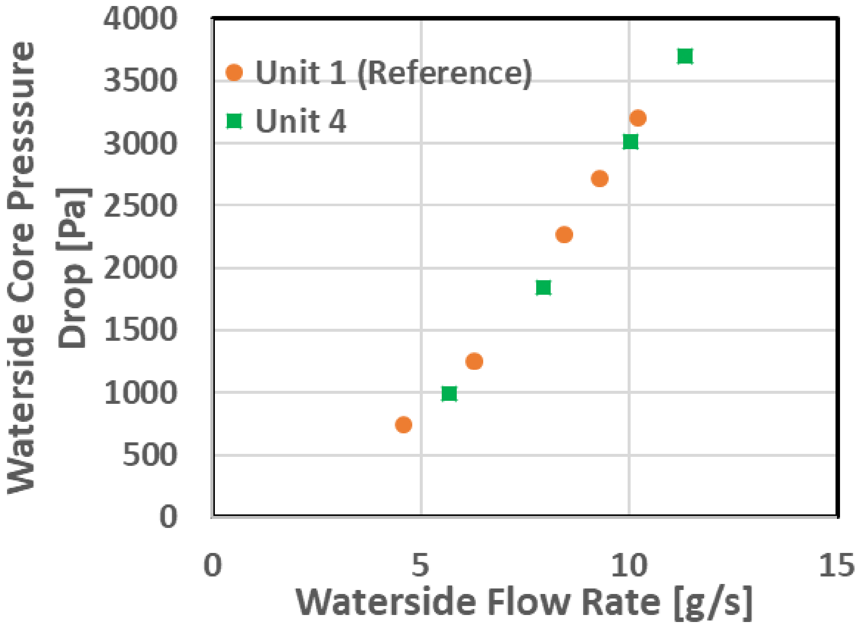

Figure 69: Comparison of waterside impedance with thinned sealant unit

on Unit 5. Since the pressure drop models (such as Euler number) are a function of Reynolds number for a given tube bank geometry [69], they should provide similar results for the same Reynolds number independent of the fluid type. Thus, the air is passed on the waterside channels with flow conditions of the same Reynolds number as one obtained by passing water on the waterside channels. Pressure drop measurements are then taken before and after applying the single sealant layer on the water channels. The two pressure drops are then compared. Figure 70 shows that the air impedance in the water channels before applying one layer of the sealant is comparable to that without applying any sealant inside the water channels, by within 11%. This suggests that the pressure drop isn't affected by the single-layer of sealant and thus doesn't help in resolving clogging if present. Thus, the disagreement between experimental and CFD results noted earlier for the same post-processing method could not be because of clogging.

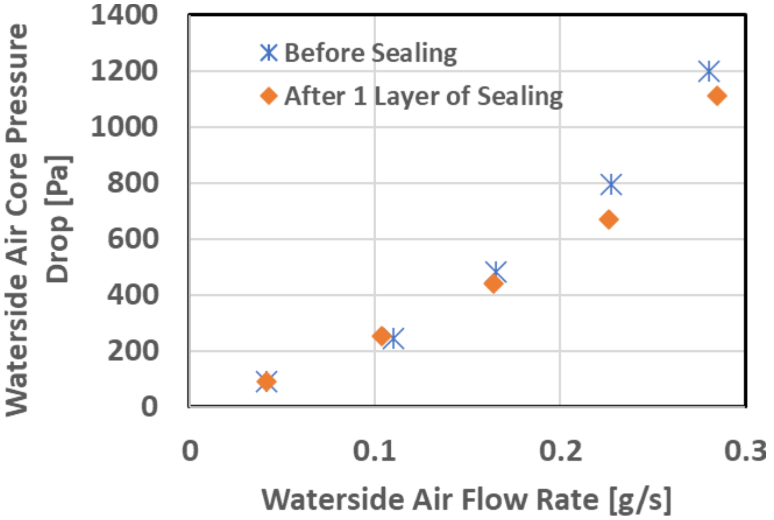

Figure 70: Comparison of air impedance on the waterside before and after sealing of Unit 4

6.1.2. Testing 2: Improving experimental and numerical approach

6.1.2.1. Experimental Setup

The schematic and image of the test setup consist of two loops: the air-side loop and the water-side loop, as shown in Figure 71. It is different from the traditional approach as it includes an additional air pre-cooler, leading to higher approach temperature and thus reduced temperature-induced uncertainties. Moreover, it also includes multiple temperature measurement points, which further reduces temperature uncertainties.

The air side is an open-loop consisting of a blower, air pre-chiller, pre-cooler, rotameter, and static mixer. The loop starts with the blower that drives the room air inside a foam-insulated duct system. The airflow rate inside the duct is varied manually using a variable frequency drive connected to the blower. The room air then flows past the pre-cooler, which first cools the air coming from the blower to control and reduce the air-side inlet temperature. The pre-cooled air moves across the rotameter, which measures the air flow rate. The air flows through the duct until it reaches a static mixer, placed right before the test section, to provide a uniform temperature distribution entering the iCMHX. The air then passes through the test section and exhausts in an open-loop to the room.

Air-side temperatures and pressure drops across the HX are measured by thermocouples and analog pressure gauges, respectively. The temperatures of the inlet and outlet air are measured by a group of 10 thermocouples, of which each pair of parallel thermocouples is used as one thermopile. Together, the ten thermocouples are arranged in a 10-point mesh structure, placed at the inlet of the test section. The parallel thermocouples reduce temperature uncertainties due to averaged temperature readings over ten thermocouples compared to an individual reading [92]. Similarly, the outlet air temperature is measured using another ten thermocouples with a similar thermopile combination arranged in another 10-point mesh, placed at the outlet of the test section. The temperature grid is placed at locations containing well-mixed airflow for maximum uniformity in temperature. Air-side pressure-drop is measured by an analog pressure gauge, which takes differential readings between the inlet and outlet of the HX. The pressure reading at both the inlet and outlet is area-averaged via four pressure ports, each located at the inlet and outlet of the iCMHX.

The liquid side is a closed loop that includes a chiller, pump, and Coriolis-flowmeter. The loop starts with a chiller that regulates the inlet water temperature. The hot water flows via flexible plastic tubes across a pump controlled by a user-input voltage defined in LABVIEW. The water flows through the Coriolis-flowmeter, which measures the liquid-side flowrate before passing through the HX inlet. Subsequently, cold water

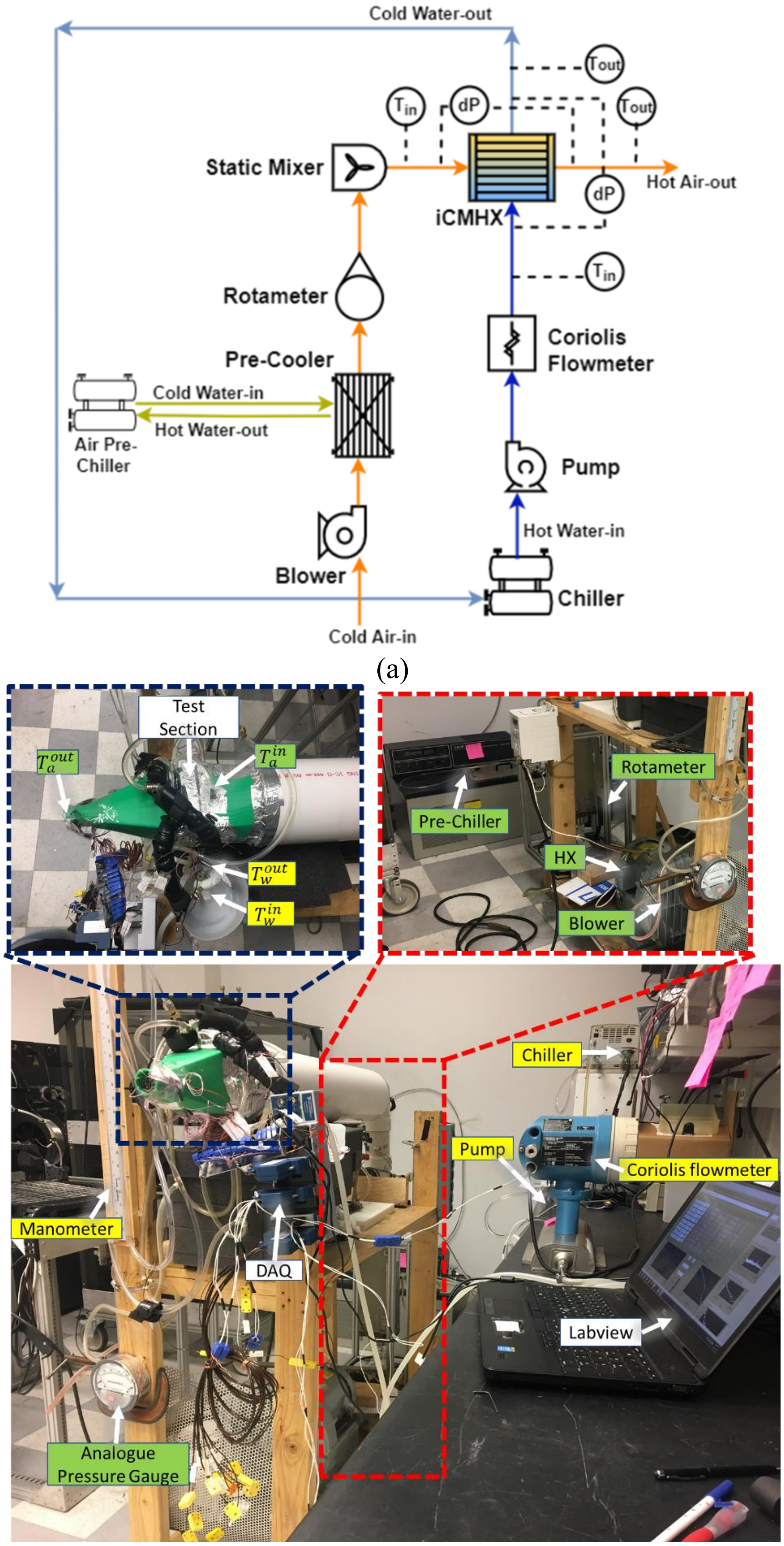

(a)

(b)

Figure 71: Experimental test loop (a) schematic (a) apparatus picture

exits via the HX outlet and flows into the sink of the chiller. The water then continues to run in the closed-loop cycle.

Similarly, the water-side temperatures and pressure drop across the HX are measured by thermocouples and a manometer, respectively. The water temperature of the inlet HX is measured by a group of five thermocouples, of which parallel combinations of two and three thermocouples are used as two separate thermopiles. Similarly, the outlet temperature is measured using another five thermocouples.

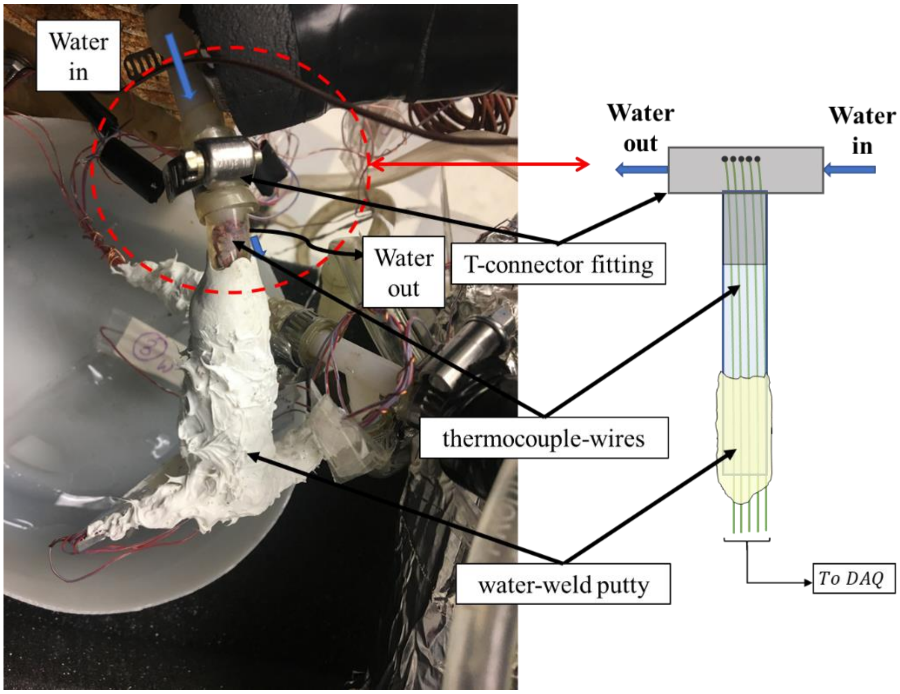

Figure 72: Sealed thermocouples in water tubes

6.1.2.2. Instrumentation and Calibration

The instruments used in the test setup are calibrated as listed in Table 28.

Table 28: Technical specifications of measuring instruments

Fluid	Equipment	Specifications	Uncertainty (±)
Water side	Chiller	ThermoNESLAB RTE 7 (R134A) 800 W heater -25°C to 150°C	NA
	Pump	Micropump I-Drive (Type 76003) 0 to 12.33 g/s	NA

	Coriolis Flowmeter	Endress+Hauser Promass 83 A Nominal Diameter: 1/12” 0 to 27.7 g/s	0.1% of measured value
	Manometer	0 to 17.85 kPa	50 Pa
	Parallel Thermopile	Omega T-type thermocouples -250℃ to 350℃	0.22℃
Air side	Blower	Baldor Industrial Motor – 3Phase (F198 series) 0 to 89 g/s	NA
	Pre-Chiller	Forma Scientific Model 2067 650 W heater -20℃ to 70℃	0.02℃
	Rotameter	Fischer & Porter (Model No. 10A4557S) 0 to 32 g/s	0.3 g/s
	Analogue Pressure Gauge	Magnehelic Dyer Instruments 0 to 64 Pa	1.25 Pa
	Thermopile Parallel	Omega T-type thermocouples -250℃ to 350℃	0.16℃

The test setup is built for operating conditions similar to a CPU radiator's in liquid cooling applications, as shown in Table 29. The air-side testing includes variable airflow rate ($\dot{m}_a$) with a specified range and a constant water flow rate ($\dot{m}_w$) kept to its maximum value. Similarly, the water-side testing includes variable water flow rates with a specified range and a constant airflow rate. A LABVIEW program connected to a DAQ recorded the testing data.

Table 29: Operating conditions for the experiment

	iCMHX		**Conventional Unit**	
	Temperature Conditions			
$\mathbf{T_a^{in}}$[°C]	12.8 - 16.6		12.5 - 15.4	
$\mathbf{T_w^{in}}$[°C]	42.4 - 45.5		44 - 48	
	Flow Conditions			
	Air-side Test	**Water-side Test**	**Air-side Test**	**Water-side Test**
$\mathbf{\dot{m}_a}[g/s]$	10 - 30.8	21.9	12 - 29	29.2
$\mathbf{\dot{m}_w}[g/s]$	9.5	3.5 - 9.5	9.6	3.6 - 9.6

6.1.2.3. Data Reduction

It follows the same methodology as discussed in Section 6.1.1.4. To add to it, it also includes the total pumping work done on the fluids, which is computed from the measured Δp_a and $\Delta p_{measured}$values as shown below:

$$P_{pumping} = \frac{\dot{m}_a}{\rho_a}\Delta p_a + \frac{\dot{m}_w}{\rho_w}\Delta p_{measured} \quad (64)$$

6.1.2.4. Uncertainty Analysis

The uncertainty analysis uses the same methodology as discussed in Section 6.1.1.5. However, the calculated uncertainties have significantly reduced as expected, as shown in Table 30. Here, ΔT is defined as $\Delta \mathrm{T} = \mathrm{T}_{\mathrm{in}}^{\mathrm{w}} - \mathrm{T}_{\mathrm{in}}^{\mathrm{a}}$.

Table 30: Calculated Uncertainties for key pressure-drop and heat transfer parameters

Derived Quantities	Calculated Uncertainty (±)
$\boldsymbol{Q_w}$	1.8% - 3%
$\boldsymbol{Q_a}$	1.7% - 2.6%
$\boldsymbol{\frac{\Delta T}{Q}}$	1.1% - 2.2%
$\boldsymbol{P_{pumping}}$	3.3 - 12%

6.1.2.5. Experimental Results

The experimental results are now validated with the 3D-based numerical approach and compared with the 2D-based numerical work.

Water-side Testing Data Analysis

The water-side testing is based on the test data showing an energy balance of up to ±1.5%, much less than the previous experimental approach. The thermal performance is tested by varying water-side flowrate on a normalized thermal parameter, ΔT/Q, as shown in Figure 73. It is observed that as the flow rate increases, ΔT/Q decreases in an inverse power law form. This is because the increased flow rate increases the water-side heat transfer coefficient (h_w) or decreases the R_w. This further reduces the overall thermal resistance, which is proportional to ΔT/Q. About 168% increase in the water-side flowrate results in about 26% decrease in ΔT/Q. The experimental results are further validated with the current numerical approach, and a match well within 8% is observed. The current numerical approach is comparable to the past 2D CFD numerical work based on nominal design. It excludes the effects due to coating, wall-boundaries in x- and z- directions (see Figure 26), and dimensional changes due to printing variabilities. The combined effects of dimensional changes and wall-boundaries on the water-side parameters such as Nusselt number (Nu_w) are more significant than that on the air-side. The water-side dimensional changes such as reduced water-channel width (W_w)and reduced transverse fin-spacing-ratio on the water-side ($2S_L/D_h$), result in a net 20% higher v_{b_w} than nominal. This significantly increases the water-side Nusselt number as compared to the past numerical work and as typically observed in the literature [93]. The Nusselt number inside the channels increases further due to augmented flow and thermal field due to the wall-boundaries. Thus, considering all the net wall and dimensional effects, the water-side resistance (R_w) is expected to decrease or the heat transfer coefficient (h_w) is expected to increase significantly compared to the previous 2D numerical study. To compute the effective water-side resistance, the coating resistance is then included. This coating effect, however, greatly reduces the effective heat transfer coefficient on the water-side (h_{eff_w}) to half of the value obtained due to dimensional changes (h_w), because h_w is comparable to the coating heat transfer coefficient (h_{coat}) in magnitude (see Equation (30)). This leads to an effective increase in R_w by 18 to 23% as compared to the past numerical study. Similarly, the combined effects due to dimensional changes and wall-boundaries affect the air-side parameters to a lesser extent as the air-side dimensions don't deviate much from the nominal. Thus, considering all the net effects, the air-side thermal resistance (R_a) is also expected to decrease slightly. However, further inclusion of coating effect doesn't affect R_a as $h_{coat} >> h_a$. This leads to an effective decrease in R_a, as expected, to about 5-5.2% than nominal. The total resistance (R_{total}), which is majorly dominated by the air-side as R_a constitutes about 63-77% of the total resistance, is thus comparable to the past numerical study to within 0.4%.

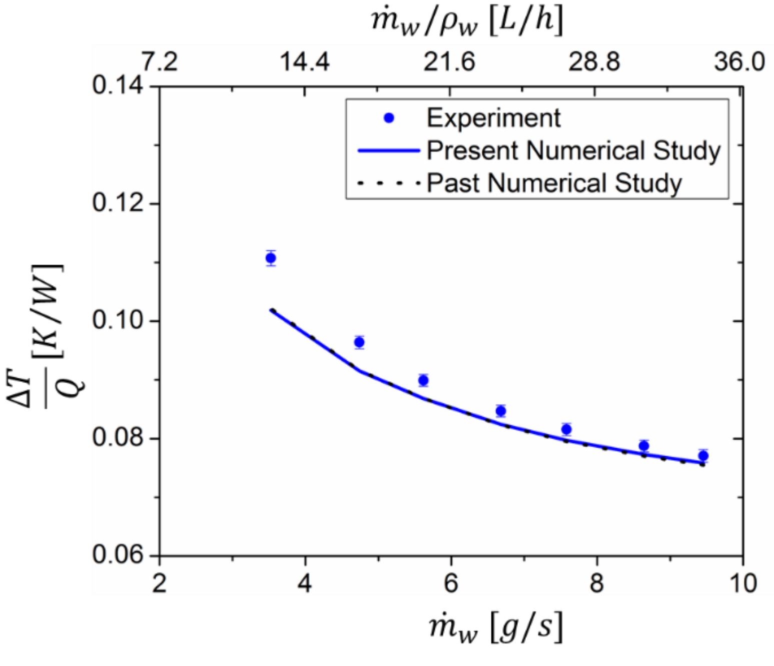

Figure 73: Comparison of experimental and numerical results of $\Delta T/Q$ for different $\dot{m}_w$

The hydrodynamic performance, Δp_wIs measured directly. However, the Δp_w includes the pressure drop from the connecting flexible plastic tubes, the integrated top-bottom liquid-side manifolds, and the HX core. Thus, Δp_w^{core} across the test section can be obtained by subtracting the extra pressure drop due to the tubes and manifolds from the measured Δp_w values, as mentioned in the previous 2D numerical study. The HX core pressure drop is observed to increase with the increasing flow rate in a quadratic manner, as shown in Figure 74.

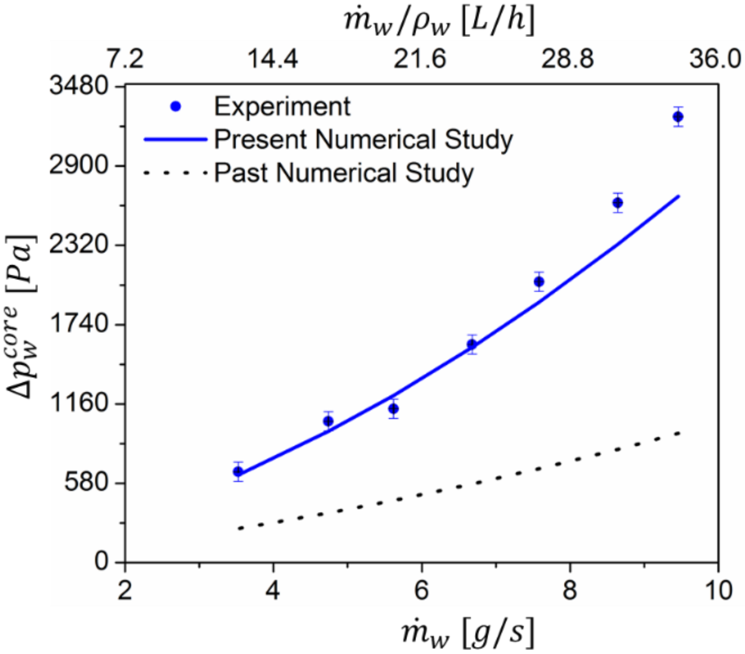

Figure 74: Comparison of experimental and numerical results of Δp_w^{core} for different $\dot{m}_w$

The present numerical study also matches the experimental results to within 17.8%. The deviation increases with an increase in water-side flowrate due to losses associated with v_w^2. The current numerical approach significantly outperforms the past numerical study, which includes the effects of wall-boundaries and water-side dimensional changes. As the dimensional changes result in 20% higher water velocity than the nominal, a higher pressure drop is expected, as observed in the literature [94]. To add to it, the squashed fin-shape on the water-side (see Figure 25 (a)) also leads to a higher pressure drop than nominal. Besides these dimensional changes, the wall-boundary effects in the x- and z-directions (see Figure 26 (b)) were not considered in the symmetric 2D CFD model of the past numerical study. Since there are a small number of $\mathrm{N_L}$ wires in the x-direction, the viscous effects of the boundary layer along the wall aren't quantified in the past numerical study. It is observed that along the x-direction a thick boundary layer is developed near the walls due to the small spacing between the wall and the nearest wires in the x direction, S. This causes the flow to choke around those wires (see Figure *75*), resulting in about 17% increase in Δp_w^{core}. To avoid choking of the flow, spacing should be increased (S') in the future. However, in practice, an optimal spacing should be selected, as large spacing can cause flow bypass. Similarly, due to narrow water channels, the wall-boundary effect in the z-direction alone leads to an almost 35% increase in Δp_w^{core} as compared to the past numerical study.

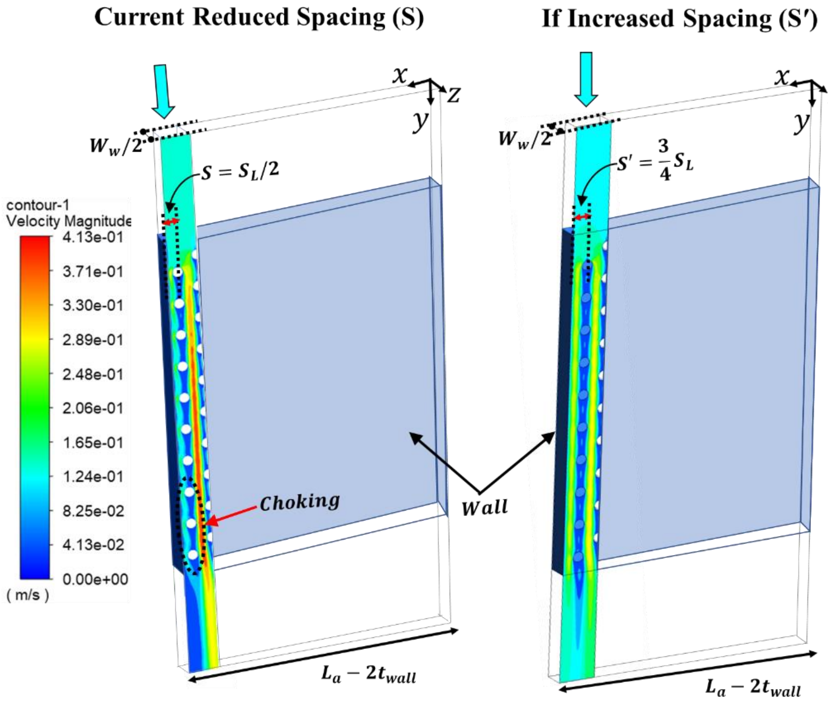

Figure 75: Choking effect around the nearest wires to the wall due to small spacing (S) (on left) and no-choking effect around those wires if S is increased (S') (on right) at some particular flow-rate

Air-side Testing Data Analysis

Similarly, the air-side testing data is based on the test data exhibiting an energy balance of within $\pm$ 2.3%. The thermal performance is studied by the effect of varying airflow rates on $\frac{\Delta T}{Q}$, as shown in *Figure 76*. As $\dot{m}_a$ increases, $\frac{\Delta T}{Q}$ also decreases in the inverse power law form due to decreasing R_a. About 153% increase in airflow rate results in about 35% decrease in $\frac{\Delta T}{Q}$. The testing results are compared with the present numerical model and match well within 4.16%. Compared with Figure 73, *Figure 76* gives a steeper slope, which confirms the earlier reasoning that the air-side is the limiting side due to $R_a \gg R_w$. These results are comparable with the past numerical study. This can be explained based on the cumulative effect in R_a due to coating, and dimensional changes, leading to comparable thermal performances, as discussed in the previous section.

Similarly, the hydrodynamic performance of the air side, Δp_a, is seen to increase with increasing airflow rates, approximately quadratically as shown in Figure 77, matching the trends observed in the literature [61] [95]. The air-side pressure drop also seems to match reasonably well with the present numerical study for low flow-rate points. However, for higher flow-rate points, the numerical predictions slightly overpredict the experimental results to within 11.7%, which could be due to the amplified losses associated with v_a^2 for the higher flow-rates. The present model also deviates from the past numerical study, which could be due mainly to the dimensional changes such as 4.5% contraction in ellipsoidal shape on the air-side as compared to that of the nominal circular shape (see Figure 25 (a)) considered in the past study. This leads to smaller wake regions, resulting in reduced pressure drop [69], as compared to the past numerical study of 2D CFD.

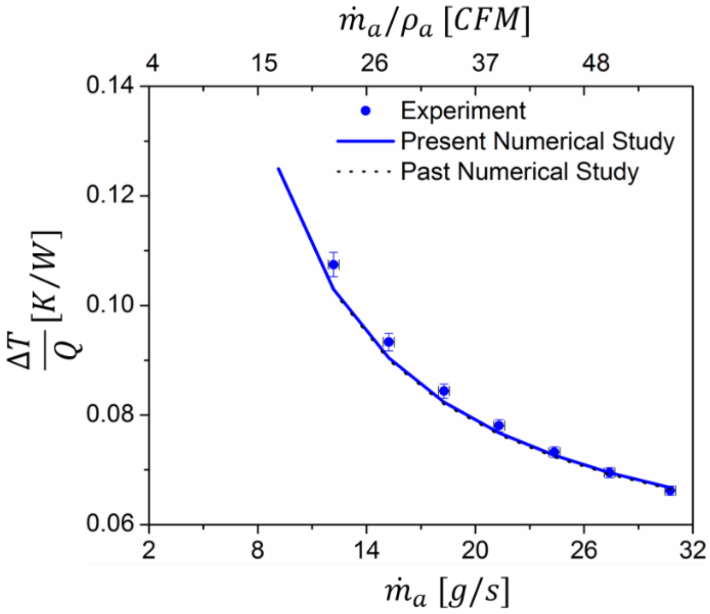

Figure 76: Comparison of experimental and numerical results of $\Delta T/Q$ for different $\dot{m}_a$

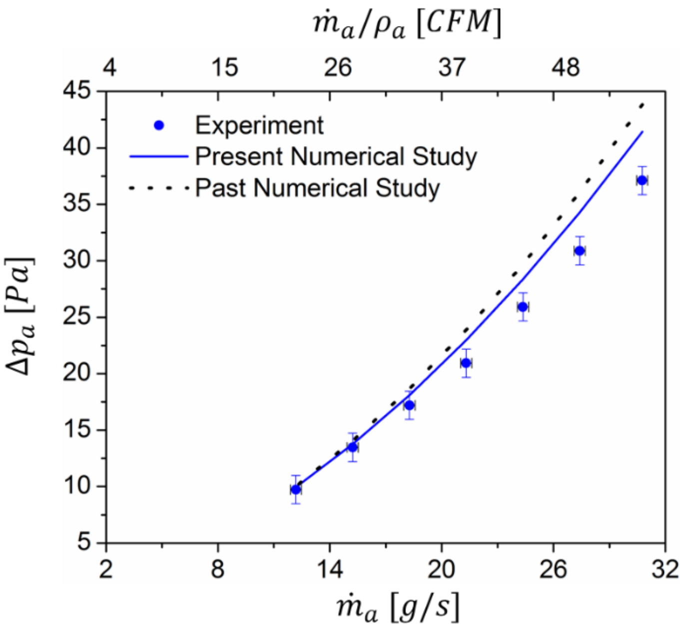

Figure 77: Comparison of experimental and numerical results of Δp_a for different $\dot{m}_a$

Comparison to a high-performance, commercially available CPU cooler radiator

The iCMHX performance was compared with a conventional, high-performance metallic CPU radiator for low temperature and pressure applications. The conventional, commercially available unit was experimentally tested in the same test setup and similar testing conditions as the iCMHX (see Table 29). The thermal and hydrodynamic performances of the two HXs were compared. The thermal performance is characterized by $\frac{\Delta T}{Q}$, while the hydrodynamic performance is characterized by the total pumping power, $P_{pumping}$. Since the pumping power is dominated mainly by the air side due to its high volumetric flow rate compared to the water flow rate, the air-side test data were used to compare the HX performances. As shown in Figure 78, the iCMHX delivers performance comparable to the conventional unit to within 10%, where the $\pm 10\%$ lines are drawn with reference to the conventional unit.

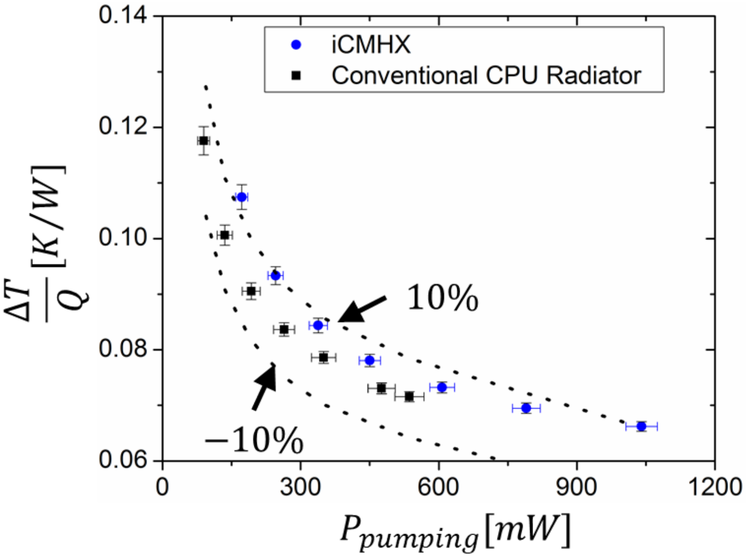

Figure 78: Comparison of experimental $\Delta T/Q$ for different pumping powers $P_{pumping}$ for both iCMHX and conventional CPU radiator

The iCMHX offers unique design advantages over conventional HX designs for comparable thermal and hydrodynamic performance. The robust additive manufacturing technique enables customized and complex yet reliable design solutions, such as the cross-media design introduced here, to offset the penalty introduced due to the low conductivity of the polymer. For example, given that the air side of the HX is the limiting side, the iCMHXs can be designed with increased air-side heat transfer area, possibly through optimal and controlled squashing of the fins into ellipsoidal and flat-ribbon shapes. These ribbon-shaped fins might, however, further increase the water-side pressure drop. This water-side impedance can be mitigated by designing the iCMHX in a counter-flow configuration instead, increasing the thermal performance over that of the present crossflow configuration. This could be done by changing the water flow direction via modified water inlet channels.

The digital design and manufacture of the iCMHX will inherently reduce costs and speed its manufacture. Added to this is the additional advantage of printing on-site/on-demand, generating additional savings in transportation and packaging costs.

6.2. Latent Energy Storage

This section was done in collaboration. Veeresh Ayagari, another Ph.D. student at the AHXPI laboratory, did the experimental testing. Additional details of these experiments can be found in the reference mentioned in Section 7.3. The experimental results were used for validation of 1D ROM.

6.2.1. Experimental Set-up

The experimental set-up is built, as shown in Figure 79. The PCM used is n-hexadecane for preliminary studies. It is an open loop on the airside with a blower to drive the airflow. The airflow rate in the loop is controlled by a variable frequency drive (VFD) connected to the blower. Two air coolers connected to two separate chillers condition the temperature of the air at the inlet of the CMTES. A Coriolis flowmeter is placed between the air coolers in the loop to measure the mass flow rate of the air. A 1.5 m long insulated square duct with a cross-section of 254 mm × 254 mm was placed before the CMTES to ensure uniform air distribution at the inlet. T-type thermocouples were placed at the inlet and exit of the CMTES to log the temperature of the air. An analog differential pressure gauge is placed across the CMTES to measure the pressure difference. The exit of the air-side is connected to the building ventilation system. A summary of the equipment used in the test section is shown in *Table 31*. National Instrument’s DAQ module was utilized to collect air's temperature mass flow rate values and was collected at a time interval of 10 seconds.

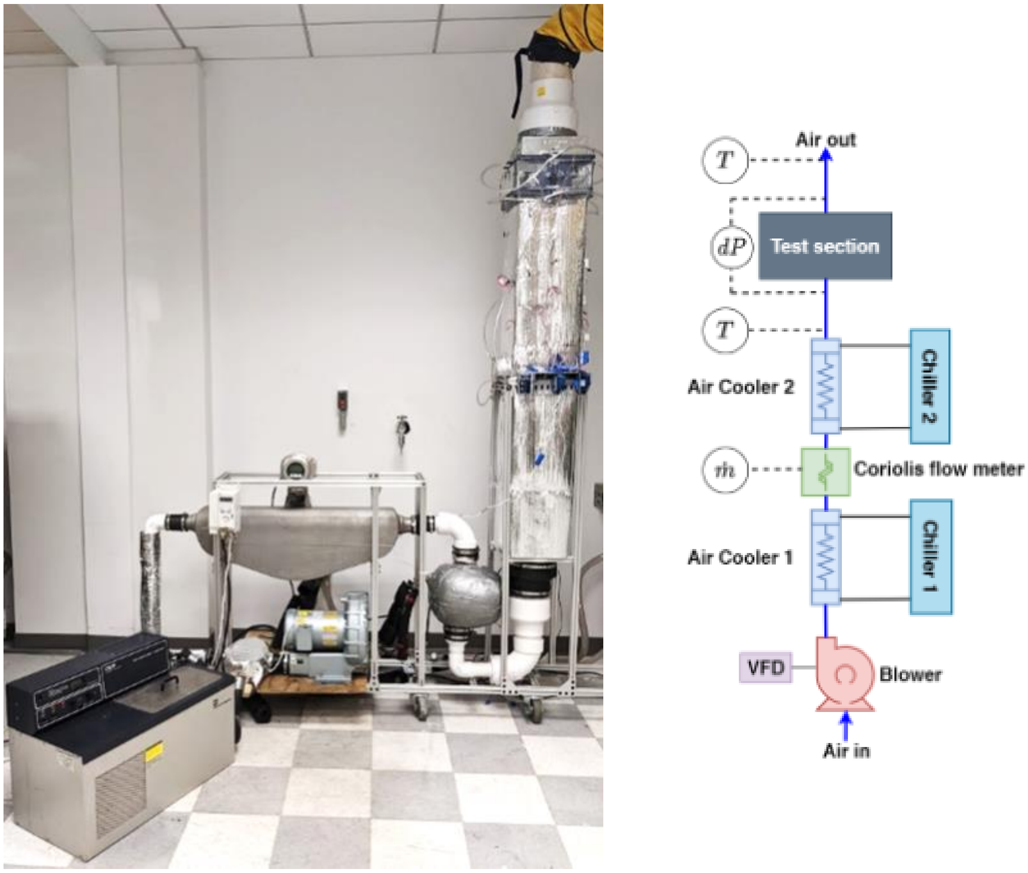

(a) (b)

Figure 79: Experimental setup for testing PCM-to-air TES unit at AHXPI laboratory (a) image (b) schematic

6.2.2. Instrumentation and Calibration

The list of instruments and their uncertainties used for this experiment can be found in Table 31.

Table 31: List of instruments and their uncertainties

Measured quantity	Instrument	Uncertainty
Mass flow rate	Endress+Hauser Promass 83 Coriolis flowmeter	± 5%
Temperature	T-type thermocouple	± 0.5 °C
Pressure drop	Differential pressure gauge	± 1.27 Pa

The experiments are carried out at 40 g/s mass flow rate of air, charging at 11 °C and discharging at 11 °C, as shown in *Table 32*.

Table 32: Operating conditions

Condition	Mass flow	Charging temp.	Discharge temp.
1	40 g/s	11	29

6.2.3. Data Reduction

The data reduction follows the same approach as discussed in the previous experiments for sensible cooling. The critical parameters of interest are: Δp_a, Q_a and charging and discharging times. All of these are either directly measured or can be computed from previous experimental studies on sensible cooling applications.

6.2.4. Experimental Results and Comparison with Numerical Study

The temperature trend at the inlet and outlet of the CMTES during the duration of the experiment is shown in *Figure 80* (a). Heat transfer rate is plotted on the secondary axis of the graphs which denotes different regimes of charging-discharging processes.

As seen from *Figure 80* (a), the entire duration of the experiment is divided into seven regimes. Regime I is the initial state of the experiment, where the entire PCM is in thermal equilibrium with the ambient. Since the ambient temperature is higher than the T_{PCM} of the PCM, the PCM inside CMTES is in a liquid state. Regime-II starts when the blower is turned ON. In Regime-II, the air flows through the air coolers and the temperature at the inlet of the CMTES drops rapidly below the T_{PCM}. This rapid cooling starts the sensible cooling of liquid phase PCM. As the inlet air temperature drops rapidly, the heat transfer from PCM to air increases momentarily, and as the liquid-state PCM starts to cool, the heat transfer rate starts to drop slowly. Phase-2 ends when Q reaches an inflection point, after which the heat transfer rate increases. This inflection in heat transfer rate is indicative of the start of the PCM crystallization, an exothermic process. Since the sensible energy is lower when compared to latent energy, phase-2 is usually very short, in order of minutes for the current design of CMTES.

In phase-3, as the inlet air temperature is below the T_{melt}, the liquid phase PCM continues to crystallize while dissipating the heat of crystallization, which increases the temperature at the outlet of the CMTES. The heat transfer rate peaks and starts to drop as more PCM crystallizes. When most of the PCM is crystallized, the PCM starts to sub-cool. The heat transfer rate is very low due to dominant sensible cooling. If the experiment is continued for long enough, the PCM will attain thermal equilibrium with the inlet temperature. For this study, it is not required to achieve thermal equilibrium as sensible energy storage is significantly lower than latent ($Ste < 0.1$). In this study, a 1°C temperature difference between inlet and outlet air is chosen as the criteria for the end of phase-3. The duration of phase-3 is defined as charging time, τ_c. In phase-4, the PCM continues to cool down sensibly. Phase-4 ends when the chillers are turned off, which halts the charging process.

In phase-5, the inlet air temperature starts to increase due to motor heat, and solid-state PCM starts to heat up to T_{melt}. In phase-6, the PCM starts to absorb the energy from inlet air to change its phase from solid to liquid, which starts when the inlet air temperature is above T_{melt}. In phase-6, the outlet air temperature is regulated, which leads to energy savings in downstream equipment. Like phase-3, the heat transfer rate in phase-6 reaches a maximum and decreases as PCM liquifies. The criteria for the end of phase-6 is when a 1°C temperature difference between inlet and outlet air is attained. The duration of phase-6 is defined as discharge-time τ_d. In phase-7, the heat transfer rate is not significant, and sensible cooling is the dominant form of energy storage. The PCM is in a liquid state, and if the airflow is kept ON long enough, PCM will attain thermal equilibrium where no heat transfer occurs. The discharge process halts when the airflow is turned off.

As the airflow rate remains constant during the charging and discharging process for each condition, the pressure drop remains constant. It is noted manually from the differential pressure gauge for each condition.

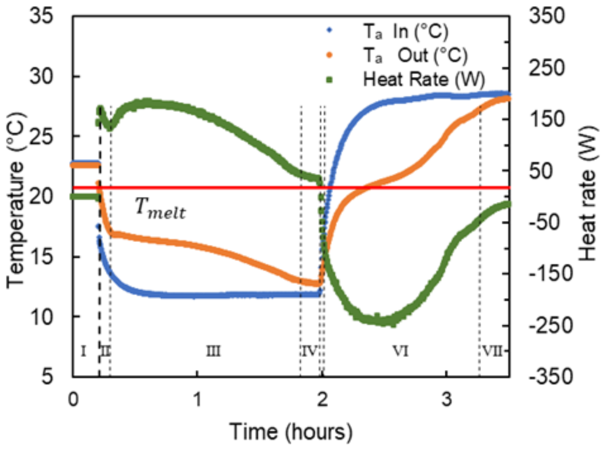

(a)

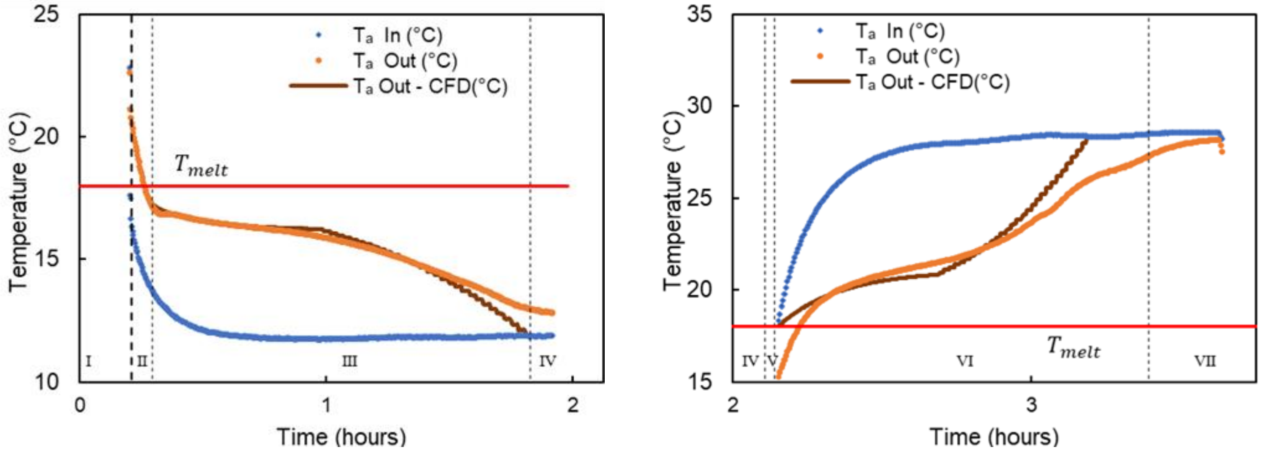

(b) (c)

Figure 80: (a) Experimentally obtained temperature and heat transfer rate trends covering I-VII regimes; and Comparison of experimental temperature trend with 1D ROM for (a) Regime I-IV and (c) Regime V-VII

Comparing the experimental results with 1D ROM, Regimes 3 and 6 are the longest in the energy storage process where LHTES is dominant and modeled numerically. For numerical calculation of τ_c and τ_d, the numerical model takes the inlet air temperature profile, timestamps, and mass flow rate of air for regimes 3 and 6 respectively as the inputs, and predicts outlet air temperature, melt fraction of PCM, and pressure drop across the CMTES at provided timestamps. The initial temperature of the bulk of the PCM for both charging and discharging processes for the numerical model is T_{PCM}. The bulk of the PCM is initially in a liquid state for the charging process, that is, 100% melt fraction. τ_c is calculated as the time required for PCM to change from 100% melt fraction to 0%. Similarly, for discharging process, the bulk of the PCM is in a solid state, that is, 0% melt fraction. τ_d is calculated as the time required for PCM to change from 0% melt fraction to 100%. *Figure 80* shows the comparison of outlet temperature obtained experimentally and numerically. According to the numerical model, the energy storage process halts when no other phase change can happen and does not consider sensible heat storage. So, charging or discharge concluded when the outlet air temperature reached the inlet. Accordingly, τ_c and τ_d are calculated graphically from *Figure 80* (a) and provided in *Table 33*. The experimental data matches with the numerical study to maximum deviation is within 17%.

Table 33: Comparison of key parameters between experimental and numerical study

Key Parameters	Experimental	Numerical	%Deviation
τ_c (minutes)	88	81	8
τ_d(minutes)	72	60	17
dP_a (Pa)	10.1	10.7	6

It is thus observed that the current design provides Q/m of 0.15 MJ/kg and Q/V of 83 MJ/m^3.

6.3. Summary

An experimental study was carried out for sensible and latent cooling applications for the HX concept studied in this thesis. The sensible cooling application focused on an air-to-water iCMHX used for liquid cooling of CPUs. It was done in two different approaches. The first approach uses the traditional method of experiments, which involves a detailed case study on a set of 5 iCMHX units. The effect of their coating on iCMHX performance is studied, along with a comparison against the traditional 2D CFD-based numerical work. When applied correctly and with a thin enough coating thickness (~ 20 microns), the coating effect on the heat transfer rate seems to be negligible for all of the 5 units studied and also matches with the 2D CFD based numerical study to within 3% and airside pressure-drop to within 13%.

Similarly, it also doesn’t affect the liquid-side pressure drop as its within 5.4%. However, a huge deviation of about 53-67% in waterside pressure-drop between experimental and 2D CFD numerical study is observed. Initially, it was speculated that such a large deviation was due to clogging in the liquid channels as the less than mature additive manufacturing's side effects. However, upon further investigation, the deviations should be primarily caused due to inaccurate prediction of the 2D CFD-based study.

Thus, a second and more accurate testing approach was carried out, which had more reduced uncertainties and results than the more accurate 3D CFD modeling approach. It was found that the fin shapes were ellipsoidal instead of the designed nominal circular geometry and that this was due to the 9% squashing on the water-side channels during the 3D printing process. The experimental thermal performance validation correlates well with the high-fidelity 3D CFD numerical model within 8%. The air-side pressure drop validates well with the numerical model, reaching 11.7%. The corresponding water-side pressure drop correlates with the numerical model within 18%. This represents significantly reduced deviations between model and experiments compared to the previous 2D CFD approach. Lastly, the comparison of iCMHX performance with a conventional metallic-based CPU cooler suggests excellent promise in the digital 3D fabrication of next-generation polymer composite heat exchangers, utilizing the digital twin of design optimization and additive manufacturing. These HXs offer essential advantages, such as lower cost, customized design and fabrication, on-demand and on-site printing of the HX, and the ability to introduce complex, yet more reliable, design solutions that offset the low conductivity of polymers.

Similarly, the experimental results for latent storage applications were analyzed and showed the TES could store 0.75 MJ of latent energy and a COP of 265. It was fabricated using low-cost materials, ABS and Aluminum, and charged with off-the-shelf organic PCM, n-hexadecane without any additives for performance enhancement, making the design cost-effective. The comparison of experimental results with the numerical model for melting time for complete PCM was within 17%, while the freezing time was within 8%, which suggests they agree with the numerical ROM.

Chapter 7: Conclusion and Proposed Future Work

7.1. Conclusion

A novel, additively-manufactured metal-polymer composite integrated cross-media heat exchanger (iCMHX) was studied numerically and experimentally. The HX is different from conventional HXs, as it includes enhanced heat transfer area on both airside and liquid side channels, which is generally absent in conventional HXs. Here, the continuous wire-fins of the HX are arranged in a tube-bank geometry, acting as fins on both air and liquid-side. The said wire-fins provide direct heat exchange between the hot and cold side fluids, independent of the low thermal conductivity of the polymer, thus reducing the overall thermal resistance of the HX. Additive manufacturing was a key enabling technology to realize the manufacturing of the iCMHX. This, in turn, demonstrated the excellent progress in the digital 3D fabrication of next-generation polymer composite heat exchangers, as these HXs offer essential advantages, such as lower cost, customized design and fabrication, on-demand and on-site printing of the HX, and the ability to introduce complex, yet more reliable, design solutions that offset the low conductivity of polymers. This study represents the first such detailed study performed for a cross-media-based HX. The HX was shown to be applicable for both sensible and latent thermal energy storage applications. The HX integrated with the PCM for latent storage applications is the TES unit or CMTES unit. The TES improves the effective thermal conductivity of the PCM-wire structure from 0.22 W/m-K to about 16W/m-K.

Since there are few correlations in the literature for a given tube-bank geometry and fin shape, the need for a CFD-based study arises. But the CFD modeling of the entire HX is computationally expensive. Thus, the dissertation developed robust segment-level CFD models that integrate the non-dimensionalized thermal and pressure-drop parameters to compute the entire HX performance. These CFD segment level models have been modified from 2D CFD to 3D CFD depending on the extent of printing variabilities on the HX. For the sensible cooling application of desktop computers, the dissertation numerically investigated the iCMHX performance using a robust and simplified 3D CFD and analytical-based model for CPU cooling application. This 3D CFD model is based on ellipsoidal fins in staggered tube banks ($S_T/D = 3.33$ and $S_L/D = 1.96$) for a laminar regime ($Re < 100$). The 3D fabrication variances from the actual design and their effect on heat transfer and pressure drops were discussed. It was found that the fin shapes were ellipsoidal instead of the designed nominal circular geometry and that this was due to the 9% squashing on the water-side channels during the 3D printing process. The experimental thermal performance validation correlates well with the numerical model, within 8% for the tested flow and operating conditions representing the selected CPU cooling application. The airside pressure drop validates well with the numerical model, reaching approximately 12%. The corresponding water-side pressure drop correlates with the numerical model within 18%. The two primary reasons for the higher pressure drop on the waterside are believed to be due to 1.7-mm narrow water channels and the small spacing between the water-side polymer walls and the adjacent wires in the x-direction. The validated numerical model is also used to obtain the optimized design of the iCMHX for different applications such as air-conditioning.

For the latent thermal energy storage applications, the literature offers limited analytical solutions for modeling the PCM wire-based design. Thus a CFD simulation was needed to compute the HX performance. But CFD, based simulations are computationally expensive considering the heat transfer problem in PCMs is transient. Thus, the dissertation presented a novel 1D ROM (reduced-order model) based on 1D radial conduction inside the PCM. The ROM analytically computes latent energy stored at the segment-level model and then integrates it with the entire TES, saving a lot of computational time. The 1D ROM was further validated with a reference 2D axisymmetric model, typically used in the literature, via commercial CFD tools such as Ansys Fluent. Some key non-dimensional parameters were identified based on time-constant (τ) and resistance ratios ($R_{wire}^{*}, Bi \cdot LR$). The 1D ROM was tested for a wide range of these parameters. It matched 10% for all ranges, except when the axial resistance in the wire embedded inside the PCM started to dominate such that there was axial conduction inside the PCM. Further, the 1D ROM was successfully used in optimizing TES units for peak-load building cooling (1.44 MJ) and pulsed-power cooling applications (19.2 kJ). The 1D ROM was validated with experimental testing for peak-load building cooling applications, and the melting times were within 17%. In comparison, the freezing times were within 8% when compared against experimental values.

Lastly, as part of ongoing work, a novel TES design was proposed, consisting of SMA wires instead of copper wires in the present TES design. This hybrid approach can increase the latent storage capacity for an estimated similar material cost and compactness. As per some preliminary studies for pulsed-power cooling applications, optimized NiTi-SMA hybrid TES outperformed the reference TES design that employs copper wires due to its high latent energy storage capacity. However, additional future work is required to build a modified 1D ROM accordingly.

7.2. Proposed Future Work

Since the present dissertation is based on numerical and experimental work, the proposed future work is also categorized based on numerical and experimental work.

7.2.1. Numerical Work

Several studies are needed to extend the present investigation, as discussed below:

For sensible cooling applications:

- Improve the current iCMHX design

The design improvements are suggested to improve the thermal and pressure drop performances. These improvements need to be analyzed for a particular problem statement and compared with the current design. The following three improvements are recommended:

1. Increase airside heat transfer area

The airside heat transfer area can be increased by changing the fin shape from circular to ellipsoidal to ribbon-shaped depending on more surface area/volume ratio.

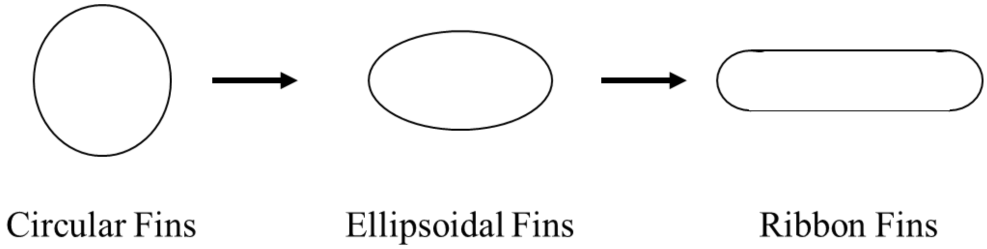

Figure 81: Different fin shapes depending on surface area/volume ratio

2. Remove waterside pressure-drop penalty

Since the previously suggested design improvement may also result in undesirable higher pressure drops, the suggested new design improvement eliminates the waterside penalty by changing the flow orientation from crossflow to counterflow. The pressure drop governed by the internal fluid path is greatly reduced in the counterflow orientation, as the flow is facilitated to flow across left to right direction (short hydraulic resistance path), as compared to the crossflow orientation, where the flow goes from top to bottom (longer hydraulic resistance path), as shown in *Figure 82*. However, the challenge in this design configuration is to facilitate uniform flow between the fins in the Z direction.

3. Reduce flow maldistribution

The above flow maldistribution issue is resolved by a third suggested design improvement, which focuses on changing the manifold area on the liquid side such as by tapering the manifolds or by shifting the ribbon-fins to ensure uniform flow distribution in between the fins along the Z direction, as shown in *Figure 83*. Further research is required to compare its performance with the present polymer HX design.

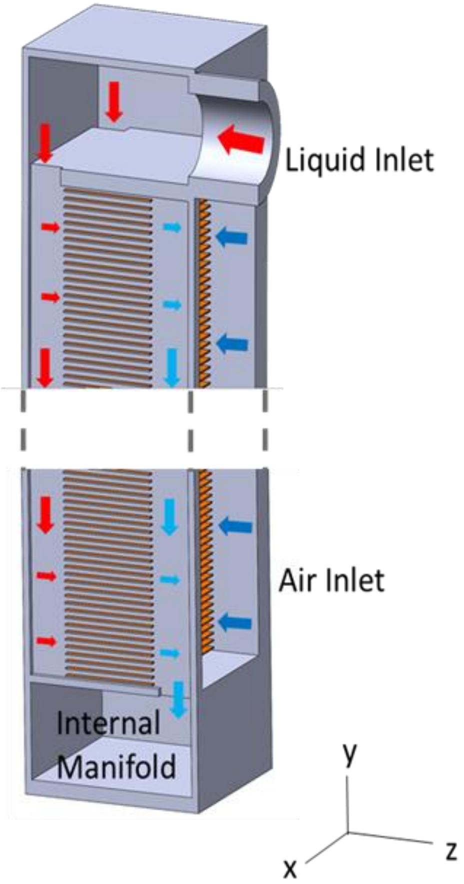

Figure 82: Internal fluid path inside the water channel in counterflow configuration for ribbon-shaped fins

- Developing more accurate CFD-based correlations for computing Eu and Nu numbers for circular and ellipsoidal-shaped tube banks for laminar and turbulent flow regimes.

Future work should involve the creation of a metamodel for developing Nu and Eu correlations for an extensive range of S_T/D, S_L/D and Re_D and Pr. The current metamodel used during design and optimization contains huge errors between the metamodel values and the actual CFD-run values for particular geometric and flow-ranges. This is because a mesh-independent and residual-independent approach was not implemented in the current dissertation, leading to 15-30% error. This has been circumvented in the present study by always performing CFD for the optimized design point to validate the accuracy of the metamodel.

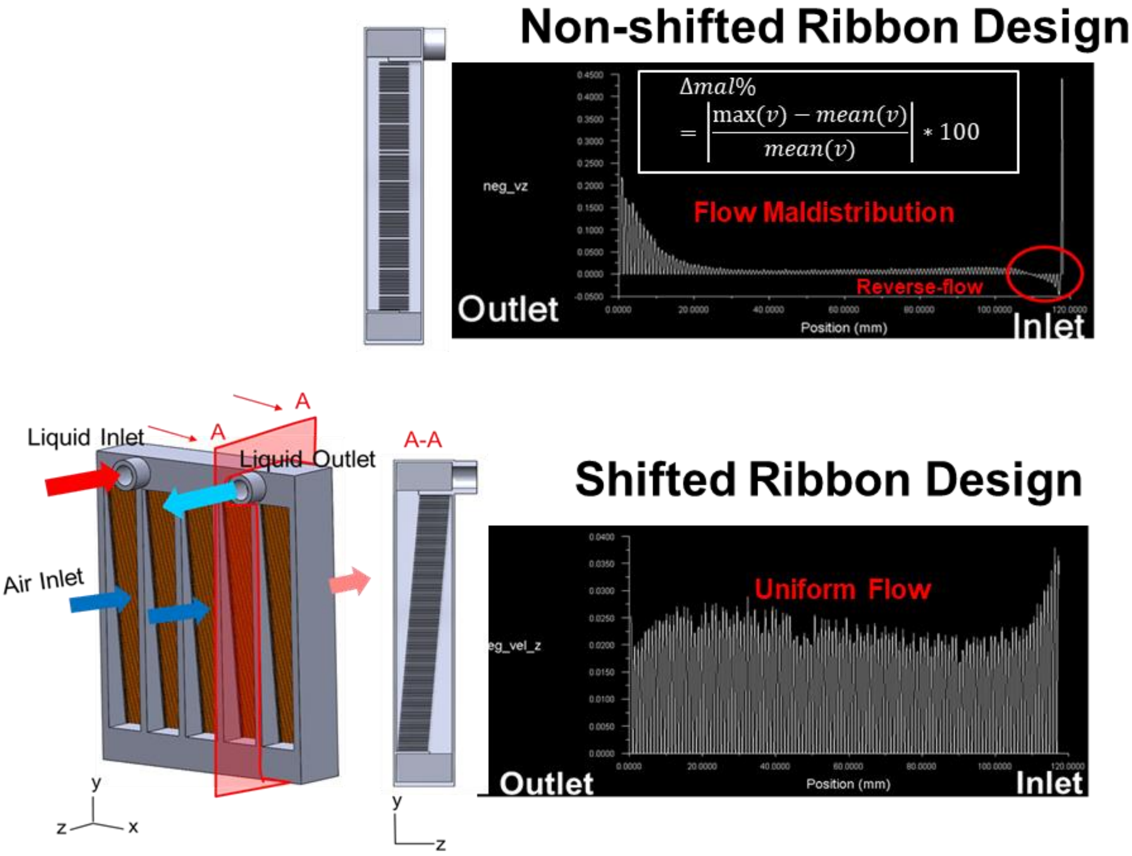

Figure 83: Shifted ribbon design facilitating uniform flow distribution

A MATLAB code has already been developed which implements the mesh and residual independence approach in the metamodel to obtain more accurate Eu and Nu values for diverse geometric and flow ranges. However, a database needs to be created. The methodology for this is further discussed below.

- Step-1: Run the MATLAB code for different Re and Pr and S_T/D and S_L/D values. The Fluent settings might be tuned to cover convergence issues during automation such as residual and monitor convergence.

- Step-2: Perform residual independence by lowering the continuity residual by an order of magnitude while keeping the other residual limits constant since continuity residual is difficult to converge.
- Step-3: Perform a mesh-independence study using the residual-independent values. This has been performed as discussed in Section 4.2.2.4.
- Step-4: Obtain the database containing mesh and residual independent values of Eu and Nu for all four variables (S_L/D, Re ,Pr, and configuration).
- Step-5: Create a metamodel by establishing a physics-based relation between Eu and Nu as a function of geometric parameters and Re and Pr. Machine learning algorithms can also be used, provided a physics-based correlation is obtained.

One of the typical plots generated from the MATLAB code is shown in *Figure 84*. Similarly, for ellipsoidal fins, a metamodel can be created to help understand the effect of fin elongation on the HX performance. Since fin-elongation is caused by the print head's precision in the wire-extrusion process, the print head should be tuned in future such that the user can control the eccentricity of the fin-shape. This would be particularly helpful if a metamodel exists to predict this behavior. At present, an algorithm has already been written in MATLAB which predicts fin-elongation for limited tube-bank spacing and flow parameters. A typical graph generated from MATLAB is shown in *Figure 85*. Here, % elongation in wire ($b = D_b/2$) with respect to the nominal radius of the circular wire ($D_h/2$) is defined as shown in the following equation:

$$\%\, b|_{elongation} = \frac{b|_{ellipsoidal} - D_h/2|_{circle}}{D_h/2|_{circle}} \times 100$$

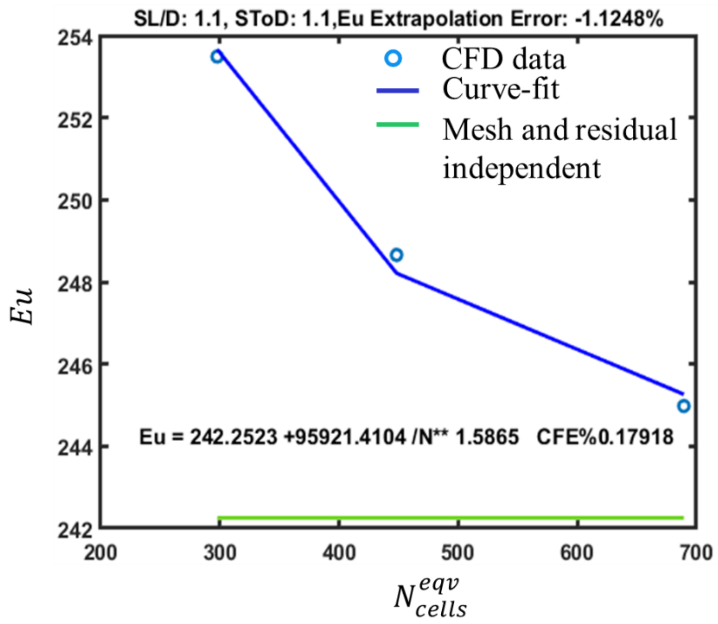

Figure 84: Typical curve-fit forms for metamodel-development generated from MATLAB code for staggered circular fins

The final step before using these circular and ellipsoidal fin-based correlations will be to perform an experimental validation study of the numerical predictions by 3D-printing samples of different tube-bank geometries and testing these different geometries.

For latent cooling applications:

- Modify the current TES design for fluid-to-PCM HX by considering solid-solid SMA as PCM and performing cost-analysis

The TES design can be further improved by increasing its latent storage capacity with the same degree of compactness as present currently. This can be done by developing a hybrid model which utilizes Cu SMAs instead of Cu wires. Thus, the latent storage capacity is increased due to the thermal mass of the PCM, such as salt-hydrate (SH) contained inside the polymer-based channels and due to thermal mas of the SMA wire. The Cu SMAs are a solid-solid type PCM that produces the least volume chang

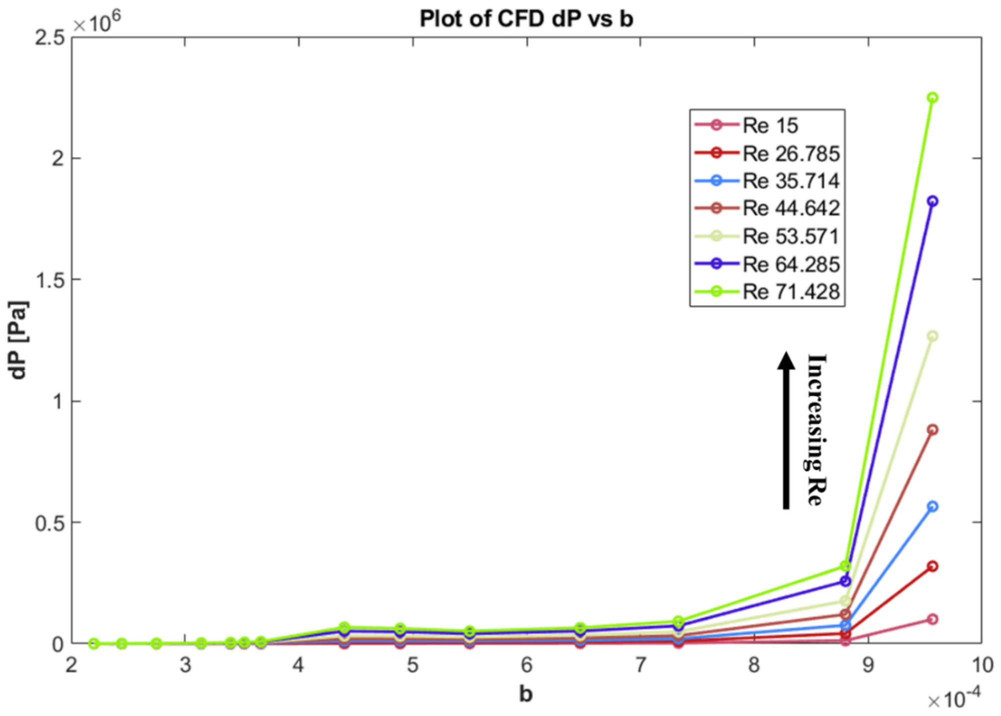

Figure 85: Effect of fin elongation (b) on fluid-side pressure-drop for different Re range

between the different phases. Research on printing Cu SMA wires and enhancing its thermo-physical properties is in progress in our group's laboratory.

Implementing this hybrid design idea, the 3D CFD-based segment level model is shown in *Figure 87* (a) for pulsed power cooling applications. The segment level model has been simulated in Ansys Fluent using its enthalpy-based PCM modeling approach. A typical contour plot for melting is shown in *Figure 87* (b), where the color red represents the melt-fraction of 1.

However, the SMAs have very low thermal conductivity than copper wire, resulting in higher axial resistance in the wire, leading to sensible conduction in the SH PCM. Thus, the amount of SH PCM and the SMA wire transitioned into another phase is underutilized since it would take much longer to melt the PCMs because of poor fin-efficiency completely. Since the thermal conductivity of the SMA wire is the main issue, for now, a straightforward optimization approach has been used by using the thermal conductivity of the SMA wires instead of copper wire. Implementing this simple approach and running 3D CFD cases on the segment level model yields the following results in *Figure 88* (a). Here, even though all the designs almost meet the target condition, the SH + Nitinol hybrid design performs the best, possibly due to the very high latent energy storage of Nitinol over Cu-SMAs. The issue of thermal conductivity is partially resolved via the simplified optimization approach; thus the lower thermal conductivity of Nitinol doesn't affect its performance. Furthermore, comparing the overall cost of the different designs is equally vital as the SMAs can be expensive to manufacture. A rough estimation of the material cost is shown in Figure 88 (b) based on a preliminary analysis. More detailed research should be conducted as SMAs are still very new.

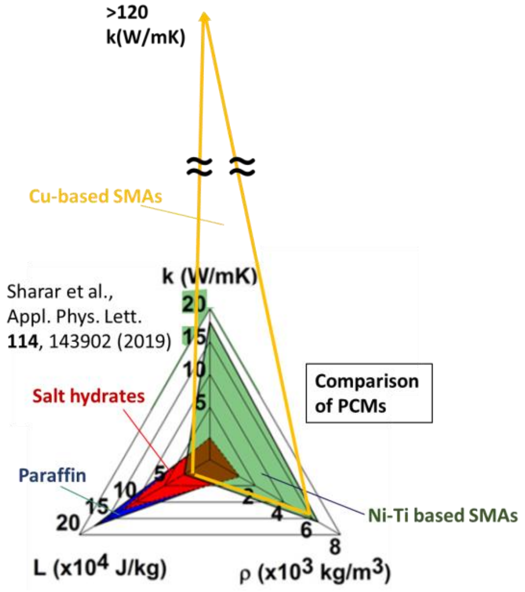

(a)

	Cu-SMA wire	NiTi- SMA wire
H[J/kg]	5700 [96]	24184 [97]
T_f[°C]	20°C*	
$\rho[kg/m^3]$	6451 [96]	6450 [97]
$Cp[J/kgK]$	420 [96]	837 [97]
$k[W/mK]$	120*	13.3 [97]

(b)

Figure 86: (a) Thermophysical properties for different PCMS: Cu SMAs, NiTi SMAs, Salt hydrates (Ongoing work by Dr. Ichiro Takeuchi) and (b) Estimation of properties of the SMAs as obtained from literature

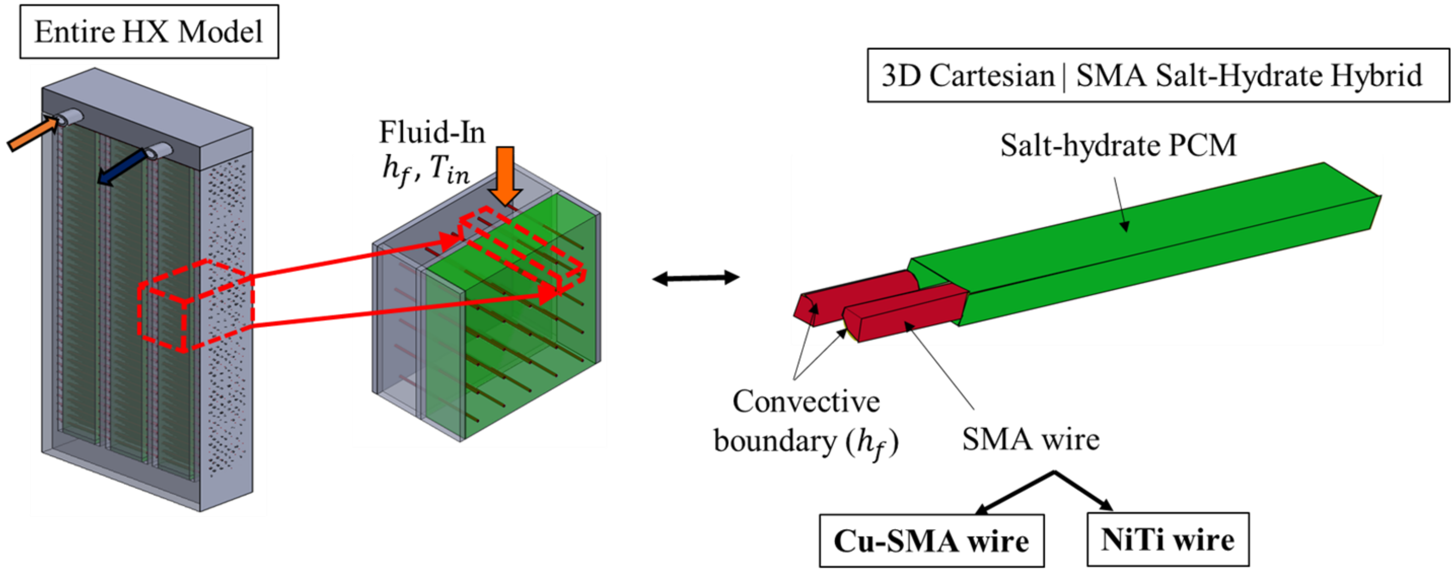

(a)

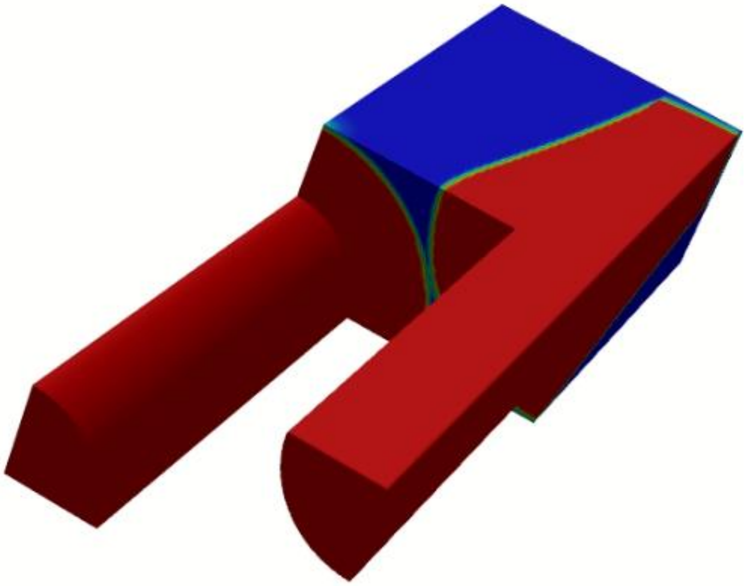

(b)

Figure 87: (a) Segment level model for hybrid SMA-SH design for TES and (b) Typical contour plot for melting of SMA-wire (NiTi) and SH (Glauber's salt) PCMs in the hybrid TES design, obtained in Ansys Fluent

But, a robust optimization technique is still required that takes account of both the thermal conductivity and the latent heat storage of the SMA wires. This creates a need to modify the present 1D ROM and avoid running 3D CFD to save computational cost.

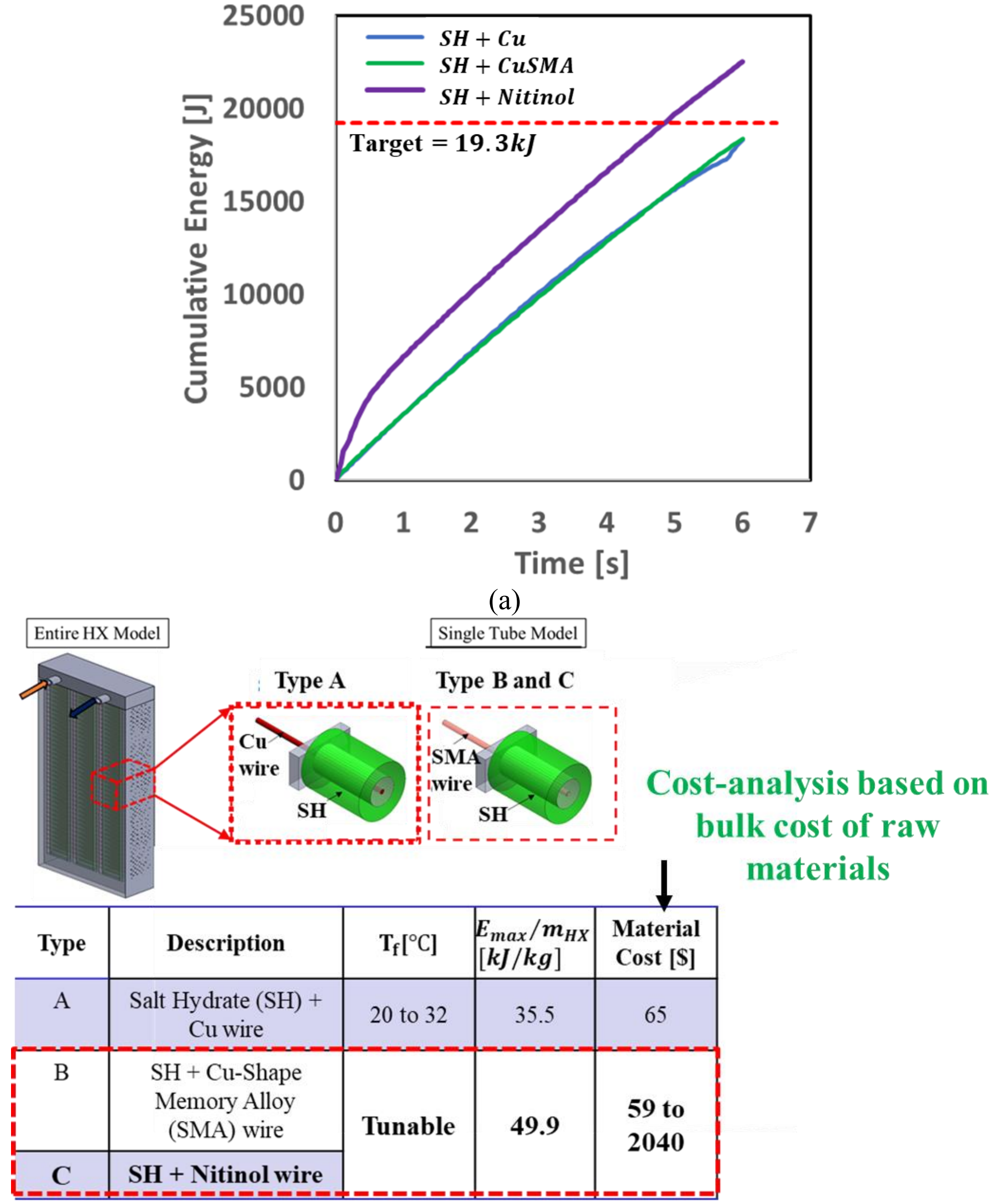

(a)

Type	Description	T_f[°C]	E_{max}/m_{HX} $[kJ/kg]$	Material Cost [$]
A	Salt Hydrate (SH) + Cu wire	20 to 32	35.5	65
B	SH + Cu-Shape Memory Alloy (SMA) wire	**Tunable**	**49.9**	**59 to 2040**
C	**SH + Nitinol wire**			

(b)

Figure 88: Comparison of different hybrid models (SH+SMA wire) and the reference TES model (SH + Cu wire) (a) Cumulative energy and (b) Cost analysis

7.2.2. Experimental Work

Regarding the experimental work, the below-mentioned ideas can be implemented as part of the proposed future work.

For sensible storage applications

- Testing iCMHX in real CPU cooling environment

The working liquid used will be ethylene glycol instead of water as used in real-life applications, equipped inside an integrated liquid pump system. The heat is supplied by a dummy motherboard which is electrically heated. The air is supplied through the fan, which a Pulse Width Modulation fan controller controls. A schematic of the test loop is shown here in Figure 89. A detailed study on the reliability of iCMHXs based on operating temperature and pressure conditions in different applications is recommended.

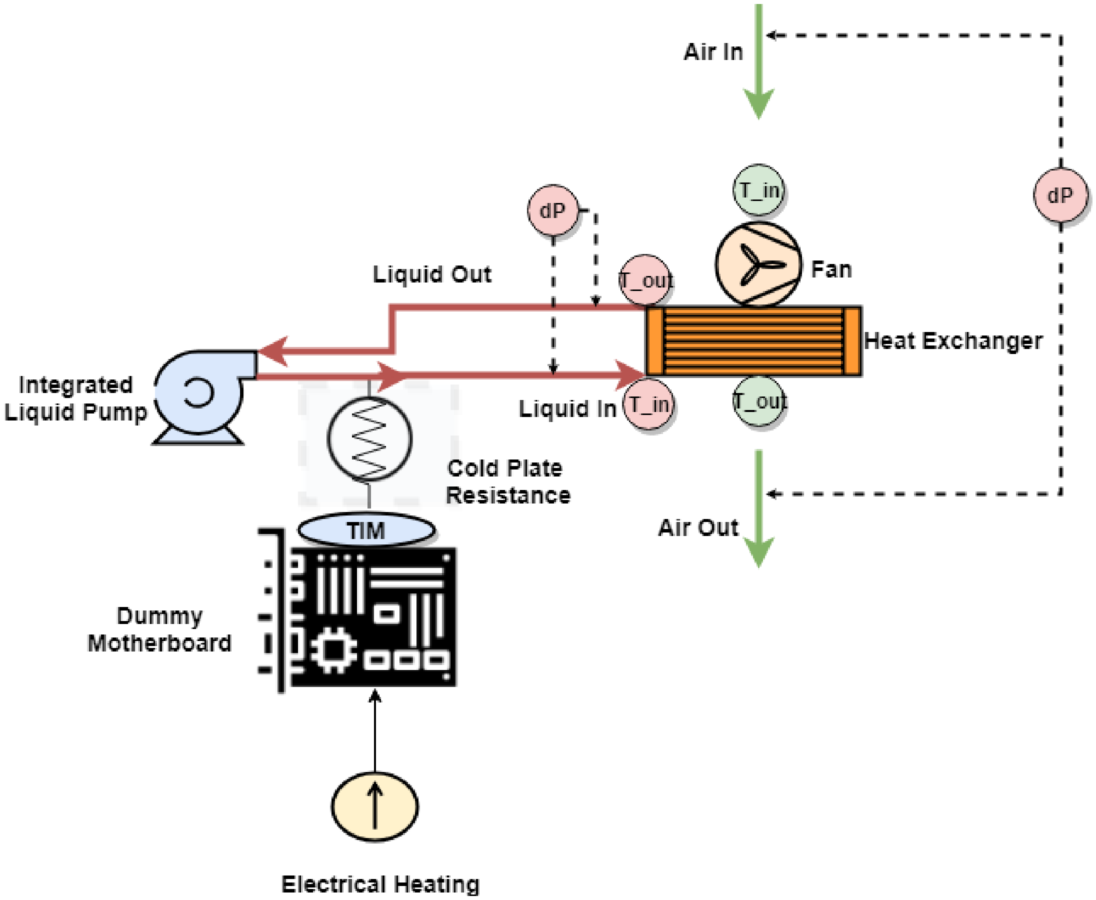

Figure 89: Schematic of test loop for iCMHX used as CPU radiator in real-life CPU cooling environment

- Wilson Plot Methodology for Finned Surfaces on Both Fluid-Sides

The methodology to compute the individual heat transfer coefficients for the present iCMHX is described below:

Step 1: Break the overall thermal resistance into the individual thermal resistances using the resistance circuit diagram. This gives us the following equation:

$$R_{total} = \left(\frac{1}{h_a A_a^{fins} \eta_a}\right)_{airside} + \left(\frac{1}{h_w A_w^{fins} \eta_w}\right)_{liquidside} + \left(\frac{t_{wall}}{k_{cu} A_{Cu}^{cs}}\right)_{walls}$$

Step 2: Identify which of the fluids have a varying flow rate. In our case, the waterside flow rate is varied, keeping the airside flowrate constant.

Step 3: Substitute h from the Nusselt correlations obtained from CFD into Equation from **Step1.**

$$h_a = \frac{k_a}{D}(a' + b' Re_a^m)$$

$$h_a = \frac{k_a}{D}\left(a' + b'\left(\frac{\rho_a v_a D}{\mu_a}\right)^m\right)$$

$$h_a = a + b v_a^m$$

Similarly, computing the same for h_w:

$$h_w = c + d v_w^m$$

Substituting into the Equation from **Step1:**

$$R_{total} = \left(\frac{1}{f_1(v_a) A_a^{fins} f_2(v_a)}\right)_{airside} + \left(\frac{1}{f_3(v_w) A_w^{fins} f_4(v_w)}\right)_{liquidside} + \left(\frac{t_{wall}}{k_{cu} A_{Cu}^{cs}}\right)_{walls}$$

Step 4: Formulate the Wilson plot equation and graphically represent the equation, as explained in the literature.

$$\frac{1}{UA_o} = \left(\frac{m}{f_3(v_w)f_4(v_w)}\right)_{liquidside} + C$$

where $f_3(v_w) = \tanh(A + Bv_w^n)$ and $f_4(v_w) = A + Bv_w^n \in A\ and\ B$ are curve-fitting coefficients.

There are four unknowns i.e., $A, B, m,$ and C which can be found from the linear regression method.

Step 5: Obtain R_{water} using m from Wilson plot as shown below in the following Equation:

$$R_{water} = \left(\frac{m}{f_3(v_w)f_4(v_w)}\right)_{liquidside}$$

Once, R_{water} is determined corresponding to the varied waterside flowrates at constant airside flowrate, the airside flowrate is now determined from Step 1. The airside flowrate computed here corresponds to the varied air flowrates where R_{water} corresponds to the similar flow rates for which it was obtained using the Wilson plot method.

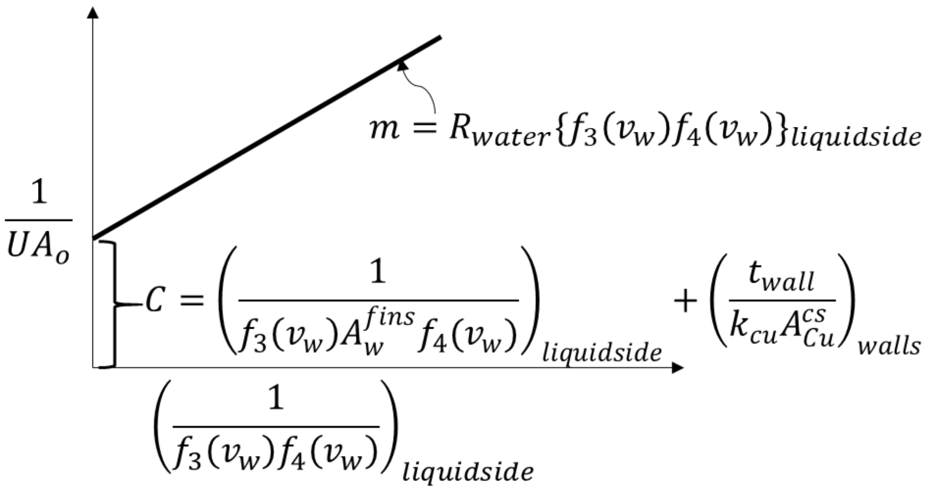

Figure 90: Wilson Plot for Waterside

For latent storage applications

A detailed analysis to study the thermophysical properties of PCMs, mainly the salt hydrates, should be done. Since the use of Glauber's salt as PCM is proposed in this dissertation, an experimental investigation should be carried out to know the composition of the salt-hydrate mixture required to have the desired phase-transition properties. There would also be some challenges, such as sub-cooling and phase-segregation, which need to be figured out.

7.3. List of Publications

Conferences

1. G. Kailkhura, R. K. Mandel, A. H. Shooshtari and M. Ohadi, "Numerical Investigation of an Integrated Cross-Media Heat Exchanger (iCMHX) for Gas-to-Liquid Cooling Applications," *2020 19th IEEE Intersociety Conference on Thermal and Thermomechanical Phenomena in Electronic Systems (ITherm)*, 2020, pp. 501-509, doi: 10.1109/ITherm45881.2020.9190398.

2. Kailkhura, G, Mandel, R, Shooshtari, A, & Ohadi, M. "Experimental Study of a Set of Integrated Cross-Media Heat Exchangers (iCMHXs) for Liquid Cooling in Desktop Computers," *Proceedings of the ASME 2020 International Technical Conference and Exhibition on Packaging and Integration of Electronic and Photonic Microsystems*. *ASME 2020 International Technical Conference and Exhibition on Packaging and Integration of Electronic and Photonic Microsystems*. Virtual, Online. October 27–29, 2020. V001T08A006. ASME. https://doi.org/10.1115/IPACK2020-2591

3. V. Ayyagari, G. Kailkhura, R. K. Mandel, A. H. Shooshtari and M. M. Ohadi, "Performance Characterization of a Novel Low-Cost Additively Manufactured PCM-to-Air Polymer Composite Heat Exchanger for Building Equipment Peak Load Shifting," *2022 21st IEEE Intersociety Conference on Thermal and Thermomechanical Phenomena in Electronic Systems (ITherm)*, 2022 (Submitted)

Journals

1. Kailkhura, G.; Mandel, R.K.; Shooshtari, A.; Ohadi, M. Numerical and Experimental Study of a Novel Additively Manufactured Metal-Polymer Composite Heat-Exchanger for Liquid Cooling Electronics. *Energies* 2022, *15*, 598. https://doi.org/10.3390/en15020598

2. Kailkhura, G.K.; Mandel, R,K; Shooshtari, A.H.; Ohadi, M., "A 1D Reduced Order Model (ROM) for a Novel Latent Thermal Energy Storage (TES) System," Energies 2022 (submitted and under review)

Appendices

Appendix A

Flow-chart for dissertation layout

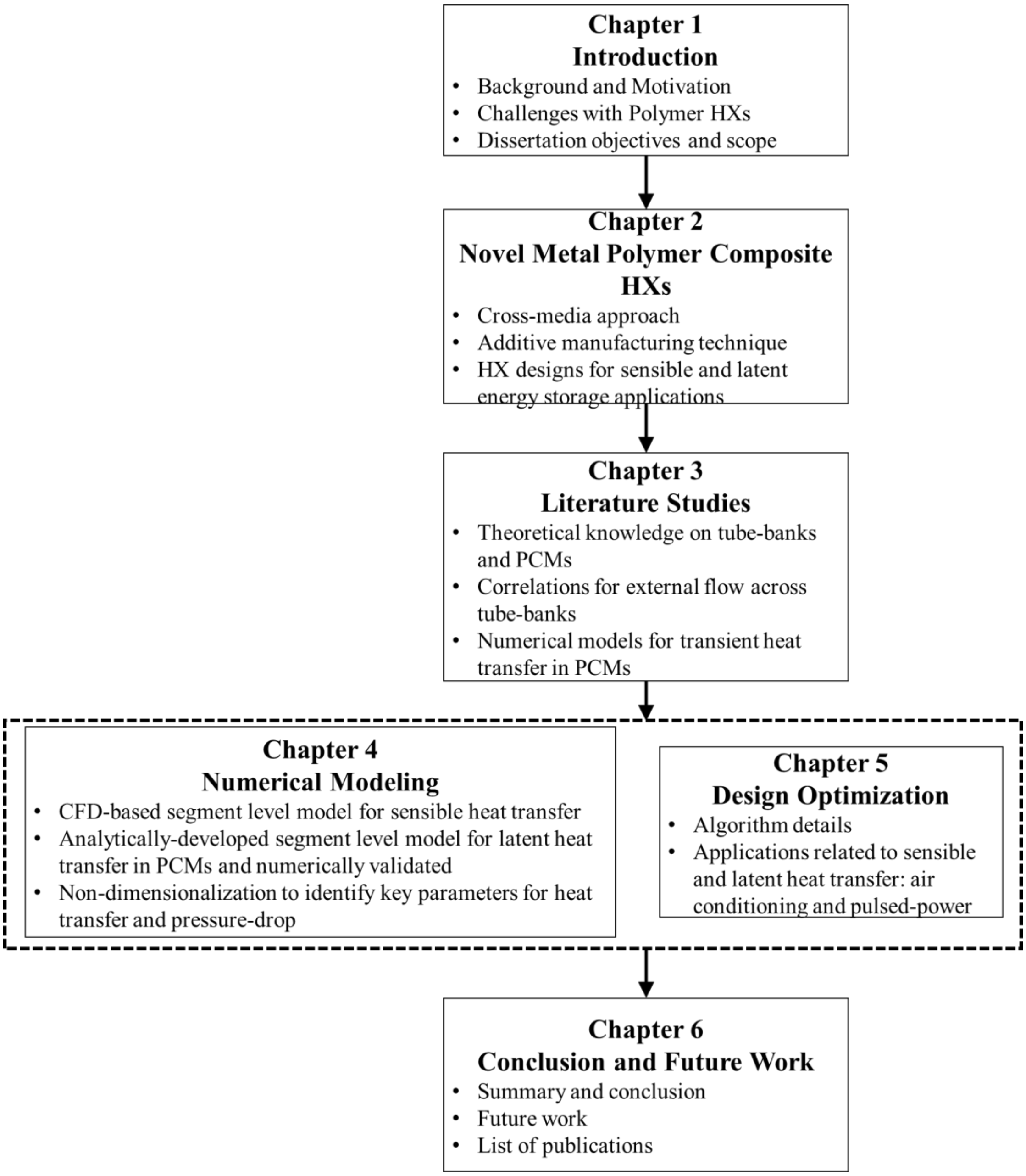

Figure 91:Organization of dissertation

Appendix B.1.

Range of Overlaps

The range of $\frac{S_T}{S_L}$ values determine the nature of overlaps. There can be majorly five cases of overlap-types depending on their geometrical spacing between the neighboring PCM cylinders.

1. Overlap in direction of S_T or S_T controlled

For this to occur, $S_T < 2r_{max}$ (see *Figure 92* (a) and (b)). Substituting r_{max} from Equation (31) and simplifying the above equation in terms of S_T/S_L, we get:

$$\frac{S_T}{S_L} < \frac{4}{\pi} \; or \; 1.27 \tag{65}$$

But for $\frac{S_T}{S_L} < 1.27$, there can also be overlaps between n-PCM cylinders kept at nS_T distance apart; when $n > 1$. For that to occur, $nS_T < 2r_{max}$ the condition should be satisfied; yielding

$$\frac{S_T}{S_L} < \frac{1.27}{n^2} \tag{66}$$

However, our present study is limited to overlaps only due to neighboring cylinders ($n = 1$). Thus, the equivalent S_T/S_L the range can be defined as:

$$0.32 < \frac{S_T}{S_L} < 1.27 \tag{67}$$

where the lower limit of S_T/S_L occurs when $n = 2$ in Equation (65).

2. Overlap in direction of S_D or S_D controlled

Similarly, for this to occur (see *Figure 92* (b), (c), and (d)), we need to meet the following conditions but instead of S_T, we have S_D:

$$S_D < 2\sqrt{\frac{S_T S_L}{\pi}} \tag{68}$$

where $S_D = \sqrt{(S_T/2)^2 + (S_L)^2}$

Expressing Equation (68) in terms of S_T and S_L and further simplification of the inequality yields the actual bounds for overlap between the neighboring PCM cylinders in the direction of S_D as:

$$0.97 < \frac{S_T}{S_L} < 4.12 \tag{69}$$

Moreover, it is found out that any overlaps possible between n-PCM cylinders ($n > 1$) aren't geometrically possible. Thus, Equation (69) gives the actual bounds.

3. Overlap in direction of S_L or S_L controlled

For this to occur (see *Figure 92* (d) and (e)), we need the minimum distance between neighboring PCM cylinders in the longitudinal direction ($2S_L$) to be less than diameter of the PCM cylinders of maximum radii. Further simplification of the inequality gives the following condition:

$$\frac{S_T}{S_L} > 3.142 \tag{70}$$

Moreover, to avoid any possible overlaps between n-PCM cylinders, the new limits for $\frac{S_T}{S_L}$ would be:

$$3.142 < \frac{S_T}{S_L} < 3.142n^2 \tag{71}$$

Thus, the equivalent range is:

$$3.142 < \frac{S_T}{S_L} < 12.6 \tag{72}$$

where the upper limit of S_T/S_L occurs when $n = 2$ in Equation (71)

Lastly, to ensure that the PCM cylinders don't overlap with the wires, the following condition must be satisfied:

$$r_0 \leq \min(r_{max}, p - r_{max}) \tag{73}$$

where $p = \min(S_T, 2S_L, S_D)$; valid for all types of overlaps in any distance

Graphically, summarizing the above the overlaps-types gives five possible cases, as shown in *Figure 92*.

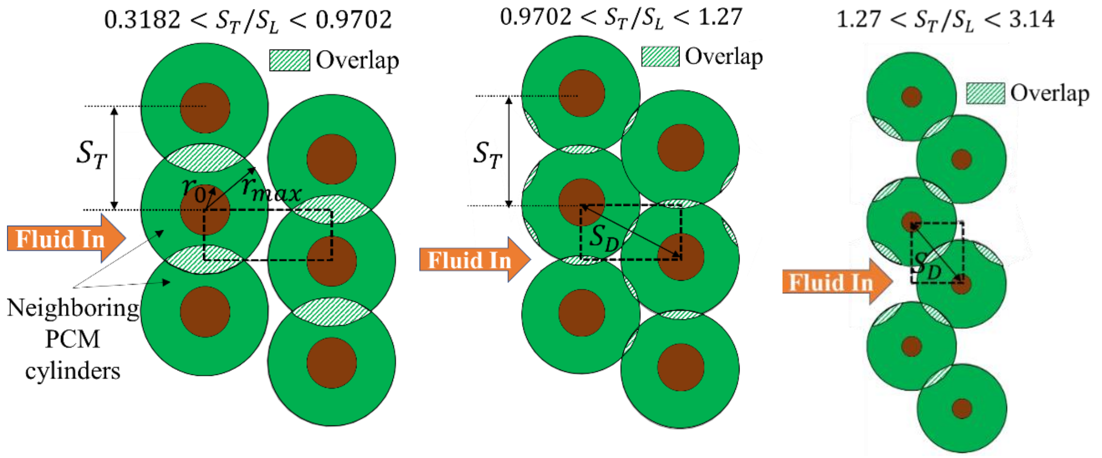

(a) S_T controlled only (b) S_T and S_D controlled (c) S_D controlled only

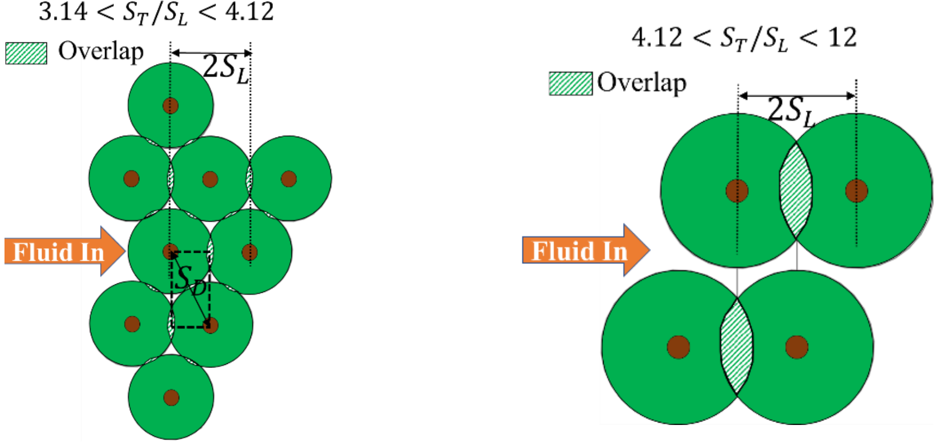

(d) S_D and S_L controlled (e) S_L controlled only

Figure 92: Range of S_T/S_L for different cases based on directions of overlap in S_T ,S_L *and* S_D

Appendix B.2.

Geometric Behavior of Overlap Regions

Mathematically, the PCM area (A_{overlap}) can be computed based on their controlled directions. For overlaps in the direction of S_T or S_L , the overlap area (A_1) is obtained, as shown in Figure 33 (b) and Equation (74):

$$A_1 = \frac{r_{max}^2}{4}(\alpha - \sin(\alpha)) \tag{74}$$

where $\alpha = 2\cos^{-1}\left(\frac{\min(S_T, 2S_L)}{r_{max}}\right)$

Similarly, for overlaps in the S_D direction, the overlap area (A_2) is obtained, as shown in Figure 33 (b) and Equation (75):

$$A_2 = r_{max}^2(\beta - \sin(\beta)) \tag{75}$$

where $\beta = 2\cos^{-1}\left(\frac{S_D}{r_{max}}\right)$

The total overlapped area, $A_{overlap}$, (see Figure 33 (b)) is:

$$A_{overlap} = 2A_1 + A_2$$

And, the ratio of the total overlapped area to the total PCM domain area ($A_{ratio} = A_{overlap}/A_{radial}$) is found out to be dependent only on S_T/S_L and r_{max}/r_0 values, as shown in Equation (76).

$$A_{ratio} = \frac{\left(\frac{r_{max}}{r_0}\right)^2\left(\alpha - \sin(\alpha) + 2(\beta - \sin(\beta))\right)}{\pi(\left(\frac{r_{max}}{r_0}\right)^2 - 1)} = f\left(\frac{r_{max}}{r_0}, \frac{S_T}{S_L}\right) \tag{76}$$

Appendix C

Non-dimensionalization of Main Governing Equation of ROM

First, the discretized form of the main governing equation of ROM (see Equation (40)), based on single PCM-wire model is obtained. Here, the nominal heat transfer rate (q_0) is substituted in terms of latent thermal energy storage (Δe_i) for a single ith PCM-wire model which is then further expressed in the discretized form (see Equation (42)) of r_i and t: $r_i(t+\Delta t)$ and Δt terms respectively.

$$\frac{T_i - T_{PCM}}{R_{fluid} + \frac{\log\left(\frac{r_i(t)}{r_0}\right)}{\eta_{PCM} k_{PCM} \pi W_{PCM}}} = \rho_{PCM}\left(\frac{W_{PCM}}{2}\right)\left(\pi\left(r_i^2(t+\Delta t) - r_i^2(\Delta t)\right)\right)\frac{H}{\Delta t} \quad (77)$$

where the index i takes the value of 1 to N_L wires

Now, the discretized PCM area term $(\pi(r_i^2(t+\Delta t) - r_i^2(\Delta t)))$ for Δt time-step is converted into a differential PCM area term ($2\pi r_i dr_i$) for dt time-step provided very small changes exist in the values of r_i between infinitesimally small intervals of Δt. Thus, the differential form of the main governing equation is:

$$\frac{T_i - T_{PCM}}{R_{total}} = \rho_{PCM}\left(\frac{W_{PCM}}{2}\right)\left(2\pi r_i \frac{dr_i}{dt}\right)\mathrm{H} \quad (78)$$

where the index i takes the value of 1 to N_L wires and $R_{total} = R_{fluid} + R_{cond} + \frac{log\left(\frac{r_i}{r_0}\right)}{(\eta k)_{PCM}\pi W_{PCM}}$.

Second, a non-dimensionalized form of Equation (78) is obtained by substituting Equation (50) and (51) which contain non-dimensionalized forms of r_i and t:

$$\frac{T_i - T_{PCM}}{R_{fluid} + R_{cond} + \frac{log(r_i^*)}{(\eta k)_{PCM}\pi W_{PCM}}} = \rho_{PCM}\left(\frac{W_{PCM}}{2}\right)\left(\frac{2\pi r_0^2}{t_0} r_i^* \frac{dr_i^*}{dt^*}\right)\mathrm{H} \quad (79)$$

where the index i takes the value of 1 to N_L wires

Performing variable separation to get r_i^* terms on RHS and t^* terms on LHS yields the following equation:

$$(T_i - T_{PCM})\left(\left(\frac{k}{H\rho}\right)_{PCM}\frac{t_0}{r_0^2}\right) dt^* \tag{80}$$

$$= r_i^*\left(\left(R_{fluid} + R_{cond}\right)k_{PCM}\pi W_{PCM} + \frac{log(r_i^*)}{\eta_{PCM}}\right) dr_i^*$$

where the index i takes the value of 1 to N_L wires

Third, the Equation (80) can now be re-arranged to form meaningful dimensionless parameters, Ste and Fo:

$$\tau\, dt^* = r_i^*\left((R_{fluid} + \mathrm{R_{cond}})(k_{PCM}\pi W_{PCM}) + \frac{\log(r_i^*)}{\eta_{PCM}}\right) dr^* \tag{81}$$

where $\tau = Ste \times Fo$ is dimensionless constant and is defined in *Table 11*.

Here, $Ste = \frac{Cp_{PCM}(T_i - T_{PCM})}{\Delta H_{PCM}}$ and $Fo = \frac{k_{PCM}t_0}{Cp_{PCM}\rho r_0^2}$ as typically used in the literature [52].

Fourth, the Equation (81) is now re-arranged by simplifying the η_{PCM} term. The η_{PCM} term is simplified from the main source Equation (38), as shown in the following equation.

$$\eta_{PCM} = \frac{\tanh\left(\sqrt{\left(\frac{2\pi k_{PCM}W_{PCM}}{\log(r_{max}^*)}\frac{\log(r_{max}^*)}{\log(r_i^*)}\right)\left(\frac{W_{PCM}}{\pi r_0^2 k_{wire}}\right)}\right)}{\sqrt{\left(\frac{2\pi k_{PCM}W_{PCM}}{\log(r_{max}^*)}\frac{\log(r_{max}^*)}{\log(r_i^*)}\right)\left(\frac{W_{PCM}}{\pi r_0^2 k_{wire}}\right)}} \tag{82}$$

where $r_{max}^* = r_{max}/r_0$

Let resistance-related parameters be defined as $R_{PCM}^{max} = \frac{\log(r_{max}^*)}{2\pi k_{PCM}W_{PCM}}$ and $R_{wire} = \frac{W_{PCM}}{k_{wire}\pi r_0^2}$. Thus, Equation (82) can be expressed as:

$$\eta_{PCM} = \frac{1}{\sqrt{R^*_{wire}}}\sqrt{\log(r_i^*)}\tanh\left(\sqrt{\left(\frac{R^*_{wire}}{\log(r_i^*)}\right)}\right) = f'(r_i^*, R^*_{wire}) \tag{83}$$

where $R^*_{wire} = \frac{R_{wire}}{R^{max}_{PCM}}\log(r^*_{max})$ is some dimensionless constant (see *Table 11*), which is also found to be equivalent to $2k^*LR^2$.

Fifth, the Equation (81) is now re-arranged by simplifying the $((R_{fluid} + \mathrm{R_{cond}})(k_{PCM}\pi W_{PCM}))$ term. Since the main computational domain is the PCM domain, the single PCM-wire model with convective boundary (h_{fluid}) circumferentially around the wires can be simplified into a PCM computational domain model (see Figure 31 (b) and Figure 93) with an equivalent convective boundary (h'_{fluid}) at the wire's cross-section such that the fluid-side resistance is the same. Thus, Equation (81) gets simplified to:

$$\tau dt^* = r^*\left(\left(\frac{k_{wire}}{h'_{fluid}(2r_0)}\right)\left(\frac{r_0}{W_{PCM}}\right)\left(\frac{2k_{PCM}}{k_{wire}}\frac{W^2_{PCM}}{r_0^2}\right) + \frac{\log(r^*)}{f'(r^*, R^*_{wire})}\right)dr^* \tag{84}$$

Let the terms be defined in known dimensionless parameters present in the literature [52]: $Bi = \frac{k_{wire}}{h'_{fluid}(2r_0)}$, and let there be simple ratios such as thermal-conductivity $k^* = \frac{k_{PCM}}{k_{wire}}$ and $LR = \frac{W_{PCM}}{r_0}$. Together these terms can be grouped as, $Bi \times LR$, which is also equivalent to R_{wire}/R_{fluid} ratio (see *Table 11*).

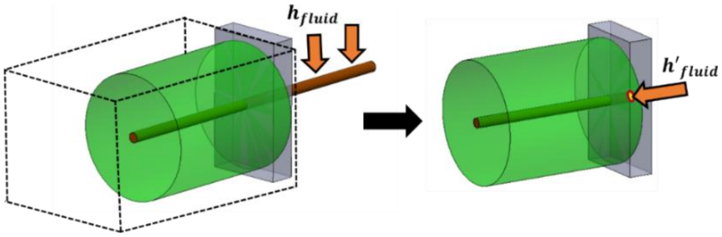

Figure 93: Simplification of the computational domain of single wire domain

Thus, Equation (81) can be expressed as,

$$\tau dt^{*} = r_i^{*}\left(\left(\frac{1}{Bi \times LR}\right)(R_{wire}^{*}) + \frac{\log(r_i^{*})}{f'(r_i^{*}, R_{wire}^{*})}\right)dr_i^{*} \tag{85}$$

Bibliography

1. Qasem NAA, Zubair SM. Compact and microchannel heat exchangers: A comprehensive review of air-side friction factor and heat transfer correlations. Energy Convers Manag. 2018 Oct 1;173:555–601.

2. Pasupathy A, Athanasius L, Velraj R, Seeniraj R V. Experimental investigation and numerical simulation analysis on the thermal performance of a building roof incorporating phase change material (PCM) for thermal management. Appl Therm Eng. 2008 Apr 1;28(5–6):556–65.

3. Sharma A, Tyagi V V., Chen CR, Buddhi D. Review on thermal energy storage with phase change materials and applications. Renew Sustain Energy Rev. 2009 Feb 1;13(2):318–45.

4. Al-Saadi SN, Zhai Z. Modeling phase change materials embedded in building enclosure: A review. Renew Sustain Energy Rev. 2013;21:659–73.

5. Bansal NK, Buddhi D. An analytical study of a latent heat storage system in a cylinder. Energy Convers Manag. 1992 Apr 1;33(4):235–42.

6. Deisenroth DC, Bar-cohen A. Ipack2015-48637 Review of Most Recent Progress on Development of Polymer Heat. 2016;1–10.

7. Chen X, Su Y, Reay D, Riffat S. Recent Research Developments in Polymer Heat Exchangers-A Review. [cited 2021 Aug 27]; Available from: http://www.matweb.com

8. Hussain ARJ, Alahyari AA, Eastman SA, Thibaud-Erkey C, Johnston S, Sobkowicz MJ. Review of polymers for heat exchanger applications: Factors

concerning thermal conductivity. Appl Therm Eng. 2017 Feb 25;113:1118–27.

9. Harris C, Despa M, Kelly K. Design and fabrication of a cross flow micro heat exchanger. J Microelectromechanical Syst. 2000 Dec;9(4):502–8.

10. Rajagopal MC, Chang HC, Man T, Kuntumalla G, Meng Y, Sundar S, et al. Materials-to-device design of hybrid metal-polymer heat exchanger tubes for low temperature waste heat recovery. Int J Heat Mass Transf [Internet]. 2019 Nov 1 [cited 2021 Aug 27];143:118497. Available from: https://experts.illinois.edu/en/publications/materials-to-device-design-of-hybrid-metal-polymer-heat-exchanger

11. Heat exchanger and method for manufacturing same. 1994 Aug 19;

12. Fugmann H, Schnabel L, Frohnapfel B. Heat transfer and pressure drop correlations for laminar flow in an in-line and staggered array of circular cylinders. Numer Heat Transf Part A Appl. 2019;

13. N. Sahiti. Thermal and fluid dynamic performance of pin fin heat transfer surfaces. Friedrich-Alexander Universit€at, Erlangen-Nurnberg; 2006.

14. Prog. RG-CE, 1965 undefined. Flexible-tube heat exchangers. ci.nii.ac.jp [Internet]. [cited 2021 Nov 20]; Available from: https://ci.nii.ac.jp/naid/10006953794/

15. Trp A. An experimental and numerical investigation of heat transfer during technical grade paraffin melting and solidification in a shell-and-tube latent thermal energy storage unit. Sol Energy. 2005 Dec 1;79(6):648–60.

16. Gong ZX, Mujumdar AS. Finite-element analysis of cyclic heat transfer in a shell-and-tube latent heat energy storage exchanger. Appl Therm Eng. 1997 Jun 1;17(6):583–91.

17. Ismail KAR, Alves CLF, Modesto MS. Numerical and experimental study on the solidification of PCM around a vertical axially finned isothermal cylinder. Appl Therm Eng. 2001 Jan 1;21(1):53–77.

18. El-Dessouky H, Al-Juwayhel F. Effectiveness of a thermal energy storage system using phase-change materials. Energy Convers Manag. 1997 Apr 1;38(6):601–17.

19. Jian-you L. Numerical and experimental investigation for heat transfer in triplex concentric tube with phase change material for thermal energy storage. Sol Energy. 2008 Nov;82(11):977–85.

20. Singh R, Sadeghi S, Shabani B. Thermal conductivity enhancement of phase change materials for low-temperature thermal energy storage applications. Energies. 2019 Jan 1;12(1).

21. Milián YE, Gutiérrez A, Grágeda M, Ushak S. A review on encapsulation techniques for inorganic phase change materials and the influence on their thermophysical properties. Renew Sustain Energy Rev. 2017 Jun 1;73:983–99.

22. Höhlein S, König-Haagen A, Brüggemann D, Koenig A, De(-Haagen@uni-Bayreuth, Brueggemann@uni D, et al. Macro-Encapsulation of Inorganic Phase-Change Materials (PCM) in Metal Capsules. Mater 2018, Vol 11, Page 1752 [Internet]. 2018 Sep 17 [cited 2021 Dec 26];11(9):1752. Available from:

https://www.mdpi.com/1996-1944/11/9/1752/htm

23. Kailkhura G, Mandel RK, Shooshtari AH, Ohadi MM. Experimental Study of a Set of Integrated Cross-Media Heat Exchangers (iCMHXs) for Liquid Cooling Applications in Desktop Computers. In: InterPACK 2020. 2020. p. 1–58.

24. Kailkhura G, Mandel RK, Shooshtari AH, Ohadi MM. Numerical Investigation of an Integrated Cross-Media Heat Exchanger (iCMHX) for Gas-to-Liquid Cooling Applications. In: IEEE Intersociety Conference on Thermal and Thermomechanical Phenomena in Electronic Systems (iTherm). 2020.

25. Arie MA, Shooshtari AH, Tiwari R, Dessiatoun S V., Ohadi MM, Pearce JM. Experimental characterization of heat transfer in an additively manufactured polymer heat exchanger. Appl Therm Eng. 2017;

26. Arie MA, Hymas DM, Singer F, Shooshtari AH, Ohadi M. An additively manufactured novel polymer composite heat exchanger for dry cooling applications. Int J Heat Mass Transf. 2020;

27. Singer F, Deisenroth DC, Hymas DM, Dessiatoun S V, Ohadi MM. Additively Manufactured Copper Components and Composite Structures for Thermal Management Applications.

28. Hymas D, Dessiatoun S, Ohadi MM. Metal/Polymer Composite Additive Manufacturing (mfc-am) and Composite Structures Formed by mfc-am. United States Patent and Trademark Office 62/405,085, 2018.

29. Hymas DM, Arle MA, Singer F, Shooshtari AH, Ohadi MM. Enhanced air-side

heat transfer in an additively manufactured polymer composite heat exchanger. Proc 16th Intersoc Conf Therm Thermomechanical Phenom Electron Syst ITherm 2017. 2017;634–8.

30. Arie M, Hymas D, Singer F, Shooshtari A, Ohadi M. Performance characterization of a novel cross-media composite heat exchanger for air-to-liquid applications. Intersoc Conf Therm Thermomechanical Phenom Electron Syst ITHERM. 2019;2019-May:933–40.

31. Hymas DM, Arle MA, Singer F, Shooshtari AH, Ohadi MM. Enhanced air-side heat transfer in an additively manufactured polymer composite heat exchanger. In: Proceedings of the 16th InterSociety Conference on Thermal and Thermomechanical Phenomena in Electronic Systems, ITherm 2017. 2017. p. 634–8.

32. Kenisarin M, Mahkamov K. Solar energy storage using phase change materials. Renewable and Sustainable Energy Reviews. 2007.

33. Hirschey J, Gluesenkamp KR, Mallow A, Graham S. Review of Inorganic Salt Hydrates with Phase Change Temperature in Range of 5 ° C to 60 ° C and Material Cost Comparison with Common Waxes. 5th Int High Perform Build Conf. 2018;1–10.

34. Chilton TH, Genereaux RP. Pressure Drop Across Tube Banks. Transacitons Am Inst ofChemical Eng. 1933;29:161–73.

35. Sieder EN, Scott, Jr. NA. Fluid Friction at Parallel and Right Angles to Tubes and Tube Banks. ASME Unpubl Pap. 1932;83.

36. Pierson OL. Experimental Investigation of Tube Arrangement on Convection Heat Trasnfer and Flow Resistance in Cross Flow of Gases Over Tube Banks. Trans ASME. 1937;59:563–72.

37. Huge EC. Experimental Investigation of Effects of Equipment Size on Convection Heat Transfer and Flow Resistance in Cross Flow of Gases over Tube Banks. Trans ASME. 1937;59:573–81.

38. Wallis RP, White CM. Resistance to Flow Through Nests of Tubes. Trans ASME. 1938;59:583–94.

39. Norris RH, Spofford WA. High Performance Fins for Heat Transfer. Trans ASME. 1942;64:489–96.

40. Gunther AY, Shaw WA. Correlation and Utilization of New Data on Flow Resistance and Heat Transfer for Cross Flow of Gases over Tube Banks. Trans ASME. 1945;67:643–60.

41. Still EW. Heat Transfer and Flow Resistance in Cross Flow of Gases Over Tube Banks. Trans ASME. 1938;381–3.

42. Grimison ED. Correlation and Utilization of New Data on Flow Resistance and Heat Transfer for Cross Flow of Gases over Tube Banks. Trans ASME. 1937;59:583–94.

43. Patterson WS. Heat Transfer and Flow Resistanec in Cross Flow of Gases over Tube Banks. Trans ASME. 1938;381.

44. Jakob M. Heat Transfer and Flow Resistance in Cross Flow of Gases over Tube

Banks. Trans ASME. 1938;384–6.

45. Boucher DF, Lapple CE. A General Correlation of Friction Factors for Various Types of Surfaces in Crossflow. Trans ASME. 1945;67(8):656–8.

46. Zukauskas A. Heat transfer from tubes in crossflow. Adv Heat Transf. 1972;8:93–160.

47. Gaddis ES. Pressure Drop of Tube Bundles in Cross Flow. In: VDI Heat Atlas Second Edition. 2010. p. 1076–91.

48. Thomas A, Apelt CJ. No Title. F Comput Eng Phys. 1961;

49. Le Clair BP, Hamielec AE. Viscous Flow through Particle Assemblages at Intermediate Reynolds Number. Ind Eng Chrm Fund. 1970;9:608–13.

50. Launder BE, Massey TH. The numerical prediction of viscous flow and heat transfer in tube banks. J Heat Transfer. 1978;

51. Safwat Wilson A, Khalil Bassiouny M. Modeling of heat transfer for flow across tube banks. Chem Eng Process Process Intensif. 2000;

52. Lane GA. Solar heat storage: Latent heat material: Volume I: Background and scientific principles. Solar Heat Storage: Latent Heat Material: Volume I: Background and Scientific Principles. 2018.

53. J S. S B Wien. Akad Mat Natur. 1889;98:473–84, 965–83.

54. Jiji LM. Heat conduction: Third edition. Heat Conduct (Third Ed. 2009;1–418.

55. Lane GA. Solar heat storage: Latent heat material: Volume II: Technology. Sol

Heat Storage Latent Heat Mater Vol II Technol [Internet]. 2018 Jan 1 [cited 2021 Nov 8];1–235. Available from: https://www.mendeley.com/catalogue/11318a62-906b-3eda-b010-555868d9e8cc/?utm_source=desktop&utm_medium=1.19.4&utm_campaign=open_catalog&userDocumentId=%7B209f7d14-683d-4975-9d66-b0424f4105c0%7D

56. Ehms JHN, De Césaro Oliveski R, Rocha LAO, Biserni C, Garai M. Fixed Grid Numerical Models for Solidification and Melting of Phase Change Materials (PCMs). Appl Sci 2019, Vol 9, Page 4334 [Internet]. 2019 Oct 15 [cited 2021 Dec 19];9(20):4334. Available from: https://www.mdpi.com/2076-3417/9/20/4334/htm

57. Dutil Y, Rousse DR, Salah N Ben, Lassue S, Zalewski L. A review on phase-change materials: Mathematical modeling and simulations. Renew Sustain Energy Rev. 2011 Jan 1;15(1):112–30.

58. Huang K, Feng G, Zhang J. Experimental and numerical study on phase change material floor in solar water heating system with a new design. Sol Energy. 2014;105:126–38.

59. Kailkhura G, Mandel RK, Shooshtari A, Ohadi MM. Numerical and Experimental Study of a Novel Additively Manufactured Metal-Polymer Composite Heat-Exchanger for Liquid Cooling of Electronics. Energies.

60. Incropera FP, De Witt DP. Fundamentals of heat transfer. 1981;

61. Rodgers P, Goharzadeh A, Ali OAE, Eveloy V. An experimental and numerical

investigation of tube bank heat exchanger thermofluids. EuroSimE 2008 - Int Conf Therm Mech Multi-Physics Simul Exp Microelectron Micro-Systems. 2008;1–10.

62. Almohammadi KM, Ingham DB, Ma L, Pourkashan M. Computational fluid dynamics (CFD) mesh independency techniques for a straight blade vertical axis wind turbine. Energy. 2013;58:483–93.

63. Mandhani VK, Chhabra RP, Eswaran V. Forced convection heat transfer in tube banks in cross flow. Chem Eng Sci. 2002;

64. Zukauskas Algirdas. Heat Transfer from Tubes in Crossflow, Advances in Heat Transfer. Adv Heat Transf. 1972;8:93–160.

65. Yoo SY, Kwon HK, Kim JH. A study on heat transfer characteristics for staggered tube banks in cross-flow. J Mech Sci Technol. 2007 Mar;21(3):505–12.

66. Mandel R, Shooshtari A, Ohadi M. A “2.5-D” modeling approach for single-phase flow and heat transfer in manifold microchannels. Int J Heat Mass Transf. 2018 Nov 1;126:317–30.

67. Yuruker SU, Mandel RK, Shooshtari A, Ohadi MM. A metamodeling approach for optimization of manifold microchannel systems for high heat flux cooling applications. In: InterSociety Conference on Thermal and Thermomechanical Phenomena in Electronic Systems, ITHERM. IEEE Computer Society; 2019. p. 982–90.

68. Žkauskas A. Heat Transfer from Tubes in Crossflow. Adv Heat Transf. 1987;

69. Gharbi N El, Kheiri A, Ganaoui M El, Blanchard R. Numerical optimization of heat exchangers with circular and non-circular shapes. Case Stud Therm Eng. 2015;

70. Ahmed MA, Yaseen MM, Yusoff MZ. Numerical study of convective heat transfer from tube bank in cross flow using nanofluid. Case Stud Therm Eng. 2017;

71. El-Shaboury AMF, Ormiston SJ. Analysis of laminar forced convection of air crossflow in in-line tube banks with nonsquare arrangements. Numer Heat Transf Part A Appl. 2005;48(2):99–126.

72. Choi DH, Lee J, Hong H, Kang YT. Thermal conductivity and heat transfer performance enhancement of phase change materials (PCM) containing carbon additives for heat storage application. Int J Refrig. 2014;42:112–20.

73. Berbish NS. Heat transfer and flow behavior around four staggered elliptic cylinders in cross flow. Heat Mass Transf 2010 473 [Internet]. 2010 Nov 12 [cited 2021 Nov 6];47(3):287–300. Available from: https://link.springer.com/article/10.1007/s00231-010-0719-y

74. Simo Tala J V., Bougeard D, Russeil S, Harion JL. Tube pattern effect on thermalhydraulic characteristics in a two-rows finned-tube heat exchanger. Int J Therm Sci. 2012 Oct 1;60:225–35.

75. Hasan A. Thermal-hydraulic performance of oval tubes in a cross-flow of air.

Heat Mass Transf 2005 418 [Internet]. 2005 Mar 9 [cited 2021 Nov 6];41(8):724–33. Available from: https://link.springer.com/article/10.1007/s00231-004-0612-7

76. Ibrahim TA, Gomaa A. Thermal performance criteria of elliptic tube bundle in crossflow. Int J Therm Sci. 2009 Nov 1;48(11):2148–58.

77. JANG J-Y, YANG J-Y. Experimental and 3-D Numerical Analysis of the Thermal-Hydraulic Characteristics of Elliptic Finned-Tube Heat Exchangers. http://dx.doi.org/101080/01457639808939936 [Internet]. 2007 [cited 2021 Nov 6];19(4):55–67. Available from: https://www.tandfonline.com/doi/abs/10.1080/01457639808939936

78. Chen Y, Fiebig M, Mitra NK. Conjugate heat transfer of a finned oval tube part a: Flow patterns. Numer Heat Transf Part A Appl. 1998;33(4):371–85.

79. Harald Mehling; Luisa F. Cabeza. Heat and cold storage with PCM. Vol. 11, Journal of Visual Languages & Computing. 2000. 287–301 p.

80. ANSYS FLUENT 12.0 Theory Guide - 17.4 Energy Equation [Internet]. [cited 2021 Dec 24]. Available from: https://www.afs.enea.it/project/neptunius/docs/fluent/html/th/node353.htm

81. Gholamibozanjani G, Farid M. Peak load shifting using a price-based control in PCM-enhanced buildings. Sol Energy. 2020 Nov 15;211:661–73.

82. Bourne S, Novoselac A. Compact PCM-based thermal stores for shifting peak cooling loads. Build Simul. 2015;8(6):673–88.

83. https://www.trutechtools.com/Measuring-Airflow-by-Pressure-Drop_c_256.html. In.

84. Qu S, Ma F, Ji R, Wang D, Yang L. System design and energy performance of a solar heat pump heating system with dual-tank latent heat storage. Energy Build. 2015;105:294–301.

85. Laser T. Zu W. Hausotter: Fibromyalgie--ein entbehrlicher Krankheitsbegriff? Versicherungsmedizin. 1998;50(4):154–6.

86. Qu S, Ma F, Ji R, Wang D, Yang L. System design and energy performance of a solar heat pump heating system with dual-tank latent heat storage. Energy Build. 2015;105(July):294–301.

87. Mandel R, Shooshtari A, Ohadi M. A "2.5-D" modeling approach for single-phase flow and heat transfer in manifold microchannels. Int J Heat Mass Transf. 2018;

88. Churchill SW, Usagi R. A general expression for the correlation of rates of transfer and other phenomena. AIChE J. 1972;18(6):1121–8.

89. Muzychka YS, Yovanovich MM. Pressure drop in laminar developing flow in noncircular ducts: A scaling and modeling approach. J Fluids Eng Trans ASME. 2009 Nov 1;131(11):1111051–11110511.

90. Mandel RK, Bae DG, Ohadi MM. Embedded Two-Phase Cooling of High Flux Electronics Via Press-Fit and Bonded FEEDS Coolers. J Electron Packag Trans ASME. 2018;

91. Taylor BN, Kuyatt CE. Guidelines for Evaluating and Expressing the Uncertainty of NIST Measurement Results. NIST Tech Note. 1994;1297:20.

92. Lang T, Lang T, Secic M. How to report statistics in medicine: annotated guidelines for authors, editors, and reviewers [Internet]. 2006 [cited 2021 Jul 5]. Available from: https://books.google.com/books?hl=en&lr=&id=kBUBRh1AWG4C&oi=fnd&pg=PR6&ots=Mkm4MokEwi&sig=ZKZeRDlcXry3lWWpRHONrYe_cl4

93. Khan WA, Culham JR, Yovanovich MM. Convection heat transfer from tube banks in crossflow: Analytical approach. Int J Heat Mass Transf. 2006;

94. Tahseen TA, Ishak M, Rahman MM. An overview on thermal and fluid flow characteristics in a plain plate finned and un-finned tube banks heat exchanger. Renew Sustain Energy Rev. 2015;43:363–80.

95. Pressure drop in cross flow across tube bundles (Journal Article) | OSTI.GOV [Internet]. [cited 2020 Jan 14]. Available from: https://www.osti.gov/biblio/6503251-pressure-drop-cross-flow-across-tube-bundles

96. Bumke L, Zamponi C, Jetter J, Quandt E. Cu-rich Ti52.8Ni22.2Cu22.5Co2.5 shape memory alloy films with ultra-low fatigue for elastocaloric applications. J Appl Phys [Internet]. 2020 Jun 12 [cited 2022 Jan 7];127(22):225105. Available from: https://aip.scitation.org/doi/abs/10.1063/5.0006301

97. Nitinol technical properties | Johnson Matthey [Internet]. [cited 2022 Jan 7]. Available from: https://matthey.com/en/products-and-services/medical-

components/resource-library/nitinol-technical-properties